Injection molded self-cleaning surfaces

Søgaard, Emil

Publication date:
2014

Document Version
Publisher's PDF, also known as Version of record

Injection molded self-cleaning surfaces

Emil Søgaard
PhD Thesis November 2014

DTU Nanotech
Department of Micro- and Nanotechnology

Injection molded self-cleaning surfaces

PhD Thesis

Emil Søgaard
November 2014

Supervisors:
Rafael Taboryski, DTU Nanotech
Kristian Smistrup, NIL Technology

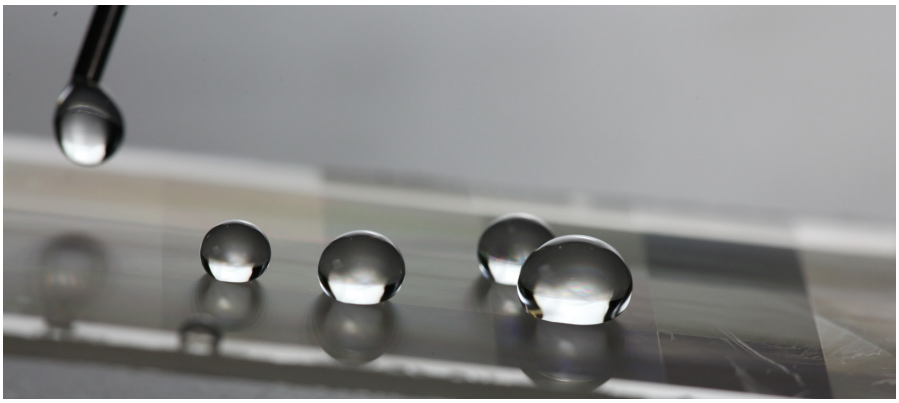

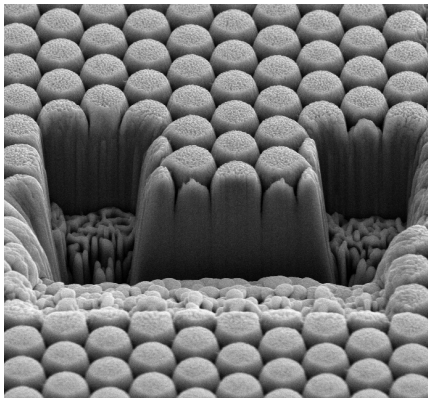

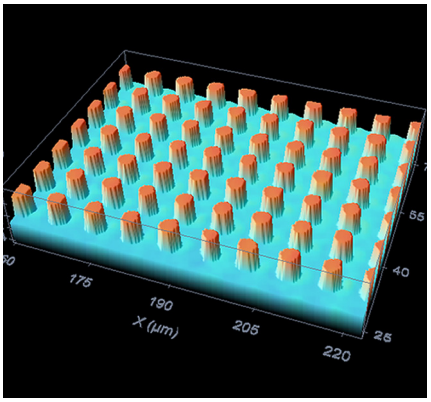

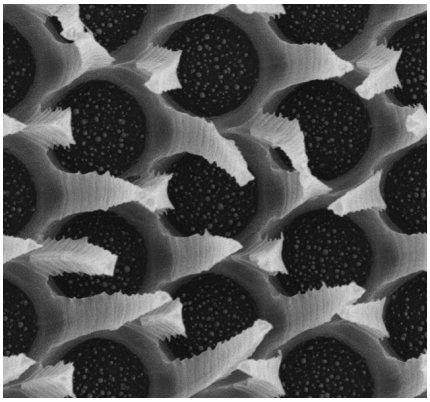

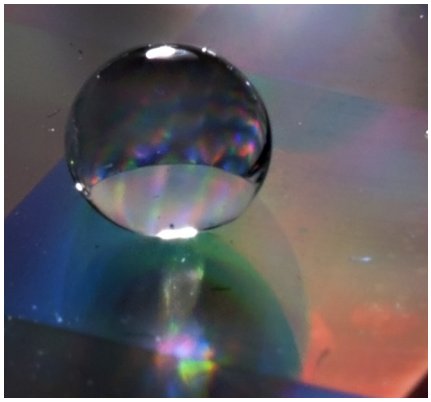

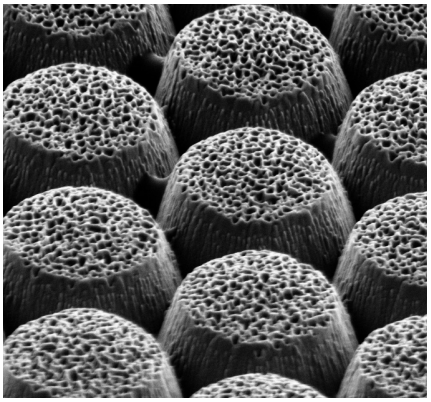

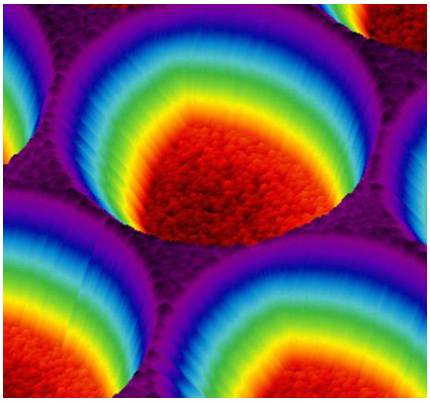

Technical University of Denmark

DTU Nanotech
Department of Micro- and Nanotechnology

Abstract

This PhD thesis concerns the development of superhydrophobic surfaces fabricated by injection molding. Today, injection molding is the prevalent production method for consumer plastic products. However, concerns regarding the environmental impact of a plastic production are increasing, especially because the use of potentially toxic self-cleaning coatings is used worldwide in a larger and larger scale.

In this context, the work in this PhD project could be seen as a scientific effort towards reducing toxic compounds in manufactured plastic parts by developing injecting molded surfaces that are superhydrophobic based on topography rather than chemical compounds.

Therefore, a novel method for fabricating superhydrophobic polymer surfaces with excellent water-repellant properties is developed. The method is based on microstructure fabrication and superposed nanostructures on silicon wafers. The nano- and microstructured silicon is electroplated with nickel and the resulting nickel shim with inverse polarity is used in an injection molding process.

A versatile injection molding process capable of producing different nano- and microstructures on areas larger than 10 cm^2 is developed. Variotherm mold heating is used to ensure complete filling of the mold and a mold cavity-depacking process step is introduced. The depacking step increases polymer shrinkage allowing the nano- and microstructures to be successfully demolded.

A systematic wetting study on injection molded polymer surfaces is performed on periodic hierarchical structures with nanograss and holes. Water wetting tests are carried out using a pressure cell to control the water pressure. Microscopic wetting behavior of the structures is studied by optical transmission microscopy. Interestingly, it is found that the surface chemistry of the polymer changes over time causing a decrease in hydrophobicity. It is concluded that the material properties of the polymer is critical for maintaining superhydrophobicity under water exposure.

A range of different structures with and without the hierarchical nanograss, pillars, micro cavities (holes), spruce like micropillars and pyramid shaped structures are examined. By employing deep ultra violet (DUV) projection lithography for mold fabrication, polymer surface feature sizes in the nanometer range could be realized over large surface areas. The superhydrophobic surfaces were fabricated from the amorphous polymer TOPAS 8007-S04 (COC) and the semi crystalline polymer PP HD601CF. An overview of the different types of structures in relation to applications is given. In particular, spruce like micropillars seems interesting. Here, the contact angles increase from 102° for unstructured polymer surfaces, to 172° for structured surfaces with a drop roll-off angle of less than 2°. Thereby, it is shown that an extremely water repellant surface can be injection molded directly with clear perspectives for more environmental and healthier plastic consumer products.

Dansk Resumé

Denne PhD-thesis beskæftiger sig med udviklingen af super-vandafvisende overflader fabrikeret ved hjælp af sprøjtestøbning, som er den vigtigste metode til at producere forskellige plastikprodukter. I dag er der fokus på plastikprodukters miljømæssige konsekvenser, specielt fordi brugen af potentielt giftige selvrensende belægninger over hele verden er stigende.

I denne sammenhæng skal dette PhD-projekt ses som en videnskabelig indsats for at reducere anvendelsen af giftige stoffer i plastikprodukter ved at udvikle sprøjtestøbte overflader, som er super-vandafvisende og baseret på topografi i stedet for kemiske stoffer.

Der er udviklet en metode til at fabrikere super-vandafvisende overflader i plastik. Metoden er baseret på fabrikation af nano- og mikrostrukturer på siliciumskiver. Nano- og mikrostrukturerne i silicium er elektroplateret med nikkel, og den fremkomne nikkel-støbeform med omvendte strukturer er brugt i sprøjtestøbeprocessen.

Der er udviklet en sprøjtestøbeproces der kan producere forskellige typer af nano- og mikrostrukturer på arealer større end 10 cm^2. I processen er der taget hensyn til at sprøjtestøbeformene fyldes helt således at nano- og mikrostrukturerne bliver præcist gengivet. De supervandafvisende overflader er lavet i to forskellige plast-typer: TOPAS 8007-S04 (COC) og polypropylen HD601CF.

Det er vigtigt at de plastikstøbte overflader kan tåle vand, så derfor er der udført en række forsøg for at undersøge hvordan de forskellige strukturer påvirkes af vand og tryk. Overfladerne er blevet undersøgt ved hjælp af optisk transmissionsmikroskopi, hvor de enkle strukturers påvirkning af vand og tryk blev observeret. Forsøg har vist at overfladen af plastikken ændres ved vandpåvirkning og at dette fører til ringere vandafvisning.

Forskellige strukturer med og uden hierarkisk nanogræs: søjler, mikrohuller, grantræs-lignende mikrosøjler og pyramider er blevet undersøgt og sammenlignet. De grantræs-lignende mikrosøjler er specielt interessante, fordi de har ekstremt gode vandafvisende egenskaber.

Forsøgene viser at det er muligt at producere ekstremt vandafvisende overflader ved hjælp af industrielbaseret sprøjtestøbning i plastik. Disse resultater har perspektiver til en fremtidig produktion af mere sundheds- og miljøvenlige plastikprodukter.

Preface

This thesis is submitted for obtaining the Philosophiae Doctor (PhD) degree at the Technical University of Denmark (DTU). The work presented here has been carried out in the Polymer Micro & Nano Engineering – POLYMIC group at the Department of Micro and Nanotechnology (DTU Nanotech) and at DTU Danchip (National Center for Micro- and Nanofabrication). The work is a part of the *Nanoplast project*.

This project was supervised by Associate Professor and Platform Leader (NanoPlast) Rafael Taboryski to whom I am grateful for support and supervision during the project period. I also want to thank my co-supervisor Process and Development Engineer Kristian Smistrup (NIL Technology) for many interesting discussions, especially on clean room fabrication, and for supervision during the project period.

I would like to thank my colleagues in the POLYMIC group, both present and former. Especially I would like to thank Ling Sun, Nis Korsgaard Andersen, Marco Matteucci, and Simon Tylsgaard Larsen who had always shared their vast knowledge with me. I would like to thank my colleagues at DTU Nanotech for many interesting conversations and fun moments. I would also like to thank the helpful staff at Danchip for running one of the best clean rooms in the world. I would also like to thank the industrial partners in the Nanoplast Project for sharing their knowledge on injection molding. Throughout the project, I have enjoyed close collaboration and beer drinking in the Friday Bar with my fellow PhD students, Emil Højlund-Nielsen, Alexander Bruun Christiansen, and Jeppe S. Clausen. I would also like to thank my students for being interested in the project and hard work.

I very much appreciate Associate Chair (Faculty), School of Mechanical & Aerospace Engineering, Professor Lam Yee Cheong, Nanyang Technological University, for his enthusiastic supervision and infinite knowledge on injection molding during my stay at his group in the autumn of 2013. I would also like to thank Lim Chun Ping and Nguyen Quoc Mai Phuong for help and interesting discussions and Martin Lim Kean Chye for laboratory support.

I show my appreciation to the Danish National Advanced Technology Foundation (now InnovationsFonden) for funding the PhD project via the NanoPlast project, and Otto Mønsted Fonden, Augustinus Fonden, and Oticon Fonden for financial support for travels.

I thank my family and friends for being patient and always supportive during three stressful years. Finally, I would like to thank my beloved Signe Agnild, whom I have missed so much, especially during the writing period.

Emil Søgaard

November 2014

List of Publications

Journal papers

Emil Søgaard, Nis K. Andersen, Kristian Smistrup, Simon Larsen, Ling Sun, and Rafael Taboryski. *Study of Transitions between Wetting States on Micro-cavity Arrays by Optical Transmission Microscopy.* Langmuir. Published online (2014). See Appendix 3.
Contribution: Development of the idea for the injection molded hierarchical nanograss structures. Microhole design. Cleanroom fabrication and injection molding of all structures. Idea, development and fabrication of pressure cell setup. Characterization of samples, data processing and analysis. Participation in manuscript writing. Drafting of figures.

Simon Tylsgaard Larsen, Nis Korsgaard Andersen, **Emil Søgaard**, and Rafael Taboryski. *Structure Irregularity Impedes Drop Roll-Off at superhydrophobic Surfaces.* Langmuir, Vol. 30 no. 17, pp 5041-5045. 2014. See Appendix 4.
Contribution: Participation in concept development of initial line based structures, and development of the fabrication process.

Conference proceedings

Emil Søgaard, Kristian Smistrup, Nis Korsgaard Andersen and Rafael Taboryski. *Injection molded superhydrophobic surfaces based on microlithography and black silicon processing.* Nanotech 2012 - TechConnect World. See Appendix 5.
Contribution: Development of the idea for the injection molded hierarchical nanograss structures. Participation in the microstructure design. Cleanroom fabrication and injection molding of all structures. Characterization of samples and data processing. Manuscript preparation.

Conference contributions

Oral presentations

Emil Søgaard, Nis Korsgaard Andersen, Rafael J. Taboryski, Kristian Smistrup. *Injection molded superhydrophobic surfaces based on microlithography and black silicon processing.* Presented at: Techcornect worldNanotech 2012.

Emil Søgaard, Kristian Smistrup, Rafael Taboryski. *Super Hydrophobic Surfaces Based on Microstructures and Black Silicon Fabricated by Injection Molding*. Presented at: Pittcon 2013.

Emil Søgaard. *Functional nanostructures on injection molded plastic*. Presented at: PRN2014 – Polymer Replication ion Nanoscale, DTU. May 2014.

Poster presentation

Alicia Charlotte Johansson, **Emil Søgaard**, Nis Korsgaard Andersen, Ling Sun, Rafael J. Taboryski. *Functional nanostructures on injection molded plastic.* Presented at: Pittcon 2014 Chicago. 2014.

Patents

Emil Søgaard, Kristian Smistrup, and Rafael Taboryski. A method for manufacturing a tool part for an injection molding process, a hot embossing process, a nano-imprint process, or an extrusion process. International Application Number PCT/DK2013/050060. 2013.

See Appendix 6.

Contribution: Development of the ideas behind the patent (injection molded hierarchical nanograss structures). Proof of concept. Participation in writing of the patent.

List of collaborators

During this work, I had the privilege to work closely with several interesting and skillful people. Below is a list with the different contributions

- A close collaboration with Nis Korsgaard Andersen with whom I have had many interesting discussion on contact angle measurement and structure design. During his master project he developed topology optimized structures, which were used in the industrial test production during this work. He further performed the wetting simulation of the meniscus intrusion in the paper in Appendix 3.
- In collaboration with my two students Martin Bjergfelt and Nikolaj Kofoed Mandsberg we together developed the concept for the pyramid structures and they performed the cleanroom fabrication of the wafers with pyramids holes as part of their project.
- Optical transmission modeling was done in close collaboration with Emil Højlund-Nielsen. He had written the basic MATLAB script and helped me modify the script to calculate the optical transmission of wettest nano- and microstructures.
- Alexander Bruun Christiansen has developed the black silicon recipe used for fabricating the hierarchical structures.
- Lim Chun Ping and Nguyen Quoc Mai Phuong helped with design and fabrication of a small environmental chamber for use with a high-speed camera, during my external stay at Nanyang Technological University (NTU). The environmental chamber was used to examine water condensation on injection molded polymer parts.
- LEGO® and Tool Partners have given the major inputs on the industrial test production and optimization on the injection molding process.

International courses

- Microscopy winter school in ETH Zurich focused on correlative microscopy and 3D reconstruction.
- Summer school in Grenoble, where I studied in one of the largest and best-equipped 12” research clean rooms in the world.

List of supervised projects and teaching

During this project, I had the privilege to supervise several talented students,

- Nis Korsgaard Andersen in a master project with title *Injection Molding and Characterization of self-cleaning surfaces* (45 ECTS)
- Nis Korsgaard Andersen and Lene Westergaard Sørensen in the special course *Experimental Studies of Single Structured Hydrophobic Surfaces* (5 ECTS)
- Martin Bjergfelt and Nikolaj Kofoed Mandsberg in two projects
    - *Superhydrophobic self-cleaning Surfaces in plastic* (10 ECTS)
    - *Special Course for the Investigation of the Superhydrophobic Properties of Hexagonal Microstructures* (5 ECTS)

Furthermore, I have worked as teaching assistant in the *PolyNano summer school* and in the course *Introduction to physics and nanotechnology* (in contact angle measurements and basic electronics).

List of abbreviations

AFM	Atomic force microscope
BHF	Buffered hydrogen fluoride
CAD	Computer aided design
CCD	Charged coupled device
COC	Cyclic olefin copolymer
DOF	Depth of field
D-RIE	Deep reactive ion etching
DUV	Deep ultraviolet
E-beam	Electron beam lithography
EDM	Electric discharge machining
FDTS	Perfluorodecyltrichlorosilane
FIB	Focused ion beam
HMDS	Hexamethyldisiloxane
LANI	Large Area Nanostructuring Initiative
LIGA	Lithographie, Galvanoformung and Abformung
MFI	melt flow index
MVD	Molecular vapor deposition
NIL	Nano imprint lithography
NTU	Nanyang Technological University
PMMA	Poly(methyl methacrylate)
PP	Polypropylene
PTFE	Polytetrafluoroethylene (Teflon)
PVC	Polyvinyl chloride
RIE	Reactive ion etching
SEM	Scanning electron microscope

Index

1 Introduction

Injection molding is among the most prevalent methods to fabricate plastic parts and components used in everyday life, ranging from the smallest components for hearing aids to entire body panels for the automotive industry. However, the efficiency and low cost of injection molding has led to a consumption-based society with environmental impact. Requirements from the end user often create a need to functionalize the plastic surface. Therefore, many plastic parts are often decorated by paint or coated in order to obtain the desired properties. The ink and coatings are often unhealthy and have large environmental impact. There is no doubt that the trend now and even more in the future will be to produce sustainable plastic products. The produced parts must be environmentally friendly and recyclable. In this context, the work described in this PhD thesis should be seen as a basic scientific effort towards reducing the use of foreign coatings on plastic parts.

In everyday life many plastic items are used in situations where they become dirty and thus detergents and soap are often required to clean the items. Adding a functionalized surface with self-cleaning properties could reduce the amount of soap used, resulting in a less environmental impact. Traditionally chemical coatings have been used to functionalize surfaces. Coatings can produce a wide range of different surface properties such as hydrophobic/hydrophilic, self-cleaning surface properties, antireflective, or color effects. However, chemically treated surfaces might be toxic, therefore, their use is limited. The potential toxicity of coatings may cause problems when used in the food and medical industry. Coated or dirty polymer items are also harder to recycle; a clean piece of polymer with no coatings is much easier to recycle since the polymer can be melted straight away with no contaminants from dirt or coating.

Furthermore, the production of coatings is time consuming and often expensive. For example, hearing aids are coated with a chemical agent for making a self-cleaning surface. The coating process can be a large contribution to the production cost. When engineered nanoparticles (particles with at least one dimension less than 100 nm) are used for surface coatings, their risk for humans and the environment must be evaluated. These particles present much smaller sizes and substantially higher surfaces to volume ratio per mass than larger particles of similar composition. These physical properties may be associated with increased toxicities which should be assessed.

The basic principle of injection molding is simple, a melted polymer fills a predefined mold and the part is removed once the polymer has solidified. An injection molding machine transforms thermoplastic granular into usable parts, the process requires almost no supervision and is fully automated. In reality, the injection molding process is complex with multiple parameters involved. The basic process comprises injection of hot melted polymer into the mold cavity followed by a cooling step so the polymer solidifies. Finally, the cold part can be removed and

the process can start again. An injection mold is also known as a tool, and often has an exchangeable cavity called an insert. This extends the life of the tool and improves versatility since different inserts can be used with same tool case. Furthermore, compared to an entire tool the insert can be replaced at a lower cost when worn out. Nanostructures are already injection molded on a big scale and with very low cost by the industry on flat surfaces; such as everyday items like DVD and Blu Ray discs. In the laboratory, it is possible to injection mold 50 nm structures[1].

Structures in the nano- and micrometer range can functionalize surfaces for a variety of different effects with the advantage that no toxic compounds are used. Examples of functionalized nanostructured surfaces that can be fabricated are anti-reflective, self-cleaning, hydrophobic/hydrophilic, and color appearance. Today, all these effects have the potential to be injection molded from flat injection molding inserts produced by lithography and electroplating of metal (normally nickel). If these effects can be realized the practical use of injection molded functional surfaces would be enormous. Surfaces with self-cleaning effects that mimic, e.g. the lotus flower, are of huge relevance for the medical and packaging industries.

1.1 Nanoplast Project

One of the largest research projects in Denmark is the *Nanoplast Project*. Nanoplast has a total budget of 91 million DKK. The partners in Nanoplast, Technical University of Denmark (DTU) and several private Danish companies have developed a process for nanostructured free form injection molding tools. These tools have been used in the production of injection molded plastic parts with different functionalities such as structural colors or self-cleaning properties (the so called Lotus Effect). The Nanoplast Project is funded by Danish National Advanced Technology Foundation (now InnovationsFonden) and several Danish companies with LEGO® being the largest. The Nanoplast protocol is based on conventional silicon wafers for the production of nanostructures, which are later transferred to injection molding tools.

The silicon wafer is used as a mold for a flexible stamp. The flexible stamp transfers the structures to a resist coated tool with nanoimprint lithography. Finally, the structures are defined in the tool steel by etching or electroplating. Injection molding is subsequently performed for the mass production of polymer[2], the process is shown in Figure 1.1. Alternatively, the structures are imprinted directly into a hard coating on the tool steel. The potential is a new type of polymer materials with functional surfaces, such as a structural color instead of painted surfaces that never needs cleaning.

This PhD project is part of the Nanoplast Project with one of the major goals to develop self-cleaning surfaces that can be produced (and hopefully sold) by the partners in the Nanoplast Project. Finally, this project contributes to the development of injection molding of nano- and microstructures with high replication quality for different polymers.

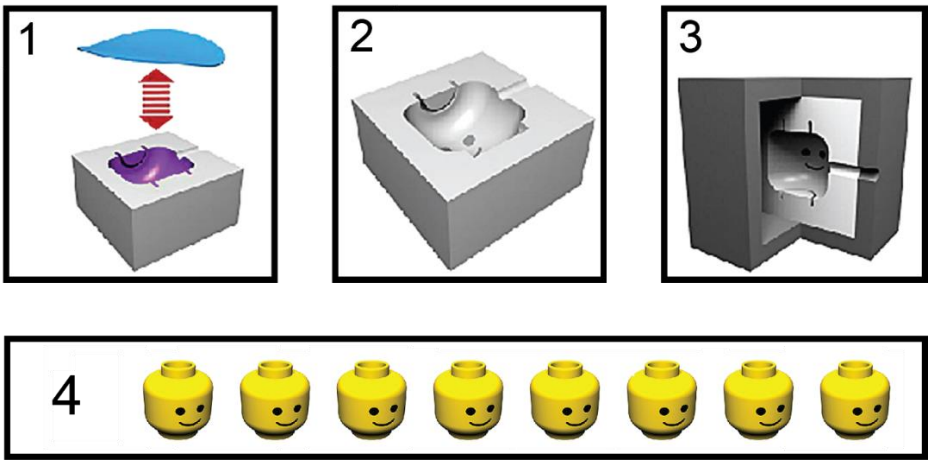

Figure 1.1. The Nanoplast *protocol for fabrication of functional nanostructures on injection molding tools: Imprint on injection molding tool, 1) Etching or electroplating of nanostructures, 2) Tool ready for injection molding, 3) Injection molding of nanostructured parts, 4) Finished parts with nanostructures. (Modified from ing.dk[3]).*

1.2 Potential applications for self-cleaning and superhydrophobic surfaces

If self-cleaning surfaces can be cost-effectively produced on an industrial scale and made environmentally friendly, they would be useful for many everyday life situations. Self-cleaning packaging of food could prevent bacterial growth. In yoghurt, approximately 10% of the yogurt remains in the container. A yoghurt container with a self-cleaning surface could reduce food waste, and make recycling of the polymer less resource demanding as shown in Figure 1.2.

Furthermore, it has been brought to public attention by the media that fluorine based coatings are often used. Fluorine residues may in some cases be transferred to the food, making it unhealthy to eat. The Danish Minister for Food, Agriculture and Fisheries, Dan Jørgensen promised in 2014 that a Danish ban of flour in food packaging would be introduced as soon as possible[4]. The injected molded self-cleaning surfaces could be the first step in developing an alternative to the use of fluorine in food packaging.

1.2.1 Medical applications

Medicine and medical equipment is often very expensive, and patient health depends on the precise dosage of medicine. If medical containers possess self-cleaning surfaces, the containers could be completely emptied allowing for a precise dosage. Furthermore, the medicine packaging can be burned or recycled as regular polymer waste. Normally special and more expensive circumstances are needed to dispose medicine packaging since it might retain residues from medicine which may be avoided by applying self-cleaning packaging. Another application is laboratory equipment such as pipette tips, syringes, etc., as shown in Figure 1.2. Self-cleaning surface may also reduce bacterial growth on medical equipment, thereby making biological and medical laboratories cleaner.

Figure 1.2. a) In the future items like this yogurt container may benefit from self-cleaning surfaces, b) Today op to 10% yogurt is left in the container, c) In the future a self-cleaning surface on a similar container could eliminate food waste, d) In the future similar effects would benefit medicine packaging and laboratory equipment (shutterstock.com).

1.2.2 Optical applications

Self-cleaning coatings are used for optics, e.g. Nikon uses fluorine based coatings on the front lens element on e.g. some of their professional lenses[5] (Figure 1.3a) and binoculars. If transparent self-cleaning nanostructures could be fabricated by injection molding, self-cleaning properties can be incorporated in more cost effective optical systems such as cell phone cameras.

1.2.3 Military applications

The interest for military applications with self-cleaning surfaces is increasing, polymers are becoming more and more used in military equipment, e.g. magazines, gun parts, and other equipment[6] (Figure 1.3b). It can be difficult to keep dirt away from critical equipment in field operations and many types of equipment must be clean and dirt free in order to function reliably. Furthermore, military personel operating in nuclear, biological, chemical zones are exposed to highly dangerous compounds. Therefore, it is highly important that military equipment can be kept clean in order to minimize exposure, in which self-cleaning properties may aid.

Figure 1.3. Application for self-cleaning surfaces, a) Nikons fluorine coat prevents the adhesion of dirt on the front lens element[5], b) More and more military equipment is made from polymer such as this AR-15 front grip from Magpul. It would be beneficial if such items could become self-cleaning[6].

1.2.4 Anti-fouling and drag reduction

The growth of biomaterials on ships possesses a significant challenge, as the biomaterial attached to a hull can increase drag and fuel consumption dramatically as shown in Figure 1.4. This increases both cost and environmental impact. Commercial anti-fouling paints for ships exist, but some have been prohibited, due to their toxic environmental impact and nonspecific targeting of bio organism. Self-cleaning surfaces may provide inexpensive environmentally friendly solutions and reducing fouling and thereby the drag[7].

Figure 1.4. Example of bio-fouling[8]. Drag will be increased dramatically. Self-cleaning surfaces may prevent this.

1.2.5 Discussion of commercial uptake

In general, the introduction of injection molded self-cleaning surfaces is more likely to be implemented in high value applications, where the increased production cost required to make the self-cleaning surface will be a small percentage of the overall fabrication cost. The military sector and medical sector will probably be among the first where products with injection molded self-cleaning surfaces will be marketed.

In contrast, it will be difficult to maintain the low price on mass produced food containers when adding nano- and microstructures to the mold. Instead, a special injection molding technique called in-mold labeling can be used. In in-mold labeling a structured foil with superhydrophobic properties is wrapped around the injection-molded part. The foil would be produced by a roll-to-roll embossing method, similar to the principle of a Danish research project called Large Area Nanostructuring Initiative (LANI)[9]. Such a process is already available for other functionalized surfaces based on nanostructures such as holograms. As an example the company Unifoil produced different kinds of custom food containers with holograms fabricated with in-mold labeling[10], see Figure 1.5.

Figure 1.5. a) Holographic Cups fabricated in mold labelling[11],
b) Foil with nanostructures produced by LANI.

1.3 Goal for the project

The overall goal for the PhD project was to fabricate injection molds with a novel method for superhydrophobic surfaces and subsequent produce polymer parts. A key property of the injection molded superhydrophobic surfaces is the ability to withstand submersion into water, from these considerations, one main hypothesis was set up in the beginning of this project:

Is black silicon etching a viable option for production of superhydrophobic polymer parts based on hierarchal nano- and microstructured silicon masters?

During the first part of the project, analyses of submerged samples indicated a collapse of the Cassie State with a loss of water repellency on the polymer part; therefore, another hypothesis was set up.

Can a stable Cassie State be obtained and characterized for the injection molded superhydrophobic parts?

These hypotheses lead to the following investigation plan for the project:

- Nanostructuring of superhydrophobic surfaces in the cleanroom of DTU Danchip, including state of the art electron beam lithography and nanoimprint lithography.
- Experimental study for obtaining self-cleaning properties of injection molded surfaces.
- Development of automated characterization setups, e.g. contact angle measurements, roll-off angles on inclined planes, and drop-bouncing properties.
- Mapping of polymers regarding their wetting and de-wetting properties of relevant liquids.
- Developing a method to observe the superhydrophobic stability of the injection molded samples.

As the work progressed during this PhD study some changes in the investigation plan were made as new issues became apparent and new opportunities occurred. E-beam and nano imprint lithography (NIL) were discarded in favor of DUV lithography because of its much larger production rate and useability.

The development of an automated characterization for contact angle was canceled in favor of an optical tensiometer with tilting stage and high-speed camera. The equipment was bought during the project. The canceling of the development liberated time to develop the experimental process for the injection molding of the superhydrophobic structures and to perform wetting experiments.

1.3.1 The proposed fabrication method

The proposed fabrication method is based on a LIGA derived process where a silicon master is electroplated and used as injection mold for the fabrication of superhydrophobic polymer parts. Microstructures are defined by lithography and etched into the silicon, the etched microstructures are covered with a nanostructures in a hierarchical order composed of black silicon fabricated by dry etching. The finished silicon wafer is electroplated leaving a nickel shim with inverse polarity and injection molding is subsequently carried out for the production of polymer parts. This fabrication method was patented in 2013 (Appendix 6).

1.4 Issues

In order to successfully produce superhydrophobic surfaces on an industrial scale, many issues have to be overcome. In order to get a clear overview, an issue tree was made so each issue could be addressed in a systematic manner and the challenges in the project could be overcome. The issue tree presented in Figure 1.6 is divided into three main categories;

- Surface properties
- Injection molding
- Mold fabrication

The work done for this thesis was focused primarily on surface properties and the injection molding process, while other project partners in the NanoPlast project focused on insert fabrication and mold design.

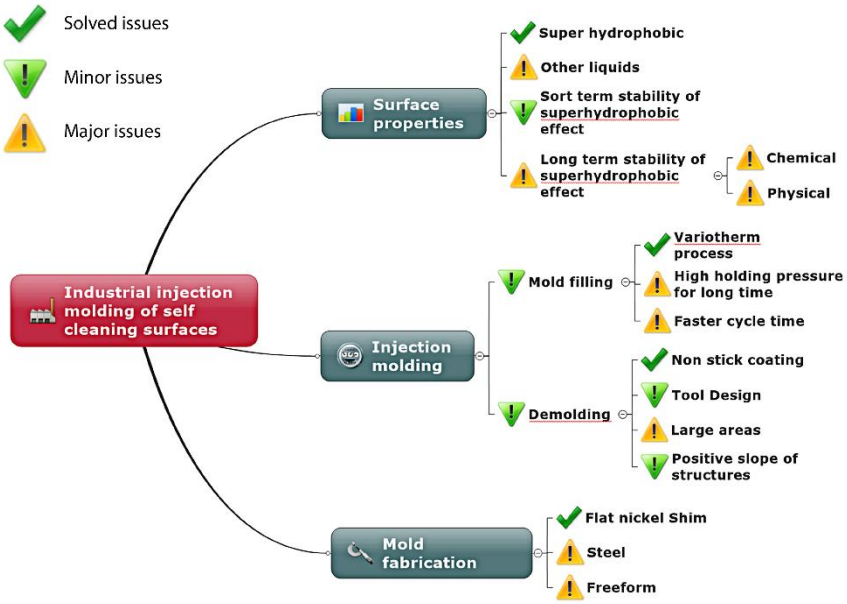

Figure 1.6. Issue tree to give an overview of the issues for industrial fabrication of superhydrophobic surfaces.

1.5 Thesis outline

The first part of the thesis is an introduction with a motivation, description of *the Nanoplast Project*, and potential applications.

Chapter 2 covers basic wetting theory required to understand the principle of self-cleaning surfaces.

Chapter 3 presents state of the art of 1) superhydrophobic surfaces, 2) injection molding and, 3) injection molded superhydrophobic surfaces.

Chapter 4 covers design of the different structures and choice of polymers.

Chapter 5 presents clean room fabrication and injection molding together with results and discussion.

Chapter 6 presents characterization methods of topography/morphology.

Chapter 7 presents results of contact angle measurements.

Chapter 8 presents the background experiment for the paper on the pressure cell.

Chapter 9 covers a summary of the fabricated structures.

Chapter 10 is the overall discussion.

Finally, conclusion and outlook, references, and appendixes are presented.

Appendix 1: Fabrication recipes

Appendix 2: Work performed on external stay at NTU

Appendix 3-5: Papers

Appendix 6: Patent

2 The theory of wetting properties

The study on the behavior of droplets on surfaces is a large research field. This chapter will provide the elementary theory and formulas in order to understand hydrophobic and superhydrophobic surfaces.

2.1 Principle of a self-cleaning surface

Most surfaces known in everyday life collect dirt over time, and intensive cleaning is needed to remove it. This can be seen especially on everyday items such as cars and bicycles. On the other hand a plant placed in the middle of a city will never become dirty. Many plant surfaces are self-cleaning.

As a general rule the initial properties can be amplified by increasing roughness. A surface that is initially hydrophilic will become even more hydrophilic if the surface is rough, and the same effect applies for a hydrophobic surface[12]. An example is shown in Figure 2.1, if the roughness is increased extensively, the surface will eventually become superhydrophobic or self-cleaning.

In this thesis a surface is assumed self-cleaning when the surface becomes extremely water repellant, so-called superhydrophobic. A superhydrophobic surface is defined by the following criteria; the surface must have a contact angle above 150°[13] and roll-off angle and hysteresis below 10. Overall, there exist two methods to produce a superhydrophobic surface 1) making a rough surface from a material with high intrinsic contact angle such as Teflon 2) modifying or coating an already rough surface with a hydrophobic material.

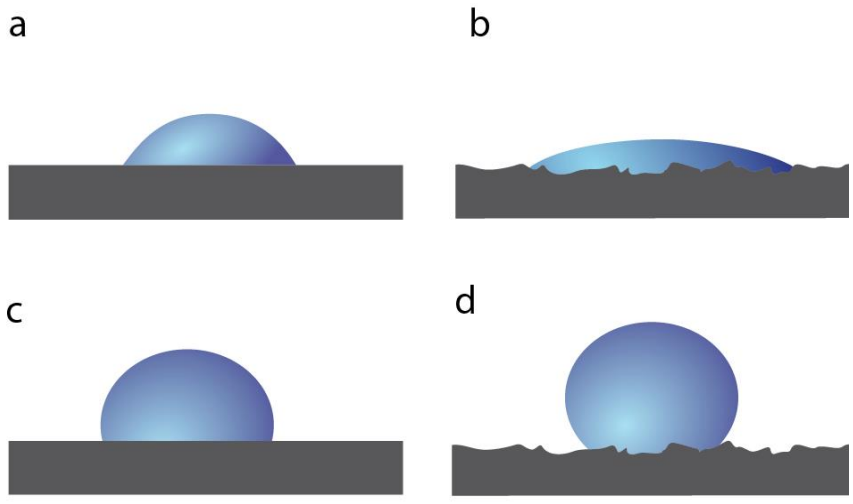

Figure 2.1. a) Smooth hydrophilic surface, b) Rough hydrophilic surface; contact angle is decreased by roughness, c) Smooth hydrophobic surface, d) Rough hydrophobic surface; contact angle is increased by roughness.

The idea behind a self-cleaning surface is that the surface is washed with water and is left spotlessly clean. Water will often stick to normal surfaces and thereby the dirt will stay on the surface. Most self-cleaning surfaces share the same principle; if the surface become sufficiently repellant towards a liquid e.g. water, then droplets will roll off the surface. Particles and dirt will be collected by the rolling drop, leaving the surface clean. On a regular surface dirt will be trapped inside the drop as is it slides off, often the collected dirt is re-deposited on the surface as shown in Figure 2.2[14].

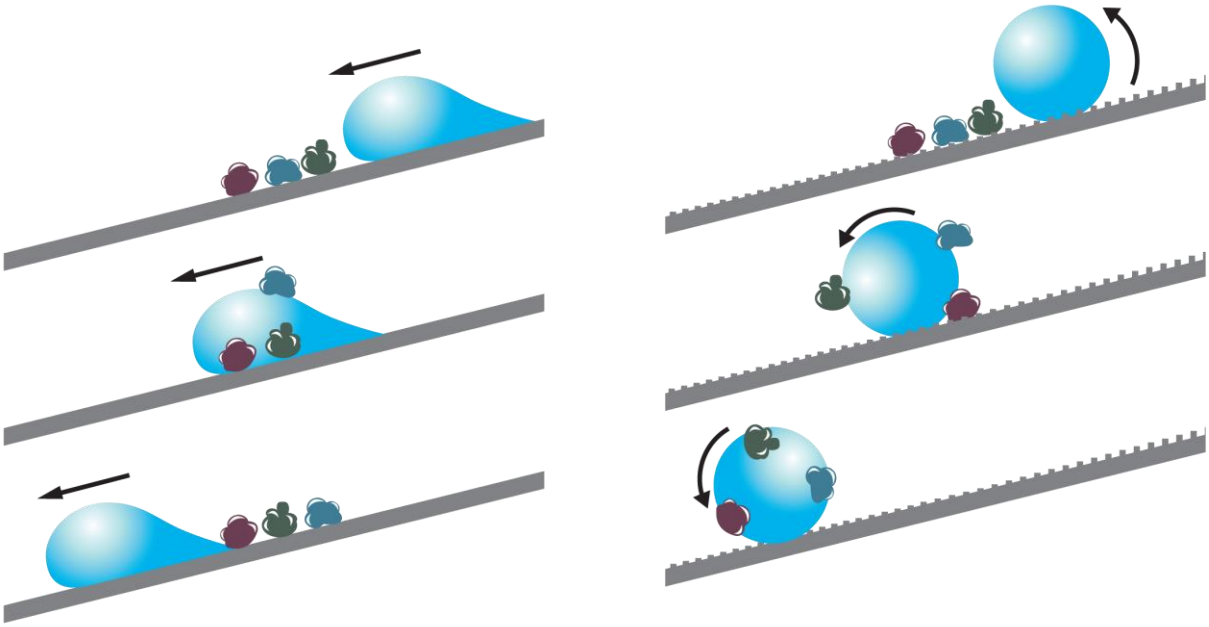

Figure 2.2. a) The particles on a smooth surface are redistributed by water, b) The particles adhere to the droplets on rough super hydrophobic surface and are removed when the droplets roll off the surface. Modified from[14].

The fundamental physical principle of a hydrophobic surface is that materials often have the lowest energy when binding to themself. Thus, it will cost energy when a surface is increased, or when an interface between two materials is created. For example a drop will try to obtain a spherical shape in order to minimize the free surface area and thereby its energy.

The energy required for forming a surface is measured as J/m^2 or as force per length N/m and is known as surface tension for a liquid-gas interface. When a drop is placed on a surface, three surface energies are present. The surface tension acting where surface (S), gas (G), and liquid (L) meet is called the triple line and the three surface tensions define the drop's shape. When the projected surface tensions (γ) at the interfaces between the solid-gas, solid-liquid, and liquid-gas are summed and equated to zero one obtains Young's equation which he derived in 1805[12],

$$0 = \gamma_{SG} - \gamma_{SL} - \gamma_{LG}\cos(\theta_0) \qquad 2.1$$

When the drop is at rest and the forces have reached equilibrium the contact angle θ_0 is defined. θ_0 is also known as the equilibrium contact angle. The surface tensions and contact angle are shown in Figure 2.3.

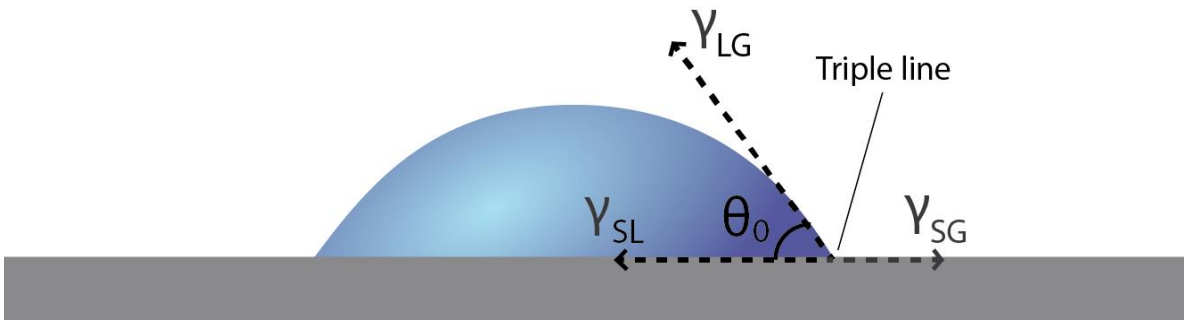

Figure 2.3. The capillary forces acting where surface (S), gas (G), and liquid (L) meets. Their intersection is called the triple line and the three surface energies define the drop shape.

Young's equation describes a perfectly flat surface, but in reality, flat surfaces rarely exist. Surfaces often have some form of roughness either naturally or artificially made. The roughness can influence the triple line and pin it, which causes the drop to be fixed either slightly or completely. When a drop moves on a surface, the pinning of the triple line influences the contact angles. At the advancing part of the drop, the contact angle increases (advancing contact angle, θ_{Adv}) and for the receding part of the drop the contact angle decreases (receding contact angle, θ_{Rec}). Normally drop movement can occur in two ways. One way is when the surface is tilted and the drop is moved under the influence of gravity, the angle where the drop starts to slide/roll is known as the roll-off angle (α). The other way is when the drop's volume is charged by injecting or sucking out small amounts of liquid (Figure 2.4). The advancing contact angle is always larger than the equilibrium contact angle and the receding always smaller. The difference between the advancing and receding is known as the contact angle hysteresis H[15,16],

$$H = \theta_{Adv} - \theta_{Rec} \qquad 2.2$$

When doing wetting experiments the chemical composition of the liquids and solids have a large influence on the results, ideally the liquid should be pure and nonvolatile. Surfaces with water contact angle less than 90° are considered hydrophilic, and surfaces with water contact angles above 90° hydrophobic. As a general rule surfaces enhance their properties if the

roughness is increased: A rough hydrophilic surface will become even more hydrophilic and a rough hydrophobic surface will become even more hydrophobic. The lowest surface energy of any flat solid surface is obtained by regularly aligned and closely packed CF3 groups. For this surface the contact angle is 120°, which is the highest contact angle a smooth surface can reach. Superhydrophobic surfaces with contact angles exceeding 120° can only be produced by increased roughness.

The roll-off angles relate to the contact angle hysteresis and can be described as a force balance between the projected gravity force and the projected line force along the triple line. This relationship between hysteresis and roll-off angle can be calculated by the following equation[17,18],

$$\rho g V \sin(\alpha) = 2\gamma a_r \left(\cos(\theta_{Rec}) - cos(\theta_{Adv})\right) \qquad 2.3$$

where ρ is the density of the liquid, g the acceleration of gravity, V the volume of the drop, γ the surface tension, and a_r the radius of the interface area between the drop and the surface.

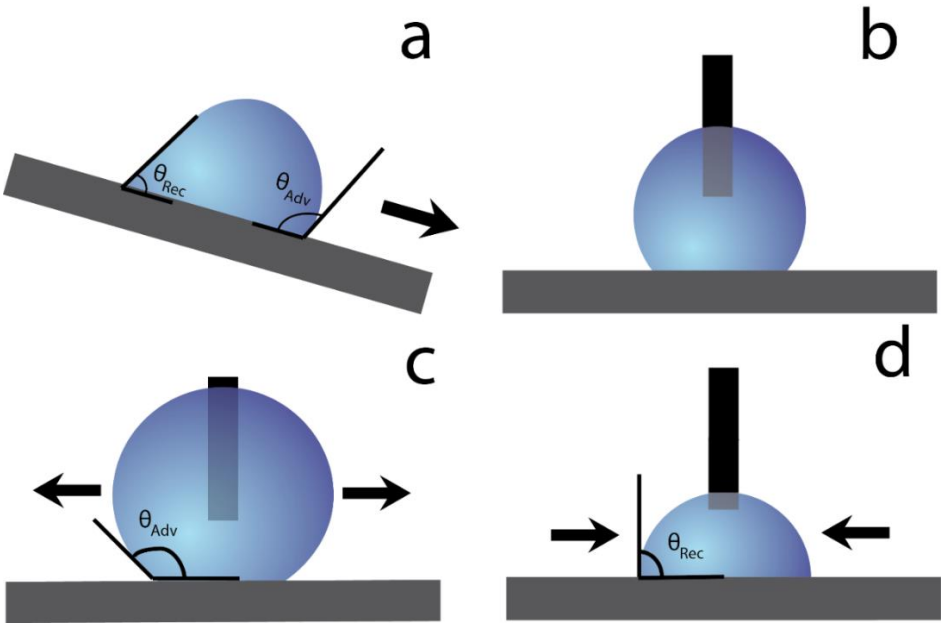

Figure 2.4. Definition of advancing and receding contact angles, a) Tilting of a surface will cause the drop move, b) A deposited drop on a surface, c) Advancing contact angle is observed when drop is enlarged, d) Receding contact angle is observed when drop size is reduced.

2.2 Chemically homogeneous surfaces: The Wenzel equation

Real life surfaces always have roughness. When roughness is increased on surfaces of chemically homogenous materials the surface-liquid contact area increases causing a changed surface energy. A drop on the surface will always try to minimize its energy by obtaining a new form. For hydrophobic materials a drop will form a larger contact angle and a smaller contact area.

An equation describing the relation between roughness and contact angle was published in 1936 by Wenzel. The Wenzel equation describes how a surface with the intrinsic smooth contact angle θ_0 changes contact angle θ when roughness increases. A non-dimensional roughness factor (R_f) is introduced. R_f is defined as the ratio between the total liquid area in contact with the surface A_{SL} to the projected area A_F. A_{SL} will always be larger or equal to area A_F, hence $R_f \geq 1$, the Wenzel equation can be written as[19],

$$\cos\theta = R_f \cos\theta_0 \qquad 2.4$$

where

$$R_f = \frac{A_{SL}}{A_F} \qquad 2.5$$

A drop or liquid in the so-called Wenzel State will completely wet all the surface roughness. The wetted surface roughness will cause the drop to have a large contact angle hysteresis or the drop will be completely pinned to the surface. The Wenzel State together with A_{SL} and A_F is shown in Figure 2.5. The figure also shows different intrinsic contact angles plotted as function of roughness factor to illustrate how the roughness relates to the contact angle. The plot shows that large contact angles can be achieved for drops in the Wenzel State. However, the drops will be pinned (stick to the surface) by the roughness and the surface will not have self-cleaning properties.

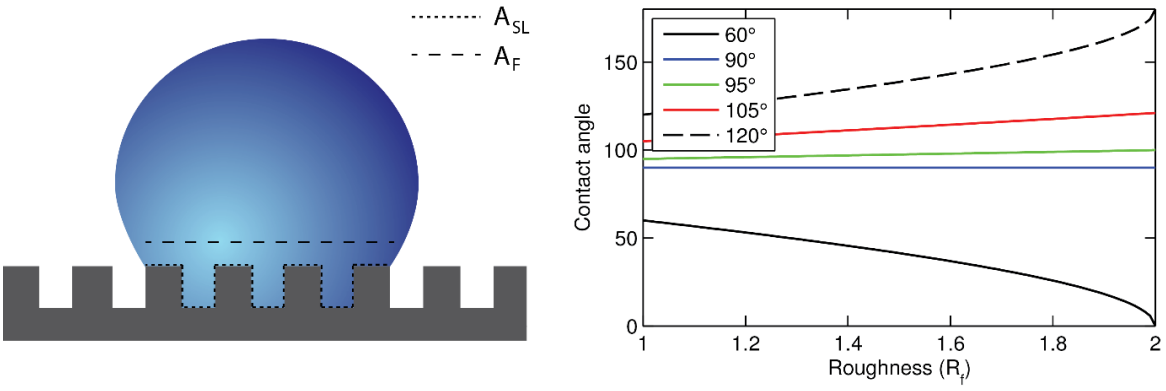

Figure 2.5. Wenzel State where the drop completely wet the surface roughness (which is schematically drawn as periodic structures). This is also known as the pinned state. A_{SL} are the total surface area and A_F the area projected by the drop. The plot shows the Wenzel equation with contact angle as function of roughness for different intrinsic contact angles.

2.3 Chemically heterogeneous surfaces: The Cassie equation

The Wenzel equation only describes how a rough homogenous surface influences the contact angle. In real life heterogeneous materials often occur. The contact angle of a heterogeneous surface composed of two materials with different contact angles was published by Cassie and Baxter in 1944[20]. The contact angle is calculated from the surface fraction of material 1 (f_1) with contact angle $\theta_1$and surface fraction of material 2 (f_2) with contact angle θ_2. Here $f_1 + f_2 = 1$ which corresponds to the total surface Cassie's Law is given by the equation below[20],

$$cos\theta = f_1\, cos\theta_1 + f_2 cos\theta_2 \qquad 2.6$$

A composite interface with a surface liquid fraction $f_1 = f_{SL}$ and a liquid air fraction $f_2 = f_{LA} = 1 - f_{SL}$ will occur if air replaces one of the two surface materials. The contact of angle of air is defined as 180° and the result is the Cassie Baxter equation[20],

$$cos\theta = f_{SL}\ cos\theta_0 - 1 + f_{SL} \qquad 2.7$$

In the Cassie State, drops or liquid will be at the top of the structures with air pockets beneath liquid (Figure 2.6). The roughness factor R_f must be included since surfaces in contact with the liquid will always have a roughness. Furthermore, R_f can be used to describe the effect of hierarchical structures were the smaller structures are in the Wenzel State. By combining equation, 2.5 and 2.7 one can end up with,

$$cos\theta = R_f\ f_{SL}\ cos\theta_0 - 1 + f_{SL} \qquad 2.8$$

The above equation is plotted in Figure 2.6. Here the contact angle is dependent of roughness factor, the intrinsic contact angle, and solid liquid surface fraction for the Cassie State. From

equation 2.8 it can be deduced that even a hydrophilic surface can become hydrophobic when f_{SL} goes towards 0, however, the required f_{SL} may be impossible to achieve because the pockets will become unstable and collapse into in the Wenzel State for a hydrophilic material. A drop in Cassie State will have a reduced surface contact since some contact area is replaced by air. The reduction in contact area causes drops to have a low hysteresis, a large contact angle, and a low roll-off angle. A stable Cassie State is important for a superhydrophobic surface.

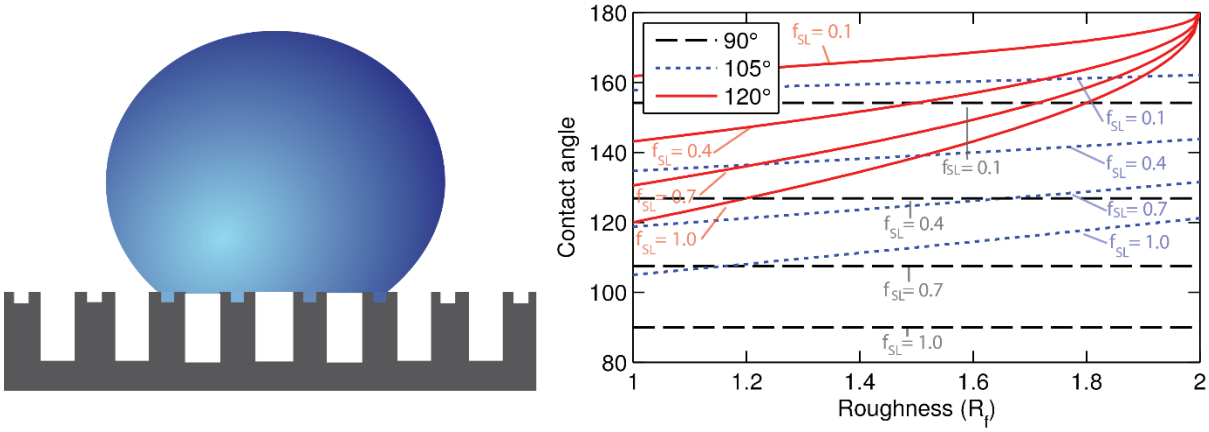

Figure 2.6. Cassie State where the drop rests on top the structures, this is also known as the superhydrophobic state. The plot of the Cassie Baxter equation with roughness compensation shows contact angle as function of roughness for different intrinsic contact angles and solid liquid surface fractions. The roughness factor shows the effect on the contact angle for hierarchical structures or surface roughness.

2.3.1 Limitations of Cassie and Wenzel equation

The Wenzel and Cassie equation cannot always predict the contact angles compared to those measured in experiments. One of the issues with the Cassie Baxter equation is that the contact angle is defined as a local force balance at the triple line, as described by Young's equation. The Cassie Baxter equation uses only the surface liquid fraction to determine the contact angle. The Cassie Baxter equation was originally derived for porous random surfaces, where the surface liquid fraction along the triple line was equal to the surface liquid fraction for the area beneath the drop. For ordered structures, this may not be the case, and the contact angle will depend entirely on the surface liquid fraction along the triple line. Contact angle calculated from the Cassie Baxter equation may therefore deviate from experimental measurements[21].

In experiments, the meniscus may not be completely on top of the structures (Cassie State) or completely wetted in the Wenzel State. A transition state, called the Cassie-impregnating

State, can occur where the menisci are somewhere between the bottom and top of the structures, this will influence the liquid surface contact area and will result in a different drop shape and contact angle[16].

A composite state can also occur where a percentage of the structure is in Cassie State and the rest of the structures in Wenzel. The equations cannot, however, be used to determine the contact angles for surfaces in the composite state. The reason for the composite can be that the structures are slightly irregular, small defects can either stabilize the Cassie State or cause the liquid to go directly into Wenzel State[16]. The composite state will change the degree of surface wetting and result in a different contact angle.

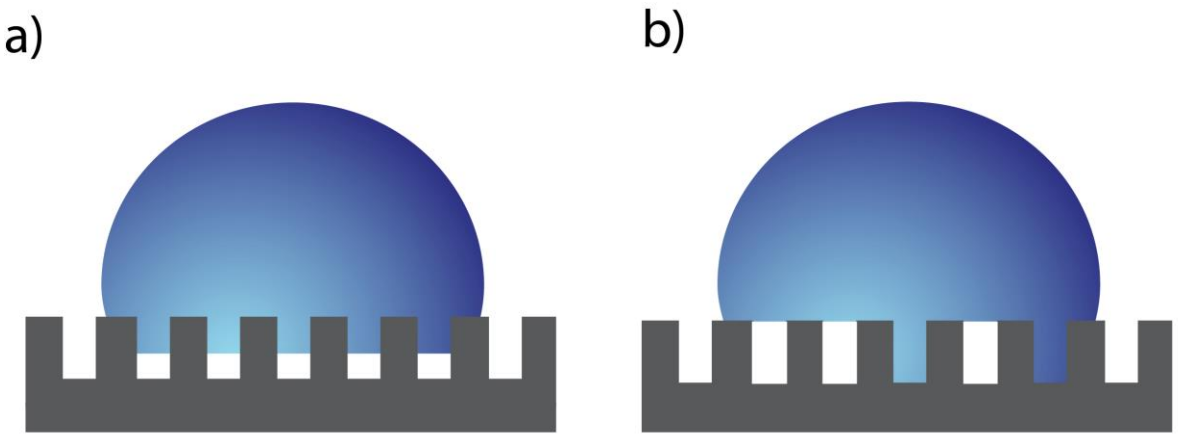

Figure 2.7. Limitation of the Wenzel and Cassie Baxter equations, partially filled structures can occur, the liquid is not completely in Wenzel or Cassie State, a) The transition state where the structures are partially wetted, in the Cassie-impregnating State, b) The composite state where some structures are in Wenzel and other are in Cassie State.

2.3.2 Stability of the Cassie State

If the Cassie State collapses and water penetrate into the structures, the drop will transfer into the Wenzel State. A drop in the Wenzel State will be difficult to move because of the increased adhesion force from the increased liquid surface contact area and the hysteresis would be much larger than for drop in the Cassie State. A superhydrophobic surface requires that the water drops are always in the Cassie State. Many factors can influence the collapse of the Cassie State. The rate at which water penetrates into the structures will vary for different materials and geometries. Water on some surfaces will have a completely stable Cassie State, while on other surfaces may collapse quickly into the Wenzel State.

Some of the important design parameters for Cassie State stability are: 1) Choice of material, the used material must have a large intrinsic contact angle. Drops with larger contact angles have less surface contact and therefore a lower adhesion to the surface. 2) The pressure of

the liquid, if a surface is submerged in water the pressure will increase. At higher pressures liquid can be forced into the air pockets in the Cassie State and the liquid will start to transition into the Wenzel State. Closed structures may prevent this since a counter pressure will be formed by the enclosed air. 3) Geometry of structures influence the stability of the Cassie State, e.g. the Cassie State is more stable when small structures are packed closely. However, the overall surface liquid fraction must still be small in order to achieve a contact angle above 150°, which is the requirement for a super hydrophobic surface. The design parameters are summarized below.

1) Advancing contact angle
    a. Contact angle of the material
    b. Sidewall roughness
2) Liquid pressure
    a. Open structures
    b. Closed structures
3) Geometry of structure
    a. Size
    b. Height
    c. Period

If a liquid is in the Cassie State and is resting on top of a porous surface, the meniscus will start to move down into the structures when the contact angle between the meniscus and the surface is larger than the advancing contact angle. A more hydrophobic material will have a larger contact angle and as a result also a larger advancing contact angle. Sidewall roughness can further increase the contact angle and the meniscus will therefore have difficulty moving into the structures and thereby a more stable Cassie State[22]. However, structures on the sidewall are very difficult to injection mold since they will be broken off during the demolding of the polymer part.

If a pressure is applied to the liquid, e.g. when the surface is submerged, then the meniscus will change shape. The shape of the meniscus is spherical as long as the dimension is smaller than the capillary length of water ≈2.7 mm. The shape of the meniscus can be calculated from the Young Laplace equation for a given pressure[12],

$$\Delta p = \gamma \left(\frac{1}{R_1} + \frac{1}{R_2} \right) \qquad 2.9$$

Where R_1 and R_2 are radii of curvature, Δp is the change in pressure over the liquid-gas interface, and γ the surface tension. For drops or structures with circular cross section the equation reduces to,

$$\Delta p = \frac{2\gamma}{R} \qquad 2.10$$

An increase in pressure will decrease the radius of curvature for the meniscus and therefore the meniscus will penetrate deeper into the structures. During this process, the sidewall contact angle will increase as well. From a geometrical perspective, the radius of curvature for the meniscus will be a function of structure diameter and contact angle,

$$R = \frac{a}{\cos(\theta)} \qquad 2.11$$

Thereby equation 2.10 can be rewritten into,

$$\Delta p = \frac{2\gamma \ \cos(\theta)}{a} \qquad 2.12$$

If no external pressure is applied, the sidewall contact angle of the structures will dictate the penetration depth; note, that the contact angle is always smaller than the advancing contact angle otherwise the meniscus will start to move. A schematic drawing of a meniscus at a given contact angle is shown in Figure 2.8. From basic geometry considerations the penetration of the meniscus into a structure can be calculated from an applied pressure (equation 2.10) or for a material with a given contact angle (equation 2.11). The penetration of the meniscus into the structures for circular hole can be calculated from sphere shape with radius of curvature *R* defined by the hole diameter *a* with the following equation,

$$h = R - \sqrt{R^2 - a^2} \qquad 2.13$$

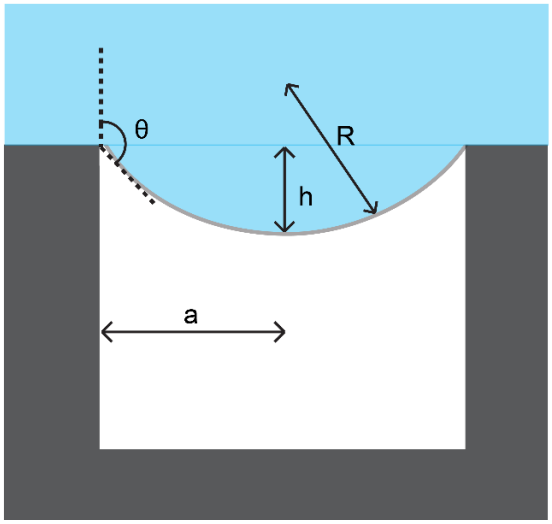

Figure 2.8. Cross-section of the meniscus inside a circular hole; a *is the radius of the hole,* R *is the radius of curvature of the meniscus,* h *the penetration of the meniscus and θ is the contact angle.*

Thereby the structure size becomes an important factor when designing superhydrophobic surfaces. Smaller structures will have lower penetration of the meniscus, and thereby perform better than larger structures, providing height and surface fractions are kept constant. Figure 2.9 shows penetration as function of the structure radius for different pressures and contact angles.

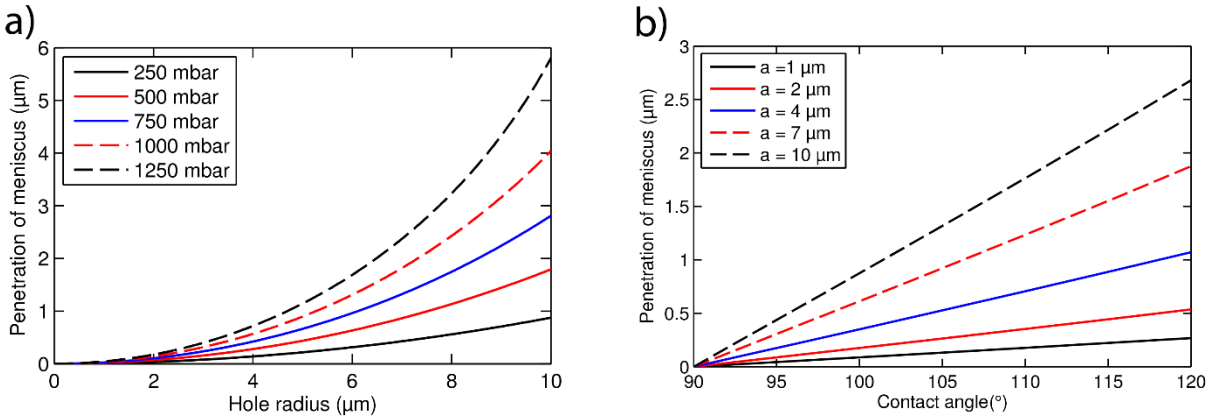

Figure 2.9. Plot of meniscus penetration, a) As a function of hole radius for different pressures b) As function of contact angle for different hole radii; Note, how meniscus penetration is less for holes of with smaller diameter.

Closed structures with holes will have a larger stability in the Cassie State than compared to open structures. In an open structure air can escape as the meniscus moves down the sidewalls. Air cannot escape from closed structures, and as the meniscus moves down, the trapped air will form a counter pressure and the overall change in pressure will decrease leading to smaller deflection of the meniscus and a larger radius of curvature according to the Young Laplace equation 2.9). Over time the trapped air will be absorbed by the liquid. The solubility of gas is proportional to the partial pressure of the gas according to Henry's Law, where P is partial pressure, k_H is a gas specific constant with units of (L bar/mol), and c the molar concentration of gas in water,

$$P = k_H c \qquad 2.14$$

When gas molecules are absorbed as Δp increases, and the meniscus again moves down the sidewalls until the counter pressure increases again and the penetration stops. This process will continue until the liquid is completely in the Wenzel State. The absorbed gas forms a gradient and diffuses from the liquid-gas interface into the rest of the liquid. The absorption of gas will be a limiting factor for the penetration rate.

Structure height is another important factor when designing superhydrophobic structure. Low structures can be problematic since the meniscus might touch the bottom of the structures, and thereby lead to a transition into the Wenzel State. As a general rule, higher structures will perform better than lower since the meniscus will have to penetrate deeper into the structures, before the liquid transits into the non-recoverable Wenzel State.

In the case of hierarchical structures, such as nano- and microstructures a special situation can occur were water only penetrates the microstructures and air is trapped in the nanostructures (Figure 2.10). This state has several names and is known as: Nano Cassie State[23], or Cassie-impregnating State[24]. In this thesis, the term Cassie-impregnating State will be used. The red rose petals have hierarchical nano- and microstructures designed specifically to wet largely spaced microstructures, but not the smaller nanostructures. As a result water will be in the Cassie-impregnating State, and water drops are strongly pinned to the surface even when rose petals are placed upside down[24]. Liquid in the Cassie-impregnating State can be recovered back into the superhydrophobic state[23]. The addition of nanostructures can thus provide a more stable superhydrophobic surface.

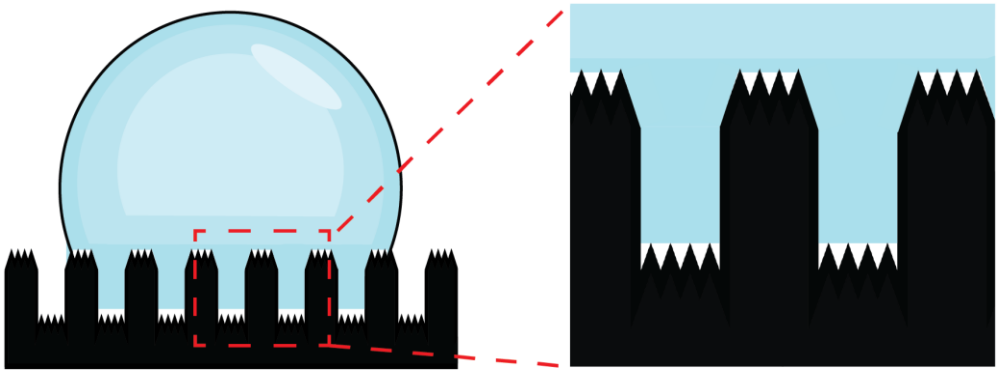

Figure 2.10. Cassie-impregnating State, also known as the Nano Cassie State. The liquid only wet the microstructure on hierarchical nano- and microstructures. The drop in Cassie-impregnating State will have high adhesion to the surface.

When designing and fabricating a superhydrophobic or water repellant surface, it is important to achieve a minimal hysteresis, since this will result in a lower drop pinning and thereby a lower drop roll-off angle. A high contact angle is in itself not enough to obtain a water repellant surface, since large roughness in the Wenzel State will cause a large hysteresis and make the water pin. This is important for water repellant surface structures, which ensure a stable Cassie State.

3 State of the art

This section covers the origin of superhydrophobic surfaces, the advances in research, and manufacturing methods in general with an emphasis on injection molding. The limitations of standard manufacturing of injection molding tools and inserts are described, along with more advanced fabrication methods needed for the nano- and microstructures required to create superhydrophobic surfaces. Finally, some papers concerning superhydrophobic surfaces together with wetting stability studies are discussed.

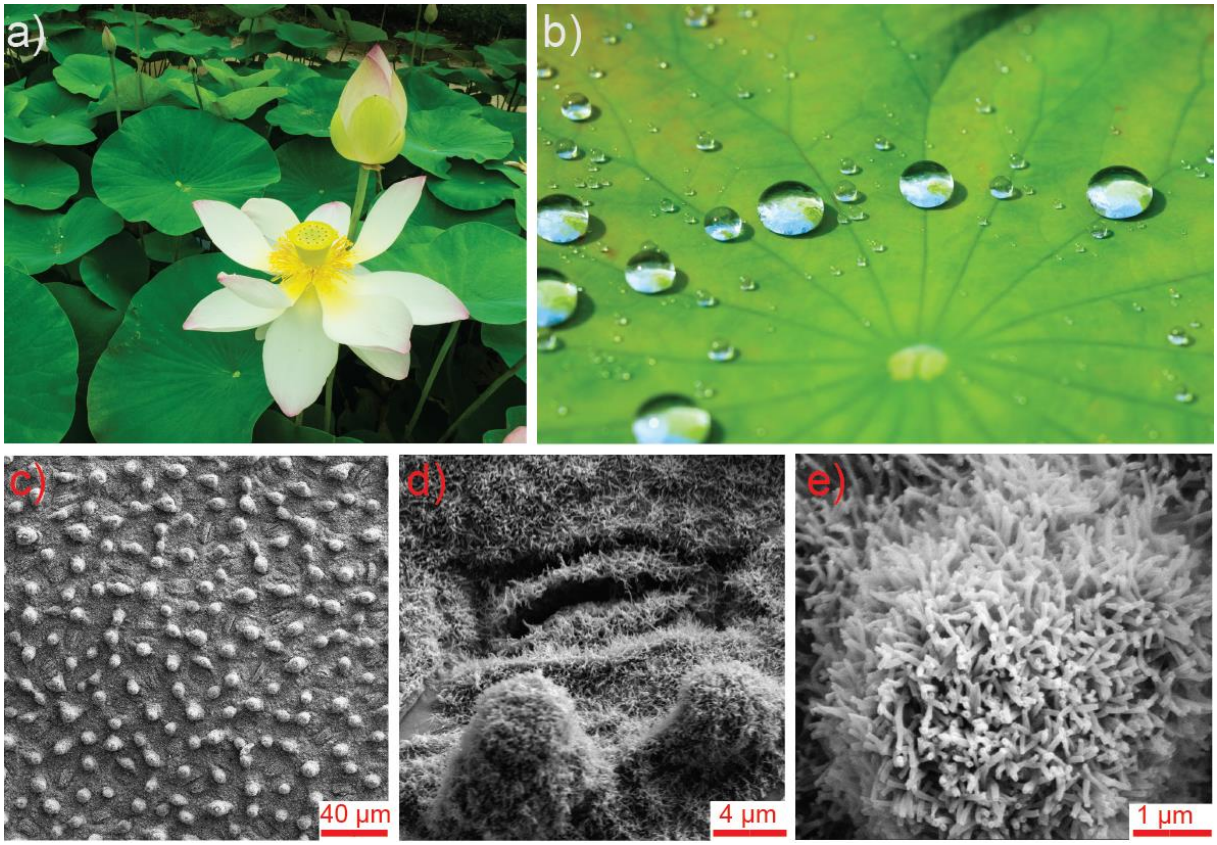

Figure 3.1. Pictures and SEM images of the Lotus plant. a) Lotus plants, b) Drops on leafs has excellent superhydrophobic effect[25]*, c) SEM images of Lotus leaf, d) Higher magnification show hierarchical nano- and microstructures, e) Even high imaginations show the delicate nanostructures.*

Superhydrophobic or self-cleaning surfaces have been found in nature for millions of years. Most plants have some water repelling effect on their leaves and the repelled water will collect dirt and other particles, leaving the plant clean so it can absorb light needed for photosynthesis. Particular water plants like the Lotus plant (*Nelumbo*) family are known for excellent self-cleaning properties and superhydrophobic effect (Figure 3.1 a,b). The self-cleaning effect

is therefore known as the *Lotus Effect*. It is reported that the Lotus Effect origins from a combination of surface chemistry and surface topography[14] (Figure 3.1 c,d,e). Leaf cells on the lotus plant produces hierarchical micro- and nanostructure from a hydrophobic wax layer that increase the contact angle to 160°[14]. Other plants have similar effects and structures[26]. Overall, the Lotus plant is an excellent benchmark for comparing with artificially made super hydrophobic surfaces. Nature has already perfected the properties required for self-cleaning surfaces and these properties could be useful for many industrial applications.

A number of studies have been carried out in order to replicate the Lotus Effect for a wide range of applications. Some studies have pure scientific value and are focused on improving the understanding and knowledge of the superhydrophobic effect, while others are closer to applications. Depending on the types of superhydrophobic surfaces, the cost and manufacturability may vary. Overall two main concepts for fabrication of superhydrophobic surface have been used, 1) A top down approach defines the surface topography of a bulk material by etching, embossing, etc. The surface will become more rough and obtain the superhydrophobic effect, 2) Material can be deposited to modify the roughened and/or chemical properties of the surface to obtain the superhydrophobic effect, e.g. fluor based coating or nanoparticles[27].

3.1 Top down approaches

Many studies have tried to replicate the Lotus Effect, some have simply made polymer replica of a Lotus leaf or leaves from other plants. However, the nanostructures on the Lotus leaf were too delicate for good replication. Casting or imprinting with the Lotus leaf require at least two imprints, a single imprint is simply not enough since the polarity of the structures are inversed in the imprinting or casting process. A second imprint will return the structures to the original polarity. Contact angles on a replicated Lotus leaf are reported to be 158° with a drop roll of angle at 8°[28].

3.1.1 Semiconductor based methods

The toolbox from the electronic industry can easily fabricate micro- and nanostructures needed for a superhydrophobic effect. Structures down to 18 nm can be fabricated with UV lithography on large areas[29]. Even smaller structures (below 10 nm) can be fabricated with electron beam lithography (E-beam). E-beam is a slow process and only suitable for small areas[30]. A wide range of etching and deposition systems can modify the surface and make high aspect ratio or hierarchical structures, such as microstructures combined with black silicon structures[31]. The fabricated semiconductor structures can subsequently be used as master for imprinting or embossing to increase the production rate and lower the cost for the superhydrophobic surface.

3.1.2 Roll-to-roll embossing

Roll-to-roll fabrication is an alternative to injection molding. Structures are embossed in foil with a structured master roll, and the finished foil is rolled and collected. The advantage of

roll-to-roll is that very large areas can be mass-produced. Roll-to-roll fabrication is a promising method for industrial micro- and nanoscale fabrication although information, particularly regarding processes and stability control, is still limited. The structures on the master roll can for instance be fabricated with the lithography-based method and then be transferred to the roll[32].

The Danish research project LANI works on fabricating self-cleaning surface on industrial equipment, here a variant of roll-to-roll called extrusion coating are used to manufacture nano- and microstructures on foils[9].

The advantage of roll-to-roll is its low cost and high production rate, although it can be difficult to transfer the structures onto the curved roll. Roll-to-roll fabrication has the limitation of flat surfaces. Although a process known as in mold labeling can transfer parts to injection-molded surface, and is widely used to decorate polymer items such as plastic cups and food containers, even structured foils e.g. holograms can be fabricated with this method[10].

3.1.3 Plasma and laser based methods

If polymer material is exposed to plasma, the surface chemistry and/or topography will be changed by the plasma exposure. It is reported that different power levels of oxygen plasma can control surface properties[33]. High power plasma will increase the contact angle on Polytetrafluoroethylene (PTFE) making the surface more hydrophobic, and low power will decrease the contact angle changing the properties of PTFE to hydrophilic[33]. Plasma can also be used to deposit different superhydrophobic coatings[34]. Chemical modification can also be performed by laser exposure, here the laser beam can change both surface topography and chemistry, a polymer material like TOPAS can be exposed, and by adjusting power and focus of the beam the surface properties can be anything from hydrophilic to superhydrophobic[35].

3.2 Bottom up methods

In a bottom up method, material is added to make the superhydrophobic surface; examples are self-assembled surfaces or nanoparticle coatings.

3.2.1 Electro spinning

Electro spinning is a method to fabricate tiny polymer fibers, these fibers form webs of nano and micro sized fibers in the 10 nm to 10 µm[36] scale. Superhydrophobic surfaces are reported from both fluorinated and unfluorinate polymers such as PP[37]. The principle of electro spinning is that a dissolved polymer or a polymer melt is sprayed through a nozzle and pulled by a strong electric field, the polymer is collected as thin fibers on an electrically grounded target[38]. The common thing for electro-spun materials is that they have a very large surface to volume ratio. An advantage of electro spinning is that the method can produce excellent superhydrophobicity with standard industrial polymers such as PP and PVC[37]. Electro spinning is marked as a low cost method where up to 20 000 000 m^2 can be produced with a single production

unit per year [39]. Although this high production rate is achieved by another fabrication method where the web is collected from a cylinder instead of a nozzle[40].

Contact angles are reported to be 178° for electro spun fibers combined with nanoparticles[41]. Contact angles from pure polypropylene webs are reported to have lower connect angle at 150°[42].

3.2.2 Coatings

Coating is a widespread method for the fabrication of superhydrophobic surfaces. The advantages of coatings are that they can be applied to a wide range of both flat and freeform surfaces. Furthermore, coatings can modify both surface topography and chemistry in one step. This make coatings a relatively cheap and easy method of fabricating superhydrophobic surface.

One method to fabricate a superhydrophobic coating is to apply nanoparticles[43]. The particles can be deposited layer by layer. If different sizes of particles are used, multistate roughness can be fabricated. Layers of particles can form a mechanically stable surface that is self-healing when damaged[44]. When one layer of particles is worn, the next layer of particles will simply take its place leaving the superhydrophobic effect intact. Alternatives to nanoparticles are fluorocarbons and silicone based materials with high intrinsic contact angles[43]. Several commercial companies produce superhydrophobic coatings such as the ones made by TC Nano[45].

3.3 Combined methods

The above mentioned methods can all fabricate superhydrophobic surface. Combinations of the different methods can be used to further enhance the superhydrophobic effect. Coatings can be used in combination with rough structures fabricated lithography, e.g. perfluorodecyltrichlorosilane (FDTS) can perform a thin (monolayer) flour carbon covalently bound to the silicon and other materials. This is useful since the high resolution and reproducibility of the lithography based method can be used to define the roughness, as the mono layer thickness will not influence the dimensions of the defined structures. What is common to the bottom up methods is that true 3D structures can be fabricated; spongelike materials will increase durability of the superhydrophobic surface. When exposed to wear some of the material may be removed. In a sponge like material a new layer would simply be exposed and the superhydrophobic effect preserved. Furthermore, a spongelike material produce overhangs which further improve superhydrophobic properties of the surface[22].

The research in superhydrophobic surfaces is a huge field with an increase in publications each year. To list all the methods described in literature would be difficult in this section. The main types of fabrication and principles are listed. The most common mentioned techniques is that they cannot match the potential of injection molding regarding manufacturability and cost.

3.4 Surface wetting

The superhydrophobic criteria are not enough to fully describe a water repellant surface. When a surface is submerged into water for either a short or prolonged time, the superhydrophobic state often collapses and water would be pinned to the surface. If pinning occurs, then the surface cannot be utilized effectively and the application range will be limited, this can be a problem for food containers, medical containers or other applications.

It is reported that Lotus leaves lose their superhydrophobic properties when submerged into water for even a few minutes or if the water pressure is increased, although the superhydrophobic effect is recovered when the leaves dry again[46]. Other plants and some insect have the possibility of trapping a thin layer of air with hairlike structures. This trapped air layer is called a plastron; a surface with plastron may effectively retain the superhydrophobic state after submersion[47].

Therefore, it is important to study the long-term effects of superhydrophobic surfaces when exposed to water. Studies show that different methods have been used to characterize the stability of superhydrophobic surfaces. Most methods are based on indirect optical methods that measure average wetting over larger areas. A few papers report direct measurement on individual structures. Some of the important papers are listed here:

Lei *et al.* (2010)[48] show a diffraction based method to characterize submerged PDMS gratings, where the diffraction pattern from a laser changes as PDMS structures are filled, they report that an almost filled structure can reverse to the Cassie State as long as the structures are not fully wetted. The diffraction patterns were projected on a screen and changes were recorded as function of pressure with a CCD camera[48].

Bobji *et al.* (2009)[49] describe an optical method based on total internal reflection to determine the Cassie to Wenzel transition for different structure types. When the superhydrophobic Cassie State collapses on a single structure, the water air interface is no longer present and the condition for total internal reflection disappears. Bright spots on the microscope image become dark when a structure has transitioned into the Wenzel State. The disappearance of dark spots was plotted as function of water depth. The smallest feature size to be imaged is 20 µm. The paper reports a correlation between mean transition time and water pressure. Thereby showing the degree of stability for different structures types[49].

Sakai *et al.* (2009)[50] describe another method based on total internal reflection to measure the amount of trapped air on a superhydrophobic sample, here the intensity of a reflected laser beam is used to determine the amount of air trapped in the structures. Two different sample types are used for experiment; one with low roughness and one with large roughness. The surface energy of the water is changed by adding ethanol. As more ethanol is added, the water air interface will penetrate deeper into the structures. The addition of ethanol shows a

decreasing intensity for large roughness sample and vice versa for the low roughness. The method is described as effective for various superhydrophobic surfaces[50].

Lv *et al.* (2010)[51] show how the air pockets in circular micro cavities (holes) collapse. The sample was placed inside a pressure cell and detailed studies with confocal microscopy show how the meniscus moves inside micro cavities. As a result, the transition from Cassie State to Wenzel State was monitored for different pressures and compared with relevant theory. The shape of the meniscus is monitored as it moves down along the structure sidewall. Furthermore, the contact angle can be determined relative to the sidewall while the meniscus moves down. Sidewall roughness will influence how fast the meniscus moves and the transition time from Cassie State to Wenzel State. The transition time as function of pressure is shown and as expected a hole will collapse faster at higher pressures[51].

3.4.1 Cassie-impregnating State

Verho *et al.* (2012)[23] show the Cassie-impregnating State that can be controlled locally with over and under pressure from a syringe, the Cassie-impregnating State is fully reversible to the Cassie State. However, if the liquid is forced into the Wenzel State, it will be impossible to go back to the Cassie State or Cassie-impregnating State. To verify that the microstructures were wetted a confocal method was developed, this confocal method used fluorescent nanoparticles which could be detected inside the microstructures[23].

Potetes *et al.* (2010)[52] characterize air layers on submerged aluminum surfaces coated with Teflon and on Lotus leaves. The surfaces were submerged at different depths and the collapse of the air layer/plastron was characterized by measuring relative reflectivity from the water air interface. Larger pressures were found to significantly decrease the air layers' lifetime. Furthermore, the decay was studied with confocal microscopy, and the mechanism behind the decay studied in detail. Several factors were found to have influence such as water pressure, Laplace pressure, and diffusion from the air into the water (Henry's Law). After air layer collapse a small reflection remained; the authors suggest that the small reflection may be based on air trapped on the hierarchical nanostructures, in the Cassie-impregnating State[52].

3.5 Injection molding

In order to fabricate effective molds for injection molding of superhydrophobic structures, the basic tool manufacturing methods must be known. The traditional mold fabrication has several limitations when it comes to fabrication of molds suitable for superhydrophobic surfaces. The traditional mold fabrication methods simply do not have the required accuracy for nano- and microstructuring, this section lists the main industrial methods and their limitations for fabrication of nano- and microstructures needed for superhydrophobic surfaces.

3.5.1 Traditional mold fabrication (Micro machining)

The standard manufacturing methods for injection molding tools are milling and electric discharge machining (EDM). These methods have especially been developed for the fabrication

of microstructures and are known as micro machining. Micro milling is a high precision CNC milling. A machine can produce structures down to 100 µm in steel[53]. EDM removes material by short electric discharges in an insulating fluid. EDM can cut all materials regardless of hardness, as long as the material is electrically conductive[54]. Conventional EDM can fabricate structures down to at least 100 µm[54,55].

3.5.2 Laser ablation

A pulse laser, typically in the nano to femto second range, can with its high pulse energy be used to evaporate metals such as steels. Under the best circumstances structures can be fabricated smaller than 10 µm[56]. Molds for superhydrophobic surfaces are produced in titanium and transferred to hydrophobic materials[57]. Other superhydrophobic surfaces defined by laser are reported[58,59]. Laser ablation has the advantage of being relatively fast and can structure freeform molds and inserts.

3.5.3 Insert based methods

In order to reduce the smallest feature size of an injection mold, parts of the tool can be designed as a removable insert. The advantages are that the entire tool does not need to be replaced when the structures are worn out, and planer inserts have the possibility to be fabricated with small features in the double digit nanometer range. Two insert fabrication methods are described below, which can both produce extremely small structures.

1) Silicon wafer

Injection molding with a silicon wafer is possible. Nanostructures can be injection molded although the lifetime of a silicon wafer is short due to the brittleness of silicon. The technique is limited to produce small amounts of parts for research purpose.

2) Lithography, Electroplating, Molding (LIGA)

A LIGA derived process can be used to fabricate thin sheets of flat metal for the injection molding of CDs, DVDs and Blu-ray discs. These flat sheets are often called shims. In a traditional LIGA process, the first step is the coating of a conductive metal layer for the subsequent electroplating process onto a substrate (glass or silicon wafer). A thin layer of resist is coated and UV or X-ray lithography is used to define the required structures. This produces a polymer replica on top of the substrate. Electro plating, typically with nickel, is subsequently carried out. The substrate and resist are removed and the shim is ready for placement in an injection molding tool[60]. Furthermore, the electroplating process can be carried out on an etched silicon wafer with a thin conductive coating. The advantages are that LIGA is based on conventional semiconductor fabrication and well defined structures of 50 nm are reported on substrates[1].

3.5.4 Companies that work with micro structuring of molds

Worldwide several companies produce micro- and nanostructured injection molding tools or inserts. Four important companies are listed here NIL Technology and InMold Biosystems are project partners in the Nanoplast project.

- *NIL Technology* sell nanostructured nickel shims that has the potential for super hydrophobic surfaces, the fabrication of these nickel shims are based on conventional clean room fabrication and electroplating[61]. Furthermore NIL Technology is the co-inventor on one of the patents in the Nanoplast project, more specifically the patent describing imprint on steel molds with a flexible stamp and subsequent etching or electroplating of nanostructures[2].
- *InMold Biosystems* claim that they can fabricate nanostructured steel molds on freeform surfaces with low surface roughness down to 3 nm (Rz). The structures are defended in a ductile coating, which is later hardened. The mold can withstand 300°C and 1500 bar for at least 66 000 injection molding cycles[62].
- *Hoowaki* fabricate functional microstructure surfaces on stainless steel and other metals. Self-cleaning metal mold surfaces, which can be used to process polymer parts are sold. Contact angles are not reported but videos that demonstrate the effect can be seen[63].
- *Lightmotif* fabricate microstructures on steel by laser machining, Lotus effect is reported with structures down to 10 µm on steel and injection molded super hydrophobic surfaces are demonstrated[59].

The small scale of the nano- and microstructures can prove hard to replicate in a conventional injection molding process, especially for larger aspect ratios.

In order to injection mold parts with nano- and microstructures it can be required to use a so-called variotherm process in the injection molding process were the mold is preheated above the polymer melt temperature, after polymer injection the mold is cooled before part ejection. Such systems are commercially available[64], but will add to production costs due to a longer process time.

3.6 Injection molded superhydrophobic surfaces

The scientific community has for some time reported polymer superhydrophobic surfaces, and many papers are published. Most of the methods described are not compatible with conventional large scale fabrication methods and therefore have limited value outside the scientific world. Different kinds of injection molded superhydrophobic structures are reported.

An EU funded project, named *Nanoclean project*, from 2009 to 2012 focused on fabricating injection molded parts for the automotive industry. The fabrication method used in the Nanoclean project was short laser pulsed structuring of steel molds by the company Lightmotif. Molds with microstructures, with nano roughness were fabricated. Superhydrophobic polymer parts were produced on both flat surface and complex freeform parts. In order to improve the superhydrophobic effect polymer, companies worked on developing new types of polymer that was optimal for water repellency and mechanical properties required by the automotive industry[59].

In Hopmann *et al.* (2013)[65] superhydrophobic surfaces made from liquid silicone rubber is injection molded. Here cold liquid silicone rubber is injected into a preheated mold, cured and ejected. The structures consist of conical pillars 5 µm to 20 µm made from steel inserts fabricated by pico second laser. The intrinsic contact angle of the flat liquid silicone rubber was reported to 115°. After structuring the contact angle was increased over 40°. It is reported that the softer liquid silicone rubber is more durable than similar structures made from thermoplastic. Liquid silicone rubber can be molded over other materials such as thermoplastic and metals, and thereby durable superhydrophobic items can be fabricated[65].

Michaeli *et al.* (2011)[58] show a method to have a fast laser based variotherm injection molding process, with a heat up rate up to 300 K/s, with no overshoot, the advantage is that only small parts of the tool are heated. In order to implement the method an insert is made from pressure resistant glass. To test the laser heated variotherm process, a mold with superhydrophobic structures were tested with laser heating versus a traditional injection molding process. Results from the paper are clear and the variotherm process is required in order obtain the replication quality required for the superhydrophobic effect.

A Finish research group led by Prof. Tapani A. Pakkanen has carried out extensive research in polymer superhydrophobic surfaces, fabricated by injection molding. A selection of their papers are presented below.

One of the first papers describing superhydrophobic surface fabricated by injection molding is Puukilainen *et al.* (2007)[66] Superhydrophobic polyolefin surfaces: controlled micro- and nanostructures. Here, aluminum molds were fabricated with a microstructuring robot that punched micro holes in the aluminum mold, hierarchical nanostructures were added by an oxidation process of the aluminum. Injection molding was carried out and hierarchical nano- and microstructures were fabricated with superhydrophobic properties; contact angles larger than 165° and roll of angle below 2.5°[66]. This paper is extremely important since it is a proof of concept that polymer superhydrophobic surfaces can be injection molded.

Nanostructures are often very fragile and easily damaged, In Huovinen *et al.* (2012)[67], a more durable superhydrophobic surface was injection molded in polypropylene. A series of hierarchical micro-micro structures were fabricated, and compared to traditional hierarchical nano- and microstructures, similar superhydrophobic surface effects were measured for both structure types before pressure and wear test. After testing the contact angle was measured again and the micro-micro hierarchical structures were reported to have better resistance to pressure and wear up to an order of magnitude[67].

In Huovinen *et al.* (2014)[68] large microstructures are used to protect smaller nano/microstructures, it is shown that the superhydrophobic effect remains even after the surface is exposed to extensive wear. Only the large protective microstructures are damaged during the mechanical wear. Superhydrophobic effect was retained after a wear test consisting of 10 cycles with

a pressure of 120 kPa[68]. This paper is important because it shows that superhydrophobic surfaces can be injection molded with resistance to mechanical wear, thereby expanding the application range.

3.7 Additives in injection molding

When superhydrophobic or self-cleaning surfaces are injection molded, the correct polymer choice is important. Additives are often used to improve the performance in the injection molding process. When a polymer is used for injection molding, additives with different properties are typically added, e.g. lubrication, antioxidants, nucleating agents to improve crystallization etc.[69,70]. A list and a short description of typical polymer additives are shown in Table 3.1 modified from Preeti Singh *et al*.[70].

Additive type	**Effects**
Antiblocks	E.g. talc, silica, clay, mica, ceramic spheres – prevent a film sticking to itself and make separation of film easier
Antifogs	Prevent the formation of fog (water vapor) on the plastic surface
Antioxidants	Prevent oxidization
Antistatic agents	E.g. carbon, metallized fillers and carbon fibers – reduce buildup of static
Biocides	E.g. preservatives and fungicides
Chemical blowing agents	E.g. sodium bicarbonate – produce gases on polymerization to produce foam
Flame retardants	Halogenated compounds, phosphorus compounds, metallic oxides and inorganic fillers – reduce flammability
Heat stabilizers	Maintain color quality at high forming temperatures
Impact modifiers	Improve ability to absorb and dissipate impact forces
Light stabilizers	E.g. mica powder – reduce degradation from UV light
Lubricants	Help the molecules to flow during forming
Mold release agents	Prevent material from sticking to molds
Nucleating agents	Improve hardness, elasticity, optical properties and transparency
Plasticizers	E.g. epoxidized vegetable oil, butadiene – make material soft and pliable
Processing aids	Improve the production rates at manufacture by removing the “sharkskin” or “orange peel” effect produced by molten polymer sticking to the die
Slip agents	Agents amides: reduce the coefficient of friction, thus helping the molecules to flow
Fillers	E.g. talc, chalk, clay – improves stiffness, strength and electrical properties (clay)

Table 3.1. A list and a short description of typical polymer additives modified from[70].

Some specific additives, often used, are listed here,

- Stearate is an often used lubricant and antisticking agent added to polymers[71]. A lubricant can decrease the polymer viscosity, and thereby reduce the required injection pressure in the injection molding process or lower the adhesion between polymer part and mold. The stearate molecule is an amphiphile as shown on the chemical formula Figure 3.2. The hydrophobic part of the stearate molecules will influence the intrinsic contact angle of the material, making it more hydrophilic.
- Crystallizers or nucleating agents can polar molecules based on benzoates or phosphates[69], which will reduce hydrophobicity of the polymer.
- Antioxidants are based on thio-ethers that decompose polymer peroxide. In combination with phenols, antioxidants offer additional long-term stability. Phenolic antioxidants are radical scavengers which prevent thermal degradation of many polymeric materials[69], polar molecules, such as alcohols, can reduce the hydrophobicity.

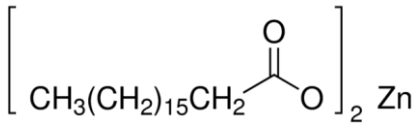

Figure 3.2. Amphiphile zinc stearate[72]; note the long unpolar hydrocarbon chain and polar oxygen molecules.

Many common additives are hydrophilic or polar molecules which reduce hydrophobicity of the polymer[69–71]. The smaller additive molecules can migrate to the surface either during polymer processing or at ambient temperature after production of parts[70,73]. This will cause a further decrease in hydrophobicity because the concentration of the polar or hydrophilic additives increase at the surface.

4 Design of structures and polymer choice

Silicon wafers with black silicon (nanograss) coated with fluorocarbons show excellent superhydrophobic properties. This is further increased by the addition of microstructures[31]. The superhydrophobic effect of coated black silicon was used as inspiration to the design and fabrication the injection molded superhydrophobic structures used in this project.

Non-fluor polymers will typically have lower contact angles compared to coatings based on fluorocarbons such as FDTS which has a contact angle of approximately 110°. The structures in this project were designed to examine whether hierarchical structures are required for superhydrophobicity when non-fluor polymer surfaces are injection molded. Microstructures were designed and fabricated and each structure type was produced with hierarchical black silicon (nanograss) or as pure microstructures. The Lotus leaf was used as inspiration for the structures, except when no overhanging structures on the sidewall could be reproduced by the injection molding process.

Black silicon structures can be produced in a wide size range and aspect ratios (Figure 4.1)[74], however, if the black silicon structures are injection molded, large aspect ratio structures are not suited, because the high thin structures would be difficult to fill and demold during the injection molding process. Low aspect ratio black silicon similar to Figure 4.1A was used in this project. Furthermore, the black silicon in Figure 4.1A was suited for injection molding because it has positive angled sidewalls. Because of the positive angled sidewalls, the black silicon is easier to demold than, e.g. nanopillars with straight sidewalls.

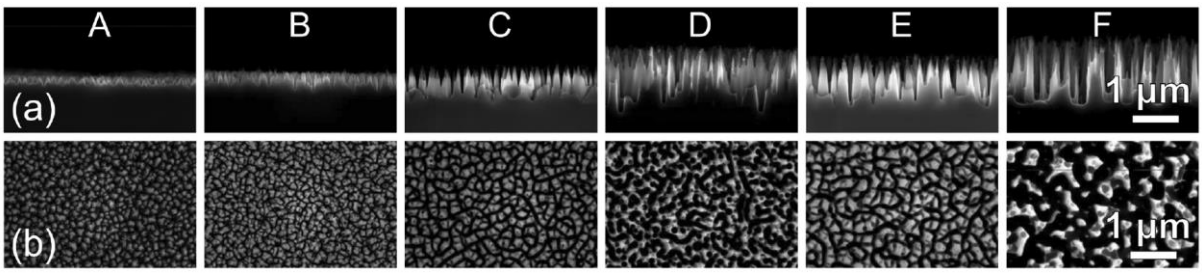

Figure 4.1. Different types black silicon, a) Side view, b) Top view. Black silicon similar to A is suited for injection molding because of the low aspect ratio. Figure from[74].

The addition of nanograss to the microstructures has two functions; first, the contact angle is increased by the nanograss induced roughness. If the liquid in contact with the nanograss is in the Wenzel State the roughness factor will be increased. If the liquid is in the Cassie State, the solid liquid fraction (surface coverage) will be decreased (higher contact angle and less drop adhesion), because the solid liquid fraction for hierarchical structures is calculated by the

surface coverage of the nanostructures multiplied with surface coverage of the microstructures. To estimate the solid liquid fraction of nanograss is a challenge, because the nanograss are random structures with different height, sizes, and sidewall angles. Due to the sharp tips, the nanograss is likely to be in a transition state where the structures are partially wetted between Cassie and Wenzel States. Secondly, a transition into the irreversible Wenzel State would be prevented, by the Cassie-impregnating State formed by the nanograss on the bottom of the surface.

4.1 Pillars based structures

Surface structures with pillars are often used to fabricate a superhydrophobic surface as either a single structure or hierarchical structures[31,58,67,75–77]. Therefore, pillars are a natural starting point for superhydrophobic surfaces. Some limitations on height and size of the structures are required for injection molding. Initially, generally aspect ratios of approximately 1 or lower were chosen, since higher structures would be more difficult to injection mold.

The initial structure design for injection molded superhydrophobic surfaces in this work is composed of different test areas with micropillars 3.00 µm, 5.00 µm, and 7.00 µm in diameter each size would have different periods. The test areas were designed to examine stability of the Cassie State by increasing the space between the pillars from 0 µm to 8 µm. Closely spaced pillars would have a lower penetrating meniscus and a more stable Cassie State, however, they would also have a larger surface liquid fraction which would result in a smaller contact angle. The smaller contact angles will be given by the Cassie Baxter equation (equation 2.7). As the space between the pillars is increased, surface liquid fraction will decrease with a larger contact angle. However, the Cassie State will be unstable, since the drop is supported by a smaller area, due to the decreased surface liquid fraction. Furthermore, the drop will have a larger meniscus penetration when the distance between the pillars is increased. Therefore, it would be easier for the drop to move into the Wenzel State. Surface coverage for the pillars was calculated from the area of one circular pillar divided by the area of a unit cell defined by the structure period as shown by the equation below,

$$f_{sl} = \frac{\pi {R_p}^2}{{P_p}^2} \qquad 4.1$$

Here R_p is the pillar radius and P_p pillar period. The pillars were designed with a maximum surface coverage of 0.79 and a minimum surface coverage 0.06. The surface coverage of the different structures is shown in Figure 4.2. One advantage of pillar based structures is that a small surface coverage can be achieved with a large structure size making pillar based structures less demanding to fabricate.

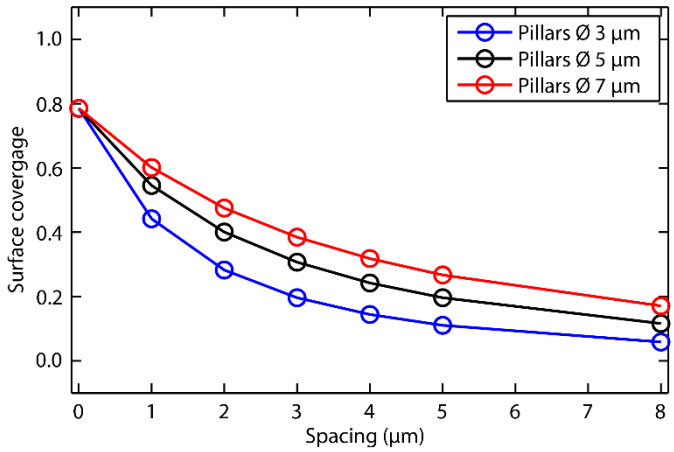

Figure 4.2. Surface coverage of pillars as function of spacing 3.00 µm, 5.00 µm, and 7.00 µm in diameter.

Two polymer part designs were available for injection molding in this project; a microscope slide 1 mm thick, and a round disc 50 mm in diameter and 2 mm thick. The test patterns with pillars were arranged so both part types could be used with the same electroplated nickel shim. The size of the test areas was 7 mm × 7 mm, otherwise the contact angle measurements on smaller areas would be difficult. A CAD file for a conventional photolithography mask was designed with the software L-edit. The layout for the mask together with examples of pillars are shown in Figure 4.3.

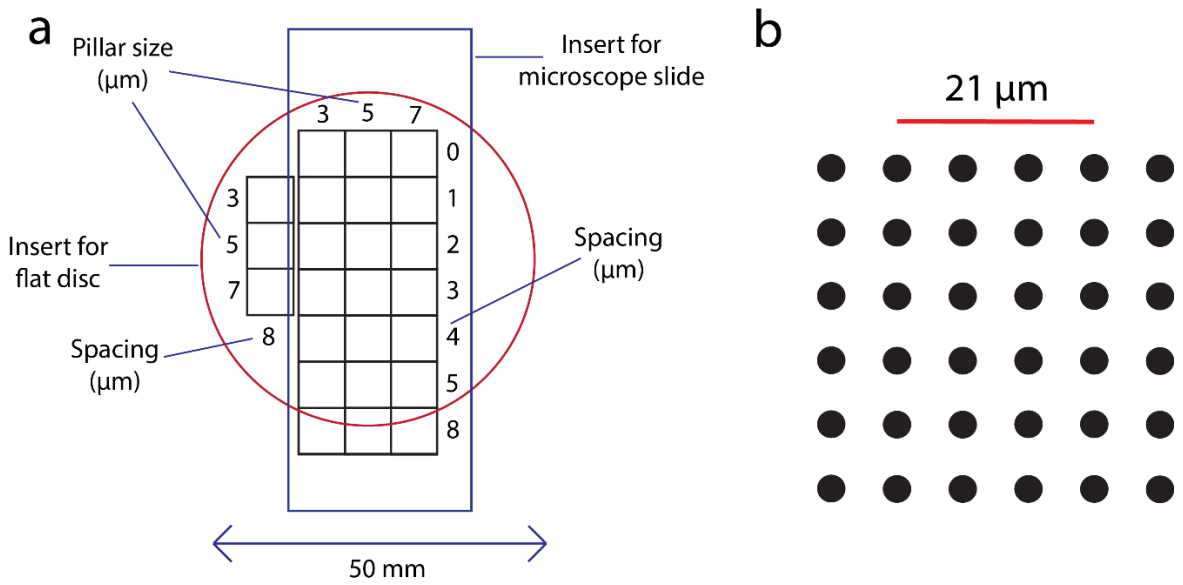

Figure 4.3. Mask design for pillar based structures; a) Mask layout pillars b) Arrangement of pillars with 3.00 µm in diameter and a spacing of 4.00 µm.

4.2 Hole based structures

Surface structures with holes will theoretically provide a more stable Cassie State since a penetrating meniscus will form a counter pressure inside the closed holes (Figure 4.4a). The same effect applies when the holes are injection molded, the nickel shim with inverse structures would be an open array of micropillars with the same diameter as the holes. Therefore, air would be able to escape when the polymer melt is injected as shown on the schematic in Figure 4.4b. To minimize surface liquid fraction, holes were hexagonally arranged. One could expect that during injection molding the large space between the holes was filled first. Polymer material separating the holes could be filled during injection molding from both top and side. The surface coverage for material separating the holes (surface liquid fraction) can be calculated with following equation[21],

$$f_{sl} = 1 - \frac{\pi}{2\sqrt{3}} \left(\frac{Ø}{P_{ho}} \right)^2 \qquad 4.2$$

Here $Ø$ is diameter of the holes and P_{ho} the period of the holes. Surface coverage as function of hole spacing are plotted in Figure 4.5 for holes with diameter of 3.00 µm, 7.00 µm and 15.00 µm.

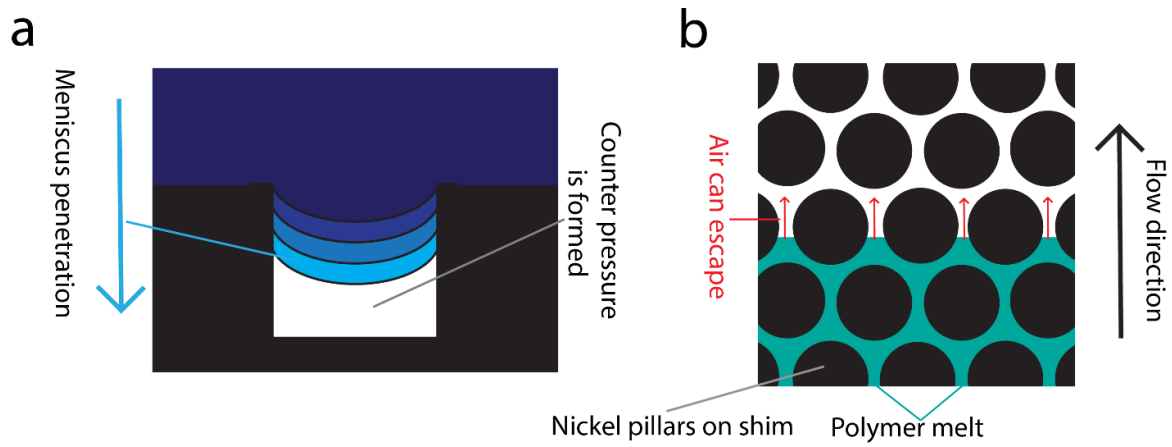

Figure 4.4. Advantages of holes, a) A counter pressure forms a more stable Cassie State, *b) Holes requires less pressure to fill during injection molding because air can escape.*

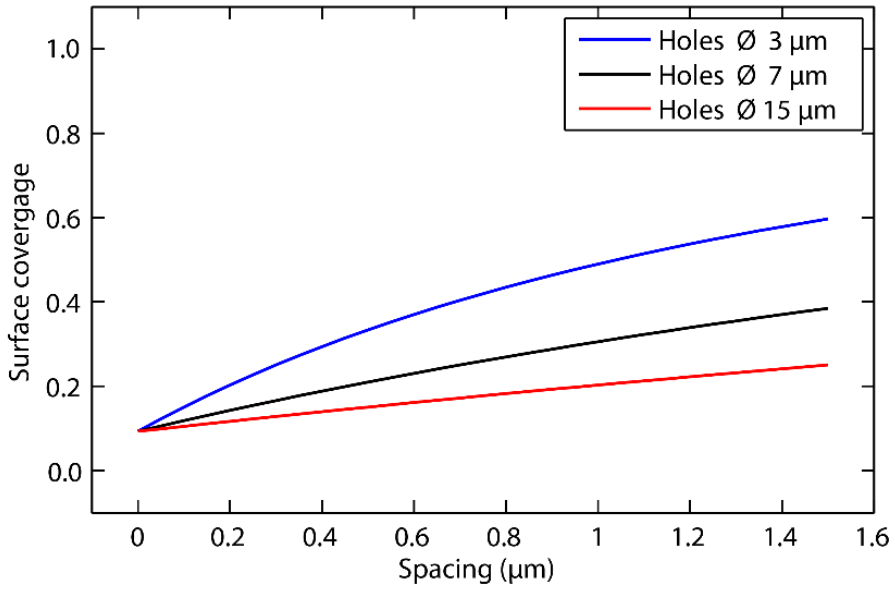

Figure 4.5. Surface coverage of holes as function of spacing.

One disadvantage with hole based structures is that a small surface coverage requires a small feature size (spacing), this makes holes based structures more challenging to fabricate and injection mold. Holes with 3.00 µm, 7.00 µm, and 15.00 µm in diameter with a spacing of 0.30 µm, 0.70 µm, and 0.90 µm for a total of 9 test areas 7 mm × 7 mm were designed. The reason for the different spacing was that the etching of black silicon would reduce some of the structure sidewalls and enlarge the holes. Three different spacings were used to ensure that sidewalls would "survive" the black silicon etch and the holes remained closed. The smaller line width required DUV lithography and a reticle was designed in the software L-edit 5 times larger due to the optical reduction in the DUV stepper. Holes with and without black silicon were fabricated to test the effect of hierarchical structures.

4.3 Spruce like micropillars

Fabrication of pillars with limited sidewall structures was designed by etching away the sidewalls separating hexagonal holes. Scallops from the Deep Reactive Ion Etching (D-RIE) process were used to etch the holes. The scallops would produce small sidewall structures on the finished parts after black silicon etching. Furthermore, the sprucelike micropillars were designed with a high aspect ratio of approximately 5. It was expected that the holes with a spacing of 0.30 µm would produce the sprucelike micropillars. Injection molding of the sprucelike micropillars with its overhanging structures was expected to be challenging or impossible due to results from Michaeli *et al.*[58]. The reason for producing these overhanging structures was their ability to increase water repellency[22].

4.4 Pyramids an pyramid holes

Pyramids and pyramid holes were designed to produce structures which were easier to injection mold. These structures were not optimized for superhydrophobic properties. A positively sloped sidewall will easier demold in the injection molding process. The reason for using pyramidlike structures is that the simple method, KOH wet etching of silicon, can produce pyramids. It was decided that three pyramid sizes were produced; pyramid holes with base length 6.00 µm, 12.00 µm, and 18.00 µm separated with line width of 2.00 µm. The height of the pyramid holes could be calculated from the base length of the pyramid and the 54.7° angle produced by the KOH etching. The height of the pyramids was calculated to 4.24 µm for the 6.00 µm, 8.47 µm for the 12.00 µm, and 12.71 µm for the 18.00 µm. A mask with three test areas each 10 mm × 10 mm was designed in L-edit.

Both pyramids and pyramid holes were fabricated. Pyramids were fabricated by a structure inversion of the pyramid holes with an embossing process in polymer foil. Both pyramids and pyramid holes were fabricated with smooth sides and with hierarchical nanograss. The finished pyramids would have inversed nanograss to the embossing process.

4.5 Polymer materials for injection molding of superhydrophobic surfaces

To produce the superhydrophobic surfaces it was important to select the best suited polymers. The polymer producer Borealis indicated that polymers with few additives would be best suited for injection molding of superhydrophobic surfaces. They recommend four polypropylenes with as few additives as possible. However, the company provides no specific details on additives. Information was only provided for compounds not added to the polymers, HD601CF, HD615CF, HC300BF, and HD312BF. These polymers were not designed for injection molding but for foil extrusion. Polypropylene is often reported to a have a large intrinsic contact angle and is often used as base material for polymer super hydrophobic surface [66–68]. Contact angles were measured for a range of different polymers. The polymer with the largest contact angle, PP HD601CF, was used as main polymer for injection molding of the different structures during this project. The TOPAS polymer is a cyclic olefin copolymer (COC) and the intrinsic contact angle was measured on flat TOPAS parts to 95°. TOPAS is a less hydrophobic material than PP HD601CF and was used to optimize the injection molding process. Furthermore, TOPAS was used to injection mold structures in amorphous polymer.

Parts made from different types of PP were injection molded in hot (100 °C) and cold (20 °C) molds. Contact angles for the different parts were measured after static electricity was removed. Contact angles were measured for three samples, plotted in Figure 4.6. The PP HD601CF had the highest contact angle of 102°. Therefore, it was used as the polymer for further fabrication of superhydrophobic surfaces. Based on the contact angle of PP and the maximum span between structures (15 µm), it was decided to use structure heights between 1.8 µm and 6.0 µm due to a maximum meniscus penetration of approximately 0.8 µm.

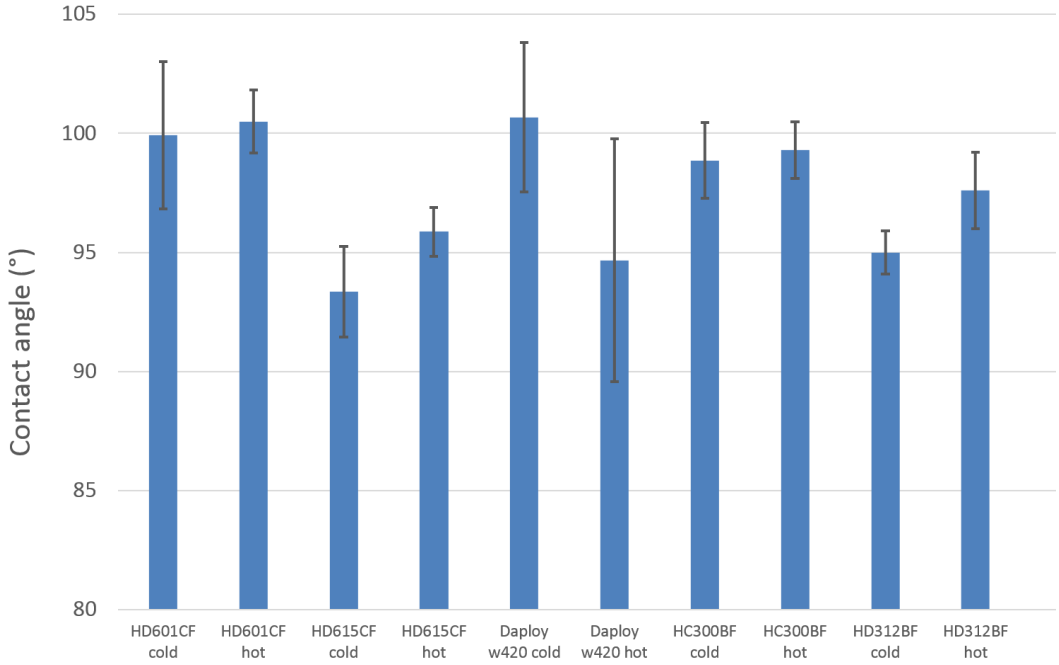

Figure 4.6. Contact angle measurement of different PP.

5 Fabrication

Fabrication of samples for this project can be divided into two major sections, 1) The fabrication of injection molding inserts (shims), 2) The subsequent injection molding process of polymer parts. Both sections were carried out in the Danish National Center for Micro and Nanofabrication (DANCHIP).

Different types of microstructures were fabricated to test the degree of hydrophobicity and manufacturability. Some structures were optimized to have an extreme superhydrophobic effect such as spruce tree like pillars. Holes were designed to give a stable Cassie State when submerged. Pyramid shaped structures were designed to have an optimal geometry for the injection molding process, especially for demolding of the polymer parts. Furthermore, a series of nickel shims with nano- and microstructures were fabricated for a test production by Nanoplast partners. Structures with a feature size larger than 1 µm (pillars, and pyramid shaped structures) were fabricated with standard contact UV lithography. The rest of the structures requires a smaller feature size and were fabricated with DUV lithography.

Working in a laboratory environment disparate from production in an industrial factory. To test how nanostructures were injection molding in an industrial setting, an industrial test production was carried out collaboration with a Nanoplast partner. To examine the quality and replication of injection molded nano- and microstructures, a tool made for nickel shims with four cavities was used, each cavity had 2 × 2 Lego like brick. The shims were designed so each cavity had different structures. The structures for the industrial test production were not designed to be superhydrophobic. They were designed to examine how different structures were filled in an injection molding process with a cycle time as short as possible. This process was similar to the processes used when large amounts of polymer parts are produced in a factory. For the test production structures with a single level were primarily used. Four different test areas were designed as shown on Figure 5.1. The four test areas each had a different structure type,

a) Topology optimized structures, designed to minimize meniscus bending (developed by Nis Korsgaard Andersen).
b) Triangular pillars with a side length of 0.6 µm arranged in a similar pattern to the spruce like micropillars.
c) 3.00 µm holes in hexagonal pattern with a period of 3.60 µm.
d) 0.25 µm pillars with a period of 1.0 µm.

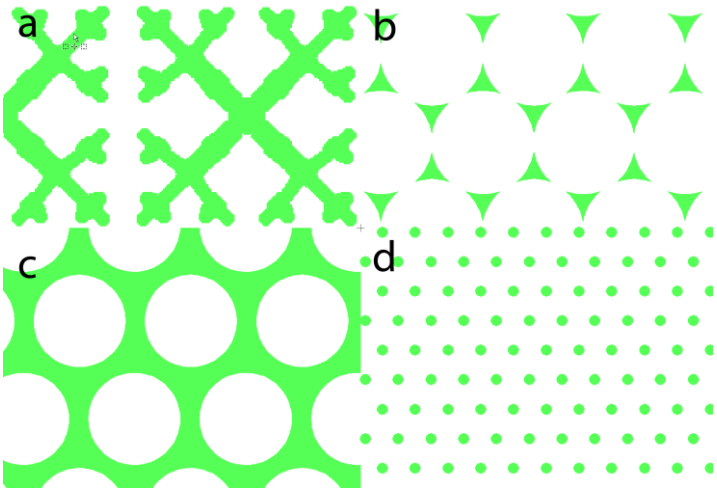

Figure 5.1. Structure for the industrial test production, a) Topology optimized structures, b) Triangular pillars with a side length of 0.60 µm, c) 3.00 µm holes in hexagonal pattern, d) 0.25 µm pillars with a period of 1.00 µm.

To examine the influence of mold filling vs mold height, three shims with different heights were fabricated. One of the shims would have nanograss. A reticle for DUV lithography was designed so each test area was at the center of the Lego brick like part in the industrial tool. The goal of the test production was to examine mold filling with different parameters. The parameters chosen were similar to those used in an industrial production e.g. short cycle times/cold mold.

5.1 Etching theory

Reactive ion etching (RIE), is a common dry etching method for fabrication of structures in semiconductor materials. RIE is a dry etching with gasses, the process is a combination of plasma, chemical, and physical etching. The principle of RIE is that an RF field between two electrodes produces plasma. The plasma consists of reactive ions, a bias accelerates the reactive ions towards the wafer, and sputtering will occur as a result. A RIE process can be difficult to control because the RF power generator controls the energy of the sputtering and the amount plasma, more specifically the ionization and dissociation into free radicals of the gases. Physical and chemical etching cannot be adjusted independently. As a result, the sidewall angle can be hard to control, structures for injection molding requires a positive sidewall angle. High-density plasma etching has been developed to a have a higher degree of etch process control. High-density plasma etching utilizes a more complicated RIE system. A second plasma generator is introduced, which allows for plasma generation and sputtering to be controlled independently, great control of the sidewall is achieved. A RIE process not only etches the semiconductor materials, typically the resist is also etched although at a lower rate. The resist can be etched completely, structure depth can therefore no longer be increased. If deep structures with vertical sidewalls are required, a process called deep reactive ion etching (D-

RIE) can be used. D-RIE is also known as the Bosch process. In D-RIE a passivation layer prevents etching of side walls and protects the resist. Passivation and etching is performed in cycles to obtain the high aspect ratios. Each cycle produces small half circle shaped roughness on the structure sidewall, this is called scallops. The difference between RIE and D-RIE is shown in Figure 5.2[78].

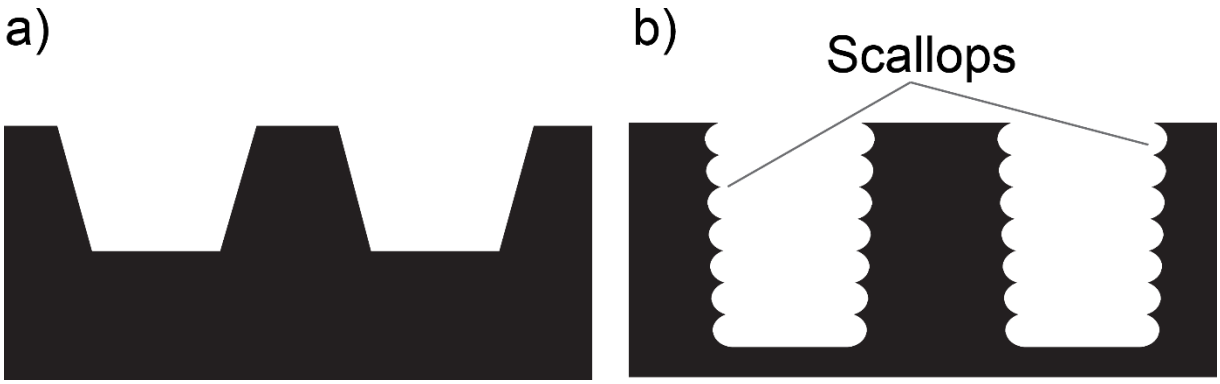

Figure 5.2. RIE principle a) Reactive ion etching produce smooth sidewalls in a semiconductor material. b) Deep reactive ion etching produces deep structures with almost vertical sidewalls, D-RIE runs in cycles and periodic sidewall roughness are formed during the process and the roughness is known as scallops.

5.1.1 Principle of black silicon etching

Black silicon (nanograss) is random cone and/or needle shaped nanostructures etched on a silicon wafer. Black silicon is fabricated regardless of crystal direction. Black silicon has anti-reflective properties which cause the wafer to have a flat black appearance when etched. The fabrication of black silicon is maskless. Etching of black silicon has been performed for many years and used for wide variety of applications, such as solar cells[79,80] or as antireflective structures[74]. In this thesis, hierarchical nanostructures were fabricated by etching of black silicon exclusively.

The advantages with black silicon are that nanostructures can be fabricated on large areas fast. An entire wafer can be processed in less than 15 minutes. The cone shape of black silicon has a sidewall positive angle that is excellent for replication processes such as nano imprint lithography, hot embossing, or injection molding. Some of the limitations with black silicon are that the random nature of the fabrication process makes the dimensions and tolerance of individual structures hard to control.

A widespread method for fabrication of black silicon is by RIE with SF_6 and 0_2 as reactive gasses. The etched process is based on local and regenerating oxide masking. Initially the silicon wafer is covered a (< 5 nm) native oxide layer (SiO_2), this layer is not perfectly uniform and

acts as an etch mask in the initial stage of the black silicon etch. The native Oxide layer is perforated in a random pattern, unmasked areas are etched, and the cone shaped structures formed. Two chemical reactions take place during the black silicon etch: The fluorine atoms from the SF_6 react with the silicon to produce volatile SiF_4, and oxygen react with fluorine and silicon to produce $Si_xO_yF_z$. The sidewall of the structures are covered with the $Si_xO_yF_z$ layer and are therefore protected against further etching, the high energy ions from the RIE removes the silicon and $Si_xO_yF_z$ layer. By balancing the etching parameters correctly, the perforated mask can be maintained (Figure 5.3). Protrusions on the surface will be slightly more protected by the $Si_xO_yF_z$ layer compared to the planar regions, and roughness will eventually form the black silicon structures[79,80].

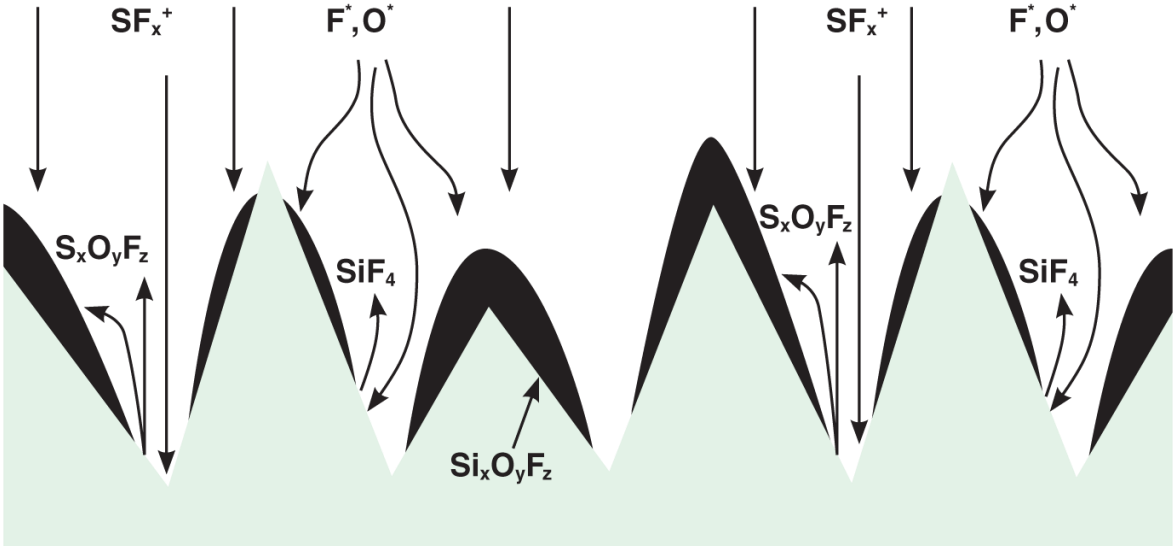

Figure 5.3. Schematic of the black silicon etch, with the self-induced masking and reactive compounds. Modified from [80].

Hierarchical structures can be made by first defining microstructures with conventional lithography and etching. The layer of hierarchical nanostructures in form of black silicon can be etched on top the microstructures[31].

5.1.2 KOH etching wet etching of pyramid shape holes

The pyramid structures had a different fabrication process than the other fabricated structures. The pyramid shaped holes were etched with an anisotropic KOH wet etch. KOH etches specific crystal planes at different etch rates on a silicon wafer. The basic principle is shown in Figure 5.4, the 110 and 100 crystal planes etches at much faster etch rates (several magnitudes) than 111 crystal plane. The result is triangular cross section of the etched structures. If an appropriate etch mask is used the pyramid shaped holes are obtained[78]. Typically etch mask are made from SiO_2 or Si_3N_4 which has much higher resistance to KOH.

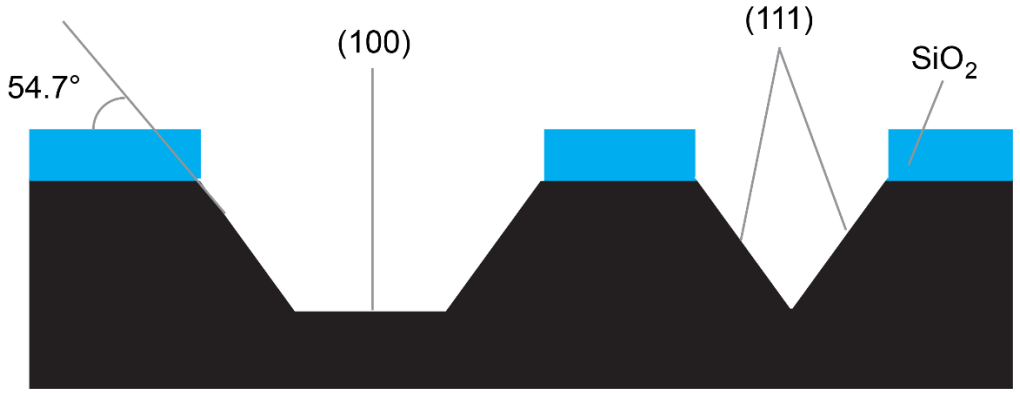

Figure 5.4. Principle of KOH etching of silicon, the (111) crystal plane are etched at lower rates and pyramid like structures are produced.

5.2 Cleanroom fabrication of injection molding inserts (shims)

The fabricated structures were divided into five categories, each with a slightly different fabrications process shown in Table 5.1. All fabricated structures were fabricated from silicon masters and made in a cleanroom.

	Pillars	**Holes**	**Nano-structures for test production**	**Spruce like micropillars**	**Pyramids**	**Pyramids holes**
Substrate preparation (spin coating)	×	×	×	×	× (oxide growth before spin coating)	× (oxide growth before spin coating)
Lithography	× (UV)	× (DUV)	× (DUV)	× (DUV)	× (UV)	× (UV)
Oxide etch					×	×
Structure etch	× (D-RIE)	× (D-RIE)	× (RIE)	× (D-RIE)	× (KOH)	× (KOH)
Black silicon (optional)	×	×	×	× (required)	×	×
Structure inversion					×	
Electroplating	×	×	×	×	×	×

Table 5.1. The fabrication processes for the different structure types.

To increase the hydrophobic effect, the microstructure roughness was increased by black silicon etching on some of the wafers. This process produced hierarchical nano- and microstructures. The black silicon etch process was carried out in the RIE system. No predefined masks were used; the black silicon was etched by perforating the native oxide layer combined with a passivation layer from the etching process[80]. The black silicon etch process produced roughly 175 nm wide cone-like structures with an aspect ratio of about 1.

After silicon wafer fabrication and characterization, injection molding inserts were fabricated by electroplating. A seed metal layer was deposited on the silicon wafer by sputter coating followed by nickel electroplating. The silicon wafer was subsequently removed by a KOH etch, leaving a nickel insert with inverse polarity. The overall fabrication process is shown in Figure 5.5, all structures have a similar fabrication process, and deviations will be described separately.

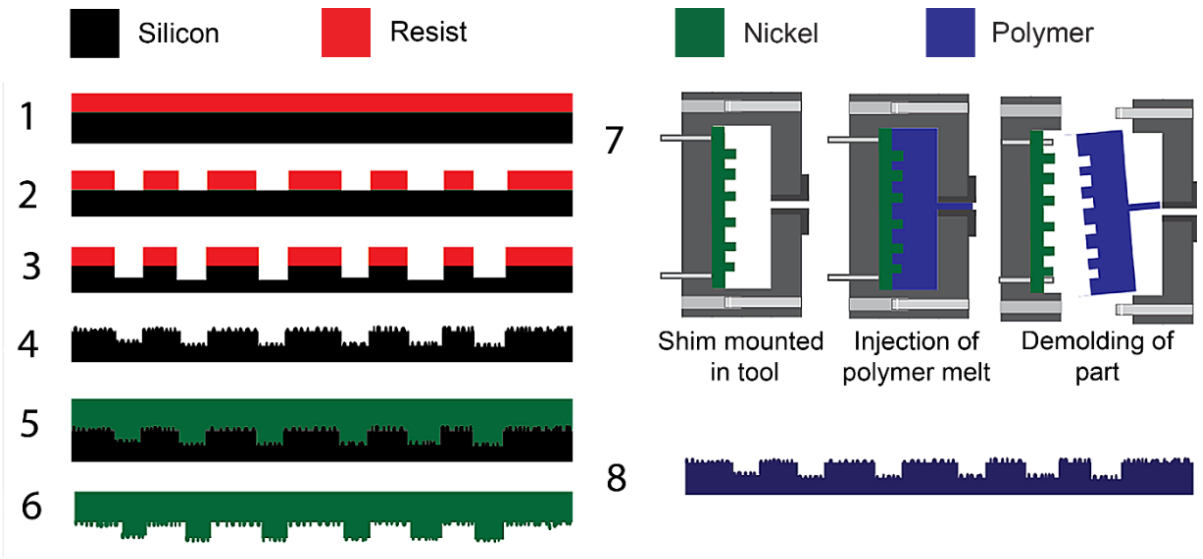

Figure 5.5. The entire fabrication method; 1 and 2) Lithography, 3) Dry etch, 4) Resist strip and black silicon etch (optional), 5) Electroplating of nickel shim, 6) Removal of silicon wafer with KOH, 7) Injection molding of polymer parts from nickel shim, 8) Finished parts with super hydrophobic surfaces.

5.3 Fabrication processes and parameters

The process details for nano- and microstructure fabrication is presented below. The used lithography processes are listed followed by the RIE, D-RIE and black silicon etch parameters. The fabrication process for the pyramid structures is slightly different when compared to fabrication of the other structures and is described separately in detail.

5.3.1 Conventional UV vs DUV Lithography

The five categories of structures all have the same starting step, a blank silicon wafer. A thin SiO_2 layer formed by atmospheric oxygen called native oxide is always present on silicon wafers. The native oxide layer is removed with buffered hydrogen fluoride (BHF) or coated with HMDS. There are small differences in the process for conventional UV and DUV lithography, as listed below.

- **UV lithography** After native oxide removal with BHF, AZ 5214E (MicroChemicals) photoresist was spin coated onto the silicon wafers using an automated spinning system (SSE Maximus 804). The photoresist-coated wafers were exposed in EVG 520 Mask Aligner and vacuum contact mode was used with an Exposure time of 2.0 s. After exposure the wafers was developed for 60 s in a solution diluted from the concentrated AZ 351B (MicroChemicals), 0.8 L AZ 351B developer and 4 L water. The developed resist in now ready for etching.
- **DUV lithography.** Similar in principle to contact UV lithography but is a more complex process with advanced hardware called a stepper (FPA-3000 EX4, Canon). The stepper used a 248 nm krypton fluoride pulsed laser as light source. DUV light is projected through reticle (mask) onto the wafer, and the pattern is reduced by a factor of five in size. A back side anti-reflective layer is needed to obtain the higher resolution compared to contact UV lithography. The DUV process start with a monolayer of HMDS applied to the silicon wafers. Followed by spin coating a BARC (DUV42P, NISSAN CHEMICAL) and 354 nm thick layer photo resist (M230Y, JSR) followed by a 90 ^{o}C baking for 130 s. The number of exposures, exposure positions, and UV light dose (exposure time) is adjusted. After exposure and post bake at 130 °C for 60 s, wafers are devolved with (MF CD-26 developer, Rohm and Haas Electronic Materials LLC) for 60 seconds. To expose the silicon surface, the BARC is removed in the developed structures with a STS Pegasus D-RIE using a pure oxygen plasma. After BARC removal the wafer is ready for the subsequent etching.

5.3.2 RIE process details

A D-RIE process was used to etch the micropillars and holes to different depths, a STS Pegasus D-RIE system was used. Each etch passivation cycle corresponds to a structure depth of approximately 250 nm. For more process details, see Appendix 1. The different nano- and microstructures for the industrial test production were etched with a RIE process (Appendix 1) on again with the STS Pegasus D-RIE, different etch time was tested for different structure depths.

Target etch depth	300 nm	600 nm	900 nm
Etch time	90 s	180 s	300 s

Table 5.2. RIE etch times.

After the structures were etched, the resist needed to be removed; this was done in a barrel asher with oxygen plasma, the parameters used are listed in Table 5.3. After resist removal, nanograss was etched with the Pegasus D-RIE using the parameters in Table 5.4. The black silicon etch process were designed to produce low aspect ratio black silicon suited for injection molding.

Time	O_2 Flow	N_2 Flow	Power
30 min	400 mL/min	70 mL/min	1000 W

Table 5.3. Plasma ashing parameters.

The nanograss etching were optional and only performed on some wafers. For the smaller structures for the industrial test production the nanograss etch time was reduced from 8:00 minutes to 2:00 minutes. After the nanograss etching, the wafers were ready for characterization and subsequent electroplating.

SF_6 (cm^3/min)	O_2 (cm^3/min)	Time (min)	Chuck temperature (°C)	RF platen power (W)	RF Coil (plasma) power (W)
70	110	8	-10	30	2700

Table 5.4. Black silicon etch parameters.

5.3.3 KOH etching of pyramids holes

The fabrication of the pyramids was as mentioned earlier based on KOH wet etching. Normal photoresist cannot be used in the etch process since the KOH will react with the resist and possible change the structure dimensions. A protective oxide layer was used as etch mask.

The protective oxide layer was deposited with thermal wet oxidation in a furnace to a thickness of approximately 500 nm. A monolayer of HMDS was applied with a HMDS vacuum oven on the oxide to promote resist adhesion; this was followed by a 1 µm photoresist layer. A mask designed to make pyramid holes was aligned to the crystal plane of the wafer and the resist exposed and developed. The developed resist structures on top of the oxide were etched through the oxide layer with a specialized dry etching machine (AOE STS) and the resist layer stripped leaving structures in the oxide. The oxide structures were thinned in BHF In order to obtain a smaller spacing between the pyramid holes. Finally, the pyramid holes could be etched with 30 wt% KOH solution heated to 80 °C. After etching the leftover oxide mask was removed in BHF. An overview of the entire pyramid fabrication process is shown in Figure 5.6.

Not only pyramid holes were fabricated. Pyramids were fabricated as well. The fabrication of pyramids was done with a simple change of polarity of the pyramid holes. The etched wafer with pyramid holes was first coated with anti-sticking coating. The anti-sticking coating consisted of a monolayer of 1H,1H,2H,2H-perflourodecyltrichlorosilane (FDTS) and was deposited with molecular vapor deposition (MVD). A process with four deposition cycles was used to ensure complete coverage on sidewalls and bottom of the structures, for more details see Appendix 1.

The coated wafer was used as a stamp in hot embossing process into a 50 µm thick foil made from the polymer TOPAS 8007-S04. After embossing, the foil was glued onto a wafer using UV glue. The pyramid holes had been inverted and the pyramids were ready for electroplating.

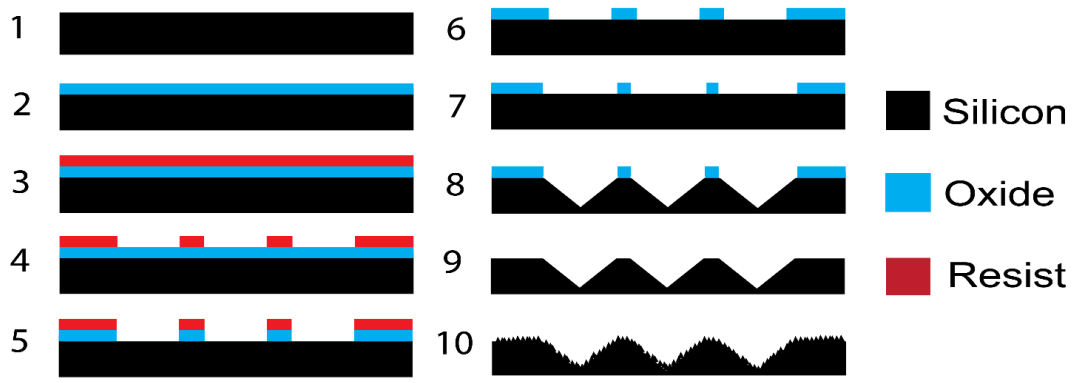

Figure 5.6. Fabrication process for pyramid holes, 1) A new silicon wafer, 2) Oxide growth, 3) Spin coating of resist, 4) Lithography, 5) Oxide dry etch, 6) Resist strip, 7) Thinning of oxide structures with BHF, 8) KOH etching, 9) Oxide removal with BHF, 10) Black silicon etch optional.

5.3.4 Etching of spruce tree like pillars

Spruce tree like pillars were fabricated for extreme superhydrophobic effect by etching of black silicon on micro holes with a diameter of 3 µm and a period of 3.3 µm. The black silicon simultaneously etched sloped sidewalls until the material separating the holes were away. This process left an array of sharp pillars with sidewall structures in the shape of horizontal grooves produced because of the stepwise scallops from the D-RIE. A CAD drawing illustrating the principle is shown in Figure 5.7.

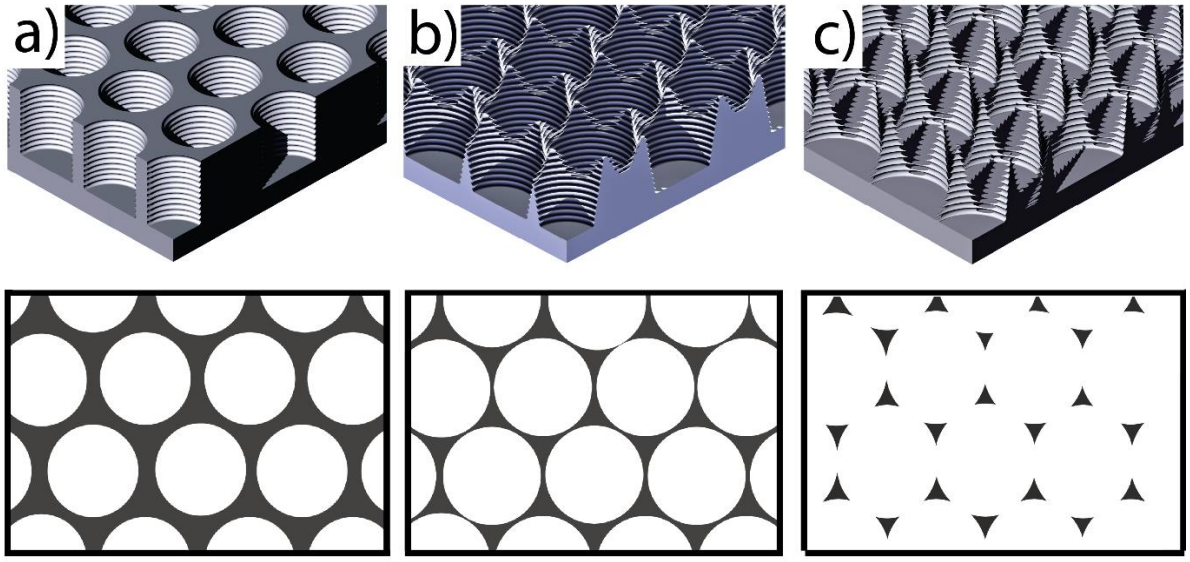

Figure 5.7. 3D and top view illustrations of the steps involved in fabrication of the silicon master, a) A D-RIE process was used to etch circular holes 3 µm in diameter in a silicon wafer. The holes were arranged in a hexagonal pattern with a pitch of 3.3 µm, b) The radius of the holes was increased with a RIE etch designed to make sloped sidewalls, c) The thin silicon walls between the holes were removed by the RIE etch forming sharp pillars with structures on the side, composed of residual scallops from the D-RIE process.

5.3.5 Electroplating

Before injection molding can be carried out, an insert of metal has to be fabricated, since silicon is too brittle for the injection molding process. The inserts were fabricated with electroplating of nickel onto silicon wafers. The electroplating process requires a conductive surface, in order to achieve this, a 100 nm thick seed layer of NiV was deposited with sputter coating. Subsequently a 300 µm thick nickel layer was electroplated with a deposition time of 12 hours. After electroplating, the wafer was completely dissolved in KOH (30 wt%) heated to 80 °C. The result was a nickel shim with inverse polarity.

The depth of the fabricated shims was measured with an optical profilometer and characterized with SEM. The final step in the shim fabrication was deposition of an anti-sticking coating. The anti-sticking (FDTS) was deposited with MVD with the process in Appendix 1. After FDTS coating, the shims were stamped to a shape that could be fitted into the injection molding tool.

5.4 Injection Molding

The principle of injection molding is very simple. A thermoplastic polymer is heated above the melting temperature and used to fill up a predefined mold for the production of parts. In reality injection molding is a considerable more complex process with many parameters to adjust[81].

5.4.1 The Injection Molding Machine and Process

The basic principle of the process is; Injection of polymer melt into a predefined mold, packaging of polymer melt to reduce part shrinkage, cooling until the polymer melt freezes and become solid, and finally de-molding of the finished polymer part. An injection molding machine converts thermoplastic granular into finished parts[81].

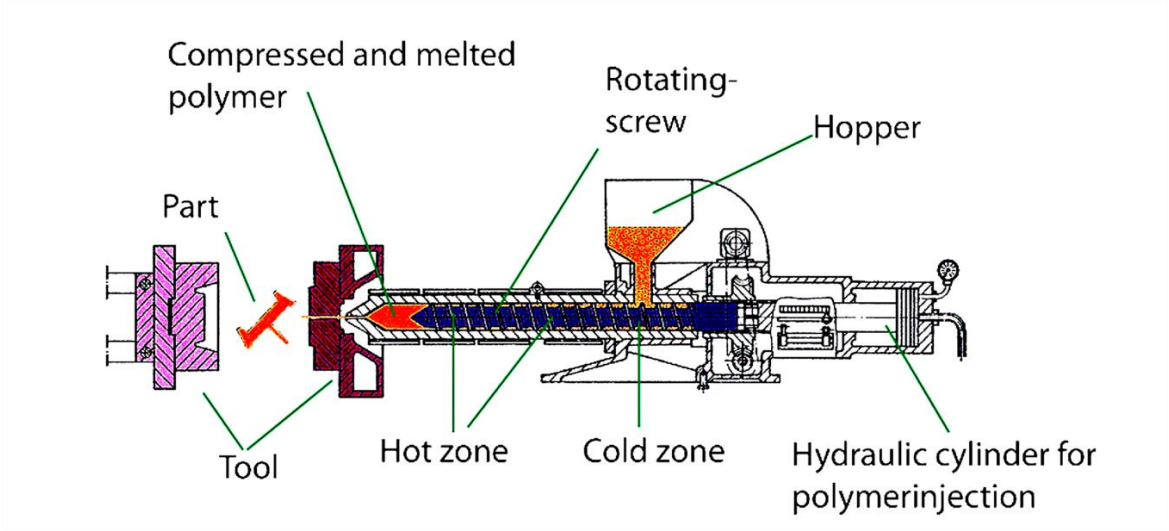

Figure 5.8. Schematically drawing of injection molding machine. Modified from[81].

The schematic drawing of an injection molding machine is shown in Figure 5.8. Polymer granular is kept in the hopper. The specified amount of polymer is fed from the hopper into the barrel with a rotating screw. The polymer will be degassed, compressed, and melted when it is transported through the barrel. The melted polymer ends in front of the screw, and as the polymer volume increase the screw will move backwards until the specified polymer amount is reached. The melted polymer is now ready for injection. The screw moves forward acting as a plunger pressing the polymer melt into the predefined mold cavity.

The polymer injection is done at high pressures of approximately 1000 bar. After the mold filling, the pressure is increased to pack the polymer. The packing is done to make sure that the finished parts are correctly dimensioned and to prevent the part from shrinking too much during cooling. After packing, pressure is applied until the polymer in the small inlet into the mold cavity (gate) solidifies. When the gate is solid (frozen) the pressure can be removed and the mold cooled until solidification of the polymer is complete. The barrel retracts to be ready

for the next shot. The mold opens for part ejection; ejection pins press the part out of the mold. The mold closes, and is ready for the next cycle[81].

The main parameters for injection molding process are:

- Filling time
- Packing time
- Cooling time
- Holding pressure
- Mold open time (open, eject, close)
- Polymer melt temperature
- Mold temperature

The listed parameters are highly depended on the type of polymers used. A polymer with a higher melting temperature will require to be heated to a higher temperature, with subsequent longer cooling time and an overall longer cycle time. Many other parameters will have to be changed, and each polymer type must be optimized to each part design; however, this is not always necessary.

5.4.2 Polymers and injection molding

The type of polymer has a large influence the on parameters required for a stable injection molding process with a stable high quality production of polymer pats. The polymer chains easily forms entangled irregular bundles when melted. Some polymers retain this irregular structure when the polymer solidifies, and an amorphous solid is formed. Polymers with these properties are known as amorphous polymers. In other polymers, the irregular bundles will crystalize into an ordered structure where some of the chains align, as the polymers solidifies. A polymer would have a low energy if all the molecular chains were aligned, however some entanglement of the polymer chains remains and only some are able to aligning. Therefore, the solid polymer will have both amorphous and crystalline regions; this kind of polymer is known as semi-crystalline polymers. The molecular composition of polymer has also an influence such as the structure, chain length and molecular structure e.g. two types of polypropylene (PP); isotactic PP will crystalizes easier than atactic PP, because the isotactic PP has regular spaced side groups on the same side of the polymer backbone[82].

A typical method for characterizing a melted polymer is the so called melt flow index (MFI). The melt flow index is used to measure how easy a polymer flows and it is defined as the mass of polymer under a pressure driven flow through an opening with a specific size during a given time. Typically; the pressure is applied by a piston with a weight, and the whole system can be heated to the desired temperature above the polymer melting temperature. MFI and viscosity are inverse proportional, and polymers with a high MFI is more suitable to injection molding[82].

When polymer melt is injected into the mold cavity, the high pressure and flow rate will cause a thinning of the polymer, this phenomena is known as shear thinning. Here, the polymer chains start to align and therefore the polymer can flow with less resistance. A fast flowing polymer has high shear rate and will have substantial different properties than a stationary polymer at the same temperature.

The polymer viscosity can change in two orders magnitude when injected into the mold as can be seen on the plot in Figure 5.9. Here the viscosity is plotted as function of shear rate. HD601CF has a high viscosity in the low shear rate range, and a corresponding low melt flow index of 8 g/10 min[83]. The high degree of sheer thinning will cause HD601CF to have a lower viscosity than for example TOPAS 5013 L10 which has a MFI of 43 g/10 min[84].

Therefore, the melt flow index can be misleading when looking for polymers that have low viscosity (easy to injection mold). The shear thinning depend on the molecular structure of the polymer, simple polymers such as PP will align more and have a higher degree of shear thinning. The TOPAS (COC) with its more complex polymer chain will not align to the same degree as PP. This alignment and stretching are called orientation.

When polymer is sheared, heat is generated, and a polymer at higher temperature will further decrease viscosity. A polymer with low viscosity will have less resistance when filling nano- and microstructures. A high polymer injection speed can often make filling of small nano- and microstructures easier. However, at high injection speed the polymer chain may, depending on polymer type, align to a higher degree. Shear rate will increase when polymer is flowing through a narrow space such as the injection gate and therefore align. Polymer molecules will retain alignment after moving through the gate. The increased alignment can cause the polymer to have a viscoelastic effect, and therefore, it will be prevented to flow into the nano- and microstructures (Figure 5.10). When optimizing an injection molding process, it is important that the injection speed is optimized to prevent this shear alignment effect[85]. The shear alignment can especially be problematic for polymers with tendency to align like PP.

The injection molding process can be divided into series of repeated phases, starting with mold filling.

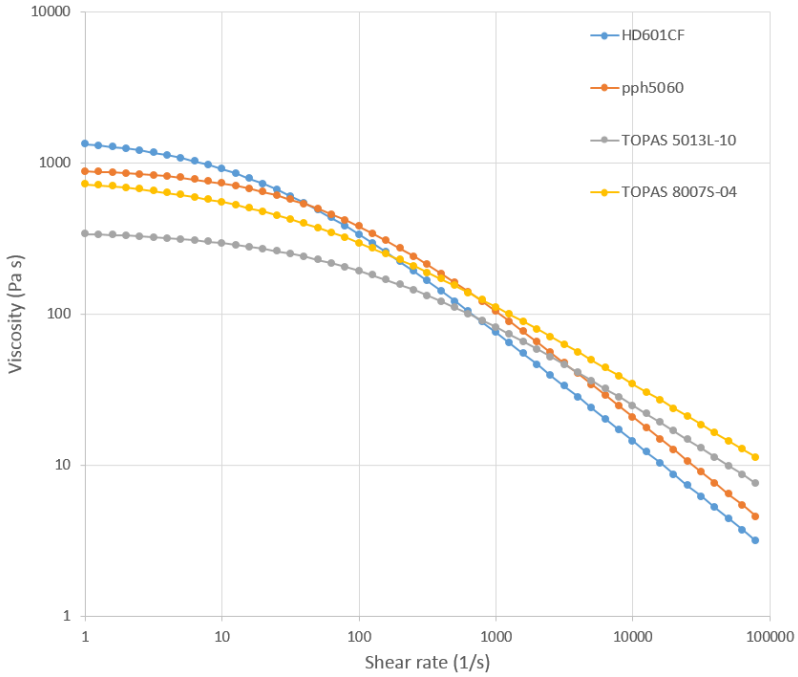

Figure 5.9. Polymer melt viscosity (melt temperature 250 °C) as function of shear rate for two different PP and two different TOPAS grades. Plotted from Autodesk Moldflow Database[86]. Typical injection molding shear rate is 10^2 to 10^5 second^{-1}.

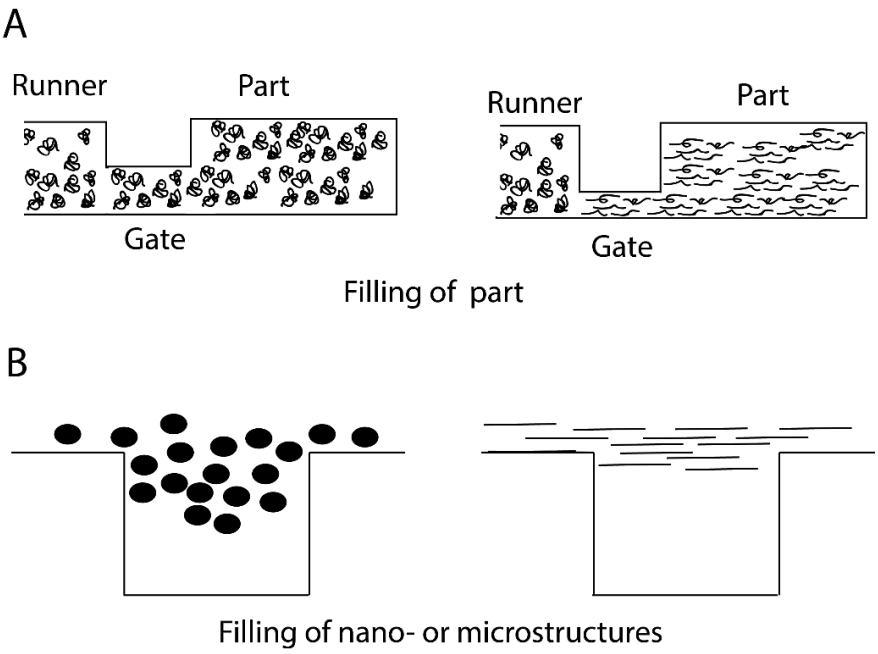

Figure 5.10. Fast injection speed can be problematic for some polymers. PP will have tendency to align, and TOPAS with its more complex polymer chain will not, A) Alignment of polymers (sheer thinning) will occur at the gate, same principles applies to other narrow part locations, B) Aligned polymers will have stronger viscoelastic effect and thereby are harder to press into the nano- and microstructures.

5.4.2.1 *Filling phase*

As the mold is filled, polymer is pushed into the mold cavity until the cavity is almost full. During this process, polymer in contact with the metal mold will solidify in a thin layer between the mold and the molten polymer. The freezing process is almost instantaneous. Once the frozen layer is formed the polymer will be static and cannot flow. Figure 5.11 shows how the frozen layer is formed and the polymer flow front expands. The frozen layer is formed in a near perpendicular direction to the flow. Heat is exchanged from the moving hot polymer into the frozen layer and from the frozen layer into the mold. The temperature exchange will cause the frozen layer thickness to reach an equilibrium, this will usually happen within the first few seconds of the injection molding process[87].

The frozen layer is a big issue when injection molding nano- and microstructures, since the polymer will have to flow into the mold cavity before the frozen layer is formed. Once formed, the frozen layer will prevent further nano- or microstructure filling.

The mold temperature becomes an important parameter when optimizing the filling process, since the formation of the frozen layer will influence the surface quality of the part. A higher mold temperature will decrease the frozen layer thickness, but increase cycle time. Typically, in industrial fabrication a compromise between replication quality and fabrication speed is made. The frozen layer can be avoided if the mold is preheated to a higher temperature than the polymer melting temperature[85].

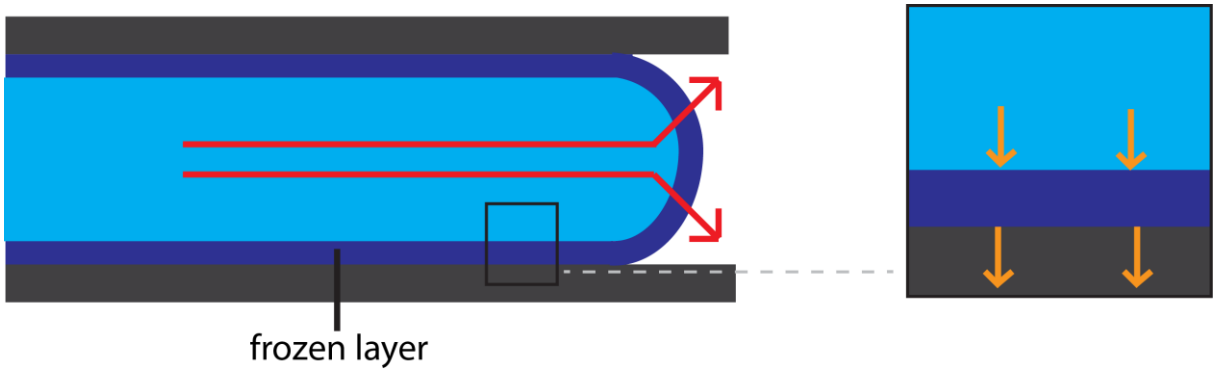

Figure 5.11. Polymer flow and frozen layer. The red arrows show the flow of molten polymer. The dark blue layers show the layers of frozen polymer against the cold mold walls. The oranges arrows indicate of heat flow from the polymer melt into the mold. At some point a thermal equilibrium will be reached and the thickness of the frozen layer will stop to increase as long as there is a polymer flow.

5.4.2.2 Packing phase

The packing phase starts after the cavity is almost full; during the packing phase, pressure is increased further forcing more polymer into the mold. Thereby shrinkage of the part will be uniform and reduced. Furthermore, warpage of the parts is reduced and the quality improved. When polymer has filled the cavity, and packing begun, material will flow to regions of the part that are less densely packed, until a uniform packing is achieved. The packing flow will be influenced by the compressibility and thermal expansion of the polymer melt. Pressure, volume, temperature characteristics of the material can be used to predict the shrinkage of polymer parts[87]. Typically, semi crystalline polymers will shrink more than amorphous polymer due to the alignment of polymer chains in the semi crystalline polymer. Over packing of the mold can occur if a high holding pressure is used, this will reduced shrinkage, and in some cases, after demolding, the parts can be larger than the mold cavity. Sometimes an over packed part can be impossible to demold.

5.4.2.3 Holding/Cooling phase

The holding phase ensures that the pressure of the polymer, and thereby the level packing is at the desired level, until the gate is frozen and pressure can be removed. Once the gate is frozen, the cooling phase will start. For a conventional injection molding process, the cooling of polymer will start as soon as the hot molten polymer comes in contact with cold mold (from beginning of the filling phase).

The cooling phase is the time from end holding phase until the mold opens and the part is ejected, the rate and uniformity affect stress and cost for parts since cooling is the longest part of an injection molding process[87].

5.4.2.4 Variotherm proses

A variotherm process eliminates the frozen skin, which improves filling and surface quality of the fabricated parts. Variotherm process has a systematical grated mold temperature over the cycle time; the mold is preheated to a temperature higher than the melting temperature of the polymer. After mold filling (and packing) cooling is started until a specified demolding temperature is reached, the part is ejected and the mold is preheated before the next cycle starts. There are several advantages of a process with variotherm temperature control vs a conventional constant temperature mold process[64].

- Longer packing and holding pressures can be applied, even on complex parts and in cavity area located far away from the gate.
- Requires a smaller injection molding machine (less injection pressure and clamping force).
- More accurate reproduction of nano- or microstructures, and very smooth surfaces.
- Better reproduction of functional surfaces such as self-cleaning or anti-reflection.
- Better dimensional stability and shot-by-shot consistency.

A variotherm process is often avoided in industrial production because of the increased cycle time and overall more complexity of the tool. Commercial systems for fast cooling rate exist that switch between pressured hot and cold water/oil[64].

5.5 The Injection molding method

Injection molding of polymer parts was in this project primarily done for polypropylene, since it has a high intrinsic contact angle among the non fluorinated polymers. PP is an excellent based material for superhydrophobic surface. TOPAS 8007 S04 was used as alternative polymer to show that superhydrophobic surfaces could be fabricated from both semi crystalline and amorphous polymers.

TOPAS was chosen as material for the initial optimization of the injection molding process, because of its low T_g (80 °C), which meant a mold temperature well above T_g, could be used if required. Furthermore would TOPAS, being an amorphous polymer, be easier to predict in the injection molding process and TOPAS was readily available in large quantities. A single cavity injection molding tool, designed for research purposes, was used for the production of polymer parts. The tool was designed with copper based insert to ensure a homogenous mold surface temperature. The used injection molding tool consist of a tool case made from tool steel (HASCO K-Standards) with a removable insert from made from beryllium copper (AMPCO). The fabricated nickel shims were mounted on the stationary side of the tool. Both tool case and insert were designed with separate cooling systems for independent temperature control. 4 × 1200 W heat cartridges were used to heat the cooper inserts and a thermocouple was used to measure the inserted temperature and provide feedback to PID controller that adjusted the heat cartridges. This ensured an accurate variotherm processing with a heating and cooling rate in the order of magnitude of 1 °C/s. A hook ejector was used to demold the finished part from the shim. In addition four pins with grooves assisted the demolding. The pins and hook fixed the polymer part to the moving tool part. A robot collected the finished part from the moving tool part and placed is on a conveyer belt.

A fan type gate with a 250 µm opening was used to inject polymer into cavity from the sprue. A CAD drawing of the tool and polymer part is shown in Figure 5.12. Two different copper inserts were used to produce the parts. An insert that produced 1 mm thick microscope slides and an insert that produced circular discs 2 mm thick with a diameter of 50 mm. Both inserts used the same nickel shim design.

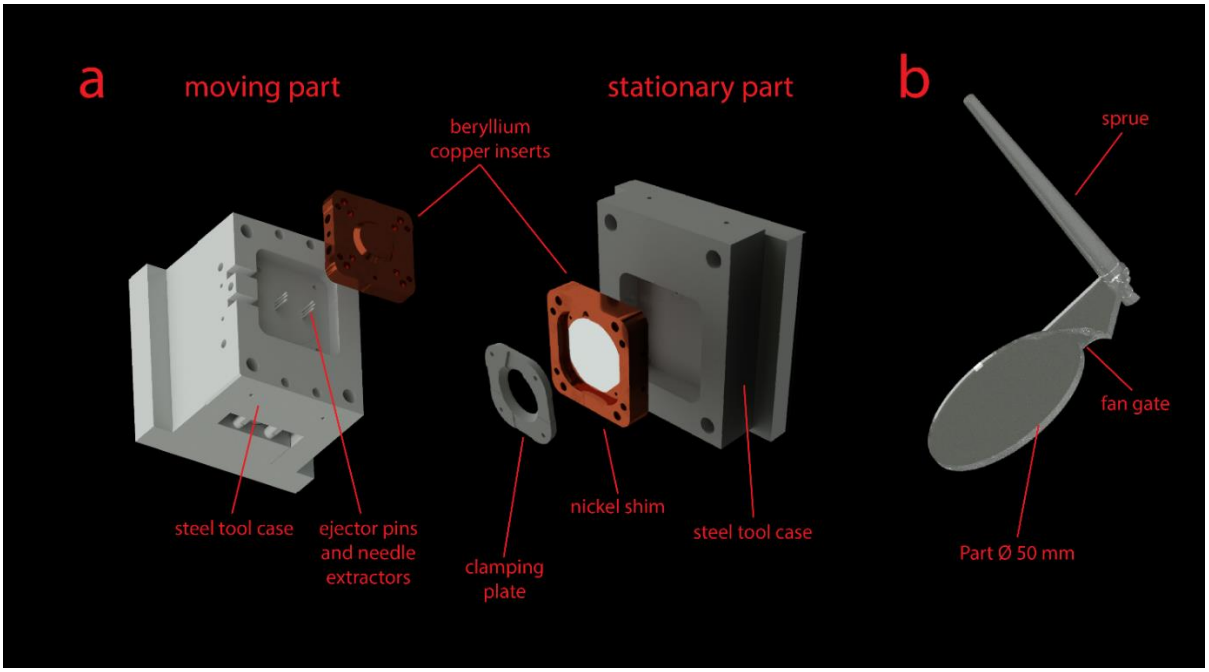

Figure 5.12. CAD drawing of tool, a) The beryllium copper inserts for the stationary and moving tool parts. Note, how the shim is mounted by the clamping plate, b) Circular disc polymer part with sprue (inlet) and fan gate.

5.5.1 Process Optimization

The initial parameter for injection molding was performed on a shim that produced micropillars with nanograss. The mold would be completely filled when the delicate nanograss structures on the bottom of the top of the pillars were filled. The polymer used was TOPAS 8007-S04. TOPAS 8007-S04 has a low T_g of 80 °C, furthermore TOPAS 8007-S04 is an amorphous polymer, with no crystallization, and little polymer alignment. These properties will make TOPAS 8007-S04 a suited material for the injection molding optimization. Since viscosity, change of the material will depend less on polymer injection speed and gate size, as can be seen on the plot on Figure 5.9. The copper insert with microscope slide was used for the initial optimization.

The injection molding optimization process was started with a constant mold temperature of 65 °C, which is 15 °C under the T_g of TOPAS 8007-S04 (80 °C). With an injection speed of 30 cm^3/s and constant packing/holding pressure of 600 bar for 40 s, the packing pressure was gradually increased to 800 bar where microstructure filling started to occur. This was not enough to replicate any significant part of the microstructures. It was decided to increase the mold temperature, instead of optimizing other parameters such as injection speed, holding pressure etc. In order improve the microstructure replication a variotherm process with a mold temperature above T_g was used. Before polymer injection, the mold was preheated to

120 °C and a constant holding pressure 800 bar for 40 s was used. This caused the micropillars to partially reproduce.

To improve structure replication the mold temperature was further increased to 130 °C, which is 50 °C above the melting temperature of the TOPAS. Micropillars were successfully replicated with an injection speed of 30 cm^3/s, and holding pressure of 800 bar, some micropillars even showed replication of nanograss at the top, indicating a complete filling of the mold. 130 °C was the mold temperature limit for a reliable and continuous polymer part production.

To further increase nano- and microstructure replication, packing/holding pressure was increased to 1200 bar. At 1200 bar the polymer part adhered completely to the nickel shim. The part ejection system broke the polymer part instead of demolding it. The polymer part adhered completely to the nickel shim. Even with the shim removed, the adhesion was similar in strength to glue, and the polymer parts still adhered even when strong mechanical force was applied.

To demold the polymer part a pair of pliers and hot plate was used. To make sure no polymer residues was left, the shim was boiled in toluene for 2 hours. The main issue in the injection molding process was no longer to fill the structures but to demold the polymer parts. To decrease the mold adhesion an antistick FDTS coating was applied to the nickel shim, and the part type changed from 1 mm thick microscope slide to the circular round disk, 2 mm thick with a diameter of 50 mm. Extractor pins would aid demolding in the flat disc insert and the thicker part would be more rigid, so a larger demolding force could be applied. The above described steps was not enough for a fully automated injection molding process. The polymer parts need to be forced from the nickel shim with a pair of pliers and the demolded polymer parts would often bend and crack in the process. An extra depacking phase was introduced to the injection molding process in order to both fill and demold the part from the nickel shim.

5.5.1.1 Depacking step

One of the advantages of a variotherm process is that polymer can remain melted for longer time. In order to completely fill the structures and to be able to demold the nano- and microstructures a new step in the injection molding process was introduced. Normally an injection molding process consists of filling, packing, holding, and cooling phases. In order to demold the polymer parts, a depacking phase was introduced. The difference between a normal variotherm process and the special type with polymer depacking can be seen in Figure 5.13.

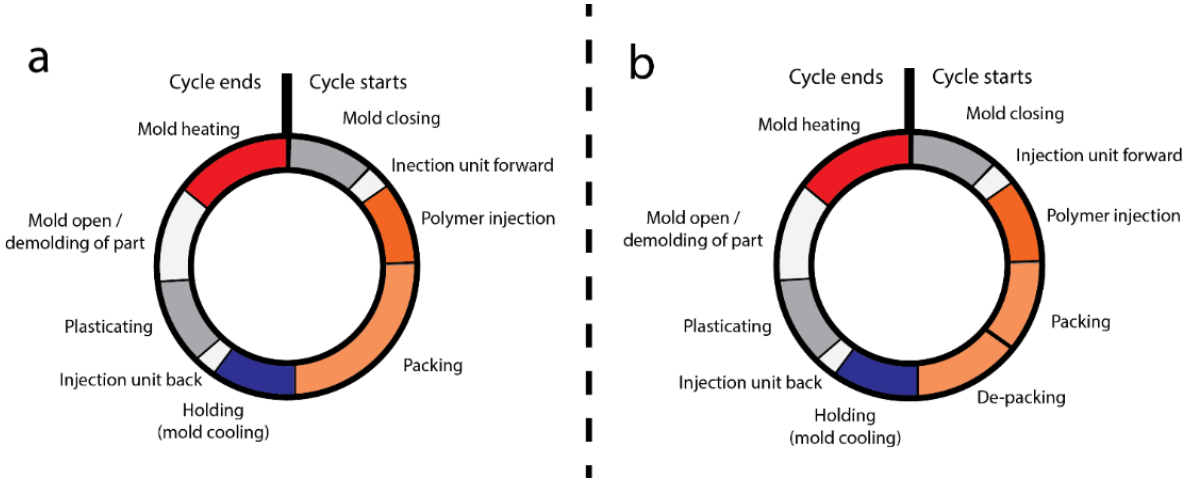

Figure 5.13. a) A normal variotherm injection molding cycle, b) The special variotherm cycle with cavity depacking developed for this work.

During the depacking phase polymer flowed backward from the mold cavity into the barrel. This coursed lower amount of polymer inside the cavity. Therefore, polymer shrinkage would increase during the cooling phase and the polymer structures would have smaller contact area with the shim and could easily be demolded. The principle can be seen in Figure 5.14.

The depacking was implemented by using a graduated holding pressure. A high initial pressure made sure that a complete structure filling, followed by a reduction in holding pressure, until the desired depacking had been achieved. As soon as the pressure was decreased, polymer would start to flow backward out of the mold. After depacking a holding pressure ensured the level of packing remained constant as the gate was cooled. The polymer parts could now be cooled and demolded in a fully automatic injection molding process.

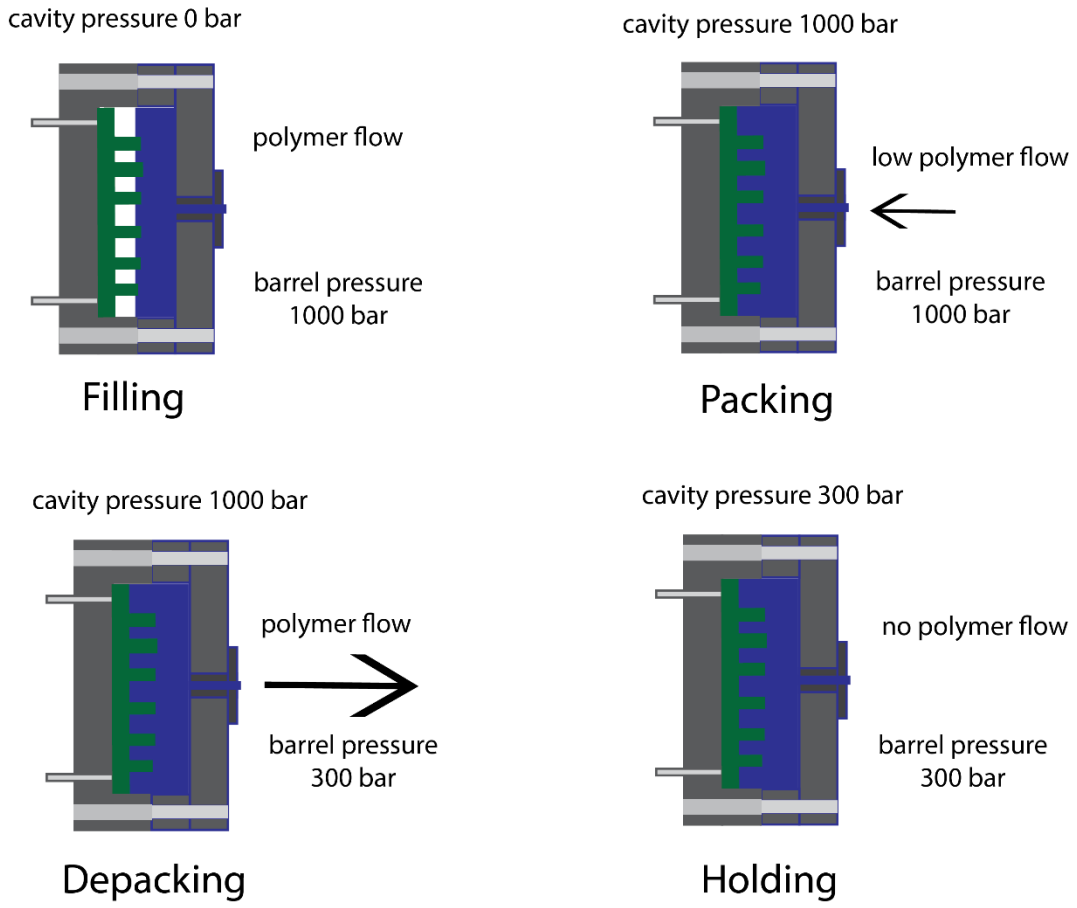

Figure 5.14. Principle of the depacking phase. A high packing pressure fills nano- and micro-structures. Depacking ensures that the part can be demolded.

5.5.2 Scratching of polymer samples

Small scratch marks were present on the nano- and microstructures on the demolded parts. The scratching could be caused by two effects. One effect is the shrinkage of the polymer, due to thermal exaptation and from when the polymer shift from melted to solid form. Shrinkage is especially a problem for semi-crystalline polymers that shrink approximately 5% compared to amorphous polymers that on shrinks approximately 1%. The polymer shrinkage will affect both the overall part and the nano- and microstructures. The overall shrinkage of polymer parts can be predicted with commercial software such as Autodesk Moldflow. However, no suited method for predicting the shrinkage of nanostructures exits.

The other effect that can cause scratching of the nano- and microstructures occurs when the tool opens for part demolding. Typically, clamping forces are measured in tens or hundreds of tons. The used machine is an Engle Victory 45 with a maximum clamping force of 45 tons. A 45 tons machine is considered as a small industrial machine. If the tool does not open straight scratching of the nano- and microstructures can occur. The used injection molding machine (Engle Victory 45) is a tie bar less machine. The lack of tie bars causes a movement in the

machine structure of approximately 1 cm which further can add to a non-straight opening of the tool. The alignment when mounting the tool is critical for straight tool mounting

A solution was found that solved the scratching problems. During the holding phase, the clamping pressure was removed when the polymer near the mold surface interface was below melting temperature of the polymer. The nano- and microstructures would be frozen while the rest of the polymer part was molten. The applied clamping force caused an elastic deformation of the tool steel of a few µm. The steel would return to its original form when the clamping force was removed. This movement would demold the nano- and microstructures either completely or partly before the overall polymer part froze and shrinkage occurred. Straight opening of the tool thus become less of an issue, since the nano- and microstructures already was demolded before the moving tool part was opened. The polymer part would also have room to shrink since the nano- and microstructures had limited or no contact with the nickel shim. The principle to avoid structure damage by shrinkage is shown in Figure 5.15. The timing of the clamping pressure removal was a critical parameter in order to avoid scratching the of the polymer parts.

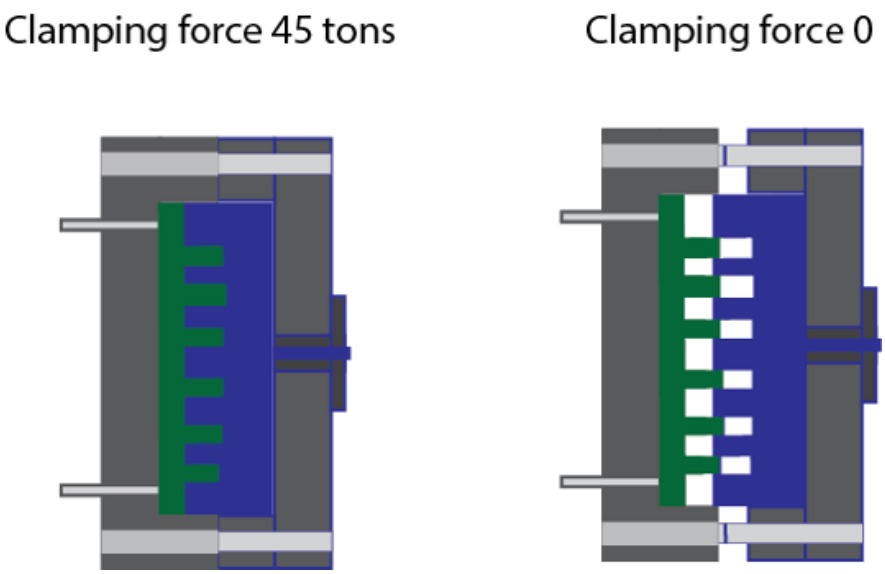

Figure 5.15. Demolding of nano- and microstructures by removal of clamping pressure when the polymer surface are frozen, only nano- and microstructures are demolded.

5.5.3 Polymer leakage

When molten polymer was injected at pressure over a 1000 bar polymer leak occurs in gaps in the tool e.g. between inserts and tool case, or between clamping plate and shim. Polymer would leak when PP (HD601CF) was injection molded. Polymer would gradually fill gaps and venting channels. Furthermore, polymer would leak between the clamping plate and the shim.

The leak became a problem after a few injection molding cycles. Polymer would block the moving parts in the tool, and frozen polymer would protrude from the mold surface. Mold protection was engaged automatically by the machine and the injection molding process stopped. The leakage continued after clamping pressure had been increased to the maximum of 45 tons. The increased clamping pressure did not solve the leaking of polymer. Thicker shims (330 µm) were used to reduce leaking between shim and clamping plate.

The problem was finally discovered, the clamping plate was slightly lower than the surface of the beryllium copper insert. This meant the clamping force was not applied to mold areas with polymer flow; therefore, polymer would leak into the tool. In order to solve the problem a new clamping plate 50 µm thicker with no venting channels was ordered from a machine shop. The higher clamping plate ensured that clamping pressures was against the clamping and not the beryllium copper insert. Small amounts of polymer flash were still present. The lack venting channels could sometimes produce diesel effect. If diesel effect occurred, venting could be added be simple placing a small Post-it® on the insert. A schematic shows the difference between the new and old clamping plate (Figure 5.16).

All issues for producing high quality injection molded parted with good structure replications have been solved and the final injection molding process can be presented.

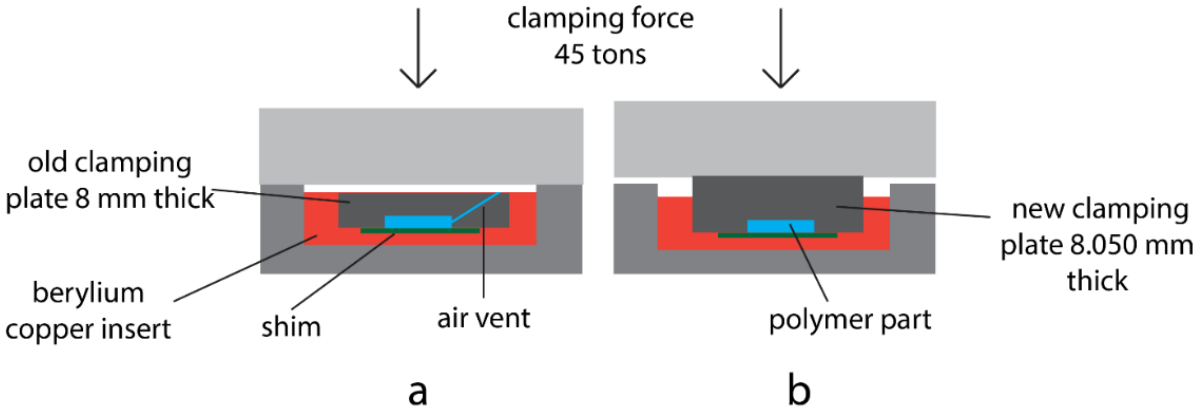

Figure 5.16. Thickness of the clamping plate was increased to prevent polymer leaking.

5.5.4 The final injection molding process

Before injection molding both polymer types of granular, TOPAS 8007-S04 (50 °C) and HD601CF (100 °C), were dried for two hours, this removed potential water inside the polymer ensuring, reproducibility in the injection molding process. Polypropylene HD601CF and TOPAS 8007-S04 were injection molded with the same parameters except the polymer melt temperature. Difference in viscosity required the polypropylene melt temperature to be lowered to 220 °C while the 8007-S04 was 250 °C. Table 5.5 shows the temperature of different heater

zone in the barrel. The volume of the injected polymer was 11.5 cm^3, which was injected with a speed of 30 cm^3/s. This required a maximum injection pressure of 840 bar. A switch over to packing pressure was applied at 99% molding filling.

	Nozzle (°C)	**Zone 4 (°C)**	**Zone 3 (°C)**	**Zone 2 (°C)**	**Zone 1 (°C)**
HD601CF	220	210	200	180	30
TOPAS 8007-S04	250	240	230	220	30

Table 5.5: Temperature of barrel for TOPAS and PP. Polymer granular enters the barrel from zone 1 and it's melted when passes through zone 2 to 4.

A variotherm injection molded process was used. The mold was heated during injection and cooled for demolding. Here, the mold temperature was 125 °C on the movable side of the tool and 130 °C on the stationary (shim) side of the tool. Even though the mold temperatures were below the melting temperature of HD601CF (164 °C)[88] 1. The lower temperature on the moveable side was used to increase polymer shrinkage and thereby increasing the friction on the ejection pins and hook.

A total holding pressure time of 30 s was used. A decreasing holding pressure was used to ensure that structures where completely filled. The lower pressure caused larger part shrinkage and made demolding possible Figure 5.17 shows the profile of the holding pressure. Before demolding, the part was cooled for 30 s to ensure that the polymer was below the melting temperature. Clamping force was removed when the mold temperature was measured to approximately 10 °C below the melting temperature of the polymer.

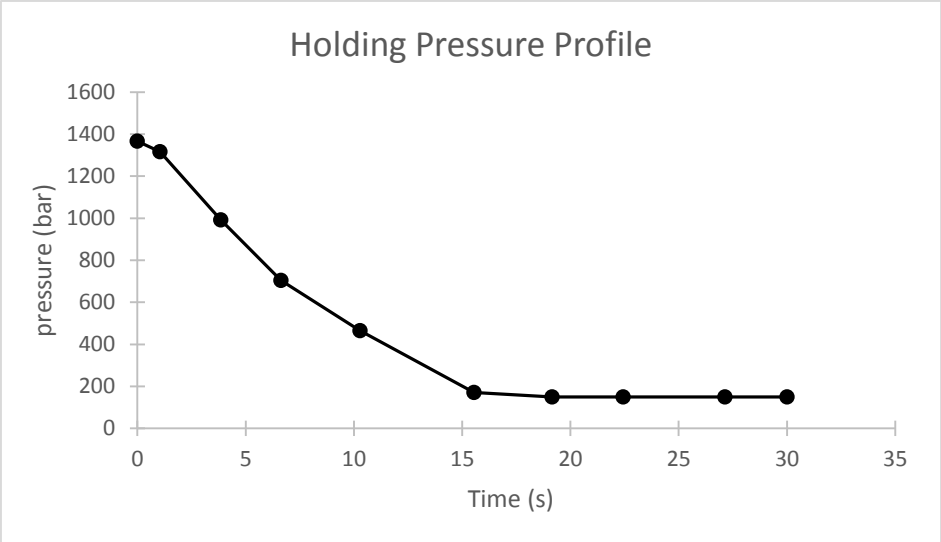

Figure 5.17. Holding pressure profile. High pressure is used to fill the nano- and microstructures. Low pressure ensures the demolding of the part.

The produced polymer parts were after injection molding inspected in an optical microscope to verify a uniform microstructure replication. The nanograss was below the diffraction limit and could not be viewed by the optical microscope. Height of the produced structures where measured for each shim with the Sensofar Neox Optical Profiler (combined optical profilometer and confocal microscope). Finally, the fabricated structures were inspected in Field emission SEM and images were recorded. An AFM was used to verify Sensofar measurement on some structures.

5.5.5 Industrial test production of polymer parts

Four different parameters for each shim were used in the injection molding of parts. The process parameters were similar to those used in industrial fabrication. Two different injection pressures (800 bar/1300 bar) were set on the injection molding machine, along with two different mold temperatures (25 °C/70 °C) measured with a temperature probe on the mold surface. The process was without any holding pressure, and overall cycle time was less than 25 s. In addition, the shim with hierarchical black silicon was injection molded with a longer process time where holding pressure was applied; the duration of the holding pressure was over 50 s. Here, the fastest filling time of the machine was used by setting the injection pressure to the maximum of 2300 bar.

5.6 Fabrication results

This section presents the results from clean room fabrication and injection molding. First the results from the injection molding optimization are presented here. SEM images from different steps in the optimization process are shown. Furthermore, the degree of mold filling is presented for each shim. This is followed by representative SEM images of all the fabricated

structure types. Images from the structured silicon master are shown with their corresponding nickels shim (inverse polarity) and finally the injection molding polymer parts. Optical microscope image of the injection molded parts are also shown together with some 3D confocal images. The last fabrication result is those from industrial test production

5.6.1 Optimization of injection molding

SEM pictures from different points in the injection molding optimization are shown in Figure 5.18. The gradual replication of structures can be seen as mold temperature and holding pressure are increased. The initial parameters 800 bar for 40 s and a mold temperature 65 °C showed nanograss replication but micro structures was not replicated (Figure 5.18a), Micro structures replication was seen when a variotherm injection molding process was used with maximum mold temperature of 120 °C (Figure 5.18b). Complete structure filling and nanograss was observed for some pillars when the mold temperature was increased to 130 °C (Figure 5.18c) holding pressure increased to 1200 bar for 40 s, antistick coating and depacking step complete nano structure filling for all structures was observed, however the structures were slightly stretched (Figure 5.18d). The final injection molding process for process with all optimization steps, note, no elongation of structures (Figure 5.18e). Even higher structures (5.8 µm) could be perfectly replicated in PP (Figure 5.18f).

An optical microscope was used to inspect large areas of the injection-molded structures. Images of polymer parts injection molded with the final parameters are shown in Figure 5.19. Holes 3.5 µm, 7.5 µm and 15.5 µm and pyramids with nanograss can be seen, only the microstructures are visible in the optical microscope.

Filling of shims was characterized with Sensofar. The height of the injection molded polymer structures in PP and TOPAS are compared with height of the nickel shims, each structure type was measured and plotted in Figure 5.20a and an example image of a polymer part (Figure 5.20b).

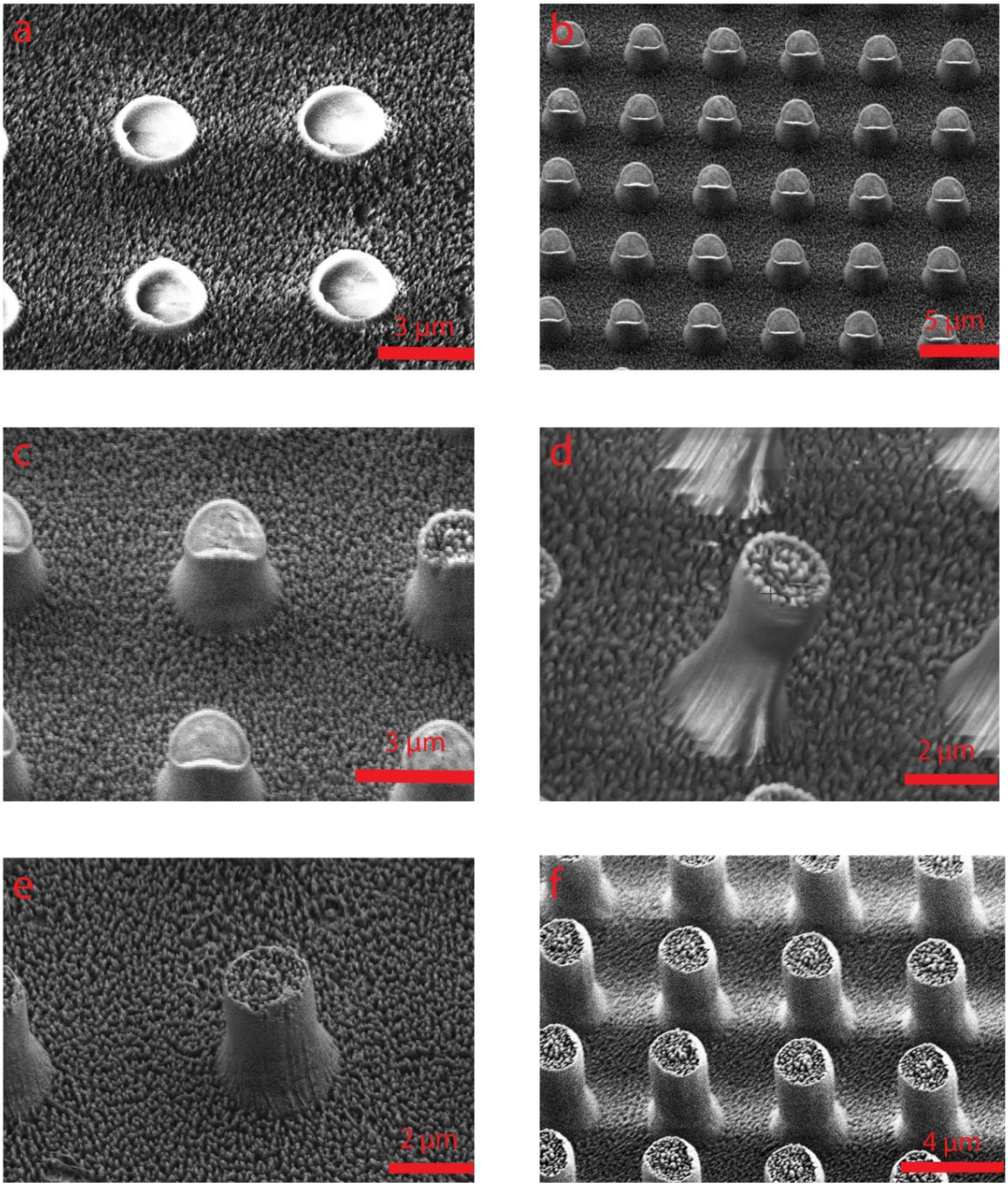

Figure 5.18. SEM images during the optimization of the injection molding process, a) The initial parameters 800 bar for 40 s and a mold temperature 65 °C, b) Microstructure replication was seen when a variotherm injection molding process was used, c) Complete microstructure filling when mold temperature was increased to 130 °C, d) Complete filling of all structures with antistick coating and depacking step, e) The final injection molding process, f) Even higher structures (5.8 µm) could be perfectly replicated in PP.

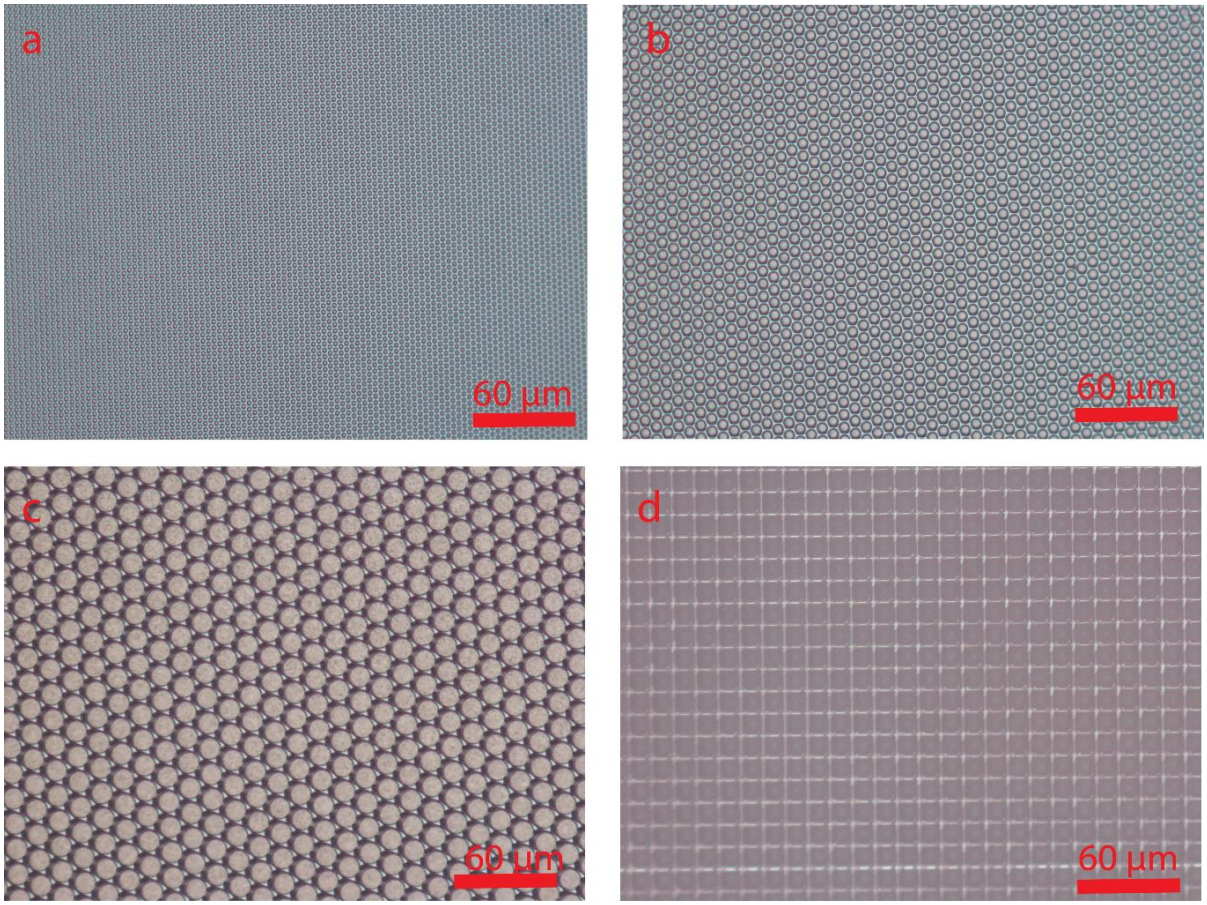

Figure 5.19. Sample images from quality control with optical microscope after injection molding optimization.

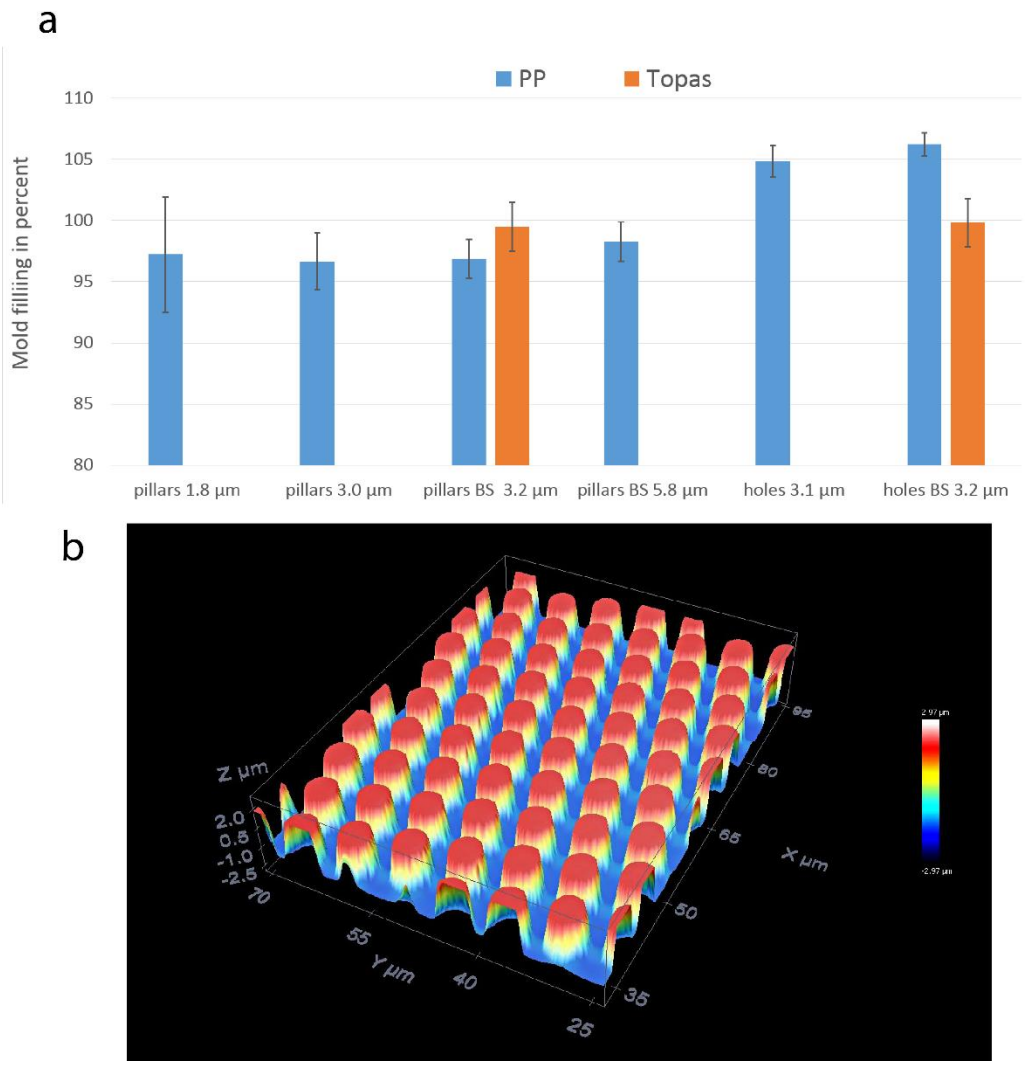

Figure 5.20. a) Mold filling in % measured with optical profilometer/confocal. Nickel shims were measured and compared with the injection molded polymer parts. All structure types was injection molded in PP and 3.2 µm high pillars and holes was injection molded in TOPAS 8007-S04, b) Sensofar showing image 3 µm polymer pillars used to determine mold filling.

5.6.2 Nanograss

The fabricated nanograss was characterized with SEM and AFM. SEM images of silicon master, nickel shim and injection molded polymer are shown Figure 5.21. An AFM image of the silicon master showed a typical structure height of 181 nm ± 81 nm with 60.5 spikes/µm^2. Furthermore, the roughness factor R_f (defined in equation 2.5) was determined from an AFM image by measurement of the total surface area to 3.39 µm^2 and the project area to 1.70 µm^2. The roughness factor was calculated to R_f = 1.99. A profile from the nickel shim made with FIB SEM is shown in Figure 5.22. Average nanograss on the shim was measured to 200.2 nm ± 62 nm.

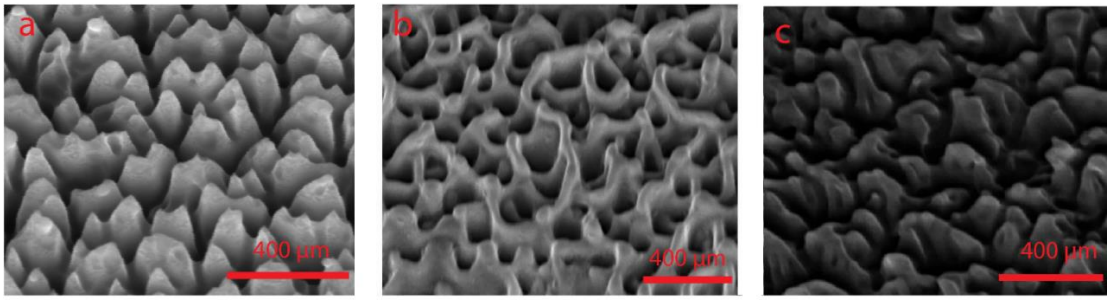

Figure 5.21. Nanograss, a) The silicon master after black silicon etching, b) Nickel shim, c) Injection molded polymer (PP).

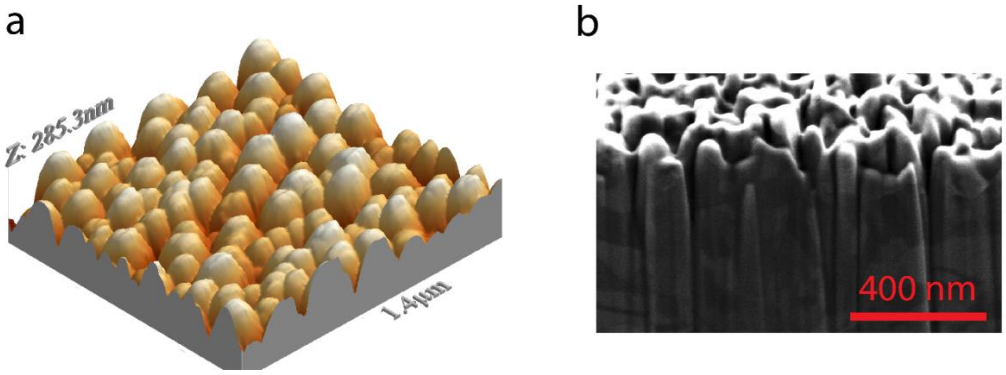

Figure 5.22, a) AFM image of silicon master, b) FIB SEM profile of nanograss on nickel shim.

5.6.3 Micropillar

The results from the fabrication of micropillars for both hierarchical nano- and microstructures and pure microstructures are shown in Table 5.6 for PP and in Table 5.7 for TOPAS. Here structure size was measured with SEM. Three measurements were performed for each sample. If the standard deviation on the measurements was smaller than the resolution of the SEM, the resolution of the SEM was used instead (pixel size of 20 nm, which corresponds to a resolution of 20 nm × 2.3 = 46 nm ≈ 50 nm).

Representative SEM images of silicon masters together with nickel shims and polymer parts (3 µm in diameter) are shown in Figure 5.23. A reduction in the size of microstructures occurred during the black silicon etch; the micropillars were reduced approximately 0.5 µm in diameter. An AFM was used to measure the height of a single silicon pillar with black silicon and of a similar hole on the nickel shim. The height was measured to approximately 3.2 µm for the hierarchical nano- and microstructures and 3.0 µm for the pure microstructures. Replication of black silicon in the nickel shim is clearly visible. Injection molding replicated both

nano- and microstructures in the polymer. 5.00 µm and 7.00 µm pillars were successfully injection molded, again the diameter was reduced with approximately 0.5 µm for the pillars with nanograss.

a) 1.8 µm high pillars			
Diameter on mask (µm)	3.00	5.00	7.00
Shim diameter (µm)	2.70 µm ±0.05	4.85 µm ±0.05	Ø 6.73 ±0.05
PP structure size (in % of shim)	94.1 ±4.1	95.7 ±4.0	94.4 ±1.8

b) 3.0 µm high pillars			
Diameter on mask (µm)	3.00	5.00	7.00
Shim diameter (µm)	2.75 ±0.05	4.80 ±0.05	6.77 ±0.05
PP structure size (in % of shim)	95.7±2.3	96.4±2.0	93.9±1.3

c) 3.2 µm high pillars with nanograss			
Diameter on mask (µm)	3.00	5.00	7.00
Shim diameter (µm)	2.33 ±0.05	4.35 ±0.05	6.23 ±0.05
PP structure size (in % of shim)	96.5 ±3.1	95.5±1.5	94.4 ±1.6

d) 5.8 µm high pillars with nanograss			
Diameter on mask (µm)	3.00	5.00	7.00
Shim diameter (µm)	2.31 ±0.05	4.15 ±0.05	6.13 ±0.05
PP structure size (in % of shim)	96.2 ±2.3	97.9±1.65	95.7 ±1.3

Table 5.6. Lateral measurements of injection molded micropillars (PP) based on SEM images for four different shims with different heights, a) 1.8 µm, b) 3.0 µm, c) 3.2 µm with nanograss, d) 5.8 µm with nanograss.

3.2 µm high pillars with nanograss			
Diameter on mask (µm)	3.00	5.00	7.00
Shim diameter (µm)	2.33 ±0.05	4.35 ±0.05	6.23 ±0.05
TOPAS structure size (in % of shim)	97.7 ±2.1	93.8 ±1.6	95.9 ±1.3

Table 5.7. Lateral measurements of injection molded micropillars (TOPAS) based on SEM images for the shim with nanograss and a height of 3.2 µm.

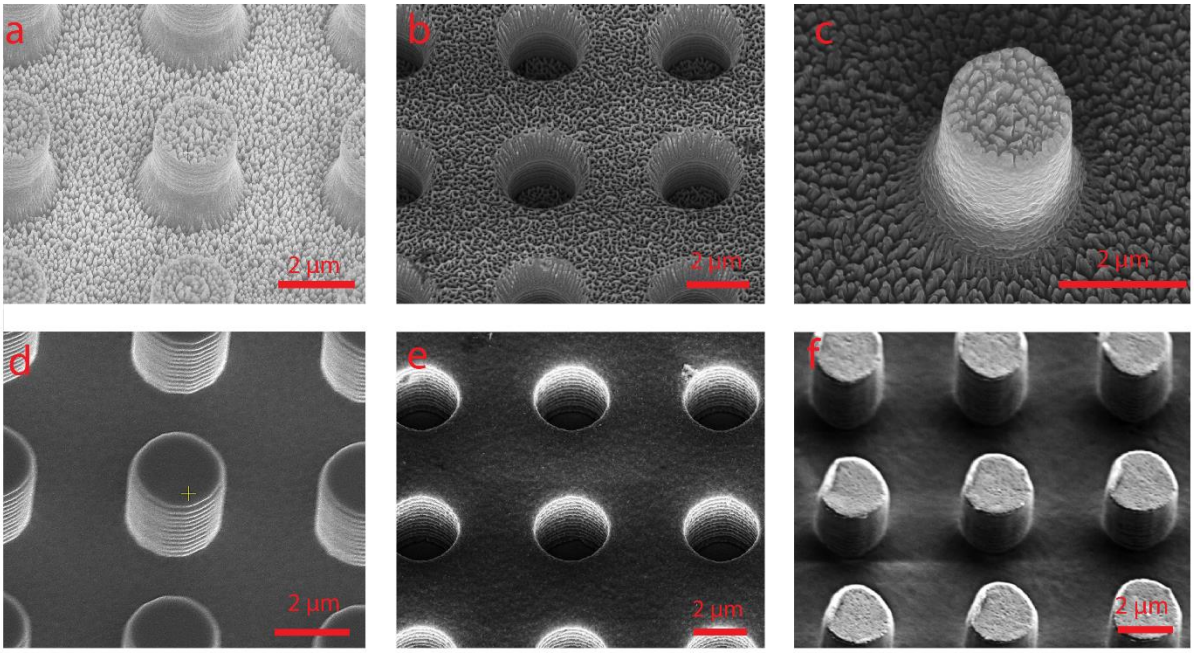

Figure 5.23. SEM images of micropillars designed to be 3.00 µm, a) Silicon master with nanograss, b) Nickel shim with nanograss, c) Injection molded PP with nanograss, d) Silicon master, e) Nickel shim, f) Injection molded PP.

5.6.4 Holes

The results from the fabrication of holes for both hierarchical nano- and microstructures and pure microstructures are shown in Table 5.8 for PP and TOPAS. Here structure size was measured with SEM. Three measurements were performed for each sample. If the standard deviation on the measurements was smaller than the resolution of the SEM, the resolution of the SEM was used instead (pixel size of 20 nm, which corresponds to a resolution of 20 nm × 2.3 = 46 nm ≈ 50 nm).

Representative SEM images of the silicon master (7.00 µm structures) are shown together with nickel shim and polymer parts of TOPAS and PP in Figure 5.24. Again the black silicon etch

has removed some of the sidewall, and the diameter of the holes were increased with approximately 0.5 µm. The sidewalls separating the holes were reduced to a thickness of 100 nm at the narrowest part. The structure height was measured with AFM to 3.2 µm on the silicon wafer. The height of the polymer parts was measured with optical profilometer (Sensofar) to 3.4 µm for PP and 3.2 µm for TOPAS. The TOPAS height was verified with AFM to 3.2 µm.

a) 3.2 µm high holes with nanograss (TOPAS)			
Designed size/period (µm)	3.00/3.60	7.00/7.60	15.00/15.60
TOPAS period	3.58±0.05	7.59 ±0.05	15.59 ±0.05
Shim diameter (µm)	3.38 ±0.05	7.50 ±0.05	15.37 ±0.05
TOPAS structure size (in % of shim)	99.9±1.5	99.4±0.7	100.0 ±0.6

b) 3.2 µm high holes with nanograss (PP)			
Designed size/period (µm)	3.00/3.60	7.00/7.60	15.00/15.60
PP period	3.60 ±05	7.62 ±0.05	15.58 ±0.05
Shim diameter (µm)	3.38 ±0.05	7.50 ±0.05	5.37 ±0.05
PP structure size (in % of shim)	98.3 ±1.5	98.6 ±0.7	99.2 ±0.75

c) 3.0 µm high holes (PP)			
Designed size/period (µm)	3.00/3.60	7.00/7.60	15.00/15.60
PP period	3.57±0.05	7.55 ±0.05	15.56 ±0.05
Shim diameter (µm)	3.01 ±0.05	7.05 ±0.05	15.37 ±0.05
PP structure size (in % of shim)	98.3 ±1.5	98.6 ±0.7	99.2 ±0.75

Table 5.8. Lateral measurements of injection molded holes based on SEM images, a) TOPAS with nanograss, b) PP with nanograss, c) PP.

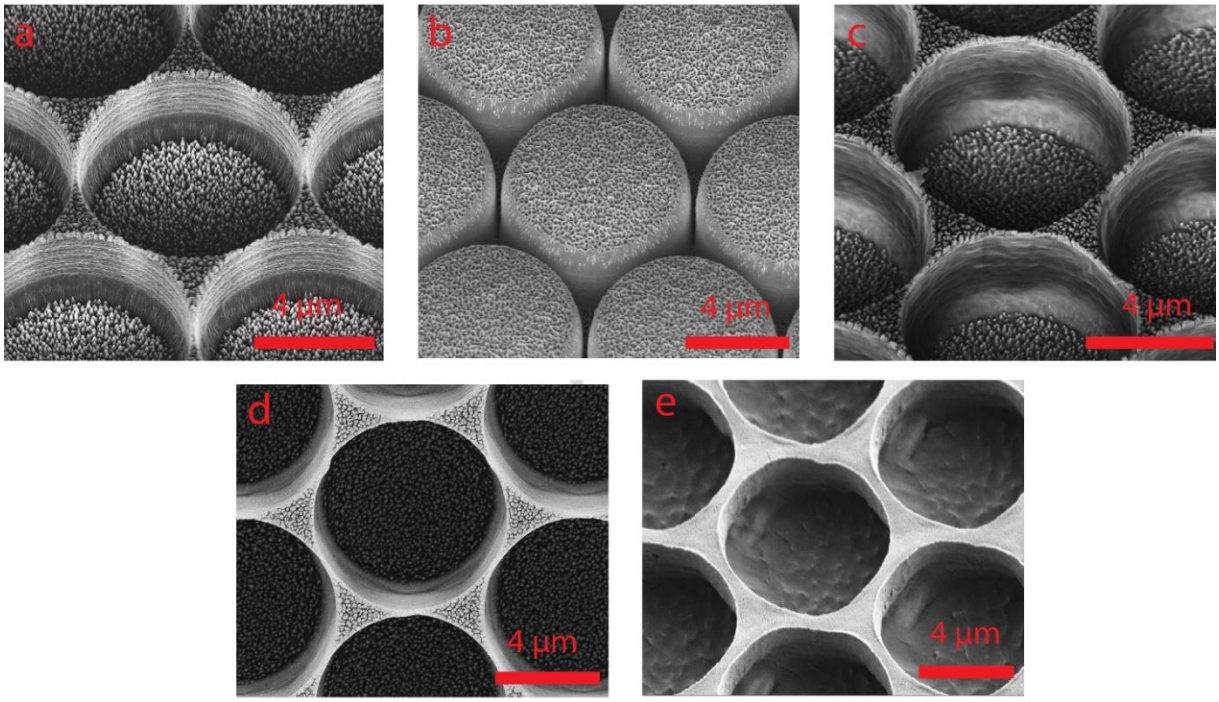

Figure 5.24. SEM images of holes, a) Si master with nanograss (diameter 7.5 µm), b) Nickelshim, c) Injection molded PP, d) Injection molded TOPAS, e) Holes with no nanograss (diameter 7 µm) (PP).

5.6.5 Spruce like micropillars

The results from the fabrication of spruce like micropillars are shown on representative SEM images of the silicon master together with the nickel shim and a polymer part (TOPAS) (Figure 5.25), note, the small overhanging sidewall structures. Both TOPAS and PP were successfully injection molded. Size measurements were not performed for the spruce like micropillars, because the electron beam from the SEM melted the structures (Figure 5.25c), and the structure height was too large for AFM.

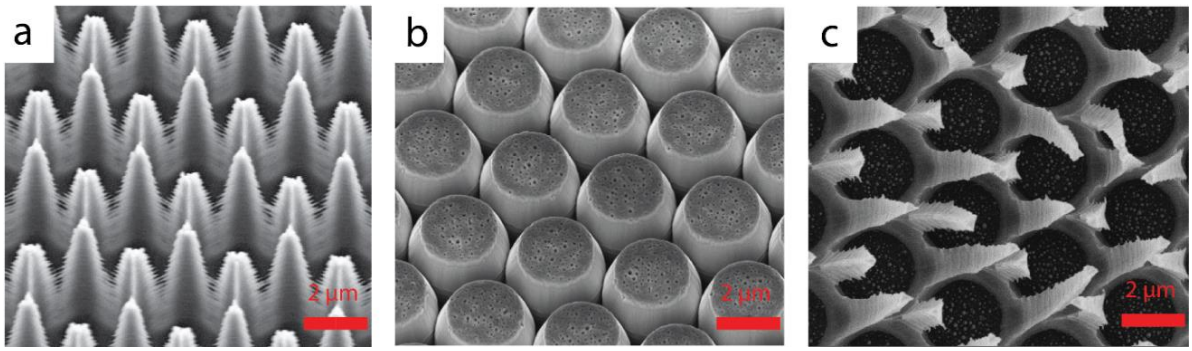

Figure 5.25. SEM images of the spruce like micropillars, a) Micropillars etched in silicon with structured sidewalls, b) Nickel shim, c) TOPAS polymer pillars fabricated by injection molding.

5.6.6 Pyramid holes and pyramids

Pyramid holes was successfully produced and representative SEM images of silicon master, nickel shim and injection molded PP part, with and without nanograss are shown in Figure 5.26, note, scratching on the PP part from the injection molding process.

Pyramid structures are shown in Figure 5.27 here the embossing to invert the structures nickel shim and injection molded polymer can be seen. Again, the PP part is scratched by the injection molding process.

SEM images showing the result of the BHF etching to reduced line width (Figure 5.28), lines down to 120 nm was produced. The designed line width was 2 µm.

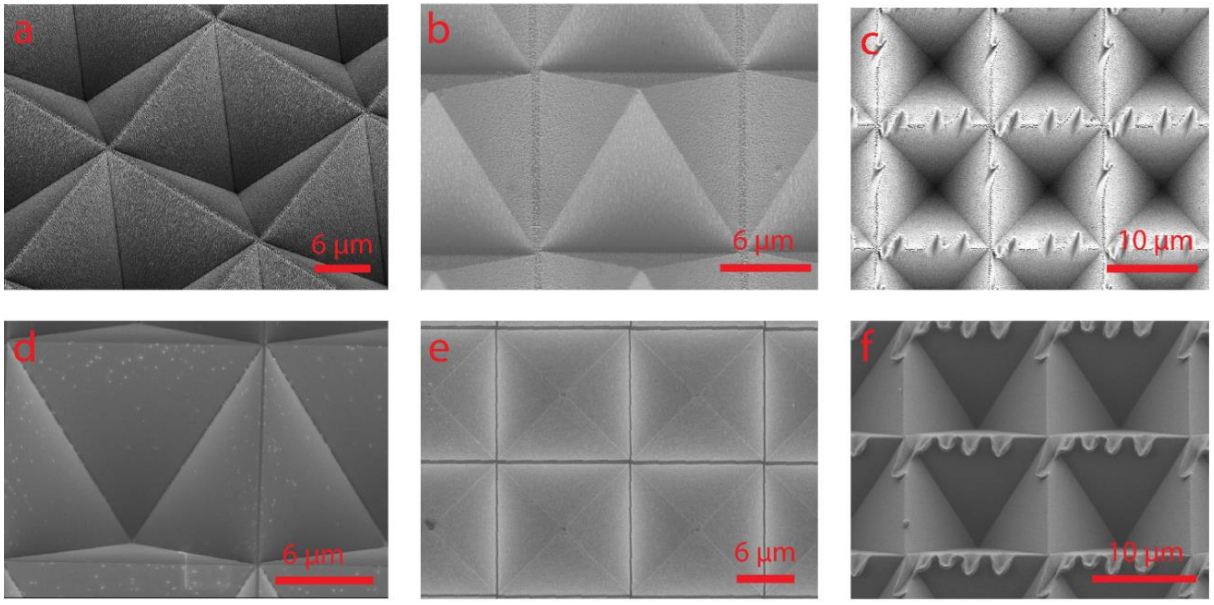

Figure 5.26. SEM images of 12 µm pyramid holes, a) Silicon master with nanograss, b) Nickel shim with nanograss, c) Injection molded PP with nanograss, d) Silicon master, e) Nickel shim, f) Injection molded PP.

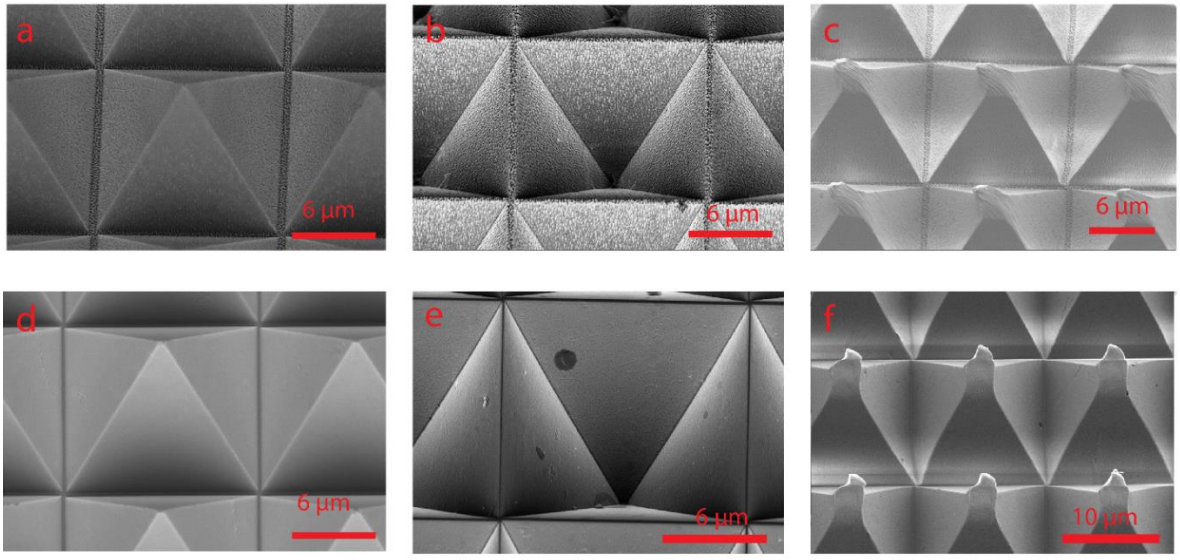

Figure 5.27. SEM images of 12 µm pyramids, a) Structure inversion of pyramids holes with nanograss, b) Nickel shim with nanograss, c) Injection molded PP with nanograss, d) Structure inversion of pyramids holes, e) Nickel shim, f) Injection molded PP.

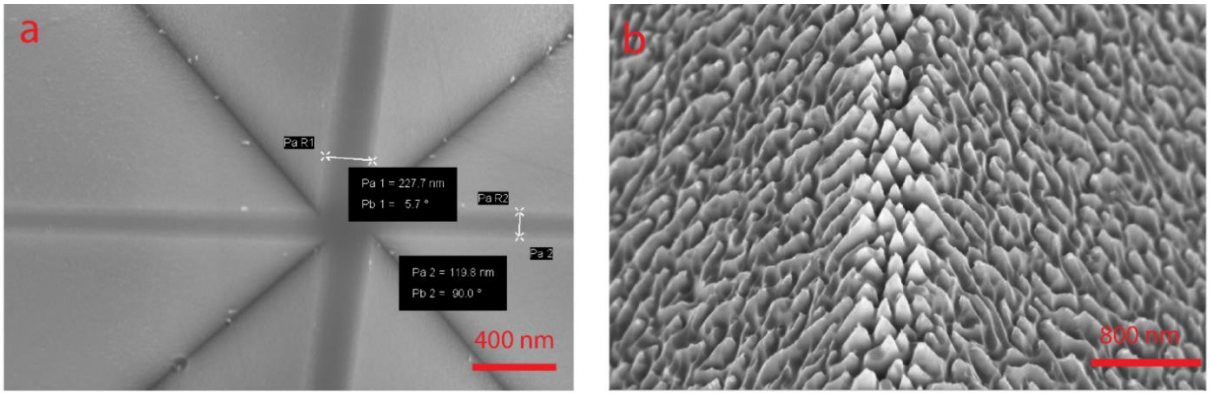

Figure 5.28. Line with reduction with BHF etching, the original sidewall was 2.0 µm, a) Smooth pyramid holes, b) Pyramid holes with nanograss.

5.6.7 Industrial test production

SEM images of silicon master, which was used to produce the polymer parts for the industrial test production, is shown in Figure 5.29. Nanopillars, triangular pillars, holes and topology-optimized structures were fabricated for the test production.

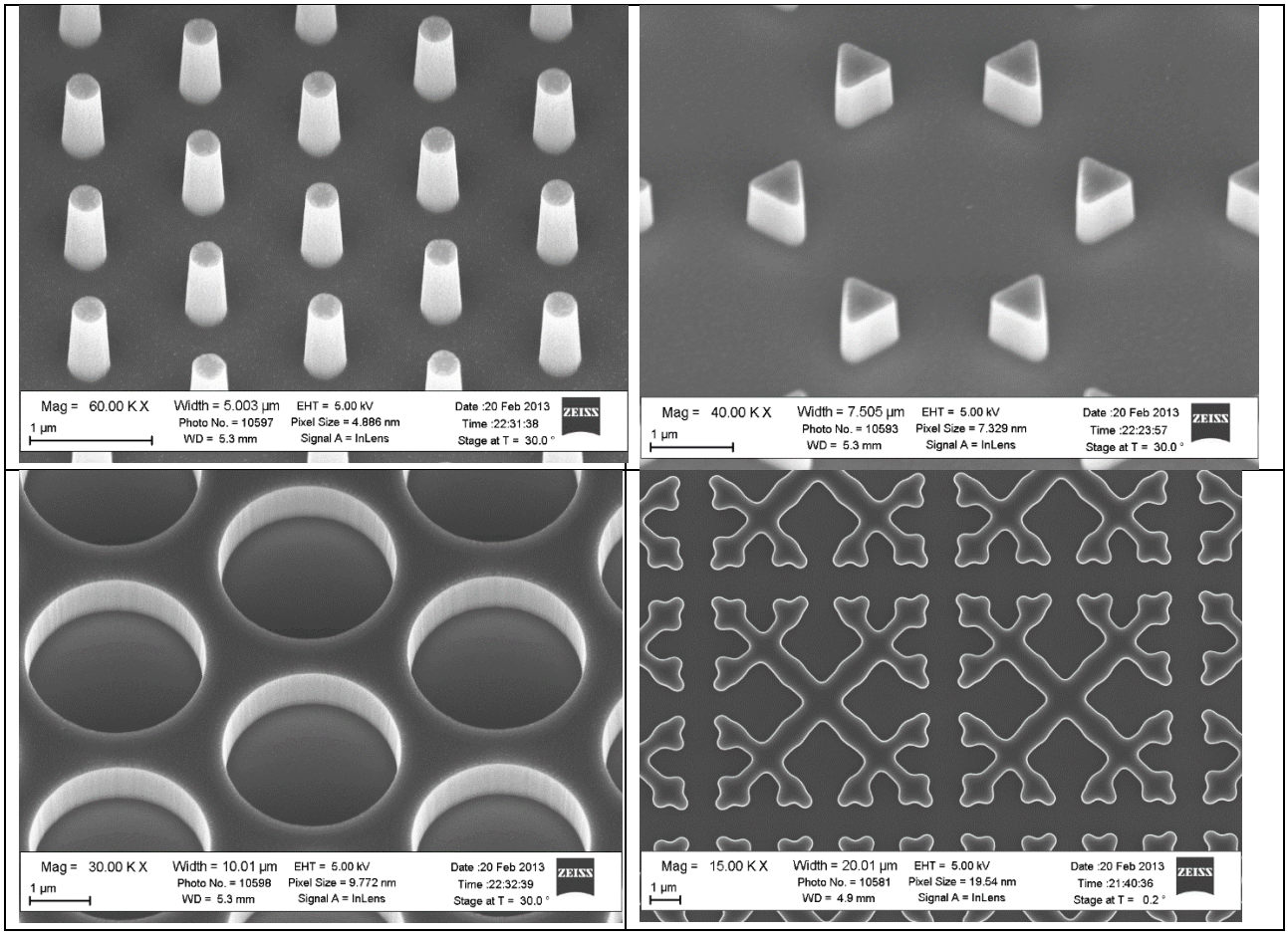

Figure 5.29. SEM images of the type of structures. Nanopillars, triangular pillars, holes, and topology-optimized structures were fabricated for the test production.

When the injection molded parts were observed with the naked eye, uneven filling of the nanostructures can clearly be seen as a change in the diffraction. This effect is present on all fabricated parts, except those made with holding pressure and fast injection speed. Examples of varying degree of replication are shown in Figure 5.30.

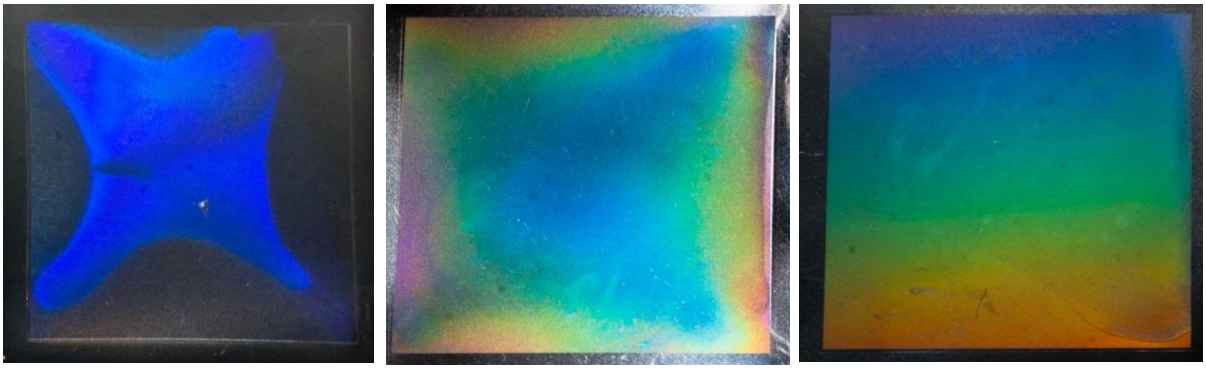

Figure 5.30. Filling of nanostructures Left: uneven filling (1400 bar/25 °C), Center: moderate filing, Right: even of filling (holding pressure and cycle time of 60 s).

To further characterize the injection-molded parts, AFM and SEM images were obtained for the center area of each part. Height measurements on the injection molded parts were compared with the structures of the silicon master. Polymer flash could be seen on all parts made with 1300 bar, the effect was less on the cold mold, but larger and quite severe on the hot mold. This flash might influence the pressure inside the mold, and therefore the structure filling on the Lego like bricks (Figure 5.31).

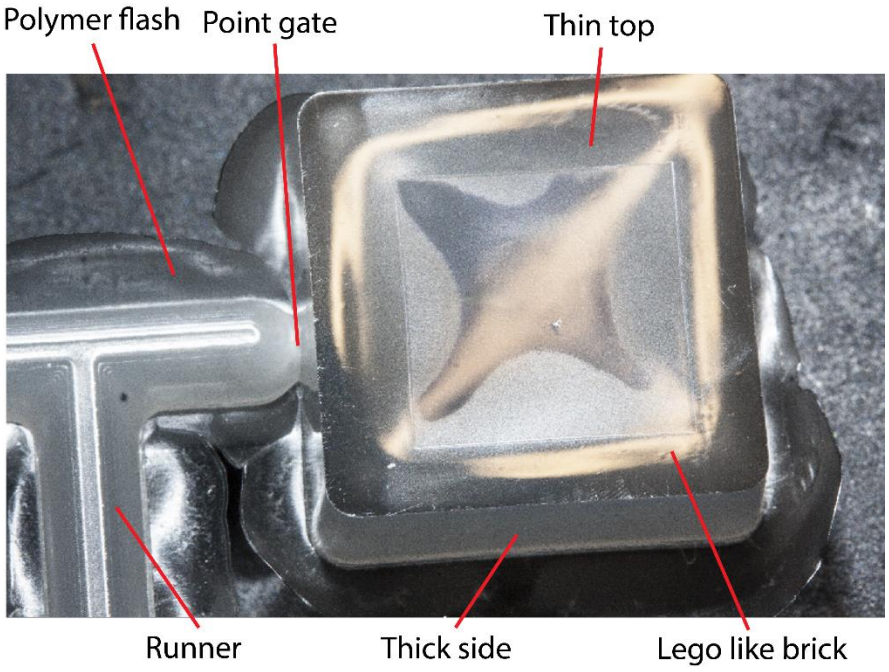

Figure 5.31. Polymer flash were present on all parts of the Lego like bricks made with 1300 bar.

The structure volume and height was compared. However, volume estimation is not trivial, since the shape of the AFM tip influence the measurement as structure height increases. The tip will be imaged together with structures and the results are a combination. This is not the case for the height measurement, which have little uncertainty. The triangular pillars were chosen for the detailed analysis of the mold filling. One image was obtained for each part and six structures were measured on each image. Example AFM images are shown in Figure 5.32. Results of the statistical measurements are shown in Figure 5.33.

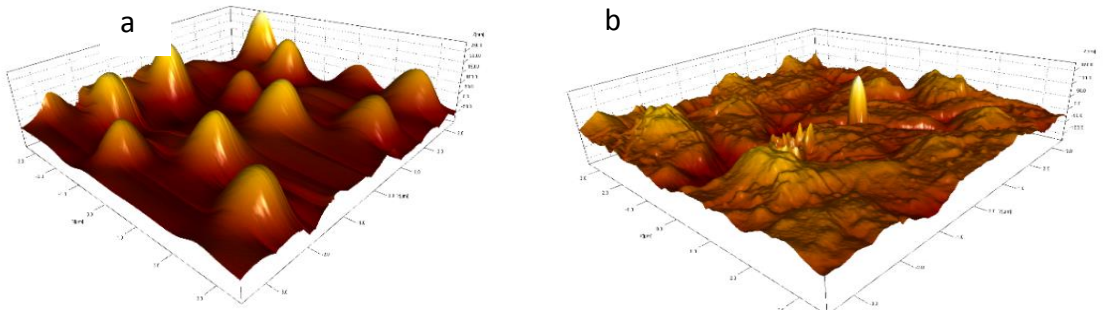

Figure 5.32. AFM images of polymer parts, a) Moderate replication at 1300 bar/25 °C, b) Poor replication 1300 bar/70 °C.

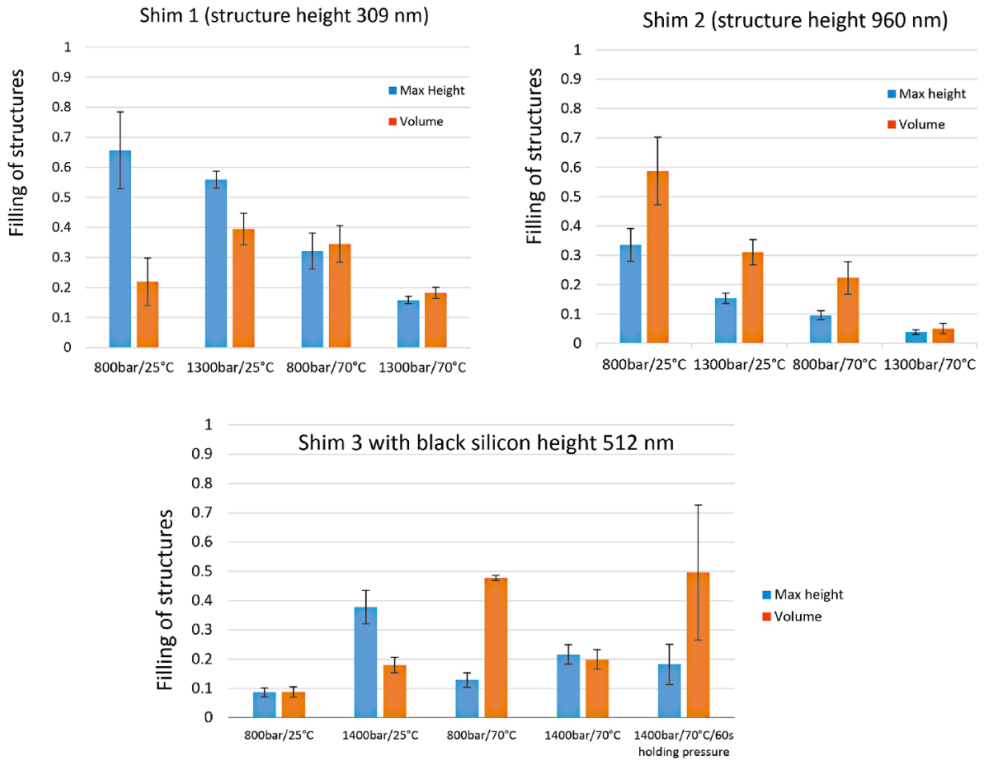

Figure 5.33. Filling of shims compared to the silicon master for three shims. On the y-axis 1 will be a completely filled mold and 0 will be empty.

5.7 Discussion of fabrication results

Overall, the cleanroom fabrication and electroplating in this project produced an excellent replication of fabricated structures and no issues were observed. A perfect inverse replica of the silicon wafers was produced. This can be seen in the figures and measurement data in the result section 5.6. No significant change in dimensions was observed between the silicon master and nickel shim.

Few earlier studies have presented injection molded structures with superhydrophobic properties[66–68,]. However, in these studies a desktop microinjection molding machine was used with process parameters fundamentally different from those used in industrial injection molding. One paper reports a superhydrophobic surface but here structure replication was poor and the structures were stretched[58].

5.7.1 Injection molding optimizations

The optimization of the injection molding process shows that a variotherm process is required for any significant structure filling. Structure replication occurs after an increase in mold temperature to above the polymer melting temperature. Stretching of the microstructures was observed during the demolding. Studies shows that the filling of nano- and microstructures can be performed by a variotherm processes similar in principle to one used in this PhD project[54,58,89–91].

In this work the optimization of the structure filling was as expected. Higher temperature and increased pressure improved the filling, until the structures were completely filled at a constant pressure at 1200 bar. However, the filled structures were impossible to demold. Demolding of nano- and microstructures are reported to be difficult or impossible without antistick coating; broken structures or stretching/scratching is reported[58,89,90].

This is in agreement with the results of this work observed for the TOPAS parts produced with a holding pressure of 1200 bar with a mold temperature of 130 °C. At this pressure demolding of the polymer parts were impossible. The depacking step combined with antistick coating made both filling and demolding of the polymer parts possible, although limited stretching was observed. The removal of clamping pressure in the cooling phase combined with fine-tuning of the injection molding parameters produced polymer parts similar to those in the silicon master. Almost no scratching was observed on the polymer parts, except on the pyramids and pyramid holes.

In this work the mold temperature was increased and a variotherm process used instead of attempting to optimize other parameters such as injection speed, holding pressure etc. The mold temperature has a large influence on structure replication, since the injection molding process is primarily driven by heat exchange. Heat will be transferred from the hot polymer melt into the tool, and the cooling rate will greatly influence freezing time of the polymer.

5.7.1.1 Pillars and holes

All measured pillars and holes have complete mold filling as shown in the plot in Figure 5.20a, because the nanograss has been replicated on the top of the structures. The height measurement of the polymer parts was less than 4% lower than the corresponding nickel shims. A similar reduction in size is observed for the lateral measurements of the structures (Table 5.6, Table 5.7, and Table 5.8). Here, the structure size reduction was below 6%. Polymer shrinkage is a possible explanation of the reduction in size on the injection molded polymer parts. No significant difference was found between TOPAS and PP. This was not expected since TOPAS is an amorphous polymer and PP semi crystalline. It would be expected that PP had a larger shrinkage[81]. The explanation could be that fast freezing of PP occurred in the nano- and microstructures and therefore, the PP did not have time to crystalize due to increased surface to volume ratio of the nano- and microstructures[85]. Measurement of the structure period on the injection molded holes showed no significant deviation of the designed period.

In this work a slight stretching of the PP parts with holes was observed (105 percent of the shim height), although PP has a larger material shrinkage, PP is also less viscous than the TOPAS at high shear rates as seen on Figure 5.9. The origin of the stretching could be that the PP would flow, into small overhanging nanodefects on the shim. When demolding the part the PP structures would have a larger adhesion force, and be more difficult to demold with stretching as a result.

The structures with black silicon were better replicated than the pure microstructures, e.g. the pure micro holes showed some sidewall deformation even though the sidewalls was 500 nm thicker. This deformation is properly caused by the scallops from the D-RIE process, the overhanging scallops on the shim would adhere strongly to polymer part and the circular holes would be deformed during demolding. The black silicon etch removed most of the scallops and produced a positive slope angle, which would ensure a better demolding.

The injection molding of the nanograss showed some stretching which resulted in slighter higher nanograss structures on some polymer parts.

Overall, the optimized injection process produced good replication of all fabricated micropillars and holes. An excellent uniformity of the sample was observed when the sample was inspected with the naked eye and in an optical microscope. Furthermore, complete mold filling was observed for all pillars and holes.

5.7.1.2 Spruce like micropillars

The fabrication process for the sprucelike micropillars showed good replication in each step. The SEM images (Figure 5.25) shows the structures at the main steps of the fabrication process; the holes in silicon after D-RIE etching, the electroplated nickel shim and the injection molded polymer. It is clear that the black silicon etch removed the 300 nm wide walls separating the holes. From the image of the nickel shim it is clearly visible that the polarity of the

structures is inverted. Many of the sidewall structures which can be observed at the silicon pillars have an overhang, which will improve superhydrophobic properties. However, structures with overhang can be problematic during injection molding, since the overhanging polymer sticks to the mold. It is clear that the injection molded polymer has fewer and less protruding structures on the sidewalls than the silicon master. This damage of the sidewall structures may be caused by one of the following effects; 1) the removal of the silicon wafer with KOH, 2) incomplete polymer filling of the nickel shim during injection molding or 3) damage during demolding. It is difficult to assess if the sidewall structures are present on the nickel shim, since imaging of whole structures by SEM is difficult, FIB SEM was attempted, but provided no concrete results, since structures could not be imaged and milled in the same microscope.

Michaeli *et al.* 2011[58] reports that ductile material behavior is required for the injection molding of structures with overhang. Parts from brittle polymers like poly(methyl methacrylate) (PMMA) would be destroyed during the demolding process and clogging of the mold was observed, and more ductile materials would be stretched[58]. The spruce like micropillars in this work were replicated in both TOPAS and PP. Stretching was observed, even when the depacking step was used. Overhanging structures were still present on the finished polymer parts.

5.7.1.3 Pyramids

The pyramids proved difficult to characterize, since no flat surfaces for light reflection were present, this meant that optical methods could not be used and even the smallest pyramids (6 µm base length) was too high to be measured with AFM.

The reason for designing and fabricating pyramids and pyramids holes in this work were that the sloped sidewalls with an angle of 54.7° would lower adhesion between the polymer part and the shim and thereby reduce the force required for demolding. However, for the optimized injection molding process, all injection molded pyramids showed significant defects.

For the pyramid structures, it seems that the tip of the pyramids was stuck in the bottom of the shim during demolding. The pyramid tips were pulled and deformed during the demolding process.

For the injection molded pyramid holes the structures was scratched by the tip of the harder nickel shim. The scratching of the pyramids was reproduced all over the polymer parts. Although the pyramids were supposed to be theoretical easy to fabricate, this was not the case when they were injection molded.

5.7.2 Tools

The problems with polymer leaking remained throughout the project period although leaking was reduced by the new clamping plate. For PP the melt temperature was limited to 220 °C. Otherwise, the PP would leak through the entire tool. The leaking of PP compared to TOPAS

was increased because HD601CF has a high degree of shear thinning as shown from the plot in Figure 5.9. The leaking tool made optimization of the injection process difficult since the full range of parameters on the injection machine could not be used. Mold temperature, melt temperature, injection speed, and holding pressure all had to be limited. A higher demand on precise tool tolerances is required, when nano- and microstructures are injection molded with a variotherm process.

Injection molding literature write that a good mold temperature is 40 °C lower than the polymer melt[54]. Kim *et al.* (2007)[90] reports full structure replication when mold temperature is equal to the melt temperature[90]. A tool with vacuum in the mold cavity would make filling easier and since no air could be compressed and prevent filling. Furthermore, an overall increase in structure quality is reported when vacuum is applied[92].

It possible that a better tool with no leakage and a higher mold temperature would make optimization on other part design faster, and that the tool could produce structure of better quality faster.

5.7.3 Industrial test production

The uneven filling is a problem for the injection molding of structures with self-cleaning properties. Overall, none of the molds has been completely filled. As the structure height, increased filling becomes less. This indicate the polymer will flow a certain distance and then be cooled to under the melting point and therefore become solid. The maximum structure height of 400 nm shows that it is possible to injection mold small structures with an industrial like process. However, the uneven filling will have to be solved. The parameters with low mold temperature seems to have a higher degree of filling, than those with high temperatures, this might be related to air trapped in the mold. A polymer will be cooled slower in a hotter mold and will have a larger shear thinning when injected at higher pressures. Therefore, the viscosity will decrease and the polymer will have a higher flow rate in the mold cavity. The polymer may fill the sides of the Lego like brick first, because the sidewall is thicker than the top of the part with the structures (Figure 5.31). Air might be trapped in the center of the part and prevent filling of structures. At high flow rates the air will not have time to escape, and therefore the trapped air will prevent structure filling. The trapped air could properly be reduced by changing the gate location and type. An optimized fan gate with even flow front of polymer, placed close to the structure, could reduce the trapped air and produce even replicated structures. The results show that more parameters such as gate location and size is needed to be considered when more complex parts with nano- and microstructures are injection molded.

5.7.4 Discussion summery

The injection molded superhydrophobic structures made by Tapani A. Pakkanen's group are reported to have a high replication quality, which is showed in the SEM images in their papers where no stretching or scratching of structures are visible[66–68]. The used injection molding

machine is not a standard industrial machine with lower injection and holding pressures[66–68]. It is possible that the lower injection and holding pressure produce less mold adhesion and larger shrinkage making demolding without stretching or scratching possible.

In this work the developed optimized injection molding process was extremely versatile since it could replicate a range of different structures with good quality. Sidewalls 100 nm wide at the narrowest part was reproduced for 3.2 µm high structures. The injection molding machine used in this project is a standard machine for large-scale industrial fabrication. Therefore, the described fabrication method can easily be converted to industrial fabrication as long as the longer cycle time of a variotherm process is acceptable.

6 Characterization methods

In this PhD project characterization can be divided into two parts: 1) Morphology/topography characterization of fabricated nano- and microstructures during the entire fabrication process. 2) Characterization of wetting properties of the injection molded samples. A new optical characterization method based on transmission microscopy and pressure cell was developed.

Three optical based methods were used for structure characterization together with SEM and AFM. Here is a brief description of the used equipment and their advantages and disadvantages, with emphasis on materials and structure types. Since injection molding was performed, a larger number of samples needed to be characterized. Fast characterization methods with a large field of view was preferred. The large field of view is important when characterizing injection molding samples. If a narrow field of view is used structure variation and defects might be overlooked. To successfully fabricate superhydrophobic surfaces, samples with few defects are needed, because the liquid can pin on the defects.

What is common for optical methods is that they are fast, easy to use and has a large field of view. Furthermore, more complex optical characterization tools such as confocal microscope and optical profilometer can provide accurate height information down to a few nm. Common to all optical methods is a transverse resolution limit to approximately 300 nm in air.

6.1 Optical microscope

Optical microscope is a quick and simple tool for viewing samples beyond size of the human vision. A modern optical microscope often uses a white light source, the resolution is diffraction limited by the selected objective, and adjustment of the microscope apertures. High resolution requires high numerical aperture. The resolution (R) of an optical microscope can be approximated by equation 6.1, where λ is the wavelength of illumination light and *NA* is the numerical aperture for the objective and the condenser[93].

$$R = \frac{1.22\lambda}{NA(obj)+NA(cond)} \qquad 6.1$$

An often-neglected error in optical microscopy is illumination adjustment. For an optical microscope to perform optimally (with good contrast, high resolution) and provide reliable measurements, proper illumination adjustment is required. The emitted light from the lamp must be focused correctly, and the numerical aperture of the condenser adjusted for each objective. For a perfectly adjusted microscope the resolution becomes optimal and equation 6.1 reduces to equation 6.2[93].

$$R = \frac{0.61\lambda}{NA} \qquad 6.2$$

As widespread method of microscope illumination is called Köhler illumination. It was discovered by Dr. August Köhler in the late 1900s. Köhler illumination ensures that the specimen

plane is bright, even, and with good contrast. In Köhler illumination the illumination light is adjusted to match the focus plane of the microscope objective and the numerical apperature of the illumination matched to the microscope objective.

One property of an optical microscope is that the depth of field (DOF) is limited by numerical aperture. DOF can be approximated by equation 6.3. A high resolution cannot be obtained simultaneously with a large DOF[94].

$$\mathrm{DOF} = \frac{\lambda}{NA^2} \qquad 6.3$$

An optical microscope is excellent for providing fast limited information on small well-defined features in regular patterns even when the structures are smaller than the resolution of the microscope. Potential areas with defects and irregularities are quickly located in the different fabrication process steps; few other characterization methods can rival the optical microscope for simplicity and fast measurements.

Optical microscopy was used extensively in this PhD project for quality control during the fabrication process and especially for optical transmissions measurement of wetting states in the pressure cell setup. In the pressure cell setup an AX10 Observer A1 made by Zeiss was used with a halogen lamp for sample illumination. The images were recorded by a CCD camera (AxioCam IC made by Zeiss). A Nikon L200 optical microscope was used for quality control during the cleanroom fabrication. At each process step the samples were inspected for uniformity, correct structure size, defects in the fabrication process and contaminations. A similar optical microscope produced by Leica was used to inspect polymer parts during the injection molding process. Microstructures could quickly be inspected and corrections to the injection molding parameters performed. Furthermore nickel shims with suspected polymer residues could quickly be characterized before additional polymer parts were produced.

6.2 Confocal microscope

A confocal microscope is a versatile method for obtaining true 3D measurement of a sample using florescence, or in reflectance accurate 2½D topographic information. A confocal microscope is similar to an optical microscope in many ways. The main difference is sample illumination and light collection. In a confocal microscope, the illumination of the sample is achieved by scanning one or more point light sources across or inside the sample. Sample illumination and light collection is from a single diffraction limited point on the sample[95]. By acquiring data from different focus planes. The collected data can be combined into a 3D image and topographic information determined. Overall, a confocal microscope is a fast and versatile characterization tool. Due to the diffraction limit, confocal microscope is limited to characterization of large nano- and microstructures.

A Zeiss model LSM 5 confocal microscope was used to characterize the Cassie and Wenzel States on an injection molded TOPAS 8007 S04 sample. Both fluorescence and reflectance measurement were acquired. Here, the confocal microscope was required, because the light

could be collected from either top or bottom of the structures, any light from the meniscus would in theory be reflected, light from reflected from the bottom of the structures would be out focused and be dark on the acquired image.

6.3 Sensofar

The PLu Neox 3D produced by Sensofar combines a high quality confocal microscope and optical profilometer. It has a possibility for both white and blue sample illumination. The confocal microscope is based on a digital micro mirror display, similar to that in a DLP video projector, to scan the light across the sample. The digital micro mirror display increase the scanning speed significantly, compared to tradition confocal microscopes. The obtained topographical accuracy of the confocal microscope mode in the Sensofar is limited by the numerical aperture of the used objective. The vertical accuracy is reported down to 2 nm for 150X objective with a numerical aperture of 0.95. If higher vertical accuracy are required, the optical profilometer function can be used[96].

An optical profilometer combines an optical microscope and an interferometer. An image of the interference pattern is recorded by a camera and is used to determine the sample topography. The advantage is a vertical resolution regardless of numerical aperture. Two different methods can be used to obtain topographical information: 1) Vertical scanning interference with a resolution down to a few nm 2) Phase shift interference can only be used for surfaces with low step heights (less than 100 nm)[97]. An optical profilometer is a fast method to determine accurate surface topography. Measurement time is typically less than two minutes per measurement, which make is excellent for measuring a large number of samples quickly. The low reflection of polymer materials can cause problems and errors in the measurement process. To overcome this, polymers surfaces may require deposition of a metal layer such as gold/palladium or iridium to increase reflectivity of the surface.

The Sensofar was used to measure the etch depth on the fabricated silicon wafers and after electroplating the degree of molding filling for the injection molded structures were measured. The height of the structures on nickel shim was first measured. These measurement were later compared with height measurements of the injection molded polymer samples and the mold filling could be compared in percent. The Sensofar microscope was used as the primary method for obtaining topographic information in this PhD project, it a fast versatile tool, with excellent accuracy when used correctly.

6.4 Scanning electron microscope (SEM)

A scanning electron microscope (SEM) is a type of electron microscope that can resolve features much smaller than a conventional optical microscope. The electron beam is focused and penetrates into the top layer of a sample, scattering of electrons produce an electron cloud in the material. A long the electron path secondary electrons are exited, the secondary electrons can only escape from the first few nanometers of the surface. Typical the number of secondary

electrons are detected while the beam is scanning, intensity is the plotted for each position and the image is generated[98].

The smallest features that can be distinguished in a SEM is typically a few nm. Furthermore, a SEM has a large depth of field. Due to the electron flow SEM is limited to picturing conductive materials e.g. metals. The incoming electrons will charge insulators and consequently the image is distorted. This happens especially for polymer materials. This can be overcome by coating the sample with a thin layer of metal e.g. gold/palladium or iridium. The easiest process to overcome the charging issues is applying 5-10 nm of metal to polymer samples. SEM is an excellent tool for characterization of wafers, nickel shims, and injection molded parts. SEM provides fast method for obtaining 2D sample information and the field of view can be adjusted from a wide field to a very narrow field, this allows for a good all round characterization of samples. If the sample is tilted qualitative 3D information can be obtained.

Two different field emissions SEMs (FEI Nova NanoSEM and a Zeiss Supra VP40) were used to characterize, nano- and microstructures on silicon wafers and their corresponding nickel shims. The injection molding samples were also characterized with these microscopes. Before SEM characterizations the samples were sputter coated with a 5 nm thick layer of gold palladium. Some polymer samples was characterized directly without any conductive coating in high vacuum mode, here an elevated pressure in the microscope conduct electrons away from the surface, however some resolution is lost in the process. So the metal coating was preferred. SEM was used to measure precise lateral structure dimensions of fabricated samples, and to get an overall impression of the quality of the fabricated samples, especially those with nanograss. SEM was used extensively during optimization of the injection molding process to characterize the effect when different injection molding parameters were changed.

6.4.1 Focused ion beam SEM

Focused ion beam (FIB) SEM is a versatile tool with many different applications for high value task. The FIB can locally sputter a surface to fabricate micro and nanostructures or deposit materials. When FIB and SEM are combined the fabrication can be monitored. A standard SEM can only view surface structures, if characterization off bulk material or true 3D sample is required, the FIB can remove material to perform cross-sections of the sample. An image with a plane perpendicular to the surfaces becomes visible. This process is also known as slice and view. Scanning of the beam makes FIB a serial process, only one structure can be milled at a time, FIB is therefore a slow process and not suited to fabricate micro or nanostructures, or to perform slice and view over large areas. This could easily take days in time. The ion beam removes material so slice and view will destroy imaged area on the sample. The imaged area is impossible to view later on. Even with the slow speed and destructive nature of the sputtering do FIB has advantage of provide true 3D sample information, even when objects are embedded in bulk material. A quality FIB SEM can easily obtain a voxel size of 10 nm. Few

other tools are capable this. Confocal microscope with fluorescence can provide similar information at a lower resolution if the sample is transparent.

FIB SEM is an excellent tool for obtaining cross-sections of fabricated nickel inserts, which otherwise are hard to obtain. Cross-sections are hard to acquire for polymers because the material may melt during the FIB process. FIB SEM is relative slow and expensive technique, and is limited to a few samples and small areas.

A Tungsten filament FIB SEM (FEI Quanta 200 3D SEM-FIB) was used to obtain cross-sections of nanograss and the spruce like micropillars on the nickel shims. After FIB milling a Zeiss supra VP40 was used for imaging, since the VP40 produced images at higher resolution when imaging the magnetic nickel shim. The shim with spruce like micropillars is hard to characterize with other methods, since the structures are small holes with high aspect ratio.

6.5 Atomic force microscope

An atomic force microscope (AFM) is based on a physical scanning technique where the surface is physically probed with a small tip mounted on a flexible cantilever. A high resolution image is generated from the recorded data. AFM can perform measurements on all types of surfaces regardless of conductivity and other material properties, which makes it excellent for the characterization of polymers[99]. One of the limitations in AFMs is that the shape of the tip influences the measurement. This phenomenon is called tip convolution. Tip convolution is more problematic for small structures with high aspect ratios. Tip convolution can be seen by a widening of protrusions and shrinkage of holes[100].

In this project, AFM was used to obtain topographic information shallow nanostructures (lower than 2 µm) that is too small to be detected by the Sensofar microscope. Overall AFM is a slow method with a small field of view, so an AFM is of limited use when characterization many samples and large areas. An AFM (Dimension 3100 manufactured by Veeco) was used to verify the height measurements made by the Sensofar, and to characterize the fabricated nanograss on silicon wafers.

A Park Systems XE-150 AFM was used to measure the structure filling on the nanostructure produced by the industrial test production. These structures were below the diffraction limit of the Sensofar and could therefore not be characterized by confocal microscope or optical profilometer.

6.6 General concepts on characterization of superhydrophobic surfaces

Wetting on surfaces is often characterized with an optical tensiometer also known as contact angle goniometer. For measuring contact angles a technique called the sessile drop method is typically used. Here a drop consisting of known probe liquid is placed on the surface, and a camera records a sideways image of the drop. The drop shape is determined by software and fitted to various theoretical models. The contact angle is calculated from the drop shape. Dynamic contact angle data can be acquired by either tilting the entire machine or enlarging/reducing the drop on the surface.

Wetting properties of a surface is related to oleophobicity, hydrophobicity, easiness of coating and surface adhesion. Characterization of the wettability is fundamental study for any polymer surface. Wetting measurements are common and simple method for surface analysis, the most useful method for characterization of solid polymer like injection molded parts is contact angle measurements, it provides quantitative data, are relatively low cost, and instruments can be acquired as off the shelf products with simple operating procedures. Characterization of contact angles is a wide spread method for both academic research and industrial production[15]. However, errors in the measurement process often occurs and the result in the collected data over interpreted[101].

When the drop is placed on a surface, it will always have a contact angle, regardless of liquid and surface type. As contact angles are characterized, it will become apparent that a drop can have a range of contact angles on a specific solid surface. The contact angle range has a maximum called the advancing contact angle and minimum called the receding contact angle.

The advancing contact angle is measured at the triple phase line when liquid moves towards an unwetted area, and the receding contact angle is measured at the triple phase line when the liquid moves from a previously wetted area. If drops is placed on an ideal surface (atomic flat, chemical homogenies, and with no liquid surface interaction) the advancing and receding contact angle will be identical and equal to the equilibrium contact angle. In real life ideal surfaces are extremely rare; most surfaces have some sort of roughness and/or chemical variation[15].

Real life polymer surface always have some hysteresis, due to roughness or chemical variation of the surface. Very low hysteresis can in some cases be observed and a hysteresis above 50° is often observed. When measuring the contact angle both the advancing and receding contact angel should always be measured so the hysteresis can be calculated. Many scientific papers report that is possible to put a drop on a surface and measure the contact angle, this is normally called static contact angle. A static contact angle provides little information of the surface since the contact angle can have any value between the advancing and receding contact angle. The advancing and receding contact angle provide information on the roughness and chemical homogeneity off the surface[15].

One of the often overlooked errors when measuring contact is electric charging of the surface, a charged surface can induce variations in the contact angles measurement for polymer surfaces. Therefore, the surface must be discharged prior to placing the drop on the surface[102]. Discharging can be a challenge for a nonconductive surface, but it is reported that alpha radiation can neutralize all surface charging such as Po210 alpha source[15].

Researches often want to estimate the surface energy of a sample; here contact angles are used to estimate solid surface energies with one of the different theories. Researchers often focus on Young's equation (equation 2.1), and solid surface energy estimates, and the researches often overlook the limitation of the contact angle data. It makes little sense to calculate the surface energy components for most polymer surfaces since it's very hard to obtain the equilibrium contact angles required for Young's equation on real life polymer samples. It is much more important to acquire high quality contact angle data where one or two test liquid is used to measure advancing and receding contact angles. The exact method used should be thoroughly described[15], for example the way the drop is deposited on the surface influence the measured results. A drop can be compressed when the drop is detached from the needle in an optical tensiometer; the drop will be deformed and flatten, after some time it may relax, during the deposition the meniscus may be pushed deeper into the structures. Alternatively, the drop may fall a short distance from tip of the needle onto the surface, the drops distance must be considered carefully so the kinetic pressure from the impacting drop is limited. The drop will be deformed by the impact and in some cases bounce, the kinetic pressure will cause the meniscus to penetrate into the structures[16].

Water is good probe liquid for contact angle measurements; because aqueous systems are used, many place in industry and in the scientific world. Furthermore, does water has the highest surface tension of normal test liquid. Therefore, water has a measurable contact angle for most polymer materials. A critical examination of interactions between probe liquid and surface are required for accurate contact angle measurements, such interaction can be: water adsorption, swelling, and change of surface chemistry. If liquid surface interactions are present they can affect the contact angle results and the performed measurement become inaccurate[15].

6.7 Method for measuring contact angles

Hydrophobic properties of the injection-molded polymer parts were characterized by determination of static contact angles, contact angle hysteresis, drop roll-off angle, and bounce experiments with water. Before contact angle measurements static electricity were removed on all samples with an antistatic gun (Milty ZeroStat 3). An Attension Theta Optical Tensiometer with high-speed camera (3000 fps) was used to perform the measurements using a sessile drop method. Static contact angles were measured by fitting drop shapes both with polynomials and the Young Laplace equation, whereas dynamic contact angles only were fitted using

polynomials. For all contact angle measurements the baseline was determined by the auto baseline function in Attension Theta Software Version 4.2.

The contact angles measurements were performed with a drop size of 10 µL. The drops were deposited on the surface by hanging the drops from the deposition needle in the tensiometer, as the drop expended it would come in contact with surface. After a drop volume of 10 µL was reached the deposition needle was raised and the drop would now rest on the surface. Five frames were a for static contact angle calculation. The entire tensiometer was tilted with a speed of 0.7° per second while recording one frame per second. The advancing and receding contact angle were recorded just before the drop would begin to slide or roll.

7 Results of contact angle characterization

7.1 Results from pillars

Initial results from investigation of the pillars are presented in the conference paper in Appendix 5. However, it was discovered that the superhydrophobic effect was due to static electricity on the polymer surface. The super hydrophobic properties of the structured parts were characterized by contact angle and drop roll-off measurements. Results indicate a contact angle increase from 95° (TOPAS) for the unstructured polymer to a maximum 150°, obtained for 3.0 µm pillars with a spacing of 8.0 µm. Roll-off angles were measured as a function of pitch size for different pillar diameters and the results are plotted in Figure 7.1. After removal of the static electricity all drops on TOPAS pillars were pinned. Static contact angles were measured between 130° and 150° for pillars with nanograss.

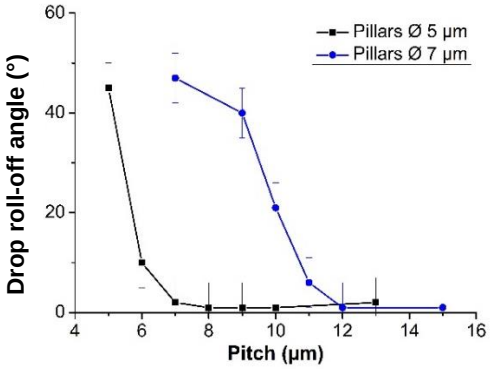

Figure 7.1. Drop roll-off due to static electricity. Roll-off angles plotted as function of pitch on TOPAS pillars with nanograss.

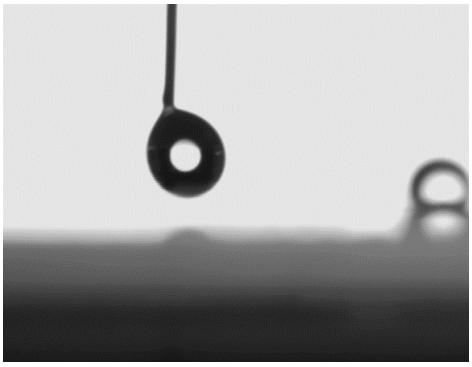

Figure 7.2. Static surface charge will push drops away before they touch the surface. Even negative roll-off angles were observed for some samples.

PP pillars without nanograss were similar to the TOPAS pillars and drops were pinned to the surface even when the surface was tilted to vertical (90°). Pillars with in PP showed slightly better performance with contact angles between 130° and 155° and drops had roll-off angles from 20° to 90° (pinned). The hysteresis was similarly large and above 25°. The pillar structures were therefore not superhydrophobic.

7.2 Results from holes

Results from the contact angle measurement of the holes are presented in Table 7.1. Contact angles were measured for three different samples. PP holes with nanograss showed superhydrophobic properties with contact angles up to 164° and roll-off angles down to 7°. TOPAS holes showed high static contact angles up to 158°, but all drops were pinned. The smooth structures without nanograss made from PP pinned the drops on the 3.0 µm and 7.0 µm holes;

however, the holes with a diameter of 15.0 µm had a drop roll-off angle at 48° with a hysteresis of 45°.

Material	Micro-cavity diameter (µm)	Contact angle (˚)	Hysteresis (˚)	Roll-off angle (˚)
TOPAS (nanograss)	3.5	145 ± 5	Pinned	Pinned
	7.5	158 ± 1	Pinned	Pinned
	15.5	153 ± 6	Pinned	Pinned
PP (nanograss)	3.5	156 ± 3	22 ± 3	15 ± 4
	7.5	164 ± 3	11 ± 1	7 ± 1
	15.5	162 ± 2	12 ± 2	7 ± 1
PP (smooth)	3.0	126 ± 10	Pinned	Pinned
	7.0	146 ± 2	Pinned	Pinned
	15.0	151 ± 1	48 ± 6	45 ± 3

Table 7.1. Contact angles measured on holes after removal of static electricity.

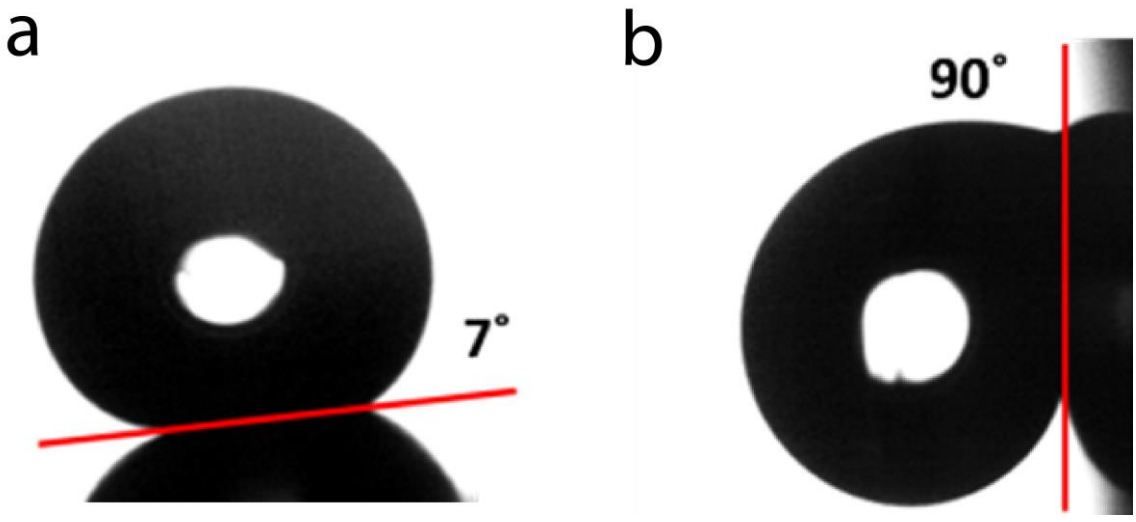

Figure 7.3. Images from the optical tensiometer, a) PP nanograss holes 7.5 µm in diameter show superhydrophobic effect with drop roll-off at 7˚, b) TOPAS nanograss holes 7.5 µm show strong adhesion with pinned drops even when tilted 90˚.

7.3 Results from spruce like micropillars

Results from the contact angle measurement of the sprucelike micropillars are presented in Table 7.2. Images from the optical tensiometer, where sprucelike micropillars made from TOPAS were compared with flat TOPAS, are shown in Figure 7.4. The arithmetic mean value of the contact angles were calculated to 170° ±4° and 173° ±2° both TOPAS and PP showed extreme superhydrophobic properties and it was almost impossible to deposit drops on the surface for contact angle measurements.

A drop bounce experiment was made with an optical tensiometer (Figure 7.5). Here a 6.5 µL drop impacts the structured polymer surface. At time zero, the drop is hanging from a needle, after 51.9 ms the drop has reached its maximum altitude after impact. During impact, the drop shows very little adhesion to the surface, resulting in the high altitude of the rebound. The drop bounced more than 10 times before it finally rested on the surface.

Material	Contact angle (˚)	Hysteresis (˚)	Roll-off angle (˚)
TOPAS	170 ± 4	5 ± 4	4.6 ± 0.6
PP	173 ± 2	6 ± 5	<2

Table 7.2. Contact angles of spruce like micropillars after removal of static electricity.

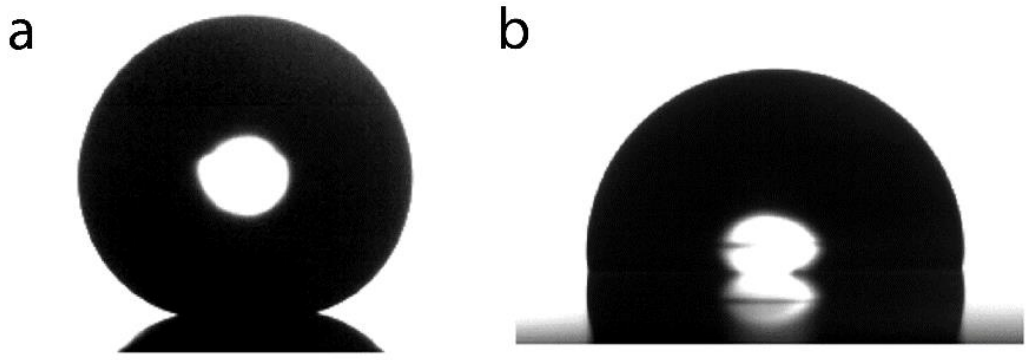

Figure 7.4. Images from the optical tensiometer, a) TOPAS with spruce like micropillars contact angle 170°, b) Flat TOPAS a as reference.

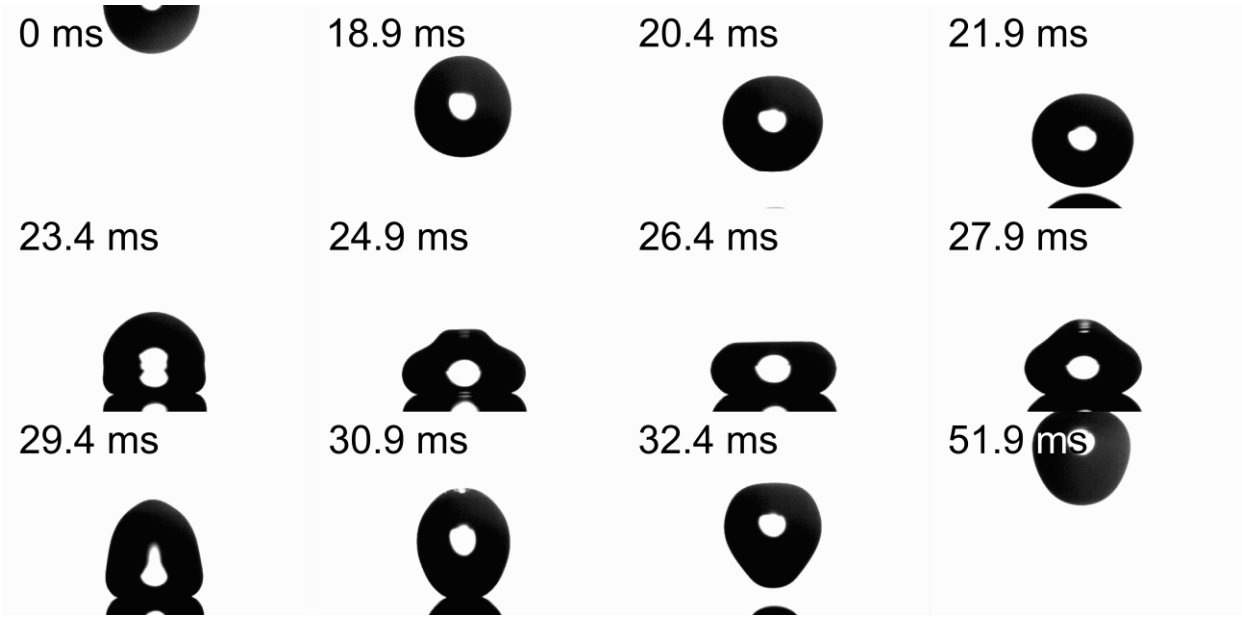

Figure 7.5. Image sequence showing a 6.5 µL drop impacting the structured polymer surface. At time zero, the drop is hanging from a needle, after 51.9 ms the drop have reached its maximum altitude after impact.

7.4 Results from pyramids and pyramid holes

Contact angle measurements of pyramids and pyramid holes were measured for three samples (Table 7.3). None of the fabricated pyramids showed superhydrophobic properties and drops were pinned on all test areas except on the pyramid holes with nanograss, which showed roll-off angles between 18° and 39°.

Material	Base length (µm)	Contact angle (˚)	Hysteresis (˚)	Roll-off angle (˚)
Pyramids PP (smooth)	6	128 ± 10	Pinned	Pinned
	12	140 ± 3	Pinned	Pinned
	18	140± 5	Pinned	Pinned
Pyramids PP (nanograss)	6	149 ± 11	Pinned	Pinned
	12	144 ± 12	Pinned	Pinned
	18	152 ± 3	Pinned	Pinned
Pyramids holes PP (smooth)	6	145 ± 5	Pinned	Pinned
	12	148 ± 2	Pinned	Pinned
	18	144 ± 1	Pinned	Pinned
Pyramids holes PP (nanograss)	6	156 ± 4	35 ± 8	27 ± 2
	12	164 ± 1	35 ± 5	18 ± 3
	18	163 ± 2	48 ±8	39 ± 5

Table 7.3. Contact angle measurements.

7.5 Polymer degradation

During this work, it was discovered that the polymer became less hydrophobic when exposed to water. Superhydrophobic properties of all samples, except the sprucelike micropillars, would disappear within 1½ hour when the samples were submerged in water. The drops were pinned complete to the samples. This was a non-recoverable effect even when drying of samples on hotplate at 100 °C or in the polymer dryer on the injection molding machine at 100 °C.

Drops would continue to be pinned. Only the sprucelike micropillars retained their superhydrophobic properties. To further characterize this effect PP nanostructured (flat) PP parts were floated (HD601CF) on water so one side was in contact with the water. Parts were removed in batches of three and dried for 2 hours on a 100 °C hotplate with increasing submersion times and contact angles were measured (Figure 7.6). The measured contact angle dropped from 101 to 59. This showed that PP became hydrophilic.

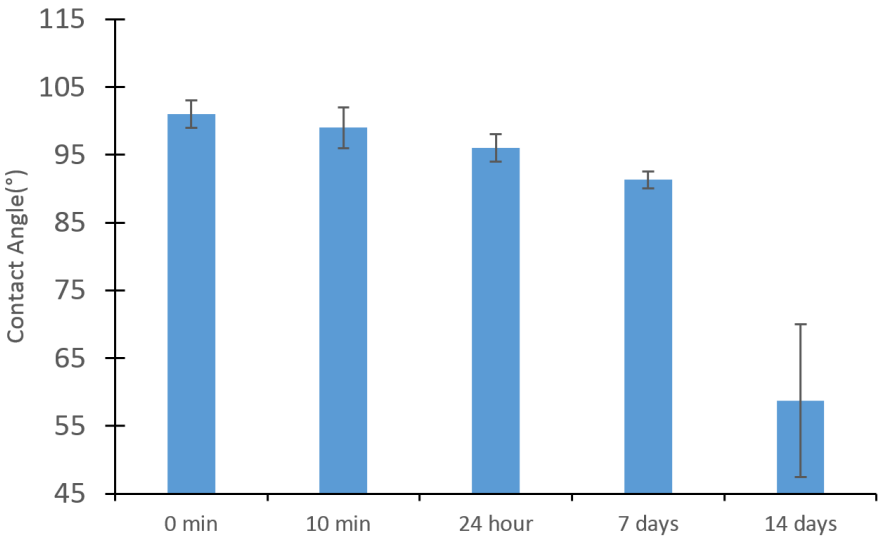

Figure 7.6. Contact angle measurements on flat PP samples, after water submersion and drying on hotplate, performed for different submersion times.

8 Pressure cell experiments

During this work, it was observed that the wetting state of microstructures was observable in an optical microscope. A method for studying the transition between wetting states was developed. This method was able to study the influence of time and pressure on submerged samples. It was decided to characterize the stability of the injection molded superhydrophobic structures when they were submerged in water and systematically study the Cassie State to Wenzel State transition at elevated pressures (0-400 mbar). Open structures (pillar based) collapsed immediately to the Wenzel State (even at atmospheric pressure) and closed structures had a stable Cassie State. The stability of the fabricated holes (micro cavities) with nanograss was studied systematically in order to observe how long the superhydrophobic Cassie State could be maintained. For this experiment, a pressure cell was designed and fabricated in clear polycarbonate by micromilling. A schematic and image of the pressure cell is shown in Figure 8.1.

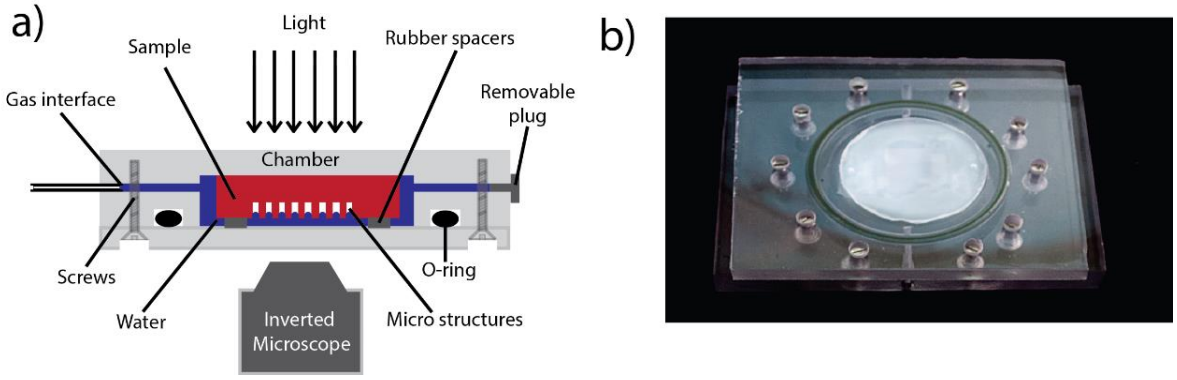

Figure 8.1. The pressure cell, a) Schematic side view of the pressure cell, b) Photo of the assembled cell with PP sample.

The pressure cell experiment is described in the paper; *Study of Transitions between Wetting States on Micro-cavity Arrays by Optical Transmission Microscopy* (Appendix 3). In this paper, a simple and fast optical method, based on transmission microscopy, is presented. The purpose was to study the stochastic wetting transitions on nano- and microstructured polymer surfaces immersed in water. The influence of immersion time and the liquid pressure on the degree of water intrusion in individual micro-cavities on these surfaces, as well as the lifespan of their superhydrophobicity is presented. The transitions between the different wetting states can be explained by taking into account both the Young Laplace equation for the water menisci in the cavities and the diffusion of dissolved gas molecules in the water. In addition, the wetting transitions had a stochastic nature, which resulted from the short diffusion distance for dissolved gas molecules in the water between neighboring cavities.

The transition between the different wetting states are shown in Figure 8.2. Here, the number of filled holes is plotted as function of time and compared to a theoretical model. The three wetting states (Cassie, Cassie-impregnating, and Wenzel) are observed with a certain pressure threshold (300 mbar for a hole diameter of 7.5 µm). Below this threshold, the transitions between the Cassie and the Cassie-impregnating States are reversible, above this threshold, irreversible transitions to the Wenzel State start to occur. Furthermore, the experiment shows that a Cassie State is maintained for the holes for at least 24 hours at atmospheric pressure for both PP and TOPAS Samples.

The experimental observations indicate that both the diffusion of gas molecules in water, and the wetting properties of nanostructures are important for understanding the sustainability of superhydrophobicity of surfaces under water, and for improving the structural design of superhydrophobic surfaces.

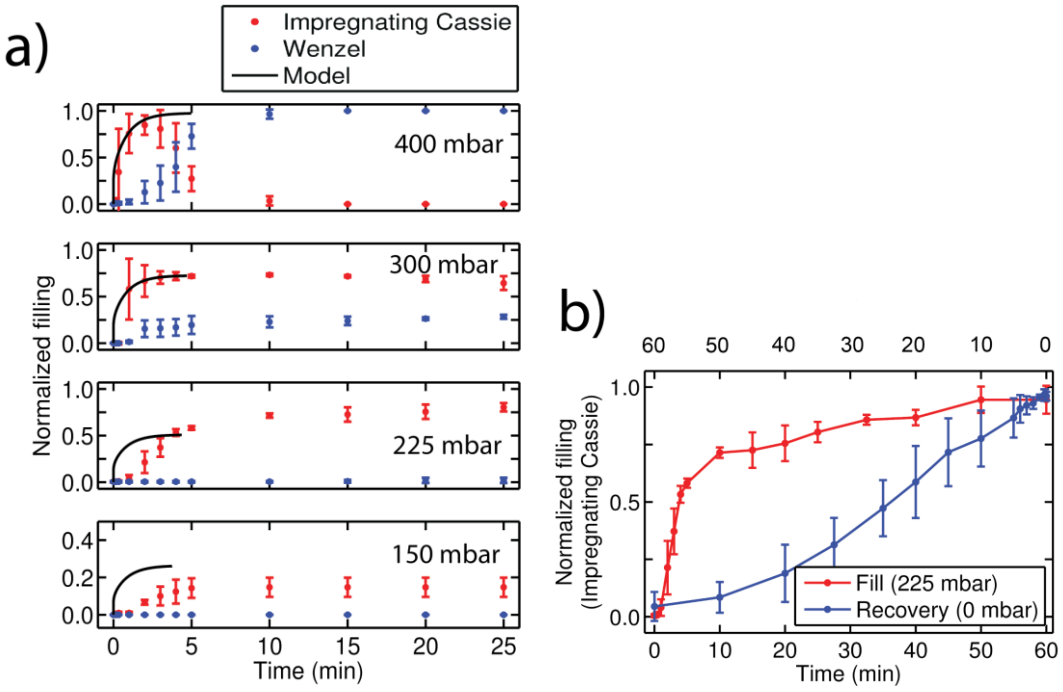

Figure 8.2. a) Transitions between wetting states over time at different Δp: 150, 225, 300, and 400 mbar. The model data (until saturation at about 3 min) were based on the degree of intrusion of a single cavity using the 1D diffusion model, b) Recovery of the Cassie-impregnating to Cassie State after the reduction of Δp to 0. Error bars in both a and b are obtained as the standard deviation for measurements on three different samples.

8.1 Adjustment of the microscope and image processing

This section describes how the microscope was adjusted, and how the optical microscope images were adjusted necessary to observe the Cassie-impregnating State.

In order to make interpretation of the optical microscope images easier. Contrast and brightness where adjusted in the optical microscope camera software (Zeiss AxioVision) by performing an intensity remapping of the image (Figure 8.3) to further enhance the contrast a gamma correction was applied of approximately 1.2. Time-lapse series of images were recorded in 16 bit tagged image file format. The recorded images were later processed with a MATLAB script, here the script performed an auto remapping of the images to ensure even tonality of all images, tunable background correction. Finally, fine adjustment of contrast was applied. Structures with different wetting states were counted and the number of holes in Cassie State, Cassie-impregnating State, and Wenzel State recorded.

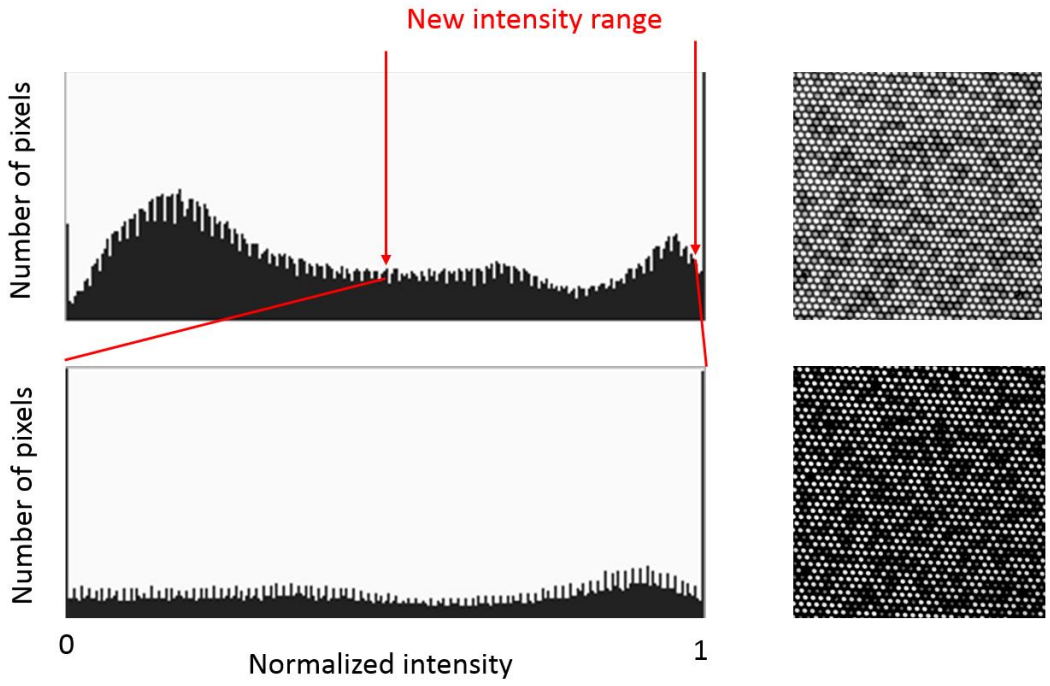

Figure 8.3. Intensity remapping of the microscope images, the red arrows indicate the new intensity range. Intensities smaller than the new range is set 0 and intensities larger than the range are set 1.

Images from an initial test experiment are shown in Figure 8.4. Here, the liquid starts in Cassie State, when pressure is applied the microstructures starts transition to the Wenzel State and a hybrid state was formed. Structures in the Wenzel State had a higher intensity on the image due to the smaller difference in refraction index of polymer and water compared with polymer

air interface the Cassie State. By adjusting on the optical microscope with a perfect Kölher illumination the Cassie-impregnating State was also observed as third intensity level (Figure 8.5) when the focus plane of the objective were matched with the focus plane of the illumination and a fine adjustment of the condenser aperture was performed.

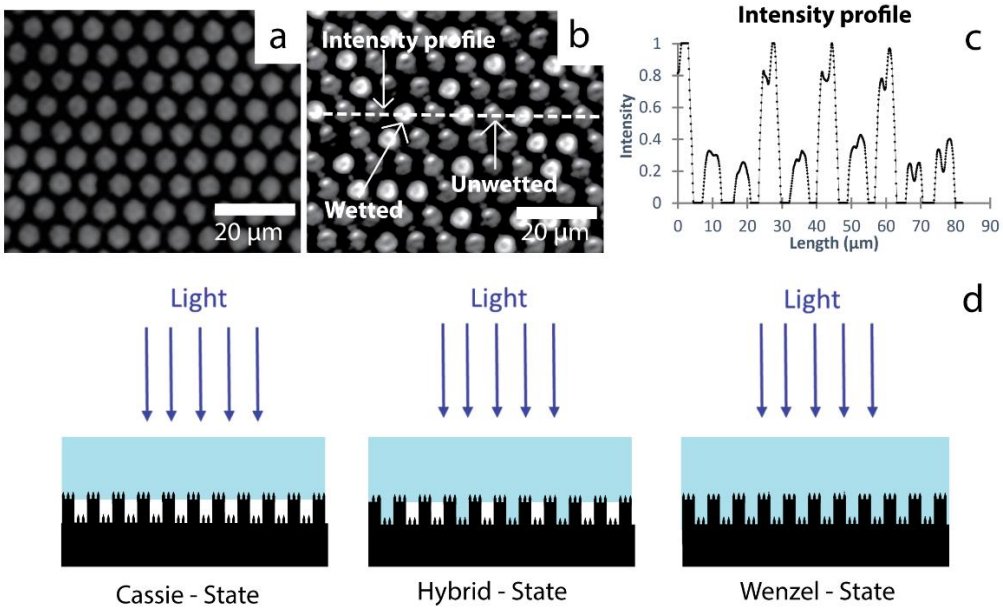

Figure 8.4. Initial result from test experiment wetting state on a microstructure surface could be seen in an optical microscope, a) Sample submerged in water inside the pressure cell, b) Micro cavity filling occurred when pressure was applied, c) Intensity profile from b) showing a clear difference in intensity, d) The different wetting states.

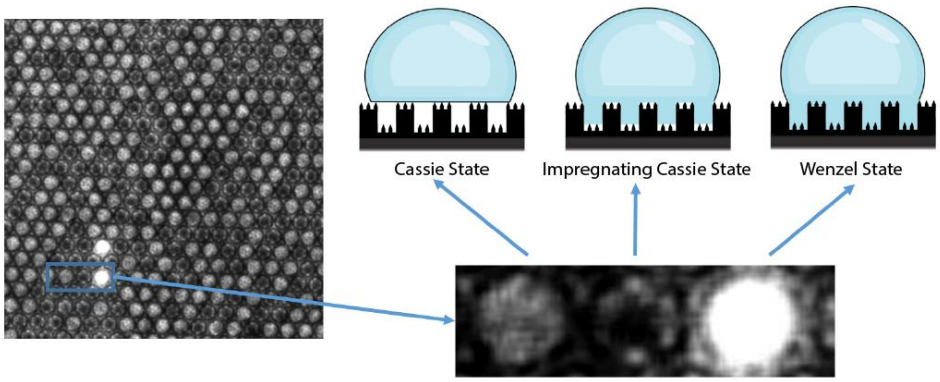

Figure 8.5. The Cassie-impregnating State was observed after optimal microscope adjustment.

8.2 Validation of the microscope observation

Prior to performing the experiments in the paper as a series of initial validations were performed to ensure accurate data. The validation consisted of 1) a confocal experiment where intensity was compared for the Cassie and Wenzel State 2) an optical transmission calculation to model the three wetting states and corresponding intensities observed in the optical microscope. To validate the observation in the optical microscope a TOPAS sample with holes were characterized with a confocal microscope (Zeiss model LSM 5). A coverslip with a drop of rhodamine solution was placed on the sample with doubled sided tape so a cavity of approximately 10 mm × 10 mm was formed. Pressure from mounting the coverslip caused some micro cavities to transit into the Wenzel State. A reflectance image was acquired together with a fluoresce image (Figure 8.6). Air bubbles can be seen in the reflectance images showing the Cassie State. As expected an inverted image was observed for the fluorescence image, here micro cavities in the Wenzel State are bright, because the filled holes has a larger amount of fluorescent dye. The confocal images support that the intensity difference observed in the optical microscope is the Cassie and Wenzel State.

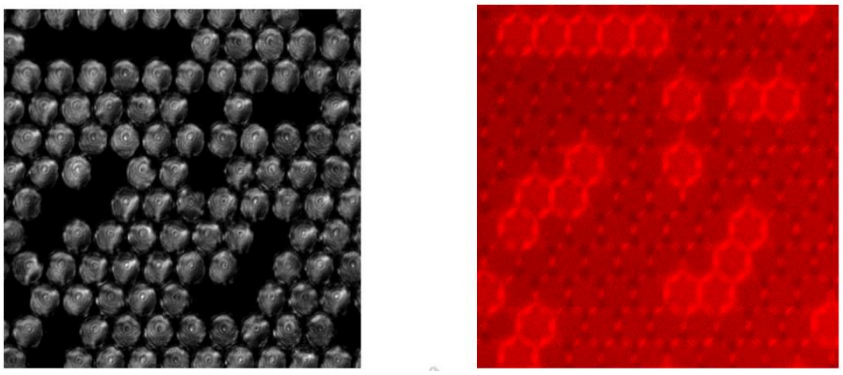

Figure 8.6. Confocal validation experiment. a) Reflection image dark areas are in Wenzel State, b) Corresponding fluorescence image bright red micro cavities are in Wenzel State. Note, how the two images are inverted.

8.3 Theory of the optical setup

The basic theory needed to understand the optical effects observed in the experimental setup is presented in this section. The three different wetting states (Cassie, Cassie-impregnating and Wenzel) will influence the transmittance and reflectivity of light. The interface and an intensity difference can be observed in the optical microscope when there is a transition between the wetting states. A MATLAB script was used to calculate the transmission for the different stages.

Light will be reflected at the interface between two materials with different refraction index. The reflection and transmittance coefficients for the interface can be determined by the Fresnel equation, which for normal incidences is given by,

$$R = \left(\frac{n_1 - n_2}{n_1 + n_2}\right)^2 \qquad 8.1$$

Here R is the reflectivity n1 and n2 refraction index of the two materials.

Studies in literature shows that nanograss-like structures will have antireflective properties[31,74]. Because of that, nanograss will influence the transmission through the pressure cell and therefore the transmission coefficient is increased. The anti-reflective effect can be described by effective medium theory; here, the conical shape of the nanograss eliminates the abrupt change in refraction index at the interface between the two materials. This causes a larger amount of light to be transmitted through the polymer part. Effective medium theory eliminates the need for calculating transmittance of individual nanograss structures and replace them with a layer composing of a gradual refraction index. In order for the effective medium theory to be valid, the characteristic length scale of the nanograss needs to be smaller than the diffraction limit, otherwise scattering and diffraction will have an effect, which will cause the effective medium theory to be invalid[103]. Only 0^{th} order propagation is allowed. As long as the light cannot resolve the individual nanograss structures, the light will not "sense" any sudden change in refraction index, but only a layer with graduated change.

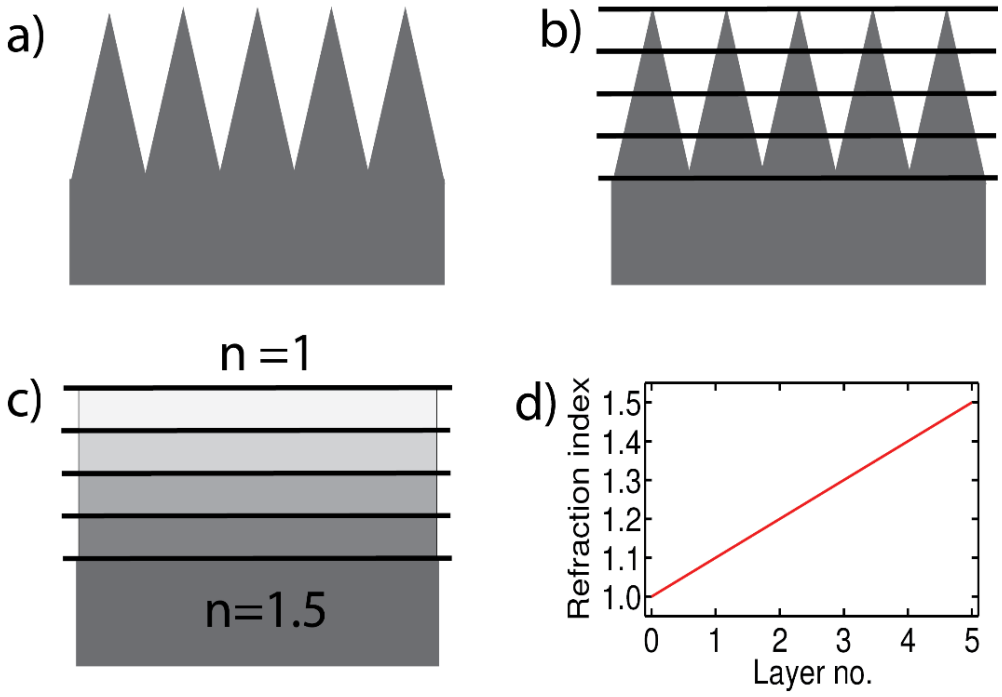

Figure 8.7. Example of effective medium theory, a) Nanograss structures smaller than the diffraction limit, b) Nanograss divided into layers, c) Refraction index calculated as a volume fraction for each layer, d) The effective refraction index as a function of layer number, showing the graduated change in refraction index.

By applying Maxwell equations the total transmission of the pressure cell can be calculated. The electromagnetic wave equations are used to describe electric fields.

$$\nabla^2 E(r,t) = \frac{\varepsilon}{c^2}\frac{\partial^2}{\partial t^2}E(r,t) \qquad 8.2$$

$$\nabla^2 H(r,t) = \frac{\varepsilon}{c^2}\frac{\partial^2}{\partial t^2}H(r,t) \qquad 8.3$$

Where *E* is the electric field, *H* the auxiliary field, *c* the speed of light and *ε* the permittivity of the material. The operations performed by the MATLAB script are presented in the short list below. Followed by a more detailed description of each step:

1. Calculations of Fresnel coefficients for each interface.
    a. (+) from surface to bulk.
    b. (-) Internal reflection from bulk to surface.
2. Calculation of incident and reflected electric fields moving from bulk to surface at each interface using the above Fresnel Coefficients and the phase to account for interference effects.
3. Finally, the reflection and transmission for the entire surface can be calculated from the electric fields at the top interface.

1) The script first calculates the Fresnel Coefficients for each interface for both polarization types: Fresnel Coefficients for parallel polarization *p* are given by equations 8.4) and 8.5) and polarization perpendicular to the plane *s* by equation 8.6) and 8.7). In the general the four Fresnel Coefficients *f* are given by:

$$f_{R,p} \equiv \frac{\tilde{E}_{0,R}}{\tilde{E}_{0,I}} = \left(\frac{n_1 \cos(\theta_T) - n_2 \cos(\theta_I)}{n_1 \cos(\theta_{T)} + n_2 \cos(\theta_I)}\right) \qquad 8.4$$

$$f_{T,p} \equiv \frac{\tilde{E}_{0,T}}{\tilde{E}_{0,I}} = \left(\frac{2n_1 \cos(\theta_I)}{n_1 \cos(\theta_{T)} + n_2 \cos(\theta_I)}\right) \qquad 8.5$$

$$f_{R,s} \equiv \frac{\tilde{E}_{0,R}}{\tilde{E}_{0,I}} = \left(\frac{n_1 \cos(\theta_I) - n_2 \cos(\theta_T)}{n_1 \cos(\theta_{I)} + n_2 \cos(\theta_T)}\right) \qquad 8.6$$

$$f_{T,s} \equiv \frac{\tilde{E}_{0,R}}{\tilde{E}_{0,T}} = \left(\frac{2n_1 \cos(\theta_I)}{n_1 \cos(\theta_I) + n_2 \cos(\theta_I)}\right) \qquad 8.7$$

Where ϑ is the angle (in this case $\vartheta = 0$), the subscript *T*, *R* and *I* marks transmitted, reflected, and incident respectively.

Since internal reflection occurs between the layers two sets of Fresnel Coefficients are needed; one set going from surface to the bulk (+) and one set from the bulk to surface (-). The difference between (+) and (-) is simply a switch of the refraction index for each interface when calculating the Fresnel Coefficients, due to the opposite direction of the internal reflected electric field.

2) The next step of the MATLAB script is calculation of the incident and reflected electric fields. The script compensates for interference between layers by applying the phase φ given by

$$\tilde{\varphi} = \frac{2\pi}{\lambda}\, n_{j-1}\, (\Delta z)_{j-1} \cos(\theta_{T,j}) \qquad 8.8$$

Here λ is the wavelength, Δz layer thickness, and j the layer number. Note that the phase is different of the one presented in[103] and instead the phase given in Born M. & Wolf (1999) is used[104].

3) Once all the electric fields are calculated, the transmittance *T* and reflection *R* of the entire sample can be determined from the top layer with equation 8.9 and 8.10. Because the light in the microscope is unpolarized, *s* and *p* polarization are weighted equally.

$$R \equiv \frac{I_R}{I_I} = \left(\frac{\left\|\tilde{E}_{0,R}\right\|}{\left\|\tilde{E}_{0,I}\right\|}\right)^2 \qquad 8.9$$

$$T \equiv \frac{I_T}{I_I} = \left(\frac{n_{2}\,\cos(\theta_T)}{n_{1}\,\cos(\theta_{I})}\right)\left(\frac{\left\|\tilde{E}_{0,T}\right\|}{\left\|\tilde{E}_{0,I}\right\|}\right)^2 \qquad 8.10$$

Overall, the method is widely used in optics and further details can be found in the original paper Stephens, R. B. & Cody, G. D. *Optical Reflectance and transmission of a textured surface* (1977)[103].

8.4 The modelling of optical setup

In order to validate the optical part of the pressure cell, the transmission of the different wetting states were calculated. Transmission coefficients for the Cassie State, Cassie-impregnating State and Wenzel State were calculated. The measured superhydrophobic surface consisted of a hexagonal array with micrometer-sized holes. In order to simplify the calculations for the optical transmission coefficient of the pressure cell, a number of assumptions are required: 1) The diffraction and scattering of the micrometer-sized holes are ignored. 2) A single

hole is modeled and potential cross talk between holes is ignored. 3) Normal incidence of light is assumed. 4) No dispersion in TOPAS is present, since the material has excellent optical properties in the visible wavelength range. 5) The single hole is modeled as layers consisting of water, air, nanograss and bulk. Here, the transmission coefficient can be calculated for the water, air, and bulk layers, however, the nanograss layer need to be simplified, since the individual structures of the nanograss is difficult to model. The nanograss layer can be described by effective medium theory.

The region with graduated refraction index can be described by a series of layers each with a small change in refraction index, due to the non-linearity of the Fresnel equation the overall transmission will be higher compared to a planar surface. The total transmission of the system can be calculated by summing the transmission and reflectance of each layer.

A script in MATLAB was written to simulate the three wetting states of the holes. The overall model was based on Maxwell equations and the method described in Stephens, R. B. & Cody, G. D. *Optical Reflectance and transmission of a textured surface* (1977)[103].

1. 500 µm layer water (thickness of pressure cell).
2. 3 µm layer with air in the Cassie State and water in the Cassie-impregnating State and Wenzel State.
3. The nanograss layer is divided into sub layers each 1 nm thick, with graduated change in refraction index, the refraction index for air and TOPAS is used for Cassie and Cassie-impregnating States. For the Wenzel State a refraction index for water and TOPAS is used. The refraction of each layer is determined by effective medium theory. The transmission of all the sub layers are summed and used to calculate the overall transmission for the nanograss layer.
4. 2000 µm layer of polymer (TOPAS).

The graduated nanograss layer is approximated by a volume fraction of polymer and water or air interface. The nanograss was assumed to be a circular conelike structure, the half angles of the cones were approximated from SEM images to a mean angle of 25° ±6°. The model was configured so it calculated the transmission spectrum for each wetting state. In order to improve accuracy of the model, the microscope lamp and camera must be taken into account; a spectrum of the lamp was obtained and used to correct the calculated data from the model. The calculated data were multiplied with a normalized emission of spectrum of microscope lamp as shown in Figure 8.8. The greyscale CCD in the camera has a nonlinear wavelength sensitivity, and Zeiss provided a correction data[105]. The data were normalized and multiplied with illumination corrected spectrum. After the correction, the mean intensity was calculated for each wetting state. The mean intensities should now correspond to the intensities measured with the microscope camera.

Where the meniscus intruded gradually into the micro cavities a transmission calculation was made. A series of 60 corrected transmission spectrums similar to the ones in Figure 8.8 were calculated for different meniscus heights. The mean intensity of the spectrums where calculated and plotted as function of meniscus penetration in Figure 8.9a (microstructures) and Figure 8.9b (nanograss). The calculated transmissions assume a flat-water air interface (meniscus). To compensate for the hemispherical shape of the meniscus the real system the intrusion depth was smoothed by averaging over intervals of 400 nm, corresponding to the order of magnitude of the meniscus protrusion for 7.5 µm micro cavity (Figure 8.9c).

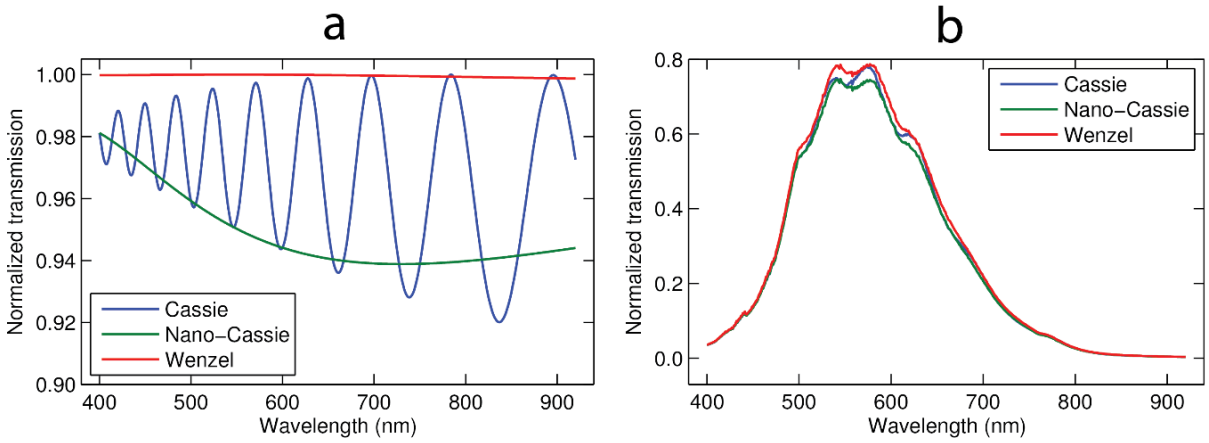

Figure 8.8. Spectra from the model, a) Raw spectra, note, the stong interference effect for the Cassie State, b) Spectra after illumation and camera sensitivity correction.

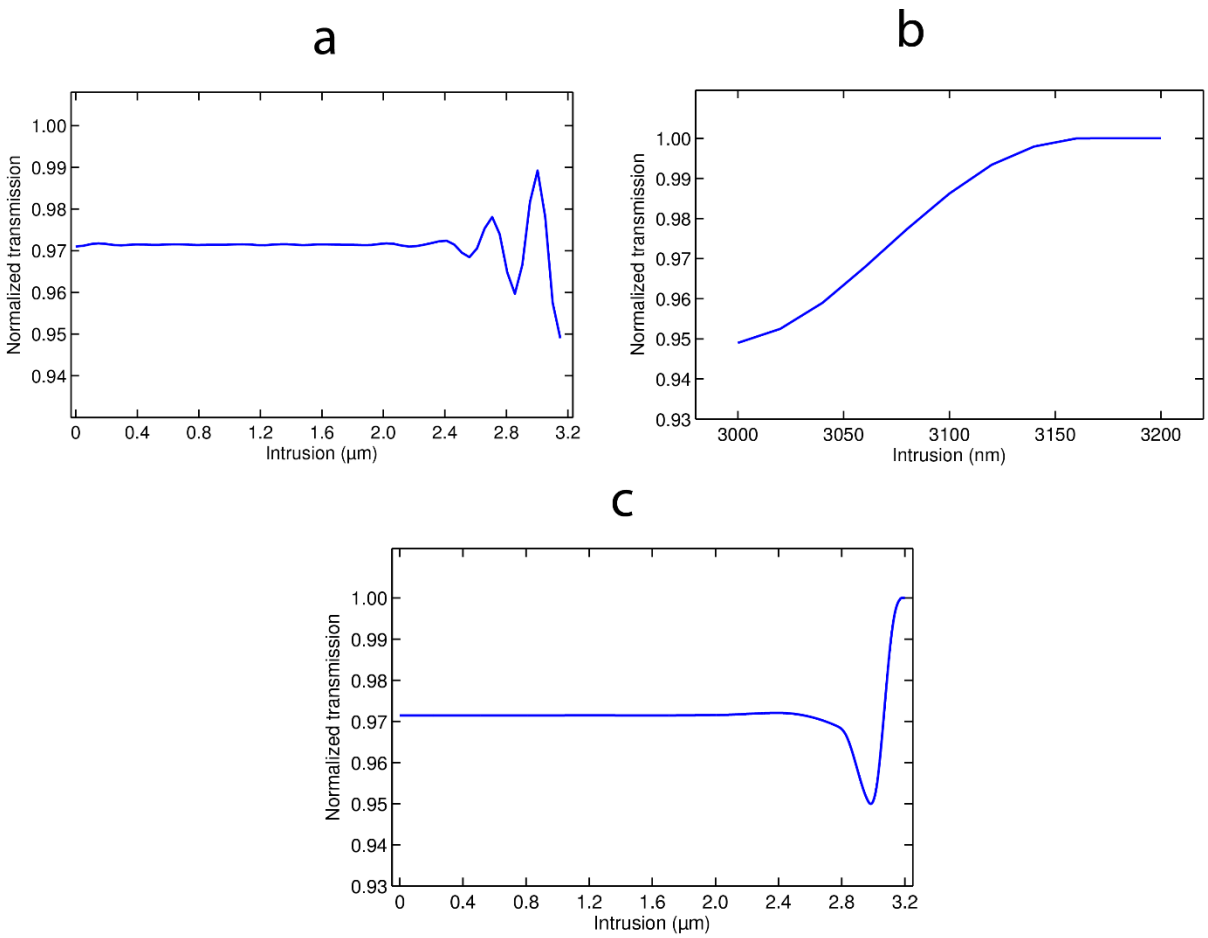

Figure 8.9. Calculated mean transmission as function of filling, a) Filling of the micro cavities, note the interference, b) Filling of the nanograss, c) Combined plot a) and b) with smoothing to account for the meniscus shape.

8.4.1 Transmission changes during structure filling

The model shows an almost constant transmission for the Cassie State while the meniscus moves down a micro cavity. At 80% filling interference effects will change the transmission. A peak value of 0.99 at 95% filling was observed. The microscope measurements were performed with 12-bit camera with the intensity resolution to measure intensity changes of 0.0002. The calculated difference 0.01 is therefore well within the camera sensitivity and can easily be distinguished.

The model shows that when the meniscus moves closer to the nanostructures destructive interference effects will reduce the transmission to 0.95 (impregnating Cassie State). The transmission for the Cassie-impregnating State is at an overall minimum. As the antireflective nanograss was filled, the transmission gradually increases and at 40% nanograss filling the transmission was equal to the transmission of the Cassie State. The filling only has to increase

10% or 20 nm before the transmissions become clearly different. When observed in the microscope switching between transmissions are fast (<5 seconds) and appear in one-step, both from Cassie State to Cassie-impregnating State and from Cassie-impregnating State to Wenzel State.

A raw microscope image was used to determine the different transmissions of each wetting state in the pressure cell. Three intensity profiles with length of 6.7 µm were measured over the center of three different micro cavities, each in a different wetting state. The mean intensity of each profile was calculated and normalized to the Wenzel State. Difference between model and experiment is shown in Figure 8.10. The experimental data has a lower transmission than the model, this is expected since scattering and absorption will occur.

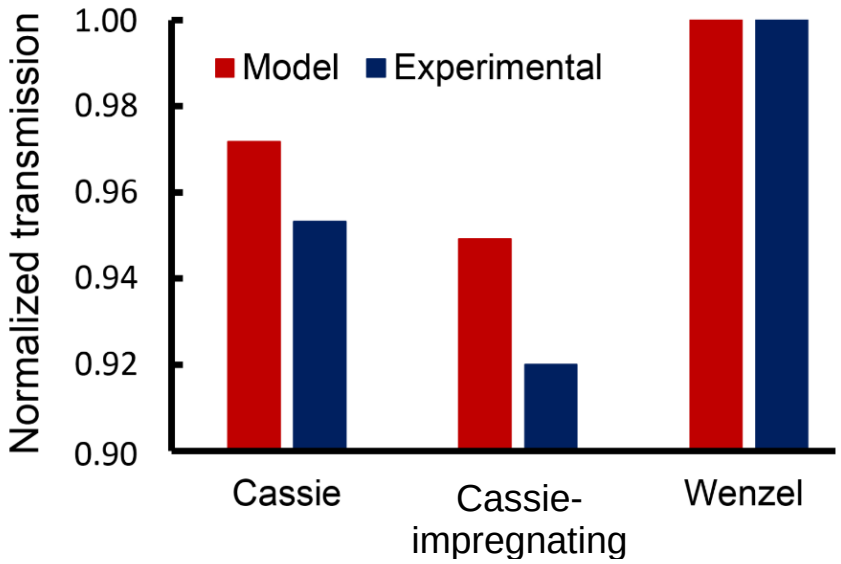

Figure 8.10. Experimental transmission compared to the model.

9 Summary of fabricated structures

An overview of the hydrophobic properties for the different structures is presented in Table 9.1. Here, five different wetting criteria are listed. 1) The used polymer type, 2) Does the surface pin drops? 3) Is the surface superhydrophobic? 2) Does the surface have a stable Cassie State when submerged in water? (This is required for drop roll-off), 5) Is the effect of polymer degradation observed when the sample is submerged in water within 1½ hour?

Structure type	**Material**	**Drop pinning**	**Superhydrophobicity**	**Stable Cassie when submerged**	**Observed effect of polymer degradation**
Pillars (Smooth)	PP	X			X
Pillars (nanograss)	PP				X
Pillars (nanograss)	Topas	X			X
Holes (smooth)	PP	(X)		X	X
Holes (nanograss)	PP		(X)	X	X
Holes (nanograss)	TOPAS			X	X
Pyramids (smooth)	PP	X			X
spruce like micropillars	Topas/PP		X		(none)
Pyramids (nanograss)	PP	X			X
Pyramid holes PP (smooth)	PP	X		X	X
Pyramids holes PP (nanograss)	PP			X	X

Table 9.1. Summary of the different structures and their properties. X indicate positive effect, X indicate negative effect, regarding water repellency.

10 Discussion

In this section the wetting results (contact angle measurements) of the fabricated structures are discussed. The discussion of structures that were superhydrophobic is given main priority together with the effects of static electricity and degradation of the polymer. Discussion of fabrication of structures is already presented in Chapter 5.7, page 185. Discussion of the pressure cell is presented in the paper in Appendix 3.

Static electricity has a profound effect on the superhydrophobic properties on the injection molded polymer parts. With static electricity present, all samples with nanograss showed superhydrophobic properties. After removal of the static electricity, only the PP holes with nanograss and sprucelike micropillars remained superhydrophobic. It is reported that electric charge can cause variations of the measured contact angles[15]. However, this study shows that a structured polymer surface will have a dramatic reduction in hydrophobicity, and drops are likely to be pinned when static electricity is removed. The effect of static electricity is not reported for other injection molded super hydrophobic surfaces [58,59,66–68].

In this study, only the sprucelike micropillars and PP holes with nanograss and a diameter of 7.5 µm and 15.5 µm showed superhydrophobic properties. The hysteresis of the holes was 12°, which is 2° above the superhydrophobic criteria. Roll-off angles were measured to 7° making the surface water repellant and practically superhydrophobic.

Overall, the fabricated surfaces can be divided into three categories, superhydrophobic, hydrophobic with drop roll-off, and hydrophobic with drop pinning. The different structures are grouped below,

- **Hydrophobic with drop pinning**
  - Pillars PP (smooth)
  - Holes TOPAS (nanograss)
  - Pyramids PP
  - Pyramids PP (nanograss)
  - Pyramid holes PP
  - Holes PP, 3.0 µm and 7.0 µm

- **Hydrophobic with drop roll-off**
  - Pillars PP (nanograss)
  - Holes PP, 15.0 µm
  - Holes PP (nanograss), 3.5 µm
  - Pyramid holes PP

- **Superhydrophobic**
  - Spruce like micropillars both PP and TOPAS
  - Holes PP (nanograss), 7.5 µm and 15.5 µm

During this work, the addition of nanograss to the microstructures has shown two effects that will influence the wetting properties of the samples, 1) The change in dimension of approximately 0.5 µm of the fabricated structures; the decrease in structure size reduced the surface liquid contact area in the Cassie State and increased the contact angle as described by equation 2.7. 2) The nanograss increased the roughness on the surface and thereby the overall contact angle. It is difficult to determine if the liquid in contact with nanograss is in the Wenzel or Cassie State. Most likely the liquid is in a transition state where the top of the nanograss is wetted and air pockets are trapped in cavities below. The likeliness of this transition state makes determination of the surface liquid contact area difficult. Therefore, theoretical values cannot be accurately calculated with Wenzel and Cassie Baxter equation. Nanograss showed an improvement of water repellency compared with the smooth structures.

All smooth structures shows drop pinning except the 15.0 µm PP holes. It is difficult to characterize the effect of nanograss when the drops are pinned. Measurement of the nanograss effect with static contact angles on pinned drops provide little information, since the static contact angle is dependent on how the drops are deposited on the surface, dynamic properties are needed for accurate characterization[15]. However, drop roll-off on the 15.0 µm holes at 45° ±3° with a hysteresis of 48° ±6° was observed. On similar holes with hierarchical nanograss drops roll-off at 7° ±1° with a hysteresis of 12° ±2°. This corresponds to an improvement of drop roll-off angle of 38° and an improvement on the hysteresis of 36°.

Other injection molded superhydrophobic surfaces made from PP, can show an improvement of approximately 30° for both hysteresis and drop roll-off angle when hierarchical structures are introduced. Hysteresis and drop roll-off angles of 2° and 1° are reported[67]. Studies in the literature show improvement for both hysteresis and drop roll-off of water repellency for hierarchical structures which were fabricated with other methods than injection molding and from wax materials[106]. Hysteresis and roll-off angles are improved by approximately 30° for both hysteresis and drop roll-off [106].

It is reported that hierarchical structures are required for obtaining superhydrophobic surfaces from non-fluorine based polymers[59,66–68]. Except in Michaeli *et al*. (2011)[58] were the injection molding structures have been stretched to high aspect ratios[58]. However, the structures presented here, are all based on open pillar designs. Based on the results obtained during this work the Cassie State of open structures made from polymer will collapse to a hybrid or Wenzel State immediately. Therefore, it is likely that the presented structures would not have a stable Cassie State when submerged into water[58,59,66–68]. Furthermore, the effect of polymer degradation is not reported for any of their presented surfaces[58,59,66–68].

In this work both pyramids and pyramid holes showed significant defects in the injection molding fabrication process. The defects were shown as scratch marks on the pyramid holes and stretching of the pyramid tip. These defects made it difficult to determine the exact reason

for drop pinning. The addition of nanograss caused the pyramid holes to have a high static contact angle 164° ±1° with a hysteresis of 35° ±5° and drop roll-off angle of 18° ±3°. The static contact angle fulfills the superhydrophobic criteria of 150°[13]. However, the hysteresis of 35° ±5° and drop roll-off angle of 18° ±3° is not in the superhydrophobic range. The poor wetting performance can be explained by the meniscus moving down the sloped sidewall (slope angle 54.7°). This will increase surface liquid adhesion and cause drops to pin. In general, the pyramids and pyramid holes showed poor wetting performance and there were difficulties in the fabrications process.

Practically identical structures made from different materials were here used to study the effect of surface chemistry. Contact angles of different samples made from TOPAS 8007-S04 and PP HD601CF were compared. Pillars with nanograss, holes with nanograss, and sprucelike micropillars were injection molded in both PP and TOPAS. Common to all structure types, surfaces made from PP have higher static contact angles than those made from TOPAS. This can be explained by the higher intrinsic contact angle of PP HD601CF (102°) compared to the intrinsic contact angle of TOPAS 8007-S04 (95°). The difference in hydrophobicity of the polymers caused different dynamic properties. Drops on TOPAS holes and pillars were pinned to the surface; even when the sample was tilted 180°, while the PP samples had relatively low roll-off angles (below 20°).

It could be interesting to injection mold samples made from the polymer fluorinated ethylene propylene (FEP). The fluorine groups in the polymer would cause a higher intrinsic contact angle (112°)[107]. It is likely that drop pinning would be completely eliminated and that extreme superhydrophobic surfaces could be obtained. The use of fluorine-based polymers was avoided in this PhD project due to the toxicity of fluorine compounds[108]. The idea in this project was to produce superhydrophobic surfaces that were environmental friendly.

10.1 Superhydrophobic structures

The two different superhydrophobic structure types (PP holes with nanograss and sprucelike micropillars show different superhydrophobic effects. The sprucelike micropillars has static contact angles of approximately 170° with drop roll-off and hysteresis of approximately 5°. The contact angle, hysteresis and roll-off angles show that structures are above the superhydrophobic criteria (contact angle above 150° and contact angle hysteresis below 10°). The static contact angle is only 10° from the maximum achievable contact angle of 180°. These results demonstrate that the produced polymer parts with sprucelike micropillars have excellent superhydrophobic properties. Native PP polymer is only moderate hydrophobic with a contact angle of 102°. The increase in contact angle caused by the sprucelike micropillars is therefore approximately 70°, which is quite extraordinary. Often, highly superhydrophobic structures are made with more hydrophobic base-materials, e.g. fluorine based[37,43].

In general, the sprucelike micropillars have higher static contact angles and lower roll-off angles than the structures composed of holes with nanograss (contact angle of approximately 163°, hysteresis 12°, and roll-off angles 7°). The difference in the wetting properties can be explained by the difference in structure design, which was designed with different surface coverages. Disregarding the roughness originating from the nanograss, the different surface coverages were estimated from SEM images to approximately 4% for the sprucelike micropillars and 14% for 3.5 µm holes, 12% for the 7.5 µm holes, and 10% for the 15.5 µm holes. The larger surface coverage of the 3.5 µm holes increase adhesion between water and surface, which explains why the 3.5 µm holes is not superhydrophobic. The difference in surface coverage also explains why the static contact angles of surfaces with sprucelike micropillars were higher than surfaces with holes. Although sprucelike micropillars exhibited higher static contact angles and lower hysteresis than polymer hierarchical holes, their superhydrophobicity was rather unstable. The hierarchical pillars are interconnected by open channels. When one pillar turns into Wenzel State, other pillars will turn to Wenzel State, due to the inter-connected open space between the pillars whereas holes with nanograss do not contain open space. Even when the wetting state of one hole changes to Wenzel State, the rest of the holes could remain superhydrophobic, which results in co-existence of the Cassie and Wenzel State. The closed structures caused liquid to be maintained in the Cassie State when the samples were submerged in water.

Closed structures consisting of narrow lines (approximately 400 nm) similar to the ones presented in the paper in Appendix 4, may produce surfaces with excellent superhydrophobic surfaces with a stable Cassie State and potentially better resistance to polymer degradation. However, narrow line structures could be difficult to fill during the injection molding process and the narrow lines are likely to be damaged in the demolding.

Here, the results from this work are compared with other mass production methods for fabrication of superhydrophobic polymer surfaces. Contact angles from pure polypropylene webs fabricated by electro-spinning are reported to have a contact angle at approximately 150°[42]. The study does not include dynamic characterization of wetting properties such as hysteresis and drop roll-off angles[42]. Therefore, it is unclear if the presented electro-spun webs are superhydrophobic. Superhydrophobic electro-spun webs made from other non- fluorinated polymers than PP show superhydrophobic properties[37]. The webs are reported to have contact angles above 150° and drop roll-off angles below 10° and contact angles up to 170° with roll-off angles below 5° are reported[37].

Injection molded superhydrophobic surfaces produced in this work, show similar wetting properties compared to the best electro-spun fibers and with the leaves of Lotus plant which have contact angle of 160° with roll-off angle less than 5°[14].

10.2 Polymer degradation

Several factors can influence the decrease in hydrophobicity of the polymer when exposed to water; for instance migration of hydrophilic additives, water absorption, and oxidation of the polymer. Polar or hydrophilic additives can be present on the surface[70,73]. Hydrophilic or polar additives may migrate faster to the surface when the polymer is exposed to water. Therefore, the chemical properties of the additives rather than the polymer will dominate the hydrophobic properties of the surface.

The lack of information from the polymer producing companies causes some issues, because they only provide information on which additives they do not add in a polymer grade. As an example, the company Borealis only provide the following information on HD601CF; it is a homopolymer designed for metalizable cast film, and it does not contain slip, antiblock, and calcium stearate[88]. Therefore, one cannot exclude the presence of unknown additives in the polymer.

Additives can, in general, change many parameters in polymers and they can enhance certain properties[81]. One of the possibilities to overcome degradation of the polymer could be to design a certain composition of additives for producing a polymer grade, optimized for hydrophobicity. Such a polymer grade could have little or no reduction in contact angle when the polymer is exposed to water. This needs some collaboration with the polymer producers.

Absorption of water into the polymer could be a possible explanation for the loss of hydrophobicity. It is commonly known that polymers absorb water and need to be dried before processing[81]. If water is trapped in the polymer surface the hydrophobicity of the sample will be reduced, and this could be the explanation for the observed drop pinning. Presence of water on the surface is unlikely because the polymer parts were dried for two hours at 100 °C either in a polymer drier on the injection molding machine or on a hotplate, e.g. decrease in contact angle is observed even for parts which were exposed to water for 10 min.

Oxidation of the polymer can occur. The oxidation process will form polar groups on the surface. Polymer oxidation is well known to have a degradation effect on polymers[109,110]. The oxidation process is reported to be slightly faster in humid conditions[111]. The reason for the decrease in hydrophobicity could also be a combination of the mentioned effects additive migration, water absorption, and/or oxidation. The Danish book “Plast Teknologi” states on page 70 that polypropylene is easily oxidized and all commercial grades contain antioxidants[81]. Even if antioxidants are present, oxidation cannot be totally stopped[109]. Therefore, it is likely that a combination of oxidation and additives is responsible for the reduction in contact angle shown in Figure 7.6 when the polymer is exposed to water for prolonged periods.

11 Conclusion

This study concerned the development of superhydrophobic surfaces fabricated by injection molding. It was shown that superhydrophobic polymer surfaces can be fabricated by an industrial injection molding method.

First, using Deep UV Lithography combined with black silicon etching and electroplating for mold fabrication, large mold areas with well-defined topographies including nanoscale features were produced. The topographies were used to develop an injection molded process resulting in excellent replication quality with a typical tolerance less than 6% in all dimensions between polymer part and nickel shim. Materials included the amorphous polymer TOPAS 8007-S04 (COC) and the semi crystalline polymer PP HD601CF. An overview of wetting properties of different structure types and their wetting properties are shown in Table 9.1. Polymer surfaces made from PP exhibited a higher degree of hydrophobicity and water repellency compared with those from TOPAS.

The effect of the hierarchical nanograss shows an improvement of hydrophobicity in both drop roll-off and hysteresis of approximately 30° compared to pure microstructures. Contact angle properties of two structured polymer surfaces with moderate hydrophobicity (TOPAS and PP) were measured and a difference in water repellency observed. The difference in water repellency most likely originated from the difference in the wetting of nanostructures (nanograss). For smaller contact angle materials like TOPAS, water droplets pinned on the nanograss on top of the surface. The pinning of the nanograss on top of the structures was not strong enough on PP surfaces with similar structure types and instead a drop roll-off was observed. This study indicates that both nano- and microstructures are important to the wetting properties of superhydrophobic surfaces.

Two types of injection molded structures showed superhydrophobicity; sprucelike micropillars (PP and TOPAS) and holes with hierarchical nanograss (PP). The sprucelike micropillars showed excellent superhydrophobic properties with contact angles up to 173° ± 2° and roll-off angles below 2°. PP surfaces with sprucelike micropillars exhibited the strongest superhydrophobicity while the surface with holes covered with nanograss exhibited the weakest. In addition, the TOPAS surfaces with holes and nanograss showed strong drop adhesion. Although the surfaces with sprucelike micropillars showed stronger super hydrophobicity than holes with nanograss, these surfaces could not retain a stable Cassie State when immersed in water. Surfaces with holes were found to be more stable and remained in the Cassie State at moderate water pressures. After increasing the liquid pressure, transitions between the wetting states (Cassie, Cassie-impregnating, and Wenzel) were observed. For applied pressure below 300 mbar for 7.5 µm cavities, only a few transitions from the Cassie State to the Wenzel State occurred, and the transition between Cassie State to Cassie-impregnating State was reversible. For pressures larger than 300 mbar irreversible transitions from the Cassie-impregnating to the Wenzel State occurred.

Thus, it was concluded that to fabricate a superhydrophobic surface with stability against water pressure, it is necessary to isolate the microstructures and reduce the surface coverage. These findings indicate that rather deep cavity structures will perform better over shallow cavities because of the larger entrapped air pockets.

It was found that two effects reduced water repellency; removal of static electricity and changes of surface chemistry over time. Water exposure of the polymer caused a decrease in hydrophobicity. It was therefore concluded that the material properties of the polymer was critical for maintaining superhydrophobicity under water exposure and after drying.

Altogether it can be concluded from this PhD project that;

- It is possible to fabricate superhydrophobic polymer surfaces by an industrial injection molding method.
- the effect of the hierarchical nanograss shows an improvement of hydrophobicity in both drop roll-off and hysteresis of approximately 30°.
- sprucelike micropillars show excellent superhydrophobic properties.
- enclosed structures such as holes has a stable Cassie State and can form plastrons when submerged in water.
- static electricity has a major influence on drop roll-off and need to be removed to examine the native properties of the surfaces.
- polymer degradation is a major issue that needs to be solved before injection molding of self-cleaning surfaces can be commercialized.

12 Outlook

There are different routes for continued research based on the work presented in this thesis. Polymer degradation is a major issue that needs to be studied further. Most of the structures developed in this work have a reduced hydrophobicity when immersed in water. The effect of oxidation, water absorption and additives need to be characterized and the cause for the polymer degradation determined. Additives present in the bulk of the polymer have little effect on hydrophobicity, while additives in the surface can cause loss of hydrophobicity. Spectroscopy methods such as X-ray photoelectron spectroscopy or infra-red spectroscopy can be used to determine different types and locations on chemical compounds in the polymer. Two possible approaches to study the polymer degradation are listed here,

1. A study on a range of existing commercial polymers' types and grades to determine the polymers with high intrinsic contact angles and with low loss of hydrophobicity. For example, contact angle measurement can be performed for different submersion times combined with spectroscopy to characterize the change in surface chemistry.
2. Development of a new type of polymer specifically designed for injection molded superhydrophobic surfaces. Such a polymer should be developed in collaboration with polymer producers and polymer chemists. The new polymer must have a large intrinsic contact angle and no or little loss of hydrophobicity when exposed to water. As an alternative, an additive can be developed to reduce or eliminate the loss of hydrophobicity in a standard commercial polymer.

Polymer degradation and loss of hydrophobicity are not the only issues. If injection molding of superhydrophobic surfaces are to be implemented into commercial products, then the cycle time of the injection molding process must be reduced. This can be done by applying vacuum or by rapid heating and cooling of the mold, or perhaps use injection compression molding, which is used by Blue Ray and DVD industry. Furthermore, many applications require free form surfaces, which have to be produced in more durable free form steel molds.

Many issues remain before it is possible to produce superhydrophobic parts on a larger commercial scale.

13 Bibliography

1. Matschuk, M., Bruus, H. & Larsen, N. B. Nanostructures for all-polymer microfluidic systems. *Microelectron. Eng.* **87,** 1379–1382 (2010).

2. Nielsen, T. K. *et al.* Injection molding tools with micro/nano-meter pattern.

3. Jensen, L. G. Ingenøren: Nanomønstre kan give plastic den rette farve. *12-08-2014* (2010). at <http://ing.dk/infografik/nanomonstre-kan-give-plastic-den-rette-farve-111180>

4. Dilling, S. Politiken: Minister vil forbyde fluor-stoffer i mademballage. *18-09-2014* (2014). at <http://politiken.dk/forbrugogliv/forbrug/forbrugersikkerhed/ECE2399813/minister-vil-forbyde-fluor-stoffer-i-mademballage/>

5. Nikon. Fluorinecoat. *12-08-2014* (2014). at <http://imaging.nikon.com/lineup/lens/fluorinecoat/>

6. MAGPUL. MAGPUL AR grip. *12-08-2014* at <http://store.magpul.com/product/MAG440/184>

7. Magin, C. M., Cooper, S. P. & Brennan, A. B. Non-toxic antifouling strategies. *Mater. Today* **13,** 36–44 (2010).

8. Harsonic. harsonic. *14-8-2014* at <http://www.harsonic.net/wp-content/uploads/2013/06/yard-431.jpg>

9. LANI. Nanostructuring Initiative (LANI). *12-08-2014* at <http://hoejteknologifonden.dk/en/project_gallery/project_gallery/large_area_nanostructuring_initiative_lani/>

10. UNIFOIL. UNIFOIL Custom-Finishes. *12-08-2014* at <http://www.unifoil.com/index.php/products/custom-finishes/>

11. Packworld. Unifoil introduces metallized and holographic effects for in-mold labels anditle. *10-11-2014* (2009). at <http://www.packworld.com/sustainability/strategy/unifoil-corp-unifoil-introduces-metallized-and-holographic-effects-mold>

12. De Gennes, P. G., Brochard-Wyart, F. & Quere, D. *Capillarity and Wetting Phenomena: Drops, Bubbles, Pearls, Waves*. (Springer, 2004).

13. Wang, S. & Jiang, L. Definition of Superhydrophobic States. *Adv. Mater.* **19,** 3423–3424 (2007).

14. Barthlott, W., Neinhuis, C., Verlot, H. & Schott, C. L. Purity of the sacred lotus , or escape from contamination in biological surfaces. 1–8 (1997).

15. Strobel, M. & Lyons, C. S. An Essay on Contact Angle Measurements. *Plasma Process. Polym.* **8,** 8–13 (2011).

16. Kietzig, A.-M. Comments on "An Essay on Contact Angle Measurements" - An Illustration of the Respective Influence of Droplet Deposition and Measurement Parameters. *Plasma Process. Polym.* **8,** 1003–1009 (2011).

17. Larsen, S. T., Andersen, N. K., Søgaard, E. & Taboryski, R. Structure irregularity impedes drop roll-off at superhydrophobic surfaces. *Langmuir* **30,** 5041–5 (2014).

18. Robert, J. & Rousseau, E. S. The sliding of liquid drops on solid surfaces. **659,** 9–12 (1962).

19. Wenzel, R. N. RESISTANCE OF SOLID SURFACES TO WETTING BY WATER. *Ind. Eng. Chem.* **28,** 988–994 (1936).

20. Cassie, B D Baxter, S. & Cassie, B. D. Werrability Of Porous Surfaces,. *Trans. Faraday Soc.* 546–551 (1944).

21. Larsen, S. T. & Taboryski, R. A Cassie-like law using triple phase boundary line fractions for faceted droplets on chemically heterogeneous surfaces. *Langmuir* **25,** 1282–4 (2009).

22. Valipour M., N., Birjandi, F. C. & Sargolzaei, J. Super-non-wettable surfaces: A review. *Colloids Surfaces A Physicochem. Eng. Asp.* **448,** 93–106 (2014).

23. Verho, T. *et al.* Reversible switching between superhydrophobic states on a hierarchically structured surface. **109,** (2012).

24. Yan, Y. Y., Gao, N. & Barthlott, W. Mimicking natural superhydrophobic surfaces and grasping the wetting process: a review on recent progress in preparing superhydrophobic surfaces. *Adv. Colloid Interface Sci.* **169,** 80–105 (2011).

25. Steden, M. Lotus leaf with water drop. *24-08-2014* at <http://www.dreamstime.com/stock-images-lotus-leaf-water-drop-image2879754>

26. Koch, K. & Barthlott, W. Superhydrophobic and superhydrophilic plant surfaces: an inspiration for biomimetic materials. *Philos. Trans. A. Math. Phys. Eng. Sci.* **367,** 1487–509 (2009).

27. Nagappan, S., Park, S. S. & Ha, C.-S. Recent Advances in Superhydrophobic Nanomaterials and Nanoscale Systems. *J. Nanosci. Nanotechnol.* **14,** 1441–1462 (2014).

28. Fürstner, R., Barthlott, W., Neinhuis, C. & Walzel, P. Wetting and self-cleaning properties of artificial superhydrophobic surfaces. *Langmuir* **21,** 956–61 (2005).

29. ASML. TWINSCAN NXE:3300B. *19-08-2014* at <http://www.asml.com/asml/show.do?lang=EN&ctx=46772&dfp_product_id=842>

30. Højlund-Nielsen, E., Greibe, T., Mortensen, N. A. & Kristensen, A. Single-spot e-beam lithography for defining large arrays of nano-holes. *Microelectron. Eng.* **121,** 104–107 (2014).

31. Sun, G., Gao, T., Zhao, X. & Zhang, H. Fabrication of micro/nano dual-scale structures by improved deep reactive ion etching. *J. Micromechanics Microengineering* **20,** 075028 (2010).

32. Kooy, N., Mohamed, K., Pin, L. T. & Guan, O. S. A review of roll-to-roll nanoimprint lithography. *Nanoscale Res. Lett.* **9,** 320 (2014).

33. Salapare, H. S. *et al.* Stability of the hydrophilic and superhydrophobic properties of oxygen plasma-treated poly(tetrafluoroethylene) surfaces. *J. Colloid Interface Sci.* **396,** 287–92 (2013).

34. Nwankire, C. E., Favaro, G., Duong, Q.-H. & Dowling, D. P. Enhancing the Mechanical Properties of Superhydrophobic Atmospheric Pressure Plasma Deposited Siloxane Coatings. *Plasma Process. Polym.* **8,** 305–315 (2011).

35. Wang, Z. K., Zheng, H. Y., Lim, C. P. & Lam, Y. C. Polymer hydrophilicity and hydrophobicity induced by femtosecond laser direct irradiation. *Appl. Phys. Lett.* **95,** 111110 (2009).

36. Park, S. *et al.* Apparatus for preparing electrospun nanofibers : designing an electrospinning process for nanofiber fabrication. **1366,** 1361–1366 (2007).

37. Sas, I., Gorga, R. E., Joines, J. a. & Thoney, K. a. Literature review on superhydrophobic self-cleaning surfaces produced by electrospinning. *J. Polym. Sci. Part B Polym. Phys.* **50,** 824–845 (2012).

38. Greiner, A. & Wendorff, J. H. Electrospinning: a fascinating method for the preparation of ultrathin fibers. *Angew. Chem. Int. Ed. Engl.* **46,** 5670–703 (2007).

39. Elmarco. NanospiderTM Production Line. *19-08-2014* at <http://www.elmarco.com/upload/soubory/dokumenty/143-1-ns-8s1600u-profile-110207-72dpi.pdf>

40. Niu, H., Lin, T. & Wang, X. Needleless Electrospinning . I . A Comparison of Cylinder and Disk Nozzles. (2009). doi:10.1002/app

41. Asmatulu, R., Ceylan, M. & Nuraje, N. Study of superhydrophobic electrospun nanocomposite fibers for energy systems. *Langmuir* **27,** 504–7 (2011).

42. Cho, D., Zhou, H., Cho, Y., Audus, D. & Joo, Y. L. Structural properties and superhydrophobicity of electrospun polypropylene fibers from solution and melt. *Polymer (Guildf).* **51,** 6005–6012 (2010).

43. Ganesh, V. A., Raut, H. K., Nair, a. S. & Ramakrishna, S. A review on self-cleaning coatings. *J. Mater. Chem.* **21,** 16304 (2011).

44. Yang, S., Jin, X., Liu, K. & Jiang, L. Nanoparticles assembly-induced special wettability for bio-inspired materials. *Particuology* **11,** 361–370 (2013).

45. TC nano. profile_brochure. *21-08-2014* at <http://nano.expositus.com/Files/Filer/brochurer/tcnano_profile_brochure.pdf>

46. Zhang, J., Sheng, X. & Jiang, L. The dewetting properties of lotus leaves. *Langmuir* **25,** 1371–6 (2009).

47. Shirtcliffe, N. J., McHale, G. & I. Newton, M. The superhydrophobicity of polymer surfaces: Recent developments. *J. Polym. Sci. Part B Polym. Phys.* **49,** 1203–1217 (2011).

48. Lei, L., Li, H., Shi, J. & Chen, Y. Diffraction patterns of a water-submerged superhydrophobic grating under pressure. *Langmuir* **26,** 3666–9 (2010).

49. Bobji, M. S., Kumar, S. V., Asthana, A. & Govardhan, R. N. Underwater sustainability of the "Cassie" state of wetting. *Langmuir* **25,** 12120–6 (2009).

50. Sakai, M., Yanagisawa, T., Nakajima, A., Kameshima, Y. & Okada, K. Effect of surface structure on the sustainability of an air layer on superhydrophobic coatings in a water-ethanol mixture. *Langmuir* **25,** 13–6 (2009).

51. Lv, P., Xue, Y., Shi, Y., Lin, H. & Duan, H. Metastable States and Wetting Transition of Submerged Superhydrophobic Structures. *Phys. Rev. Lett.* **112,** 196101 (2014).

52. Poetes, R., Holtzmann, K., Franze, K. & Steiner, U. Metastable Underwater Superhydrophobicity. *Phys. Rev. Lett.* **105,** 166104 (2010).

53. Schaller, T., Bohn, L., Mayer, J. & Schubert, K. Microstructure grooves with a width of less than 50 μm cut with ground hard metal micro end mills. *Precis. Eng.* **23,** 229–235 (1999).

54. Menges, G., Michaeli, W. & Mohren, P. How to Make Injection Molds. (2001). doi:10.3139/9783446401808

55. Benavides, G. L., Bieg, L. F., Saavedra, M. P. & Bryce, E. a. High aspect ratio meso-scale parts enabled by wire micro-EDM. *Microsyst. Technol.* **8,** 395–401 (2002).

56. Heyl, P., Olschewski, T. & Wijnaendts, R. W. Manufacturing of 3D structures for micro-tools using laser ablation. *Microelectron. Eng.* **57-58,** 775–780 (2001).

57. Jiang, T. *et al.* Ultrashort picosecond laser processing of micro-molds for fabricating plastic parts with superhydrophobic surfaces. *Appl. Phys. A* **108,** 863–869 (2012).

58. Michaeli, W., Schöngart, M., Klaiber, F. & Beckemper, S. Production of Superhydrophobic Surfaces Using a One-Step Variothermal Injection Moulding Process. 222–225 (2011).

59. Lightmotif. Nanoclean project brochure. 8 (2012). at <http://www.nanoclean-project.eu/files/Nanoclean_project_brochure.pdf>

60. Giboz, J., Copponnex, T. & Mélé, P. Microinjection molding of thermoplastic polymers: a review. *J. Micromechanics Microengineering* **17,** R96–R109 (2007).

61. NIL Technology. nickel-shims. *19-08-2014* at <http://www.nilt.com/505/nickel-shims>

62. Inmold Biosystems. Nanostructuring. *19-08-2014* at <http://www.inmoldbiosystems.com/default.asp?Site=Info&page=73&title=Nanostructuring>

63. Hoowaki. control friction and surface tension. *19-08-2014* at <http://www.hoowaki.com/applications>

64. SINGLE Temperature Controls. www.single-temp.com EcoTemp. *07-08-2014* at <http://www.single-temp.com/products/variotherm-temperature-control/ecotemp.html>

65. Hopmann, C., Behmenburg, C., Recht, U. & Zeuner, K. Injection Molding of Superhydrophobic Liquid Silicone Rubber Surfaces. *Silicon* **6,** 35–43 (2013).

66. Puukilainen, E., Rasilainen, T., Suvanto, M. & Pakkanen, T. a. Superhydrophobic polyolefin surfaces: controlled micro- and nanostructures. *Langmuir* **23,** 7263–8 (2007).

67. Huovinen, E., Hirvi, J., Suvanto, M. & Pakkanen, T. a. Micro-micro hierarchy replacing micro-nano hierarchy: a precisely controlled way to produce wear-resistant superhydrophobic polymer surfaces. *Langmuir* **28,** 14747–55 (2012).

68. Huovinen, E. *et al.* Mechanically Robust Superhydrophobic Polymer Surfaces Based on Protective Micropillars. (2014).

69. Adeka Palmarole. Adeka Palmarole Additives. *20-10-2014* at <http://www.adeka-palmarole.com/additives.html>

70. Singh, P., Saengerlaub, S., Wani, A. A. & Langowski, H.-C. Role of plastics additives for food packaging. *Pigment Resin Technol.* **41,** 368–379 (2012).

71. Onteniente, J., Abbès, B., Haïdar, L. & France, R. Fully Biodegradable Lubricated Thermoplastic Wheat Starch : Mechanical and Rheological Properties of an Injection Grade. 112–117 (2000).

72. Sigma-Aldrich. Zinc stearate. *10-11-2014* at <http://www.sigmaaldrich.com/catalog/product/aldrich/307564?lang=en&region=DK>

73. Foldes, E. & Szigeti-erdei, A. Migration of Additives in Polymers. **3,** 1–5 (1997).

74. Christiansen, A. B., Clausen, J., Asger Mortensen, N. & Kristensen, A. Minimizing scattering from antireflective surfaces replicated from low-aspect-ratio black silicon. *Appl. Phys. Lett.* **101,** 131902 (2012).

75. Groten, J. & Rühe, J. Surfaces with combined microscale and nanoscale structures: a route to mechanically stable superhydrophobic surfaces? *Langmuir* **29,** 3765–72 (2013).

76. Koponen, H.-K. *et al.* Modification of cycloolefin copolymer and poly(vinyl chloride) surfaces by superimposition of nano- and microstructures. *Appl. Surf. Sci.* **253,** 5208–5213 (2007).

77. Bhushan, B., Jung, Y. C. & Koch, K. Micro-, nano- and hierarchical structures for superhydrophobicity, self-cleaning and low adhesion. *Philos. Trans. A. Math. Phys. Eng. Sci.* **367,** 1631–72 (2009).

78. Ziaie, B., Baldi, A. & Massood, A. in *Springer Handbook of Nanotechnology* (ed. Bhushan, B.) 231–265 (Springer, 2010).

79. Kumaravelu, G., Alkaisi, M. M. & Bittar, A. Surface texturing for silicon solar cells using reactive ion etching technique. *Photovoltaic Specialists Conference, 2002. Conference Record of the Twenty-Ninth IEEE* 258–261 (2002). doi:10.1109/PVSC.2002.1190507

80. Schnell, M., Ludemann, R. & Schaefer, S. Plasma surface texturization for multicrystalline silicon solar cells. 367–370 (2000).

81. Jensen, B., Johansen, J., Karbæk, K. & Kjærsgård, P. *Plast teknologi*. 1 –314 (Erhvervsskolernes Forlag., 2005).

82. Ehrenstein, G. W. *Polymeric Materials Structure – Properties – Applications*. 51–74 (Carl Hanser Verlag GmbH & Co. KG, 2001).

83. Borealis. Polypropylene HD601CF. 23–25 (2010).

84. TOPAS. TOPAS® 5013L-10 Data Sheet. (2014).

85. Vito, L. Understanding injection molding of thermoplastics. 2–166 (2011). at <http://www.bims-seminars.com/index.htm>

86. Autodesk. Moldflow 2013 Polymer Database. (2013).

87. autodesk. How plastic fills a mold. *24-09-2014* (2014). at <http://knowledge.autodesk.com/support/simulation-moldflow-adviser/learn-explore/caas/CloudHelp/cloudhelp/2015/ENU/MoldflowAdvisor/files/GUID-66A1762F-CC20-486D-8EAA-3001A7FFD39C-htm.html?v=2015>

88. Borealis. Product Data Sheet Polypropylene HD601CF. 3 (2014).

89. Matschuk, M. & Larsen, N. B. Injection molding of high aspect ratio sub-100 nm nanostructures. *J. Micromechanics Microengineering* **23,** 025003 (2013).

90. Kim, S., Shiau, C.-S., Kim, B. H. & Yao, D. Injection Molding Nanoscale Features with the Aid of Induction Heating. *Polym. Plast. Technol. Eng.* **46,** 1031–1037 (2007).

91. Hattori, S., Nagato, K., Hamaguchi, T. & Nakao, M. Rapid injection molding of high-aspect-ratio nanostructures. *Microelectron. Eng.* **87,** 1546–1549 (2010).

92. Yokoi, H., Han, X., Takahashi, T. & Kim, W. K. Effects of molding conditions on transcription molding of microscale prism patterns using ultra-high-speed injection molding. *Polym. Eng. Sci.* **46,** 1140–1146 (2006).

93. Nikon Microscopyu. Resolution. *06-09-2014* at <http://www.microscopyu.com/articles/formulas/formulasresolution.html>

94. Nikon Microscopyu. Properties of Microscope Objectives. *04-10-2014* at <http://www.microscopyu.com/articles/optics/objectiveproperties.html>

95. Nikon Microscopyu. Fundamental Concepts in Confocal Microscopy. *06-09-2014* at <http://www.microscopyu.com/articles/confocal/index.html>

96. Sensofar. Non-contact 3D optical profiler. *06-09-2014* at <http://www.sensofar.com/sensofar/pdf/Brochure_S_neox.pdf>

97. Fogale Nanotech. *MicroSurf 3D user manual 1.3 ed.*

98. Frase, C. G., Buhr, E. & Dirscherl, K. CD characterization of nanostructures in SEM metrology. *Meas. Sci. Technol.* **18,** 510–519 (2007).

99. Bhushan, B. & O. Marti. in *Springer Handbook of Nanotechnology* (ed. Bhushan, B.) 573–621 (Springer, 2010).

100. Tranchida, D., Piccarolo, S. & Deblieck, R. a C. Some experimental issues of AFM tip blind estimation: the effect of noise and resolution. *Meas. Sci. Technol.* **17,** 2630–2636 (2006).

101. Morra, M., Occhiello, E. & Garbassi, F. Knowledge about polymer surfaces from contact angle measurements. *Adv. Colloid Interface Sci.* **32,** 79–116 (1990).

102. Yekta-Fard, M. & Ponter, a. B. Factors affecting the wettability of polymer surfaces. *J. Adhes. Sci. Technol.* **6,** 253–277 (1992).

103. Stephens, R. B. & Cody, G. D. Optical Reflectance and transmission of a textured surface. *Thin Solid Films* **45,** 19–29 (1977).

104. Born, M. & Wolf, E. *Principles of Optics*. (Cambridge University Press, 1999).

105. Zeiss. AxioCam ICm 1 and Fluorescence Lite. *10-11-2014* at <http://applications.zeiss.com/C125792900358A3F/0/6407E93FAF0AF156C12579E5002D7079/$FILE/60-3-0021_e_AxioCam_ICm_1.pdf>

106. Bhushan, B., Jung, Y. C., Niemietz, A. & Koch, K. Lotus-like biomimetic hierarchical structures developed by the self-assembly of tubular plant waxes. *Langmuir* **25,** 1659–66 (2009).

107. Analysis-, A. D. S., Li, D. & Neumann, A. W. Contact angles on hydrophobic solid surfaces and their interpretation. *J. Colloid Interface Sci.* **148,** 190–200 (1992).

108. Magnus Bredsdorff 2011. Beviserne mod fluorstoffer tårner sig op. *05-11-2014* at <http://ing.dk/artikel/beviserne-mod-fluorstoffer-tarner-sig-op-124206>

109. Equistar. Additives: Antioxidants. *23-10-2014* at <http://www.lyondellbasell.com/techlit/techlit/Tech Topics/General/Antioxidants.pdf>

110. Kholodovych, V. & Welsh, W. J. in *Physical Properties of Polymers Handbook* (ed. Mark, J. E.) 927–938 (Springer New York, 2007). doi:10.1007/978-0-387-69002-5

111. Liland, K. B., Hvidsten, S. & Øysaed, H. Micro Calorimetric Measurements of Stabilized and Unstabilized Polypropylene Under Wet and Dry Conditions. *Adv. Polym. Technol.* **33,** n/a–n/a (2014).

Appendixes

Appendix 1 Fabrication recipes

All informations from DanChip.

D-RIE process for microstructure etch

D-RIE process with where etch passivation cycle corresponds to a structure depth of approximately 250 nm, used to etch microstructures.

Main etch (D->E)	Etch	Dep
Gas flow (sccm)	SF_6 275 O_2 5	C_4F_8 150
Cycle time (secs)	2.4	2.0
Pressure (mtorr)	26	20
Coil power (W)	2500	2000
Platen power (W)	35	0
Cycles	110 (process time 08:04)	
Common	Temperature 0 degs, HBC 10 torr, Long funnel, with baffle & 100 mm spacers	

Nanostructure RIE parameters for the industrial test production

Recipe	Gas	C_4F_8 75 sccm, SF_6 38 sccm
	Pressure	4 mTorr, Strike 3 secs @ 15 mTorr
	Power	800 W CP, 40 W PP
	Temperature	-20 degs
	Hardware	100 mm Spacers
	Time	120 secs

MVD Multi Layer stamp Recipe

- Initial Plasma treatment: O2 200 sccm, RF 250 W, Time 300 s
- Water: Pressure 6.000 Torr, Vapor 2
- FDTS: Pressure 0.500 Torr, Vapor 1
- Reaction time total: 900 s
- Repeated four times

Appendix 2

Work performed on external stay at NTU

The goal of the external stay was to study water condensation on nano- and microstructured structured polymer samples. For this purpose a small environmental chamber was designed and fabricated during my 3½ months external research stay at Nanyang Tecnological University (NTU). Condensation experiments were performed. A test of the environmental chamber is presented, together with a description of the experimental setup and results from test on polymer samples are presented. The idea was to test different parameters such as sample temperature and relative humidity while recording videos with a camera for later analysis.

Experimental setup

The environmental chamber setup was fabricated and assembled from different parts showed in Figure 1 and the setup is schematically shown in Figure 2 except that compressed air was used instead of nitrogen. The chamber lid, made from polycarbonate, was coated with a commercial anti-fog coating (M ESSENTIALS SEA QUICK) before use. This prevents water from condensing on the lid, and makes observation of the sample with a microscope or camera possible. A fresh layer of anti-fog coating on the lid will have to be applied before every experiment; otherwise, fog may form on the lid. A reduction valve on the compressed air was used to ensure a constant flow rate for different experiments. The valve was adjusted to 0.5 bar. The humidity inside the chamber can be adjusted from 10% up to approximately 80% by having a mixture of dry and humid air. The adjustment of the valves is time-consuming because the chamber has to reach a steady state before a new adjustment can be made. Mass flow controllers would make this process faster, easier and more accurate. Since mass flow controllers were not available the simple valves were used for all experiments.

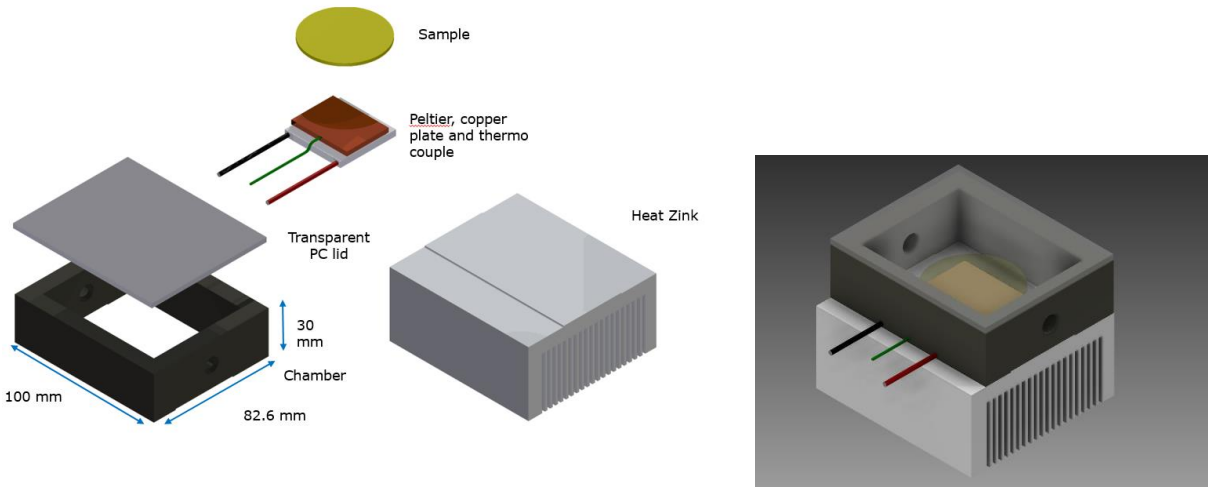

Figure 1. CAD drawing of the individual parts of the environmental chamber and the assembled chamber.

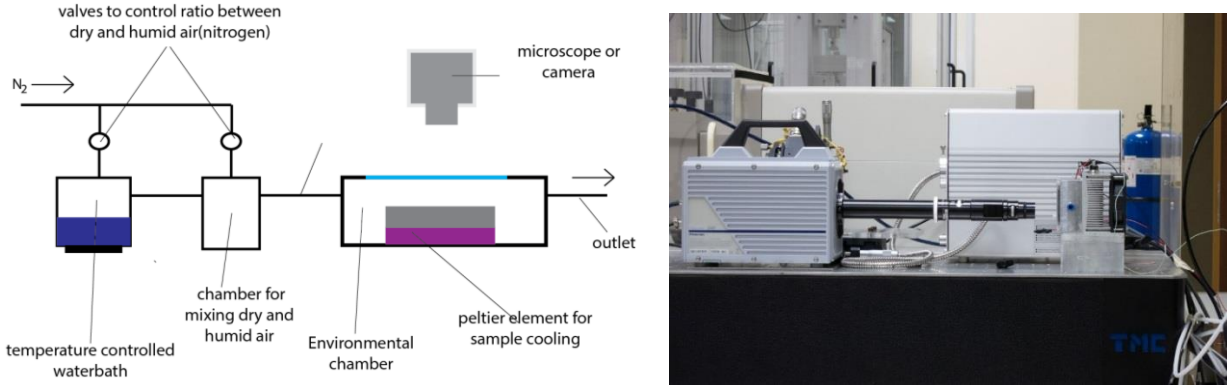

Figure 2. Left, schematic drawing of setup, humid and dry air are mixed to obtain a specific relative humidity between 10% and 80% while a peltier element controls the sample temperature. Right, the setup with high speed camera, note the powerful metal halide lamp for sample illumination.

Preliminary test

Two flat pieces of PMMA were used to test the environmental chamber. One piece was left untreated while the other was coated with a commercial anti-fog coating agent (M ESSENTIALS SEA QUICK). The temperature on the copper plate was set to 0 °C and the chamber temperature was at room temperature (measured to 20 °C). The samples were first cooled for

10 min. while purging the chamber with dry air with a relative humidity (RH) of 10%. Humid air at 70% RH was introduced to the chamber and the fog formation was observed on the two samples. The untreated sample fogged within a few seconds while the anti-fog treated sample show no sign of fogging even after 10 min. Frame grabs from recorded videos are shown in Figure 3.

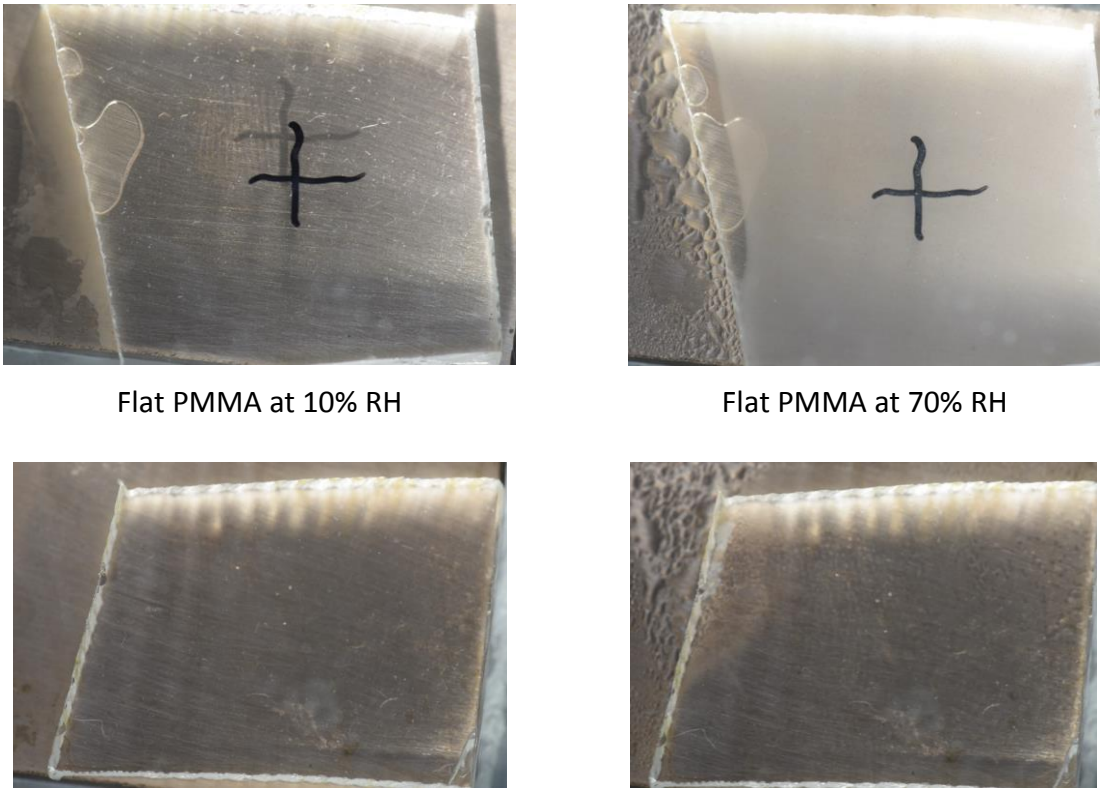

Figure 3. Frame grab from recorded videos the untreated flat PMMA fogged immediately while the anti-fog treated PMMA shows no sign of fog.

Sample test

A nano- and microstructured TOPAS samples with holes were used to test droplet formation and anti-fogging properties of the injection-molded samples. The image in Figure 4 shows condensed water drops on the surface after 10 min. A video was recorded and the droplet formation could be observed over time frame grabs from the video are shown in Figure 5; the images show the dry sample, after exposure to humid air after 5 min and after 30 min. After 30 min the droplet size had increased, which is to be expected since more water is condensed on the surface.

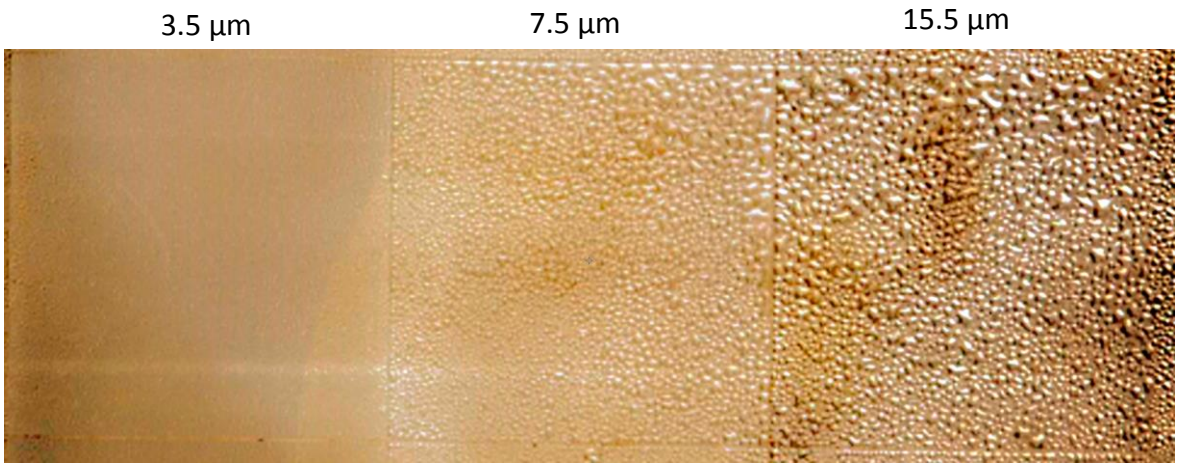

Figure 4. Photo of TOPAS sample after 10 min at 70% RH.

Figure 5. Video frame grabs from different times in a video, note how the drop size is larger after 30 min.

Condensation experiments high speed

A high-speed camera was used to characterize the first two minutes during water condensation. Condensation experiments were carried out with the same parameters and sample type as for the preliminary test. A high-speed camera set to 500 frames per second with a 10 × optical magnification lens was used to characterize how water condensed on the surface. Three frames with 15.5 µm holes at different condensation times are shown in Figure 6. Initially holes showed an increase in light intensity when the sample was exposed to water. This intensity change may indicate that water condensed first on the bottom of the holes. Condensation experiments were carried out on different hole sizes (3.5 µm, 7.5 µm, and 15.5 µm Figure 7. Surfaces with larger structure density (smaller structures), had an increased number of condensed drops. There might be a relation between droplet size and structure size. More experiments are needed before any kind of solid conclusions can be made.

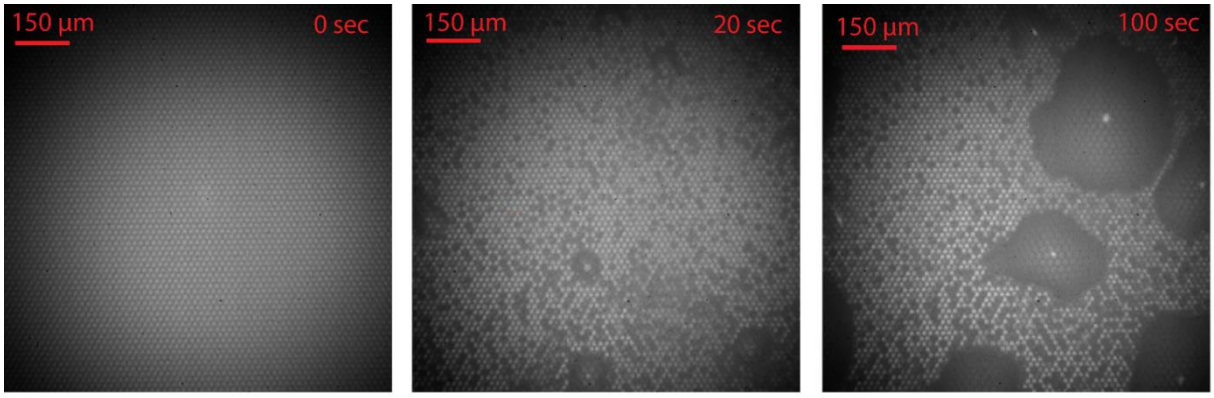

Figure 6. Frame grabs at different times on 15.5 µm holes.

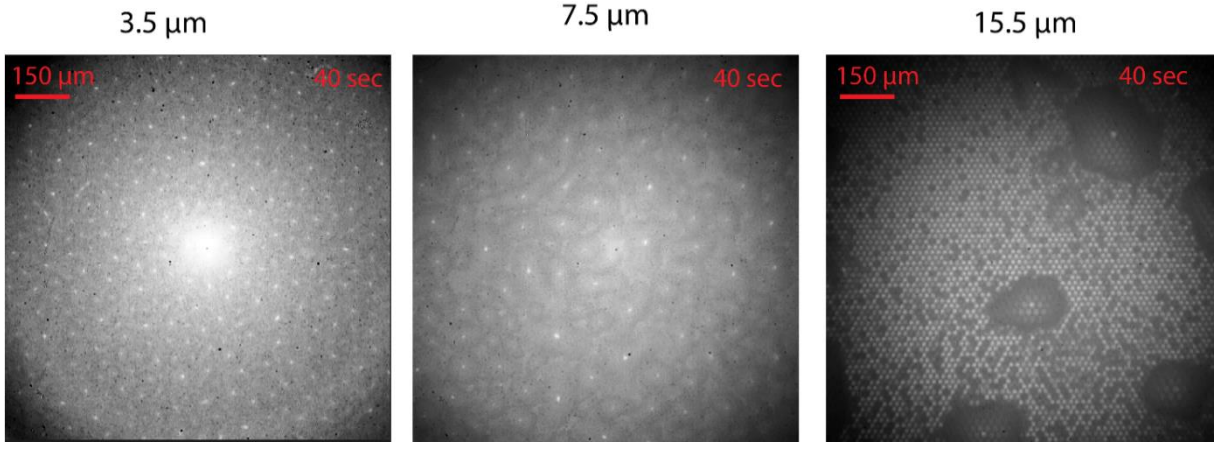

Figure 7. Condensation of drops on different structure sizes.

Appendix 3

Emil Søgaard, Nis K. Andersen, Kristian Smistrup, Simon Larsen, Ling Sun, and Rafael Taboryski. *Study of Transitions between Wetting States on Micro-cavity Arrays by Optical Transmission Microscopy.* Langmuir. Published online (2014).

Contribution: Development of the idea for the injection molded hierarchical nanograss structures. Microhole design. Cleanroom fabrication and injection molding of all structures. Idea, development and fabrication of pressure cell setup. Characterization of samples, data processing and analysis. Participation in manuscript writing. Drafting of figures.

Langmuir

Article

pubs.acs.org/Langmuir

Study of Transitions between Wetting States on Microcavity Arrays by Optical Transmission Microscopy

Emil Søgaard,[†] Nis K. Andersen,[†] Kristian Smistrup,[‡] Simon T. Larsen,[†] Ling Sun,*[,†] and Rafael Taboryski*[,†]

[†]Department of Micro- and Nanotechnology, Technical University of Denmark, 2800 Kongens Lyngby, Denmark

[‡]NIL Technology, Diplomvej 381, 2800 Kongens Lyngby, Denmark

Supporting Information

ABSTRACT: In this article, we present a simple and fast optical method based on transmission microscopy to study the stochastic wetting transitions on micro- and nanostructured polymer surfaces immersed in water. We analyze the influence of immersion time and the liquid pressure on the degree of water intrusion in individual microcavities on these surfaces as well as the lifespan of their superhydrophobicity. We show that transitions among the three wetting states (Cassie, Cassie-impregnating, and Wenzel) occur with a certain pressure threshold (300 mbar for a microcavity diameter of 7.5 μm). Below this threshold, the transitions between the Cassie and the Cassie-impregnating states are reversible, whereas above this threshold, irreversible transitions to the Wenzel state start to occur. The transitions between the different wetting states can be explained by taking into account both the Young−Laplace equation for the water menisci in the cavities and the diffusion of dissolved gas molecules in the water. In addition, the wetting transitions had a stochastic nature, which resulted from the short diffusion distance for dissolved gas molecules in the water between neighboring cavities. Furthermore, we compared the contact angle properties of two polymeric materials (COC and PP) with moderate hydrophobicity. We attributed the difference in the water repellency of the two materials to a difference in the wetting of their nanostructures. Our experimental observations thus indicate that both the diffusion of gas molecules in water and the wetting properties of nanostructures are important for understanding the sustainability of superhydrophobicity of surfaces under water and for improving the structural design of superhydrophobic surfaces.

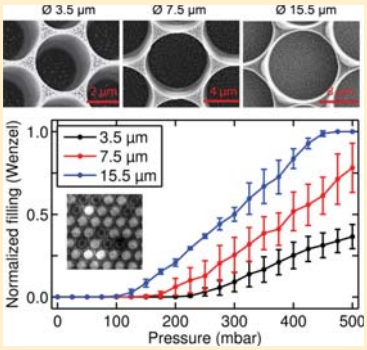

INTRODUCTION

Superhydrophobic surfaces made with artificial structures have high technological importance for applications such as self-cleaning textiles,[1−3] antifogging or antireflection coatings,[4−6] microfluidic devices,[6,7] information storage,[8] and underwater applications such as drag reduction.[9−13] Typically, surfaces with water contact angles larger than 150° are considered to be superhydrophobic. These surfaces usually possess rough and irregular topography and hydrophobic (water contact angle larger than 90°) surface chemistry.[5,14] In addition, biomimetic surfaces with regular hierarchical structures from the micro- to nanoscale present stable and relatively robust superhydrophobicity.[4,15−20]

The stability of superhydrophobic surfaces under water has attracted much attention because of their potential applications.[8,21−27] When a superhydrophobic surface is immersed in water, air pockets can be trapped between the surface structures. This wetting state is considered to be a special case of the Cassie wetting state.[28,29] However, with increasing liquid pressure and time, the volume of trapped air may decrease, leading to an intrusion of the liquid/gas interface into the structures. This metastable wetting state is often referred to as the Cassie-impregnating state.[4,8,19,30] Further increases in the liquid pressure can result in the complete collapse of the liquid/gas interface, leading to a loss of superhydrophobicity of the surface. This state, when the liquid completely wets the structures and no air pockets are left, is referred to as the Wenzel state.[31] Transitions from the Cassie state to the Cassie-impregnating state are reversible under certain conditions: by reducing the applied liquid pressure,[8] introducing additional gas and vapor,[24,32] or vibrating the system.[33] However, except for some electrochemically induced surface treatments,[34,35] transitions from the Cassie state to the Wenzel state (complete wetting) are in most cases irreversible.[36,37] Hence, prolonging the lifespan of the Cassie and Cassie-impregnating states is the key to sustaining the superhydrophobicity of surfaces immersed in water.

Though much attention has been focused on studies of superhydrophobic surfaces, few studies were focused on direct noninvasive observations of wetting transitions from the Cassie to Wenzel states on superhydrophobic samples immersed in water.[21−23,25,30,38−41] Among these studies, some either tracked the wetting transitions macroscopically using experimental techniques with less control[21,23,25,40,41] or used complex

Received: July 21, 2014
Revised: October 6, 2014
Published: October 7, 2014

   dx.doi.org/10.1021/la502855g | Langmuir 2014, 30, 12960−12968

experimental setups and numerical calculations.[26,38,39,42,43] Salvadori et al. reported on the wetting properties of microcavity arrays but did not consider the diffusion of gas molecules in water.[44] Lv et al. reported a quantitative study of the air/water interface in single microcavities submerged in water.[30,45] However, the system used was ideal, and they did not consider deviations caused by manufacturing defects or the random diffusion of gas molecules between adjacent microcavities. A systematic study of stochastic wetting transitions on superhydrophobic surfaces under water is still missing.

In this article, we present a simple and fast method of studying the stochastic wetting transitions on injection molded polymer surfaces immersed in water. We carried out water wetting experiments on these surfaces using a pressure cell to regulate the liquid pressure applied to hierarchical surface structures consisting of microcavities superimposed with nanograss and observed their microscopic wetting behavior by optical transmission microscopy. We also compared the superhydrophobicity of two polymers with moderate hydrophobicity, i.e., polypropylene (PP) and cyclic olefin copolymers (COC). We will show that a minor difference in surface chemistry and surface structures can result in very different wetting conditions and stabilities of their superhydrophobicity.

EXPERIMENTAL SECTION

Fabrication of Polymer Hierarchical Structures. Cyclic olefin copolymers (COC, TOPAS grade 8007-s04, Advanced Polymers, USA) and polypropylene (PP, HD601CF, Borealis, Austria) discs (50 mm in diameter and 2 mm thick) were injection molded using an industrial injection molding machine (Victory 45, Engel, Austria) facilitated with a prestructured nickel mold. The microcavities were etched in a hexagonal pattern by deep UV lithography and reactive ion etching on a silicon origination master, and the nanograss was subsequently fabricated by a CF_6 + O_2 plasma etching process. The nickel mold was electroformed on the silicon master, and the silicon was subsequently removed by KOH wet etching. The detailed fabrication procedure of the silicon template and the nickel mold can be found in the Supporting Information.[46] The depth of polymer microcavities H was 3.2 ± 0.1 μm, as measured by scanning probe microscopy (Nanoman, Digital Instrument, USA).

Water Wetting Experiments. The experimental setup used for the wetting tests is shown in Figure 1. The polymer sample was placed inside a transparent water pressure cell made of polycarbonate. The pressure cell was sealed with an O ring. Compressed dry nitrogen gas with a regulated pressure Δp above atmospheric pressure p_0 was applied with a pressure controller (VEMA 8, FESTO, Germany) that was connected through a gas pressure interface, as shown in Figure 1. The absolute liquid pressure in the pressure cell was thus $p_l = p_0 + \Delta p$. The dimensions of the pressure cell were approximately 130 mm × 90 mm × 20 mm (length × width × height). These dimensions are small enough for the water pressure cell to be fit into an inverted optical microscope (AX10 Observer A1, Carl Zeiss AG, Germany). Prior to each measurement, the pressure cell was flushed with dry nitrogen gas and subsequently filled with Milli-Q water for the wetting experiments. Incident light from a halogen lamp was connected to the light path in the microscope. The images were recorded with a 12 bit CCD camera (AxioCam IC, Carl Zeiss AG, Germany) and processed by ImageJ and Matlab.[46] For all water wetting tests, each experiment was repeated on three identical samples from the same injection molding batch.

Contact Angle Measurements. Contact angles were measured using an optical tensiometer (Theta, Attension, Finland) with a high-speed camera (3000 fps, MotionXtra N3, IDT, USA). Shapes of droplets were fitted by both a polynomial and the Young−Laplace fitting method for the static contact angle measurements and by the polynomial fitting method for the dynamic contact angle measurements. For all contact angle measurements, droplets of 6.5 μL volume were used. The baseline was determined using an auto baseline function in the Attension Theta software (version 4.2). For each sample, three measurements were made at different spots on the surface.

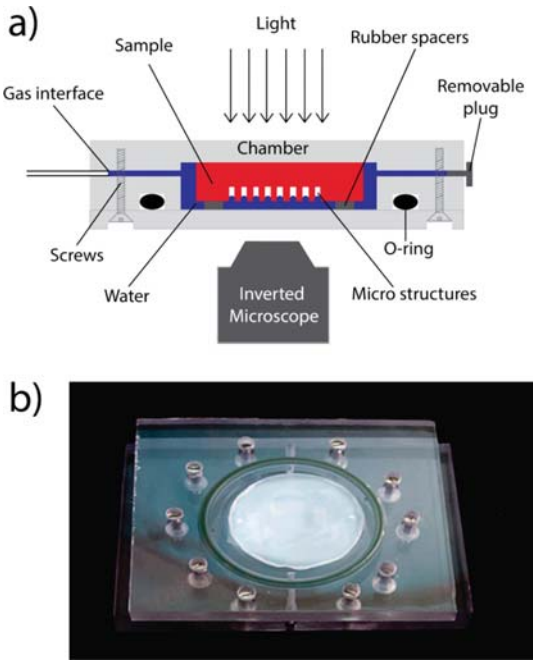

Figure 1. Experimental setup of water wetting tests: (a) schematic sketch of the experimental setup and (b) photograph of a sealed pressure cell with a sample inside.

RESULTS AND DISCUSSION

The Wenzel model describes a situation in which a surface is completely wetted by a liquid (Figure 2a),[31] and the Cassie model describes the wetting of a chemically heterogeneous surface.[28,47] A special case of the Cassie model occurs when the chemical heterogeneity stems from air patches between the solid area fractions for a surface that is only partially wetted by a liquid. In this state, air pockets are trapped between the liquid and the microcavities. Recently, a special Cassie state, the Cassie-impregnating state, has been introduced for hierarchical surfaces comprising a superposition of nano- and microstructures. In this state, air pockets are trapped between the liquid and the nanostructures, and the microstructures are impregnated by the liquid.[19,48] In other words, the volume of air pockets trapped between micro- and nanostructures of a rough surface, when this surface is immersed in liquid, determines the wetting situation, e.g., the total volume of air pockets is zero for the Wenzel state. As can be seen in Figure 2a, for the three wetting situations (Cassie, Cassie-impregnating, and Wenzel), light transmits through different materials, each with a different index of refraction and geometry. Therefore, the transmittance and reflectance of light will be different for the three wetting states. This difference will result in an intensity difference of the transmitted light in the optical microscope when there is a transition between wetting states. The nanograss structures have antireflective properties,[49] and the spikes have characteristic dimensions smaller than the diffraction limit of light. Hence, in order to compute the contribution of the nanograss layer to the transmittance, an "effective medium" theory[50] was applied such that the nanograss layer was approximated by a graduated volume

dx.doi.org/10.1021/la502855g | Langmuir 2014, 30, 12960−12968

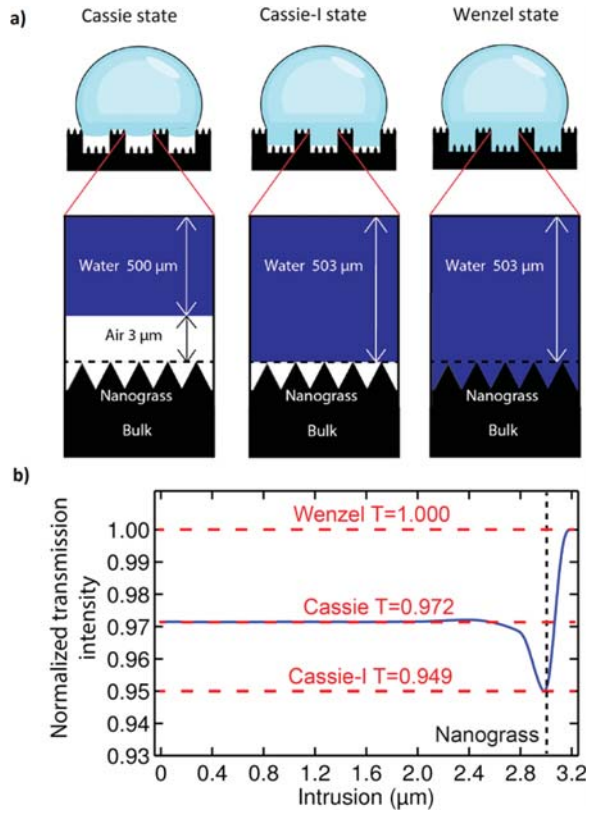

Figure 2. (a) Schematics of the three wetting states (Cassie, Cassie-impregnating, and Wenzel) and the corresponding materials stacked in each microcavity through which light passes in the three situations. (b) Normalized transmitted intensity as a function of water intrusion into microcavities, with n_{COC} = 1.53 and n_{water} = 1.33.

fraction of polymer and water when in the Wenzel state and by a graduated volume fraction of polymer and air when in the Cassie state. This graduation is attributed to the cone shape of the individual spikes, with an estimated characteristic opening angle in the range of 20−50° for the cones. The contribution of the nanograss layer was then obtained by dividing the layer into slices of 1 nm thickness and calculating the transmission and reflection of light waves at each slice interface.

To model the transmittance through the whole sample, we assumed normal incidence for simplicity and divided the sample into a stack of layers according to the appropriate optical medium (air, water, or polymer), each with its respective refractive index. For each interface, the Fresnel coefficients for the reflected and transmitted field strengths were calculated and applied to track the field strength from the last interface to the first interface with appropriately picked-up phase factors along the way of the light. This procedure produced the reflected and transmitted field strength amplitudes for the first interface and consequently also for the total stack. The transmission and reflection coefficients as a function of the wavelength are then given by $R = (\|\tilde{E}_R\|/\|\tilde{E}_I\|)^2$ and $T = (\|\tilde{E}_T\|/\|\tilde{E}_I\|)^2$, where $\tilde{E}_R$, $\tilde{E}_T$, and $\tilde{E}_I$ are respectively the reflected, transmitted, and incident field strength amplitudes for the first interface (and consequently for the whole stack) obtained from the numerical calculation. A more detailed calculation can be found in the Supporting Information.[46] To obtain the normalized transmitted light intensity, the transmission coefficient was multiplied by the normalized spectral density of the lamp and the normalized spectral sensitivity of the camera CCD chip and finally averaged over all wavelengths. Furthermore, to account for the experimental uncertainty associated with the choice of focus depth during the experiment, the resulting intensity curve versus intrusion depth was smoothed by averaging over intrusion intervals of 400 nm, corresponding to the order of magnitude of the meniscus protrusion. This procedure resulted in a theoretical transmitted light intensity of the whole stack consisting of bulk polymer, nanograss, air, and water, according to the considered wetting state as a function of the water intrusion depth (Figure 2b). The intensity is at its maximum for the Wenzel state, where all air pockets, including the ones in the nanostructure at the bottom of the cavities, are absorbed by the intruding water. At this position, we have good index matching between water and polymer and hence the highest transmission of light. However, the intensity has its minimum for the Cassie-impregnating state, where the intruding water has reached the top of the nanograss. It is worth mentioning that the calculated intensity is practically indistinguishable for intrusion from 0 μm up to about 2.4 μm (~75%). Because of the simplified 1D geometry of the transmission model, we expect the experimental transmission data to deviate somehow from the curve obtained in Figure 2b. The experimentally estimated normalized intensity (before contrast and brightness adjustment) thus fell in a larger intensity range span of 0.90 to 1.00 when compared to the intensity range span of 0.95 to 1.00 in Figure 2b. Experimentally, we thus practically distinguished the wetting states when they fell into the following estimated transmitted intensity ranges: $0.90 < I_{Cassie\text{-}I} < 0.94$, $0.94 \leq I_{Cassie} < 0.97$, and $0.90 \leq 1$. Because of the negligible variation of transmitted intensity for partial intrusion until 75% obtained from the model calculation, we should expect counting errors resulting in an underestimation of the number of cavities in the Cassie-I state if this state is dominated by only partial intrusion. However, if the Cassie-I state is dominated by full intrusion with the menisci touching the nanograss at the bottom of the cavities, we should expect fewer counting errors. Nevertheless, the model clearly supports the three wetting states being distinguishable in a transmission microscopy experiment, at least with deep intrusions for the Cassie impregnating case.

The air pockets trapped in the microcavities build up a protective layer that can sustain the superhydrophobicity of a surface for a certain time when the sample is immersed in water. The sustainability of this superhydrophobic surface under water depends on the pressure difference at the water/air interface in the cavities. In our control experiment (Supporting Information Figure S1),[46] all polymer samples were able to sustain superhydrophobicity under water for at least 24 h when no external pressure was applied (Δp = 0). When we applied a certain pressure to the system, transitions from the Cassie to the Cassie-impregnating and finally to the Wenzel state started to occur. Figure 3 is a series of representative optical transmission microscope images of a COC sample immersed in water at Δp = 225 mbar. During this experiment, optical images were captured every 10 s on the same position. The intensity of each microscope image was adjusted so that the contrast of each image became comparable. Details of this adjustment process can be found in the Supporting Information.[46] Each spot on the image corresponds to one microcavity. The intensity of the spots first decreased and then increased with time, indicating wetting transitions from the Cassie to the Cassie-impregnating and finally to the Wenzel

dx.doi.org/10.1021/la502855g | Langmuir 2014, 30, 12960−12968

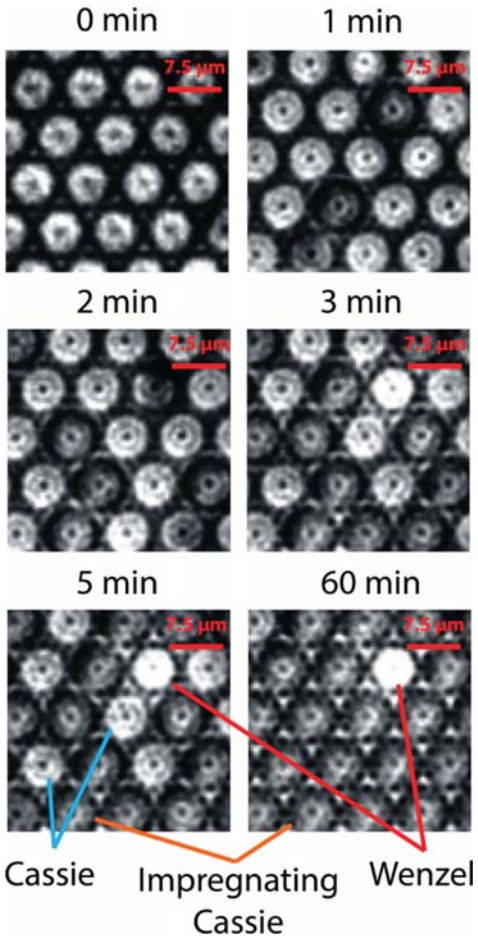

Figure 3. Optical transmission microscopy images of microcavities during water wetting experiments at Δp = 225 mbar. The colored lines indicate examples of different wetting states on the micrographs. To distinguish one state from the other visually on the images, the contrast on the images was increased (Supporting Information).[40]

state (Figure 3), $I_{Wenzel} > I_{Cassie} > I_{Cassie\text{-}I}$, which is consistent with the intensity variation predicted by our theoretical model in Figure 2b. On the image taken after 5 min, the three wetting states coexist. Similar coexistence of the Cassie and Wenzel states was theoretically studied by Koishi et al.[51] and experimentally observed.[23,36] The transition from the Cassie state to the Cassie-impregnating state was reversible, after Δp had been reduced to zero, and the transition from the Cassie-impregnating state to the Wenzel state was irreversible (Supporting Information).[46] The irreversible transition from the Wenzel to the Cassie state was also observed by Nosonovsky et al.[15] as an increasing condensation of water droplets on a patterned surface. Because of the curvature of the menisci and reflections from the side walls of the cavities, the light intensity exhibited some variations across the cavities with a dark spot in the center. To minimize this effect, we chose always to average the intensity over the same central area of the cavities, and we compared their intensity accordingly.

The results in Figure 3 proved the experimental feasibility of observing the transition between wetting states using transmission optical microscope in our experimental setup. To understand the wetting dynamics better, we conducted a series of water wetting tests on samples from the same injection molding batches at different Δp values. The normalized intensity of each image could be readily divided into three categories as described above. For each transmission microscopy image taken in a given time frame, we manually counted the number of dots N_i whose intensity fell into one of the three categories and normalized the number of counted dots attributed to each wetting state by dividing by the overall number of dots N_i/N. To minimize counting errors, we conducted this set of experiments only on COC samples because COC has a higher transparency than PP and thus a higher transmitted light intensity. For experiments taken at each applied pressure Δp (150, 225, 300, and 400 mbar), we plotted the normalized filling of each wetting state $N_{Cassie\text{-}I}/N$ and N_{Wenzel}/N versus time, as shown in Figure 4a. For

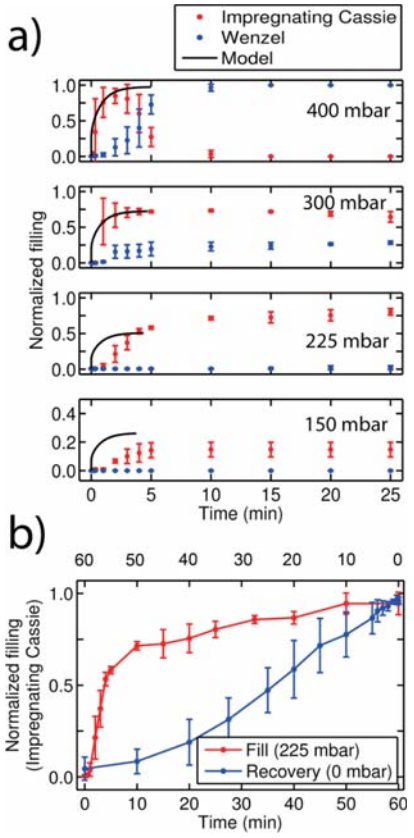

Figure 4. (a) Transitions between wetting states over time at different Δp: 150, 225, 300, and 400 mbar. The model data (until saturation at about 3 min) were based on the degree of intrusion of a single cavity using the 1D diffusion model. (b) Recovery of the Cassie-impregnating to Cassie state after the reduction of Δp to 0. Error bars in both a and b are obtained as the standard deviation for measurements on three different samples.

comparison, we also used a Matlab script to estimate N_i/N automatically using the normalized average intensity in the central area of each cavity to minimize the influence of the potential curvature change of the menisci at different Δp values, which yielded results that were similar to our manual counting.

In Figure 4a, when Δp < 300 mbar, only transitions from the Cassie to the Cassie-impregnating state occurred, and further transition to the Wenzel state occurred on only one microcavity that was defective. We thus conclude that at Δp < 300 mbar, $N_{Wenzel}/N \approx 0$, whereas when $\Delta p \geq$ 300 mbar, both transitions

dx.doi.org/10.1021/la502855g | Langmuir 2014, 30, 12960−12968

from the Cassie to the Cassie-impregnating and the Cassie-impregnating to the Wenzel states occurred. However, when looking at the wetting dynamics at $\Delta p < 300$ mbar, we found some differences: at $\Delta p = 150$ mbar, $N_{\text{Cassie-I}}/N \leq 0.15$, even after the sample had been immersed in water for 60 min (Supporting Information Figure S2), whereas at Δp 225 mbar, $N_{\text{Cassie-I}}/N \approx 1$ after the sample had been immersed in water for 60 min. There were also differences at $\Delta p \geq 300$ mbar: at $\Delta p = 300$ mbar, $N_{\text{Cassie-I}}/N \approx 0.73$ and $N_{\text{Wenzel}}/N \approx 0.23$ after the sample had been immersed in water for only 10 min, and at $\Delta p = 400$ mbar, $N_{\text{Cassie-I}}/N$ first increased to ~0.85 after 2 min and then decreased to almost 0 after 15 min. At this point in time, N_{Wenzel}/N increased to 1, indicating that at $\Delta p = 400$ mbar complete transitions from the Cassie-impregnating to the Wenzel state occurred.

The intrusion of water into individual cavities can be modeled by a very simple model resembling the Epstein–Plesset model[52,53] for gas bubbles in a liquid. However, in this case we consider a simplified 1D diffusion scheme. The phenomena we observe happen on a time scale of minutes. Walls inside the 3-μm-deep cavities are relevant to a diffusion time scale of $(3\ \mu\text{m})^2/D \approx 5$ ms. The side walls of the pressure chamber are roughly 30 mm away from the sample area. This corresponds to a diffusion time of $(30\ \text{mm})^2/D \approx 133$ h. The relevant time scale for diffusion corresponds to the thickness $b = 0.5$ mm of the water layer above the micro/nanostructured surface and amounts to $\tau = b^2/D \approx 2$ min. The opposing wall is parallel to the structured surface, and hence we should expect a 1D diffusion model to suffice for studying phenomena on the time scale of minutes. The above argument also allows us to disregard the curvature of the meniscus of water in the cavity and the effect of neighboring cavities when solving the diffusion equation. However, the volume of the meniscus is taken into account when calculating the volume of gas in the cavity. In this model, the x direction is taken perpendicular to the surface. Prior to each experiment, the pressure cell was flushed with dry nitrogen gas. Hence, when the surface is immersed in water, the nitrogen gas pressure $p_g(t)$ in each of the cavities is a function of time and is given by the ideal gas law.

$$p_g(t)\ V(t) = n(t)RT \tag{1}$$

where $V(t)$ is the volume of gas at any instant in time in each cavity, $R = 8.31$ J mol^{-1} K^{-1} is the gas constant, T is the absolute temperature, and $n(t)$ is the number of moles gas trapped in each cavity. The pressure applied to the cell by the pressure controller was applied relative to the atmospheric ambient pressure in the laboratory. The absolute pressure applied to the liquid is thus given by $p_l = p_0 + \Delta p$, where p_0 is the atmospheric ambient pressure and Δp is the applied pressure. Because the diameter of the cavities is much smaller than the capillary length (~2.7 mm), the menisci of the water gas interfaces will achieve the shapes of spherical caps with radii of curvature given by the Young–Laplace equation

$$p_g(t) - p_l = \frac{2\gamma \cos\theta_a}{a} \tag{2}$$

where $\gamma = 72 \times 10^{-3}$ N m^{-1} is the surface tension of the water/gas interface, θ_a is the advancing contact angle, and a is the radius of the cylindrical microcavities. In addition, gas exchange at the water/gas interface should not be neglected.[24] This process can be described by Henry's law:

$$p_g(t) = k_H c(x = 0) \tag{3}$$

Here, $k_H = 1640$ L bar mol^{-1} is the Henry's law constant for nitrogen in water at room temperature, and $c(x = 0)$ is the concentration of dissolved nitrogen in water at the interface. In water, the nitrogen molecules will diffuse along the concentration gradient away from the interface. This diffusion process in water is governed by Fick's second law

$$\frac{\partial c(x, t)}{\partial t} = D\frac{\partial^2 c(x, t)}{\partial x^2} \tag{4}$$

where $D = 1.88 \times 10^{-5}$ cm^2 s^{-1} is the diffusion coefficient of nitrogen in water, t is the time, and x is the distance from the interface. It is when this diffusion process is taken into account that the entrapped air volumes V and the associated gas pressures p_g in each of the cavities become functions of time, whereas the concentration of nitrogen molecules c in water becomes a function of both time and position x.

By employing a simple Matlab script in an iterative approach (Supporting Information) to solve eqs 1, 2, and 4 numerically using eq 3 as the boundary condition for the diffusion process, we were able to model the degree of water intrusion as a function of time (Figure 4a).[46] No fitting parameters were required in the calculation. In the calculation, we defined the relative degree of intrusion $h(t)/H$, where H is the depth of the cavities and $h(t)$ is the depth of water intrusion at time t. When a microcavity is filled completely (Wenzel state), $h/H = 1$, whereas $h/H = 0$ when the water–gas interface is at the entrance of the cavity (Cassie state) and $0 < h/H < 1$ when a microcavity is partially filled (Cassie-impregnating state). In the ideal case, wetting transitions should happen in all cavities simultaneously and identically. However, in reality, because of unavoidable minute geometrical irregularities, the intrusion over time is rather a stochastic process, where the degree of wetting transitions follows a normal distribution.[23] Hence, the condition for the model to allow a comparison with the light transmission data is that the dissolved volume of gas is the same in both. A configuration with 10% impregnation can be considered to be either a 10% filling of each cavity or 1 in 10 cavities filled completely. In both cases, the same number of gas molecules is dissolved in water. Furthermore, the depth of a microcavity is only around 3 μm, which is much smaller than the thickness of the water layer on top of the polymer surface, $b \approx 0.5$ mm. This configuration makes it easier for the gas molecules to diffuse between the neighboring microcavities by crossing over the wall in the middle (100 nm thin) from one cavity to another cavity than through the entire water layer. This situation further enhances the stochastic nature of the wetting process. From Figure 4a, we can see that our simple 1D model is capable of predicting the normalized filling of the Cassie-impregnating state $N_{\text{Cassie-I}}/N$ versus time for higher applied pressures Δp of 300 and 400 mbar, whereas at lower Δp values of 150 and 225 mbar there are some deviations. To summarize, the experimental transmission data were obtained by discrete counting of the three wetting states, whereas in the diffusion model shown above, the degree of intrusion into a single cavity was calculated. The optical transmission calculations indicated that the optical transmission data predominantly allows counting of the number of cavities in the Cassie-I state that are completely filled to a degree where the menisci touches the nanograss (Figure 2b). If the cavities are filled gradually, then we should expect counting errors in the optical transmission data for the number of cavities in the

dx.doi.org/10.1021/la502855g | Langmuir 2014, 30, 12960–12968

Cassie-I states and notable deviations between $N_{\text{Cassie-I}}/N$ and $h(t)/H$. Indeed we do see deviations at low Δp. At higher pressures, when some cavities also begin to populate the Wenzel state, we should compare $(N_{\text{Cassie-I}} + N_{\text{Wenzel}})/N$ to $h(t)/H$. For the higher pressures, we see a somewhat better fit and our data thus indicate that cavities are not filled evenly and gradually by the intruding water but rather abruptly one by one in a stochastic manner such that the dissolved volume of gas roughly corresponds to the gradual filling predicted by the 1D diffusion model.

Transitions from the Cassie-impregnating state to the Cassie state were reversible after Δp was reduced to 0 mbar from pressures below a threshold of approximately 300 mbar, as can be seen in Figure 4b. However, the 1D diffusion model was unable to reproduce the recovery curve. This shortcoming is expected because in this case the 1D diffusion model does not suffice to describe the process once the nitrogen molecules have been fully distributed over the whole 3D volume of the pressure cell.

The radius of the cylindrical microcavities plays a role in the gas pressure p_g in the microcavities, as explained in eq 3. We therefore conducted similar wetting experiments at increasing Δp on surfaces with microcavities of different radii and plotted N_{Wenzel}/N versus Δp (Figure 5). Here, we considered only the transition from the Cassie to the Wenzel states because this transition indicates a final loss of superhydrophobicity of a surface under water. In this set of experiments, the applied pressure Δp was increased at a rate of 25 mbar/min. The transition from the Cassie state to the Wenzel state was thus influenced by both t and Δp. In Figure 5, we can see that the applied pressure Δp required for the Cassie to the Wenzel transition was larger for smaller microcavities. The onset Δp was in the range of 220−300 mbar for $2a$ = 3.5 μm, 150−220 mbar for $2a$ = 7.5 μm, and 100−150 mbar for $2a$ = 15.5 μm. By inserting the advancing contact angle θ_a = 102°, we obtained the following calculated Δp for the three radii from the Young−Laplace equation: 173 mbar for $2a$ = 3.5 μm, 81 mbar for $2a$ = 7.5 μm, and 39 mbar for $2a$ = 15.5 μm. The measured Δp values were larger than the calculated ones, which is expected because (1) the onset of the Cassie−Wenzel transition requires at least a higher pressure than the Young−Laplace pressure given by eq 3 and (2) the characteristic time scale for the diffusion process is given by the thickness of the water layer above the polymer surface $b \approx 0.5$ mm and the diffusion constant and results in $\tau = b^2/D \approx 2$ min, which is comparable to the time it took to reach the onset pressures and comparable to the time scale obtained by Lv et al.[30] The Δp discrepancy also emphasizes the importance of taking the diffusion of gas molecules in the water into account.

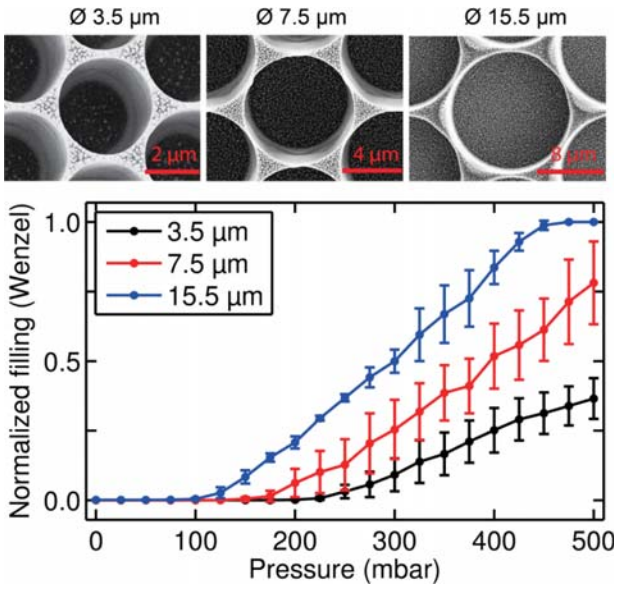

Figure 5. Plots of N_{Wenzel}/N versus Δp measured on COC surfaces of microcavities of different diameters: 3.5, 7.5, and 15.5 μm. The applied pressure Δp was increased at a rate of 25 mbar/min.

To study the effect of surface chemistry, we compared contact angles of surfaces with practically identical structures but made of different materials. Table 1 summarizes the contact angle results of COC and PP surfaces with microcavities of 7.5 μm diameter. PP surfaces have higher apparent contact angles than do COC surfaces because of the fact that the Young contact angles θ_Y for the two materials follow $90° < \theta_{Y_{COC}} < \theta_{Y_{PP}}$. Furthermore, COC surfaces have higher contact angle hysteresis than PP surfaces. In addition, droplets were pinned on COC surfaces even when the sample was tilted up to 180° (Supporting Information), whereas the PP samples have relatively low roll-off angles.

To understand the difference in contact angle hysteresis of COC and PP surfaces, it is necessary to discuss the formation threshold of air pockets in nanocavities (nanograss) along the rims of the microcavities. According to the results of the water wetting experiments and contact angle measurements, the pinning of a water droplet on a COC surface indicates a situation in which nanostructures were wetted while the microcavities remained unwetted. Similar to the situation for the microcavities, the intrusion of water into the nanocavities is governed by a balance between the Young−Laplace pressure of the water menisci and the dissolution of the tiny gas pockets trapped between the nanograss spikes in the water. According to Henry's law, gas molecules will continue to dissolve in water as long as the partial gas pressure is $p_g > k_H c$. In other words, gas molecules will continue to diffuse into water until equilibrium is reached or the gas pockets are completely empty. If the gas pockets disappear before equilibrium is reached, then the droplet will reside on the nanograss spikes in the Wenzel state, leading to the pinning of a droplet. The curvature of the menisci is, however, also influenced by the water contact angle of the substrate material. At equilibrium, $\theta_a = \alpha + 90°$, where 2α is the characteristic opening angle of the nanograss spikes and θ_a is the advancing water contact angle. This relationship can explain the observed difference in droplet pinning for the two materials, PP and COC. In Table 1 we see that droplets are pinned on the COC samples having $\theta_a \approx 102°$ (for unstructured flat surfaces) but not pinned on the PP samples with $\theta_a \approx 110°$. Assuming the same characteristic opening angle 2α for the two sets of samples, we see that 2α must be in the interval of 24−40°. This interval appears plausible when looking at the SEM image of the nanograss in Figure 6b, where the characteristic opening angle was estimated to be in the range of 20−50°.

■ SUMMARY AND CONCLUSIONS

We have presented a simple optical transmission microscopy method to study transitions between the wetting states on

dx.doi.org/10.1021/la502855g | Langmuir 2014, 30, 12960−12968

Table 1. Static and Dynamic Apparent Contact Angles of PP and COC Surfaces with Microcavities of 7.5 μm Diameter

Material	Apparent contact angle (°)	Contact angle hysteresis (°)	Roll-off angle (°)	Roll-off angle images
COC	158 ± 1	55 ± 1	Pinned	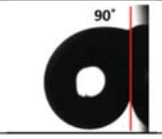
PP	164 ± 3	11 ± 1	7 ± 1	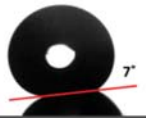

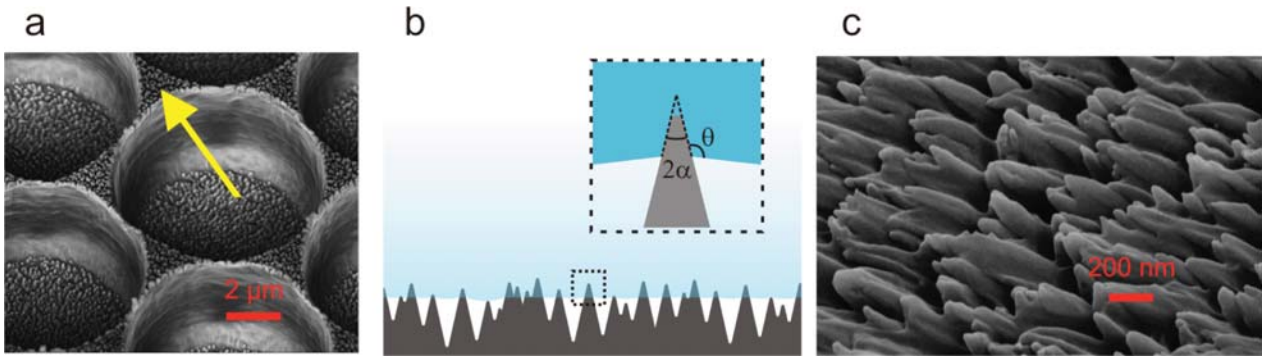

Figure 6. (a) SEM image showing nanograss on the rim of microcavities. (b) Model for the wetting situation of the nanograss showing the characteristic opening angle 2α of the nanograss spikes and the contact angle θ. (c) Scanning electron micrograph of the nanograss as it appears on one of the polymer samples (COC after the injection molding process). The micrograph was taken with the stage tilted by 30°.

polymer hierarchical surface structures when exposed to various liquid pressures. By increasing the liquid pressure, we observed stochastic transitions between the wetting states (Cassie, Cassie-impregnating, and Wenzel) in the microcavities. When the applied pressure is below a certain threshold $\Delta p < 300$ mbar (for 7.5 μm cavities), only a few transitions from the Cassie state to the Wenzel state occurred, and the transition was reversible, and for $\Delta p \geq 300$ mbar, irreversible transitions from the Cassie-impregnating to the Wenzel state occurred. We employed a theoretical model based on both the Young–Laplace equation and Henry's law to explain the degree of water intrusion h over time at different applied pressures Δp. Our model fit the experimental data well for $\Delta p \geq 300$ mbar and with some deviations at lower Δp. We attribute the deviations to counting errors resulting from insignificant intrusion depths h at low Δp. The experimental results thus confirm that the transition between the Cassie and the Cassie-impregnating states is reversible. Furthermore, our data provide experimental evidence for the stochastic nature of water intrusion into the microcavity arrays. This stochastic nature of the intrusion is primarily caused by the short diffusion distance between neighboring cavities for dissolved gas molecules in the water. This effect, we believe, is the key to understanding the sustainability of the superhydrophobicity of surfaces under water and the structural design of superhydrophobic surfaces. Furthermore, we compared the contact angle properties of two polymeric materials with moderate hydrophobicity, COC and PP, and found that the difference in the water repellency of the two materials probably originates from the difference in the wetting of their nanostructures. For lower contact angle material COC, the water droplets pinned on the nanostructures at the rim of the microcavities, but this pinning was not strong enough on the PP surfaces with similar surface structures. Our study indicates that both micro- and nanoscale structures are important to the wetting properties of superhydrophobic surfaces. This importance applies both to the case of surface repellency from liquid droplets and to the sustainability of the liquid repellency of immersed surfaces. For the immersed surfaces, our findings indicate that rather deep cavity structures will perform better over shallow cavities because of the larger entrapped air pockets, although the Young–Laplace equation dictates the same initial curvature of the menisci for both structures.

■ ASSOCIATED CONTENT

Supporting Information

Additional data including a detailed procedure for sample fabrication, intensity normalization, the optical transmission model, results from control experiments, the numerical simulation process of intrusion depth h versus time, and contact angle measurements on microcavities of different diameters. This material is available free of charge via the Internet at http://pubs.acs.org.

■ AUTHOR INFORMATION

Corresponding Authors

*E-mail: lisu@nanotech.dtu.dk.
*E-mail: rata@nanotech.dtu.dk.

Notes

The authors declare no competing financial interest.

■ ACKNOWLEDGMENTS

We acknowledge the assistance of Mr. Emil Højlund-Nielsen with the light-transmittance calculations. This work is supported by the Danish National Advanced Technology Foundation (HTF) through the Advanced Technology Platform NanoPlast (grant no. 007-2010-2).

■ REFERENCES

(1) Liu, Y.; Tang, J.; Wang, R.; Lu, H.; Li, L.; Kong, Y.; Qi, K.; Xin, J. H. Artificial lotus leaf structures from assembling carbon nanotubes and their applications in hydrophobic textiles. *J. Mater. Chem.* **2007**, *17*, 1071−1078.

(2) Xue, C.-H.; Jia, S.-T.; Zhang, J.; Ma, J.-Z. Large-area fabrication of superhydrophobic surfaces for practical applications: an overview. *Sci. Technol. Adv. Mater.* **2010**, *11*, 033002.

(3) Caschera, D.; Cortese, B.; Mezzi, A.; Brucale, M.; Ingo, G. M.; Gigli, G.; Padeletti, G. Ultra Hydrophobic/Superhydrophilic Modified Cotton Textiles through Functionalized Diamond-Like Carbon Coatings for Self-Cleaning Applications. *Langmuir* **2013**, *29*, 2775−2783.

(4) Liu, K.; Yao, X.; Jiang, L. Recent developments in bio-inspired special wettability. *Chem. Soc. Rev.* **2010**, *39*, 3240−3255.

(5) Yan, Y. Y.; Gao, N.; Barthlott, W. Mimicking natural superhydrophobic surfaces and grasping the wetting process: A review on recent progress in preparing superhydrophobic surfaces. *Adv. Colloid Interface Sci.* **2011**, *169*, 80−105.

(6) Ueda, E.; Levkin, P. A. Emerging Applications of Superhydrophilic-Superhydrophobic Micropatterns. *Adv. Mater.* **2013**, *25*, 1234−1247.

(7) Jin, M.; Feng, X.; Feng, L.; Sun, T.; Zhai, J.; Li, T.; Jiang, L. Superhydrophobic Aligned Polystyrene Nanotube Films with High Adhesive Force. *Adv. Mater.* **2005**, *17*, 1977−1981.

(8) Verho, T.; Korhonen, J. T.; Sainiemi, L.; Jokinen, V.; Bower, C.; Franze, K.; Franssila, S.; Andrew, P.; Ikkala, O.; Ras, R. H. A. Reversible switching between superhydrophobic states on a hierarchically structured surface. *Proc. Natl. Acad. Sci. U.S.A.* **2012**, *109*, 10210−10213.

(9) Marmur, A. Wetting on Hydrophobic Rough Surfaces: To Be Heterogeneous or Not To Be? *Langmuir* **2003**, *19*, 8343−8348.

(10) Choi, C.-H.; Ulmanella, U.; Kim, J.; Ho, C.-M.; Kim, C.-J. Effective slip and friction reduction in nanograted superhydrophobic microchannels. *Phys. Fluids* **2006**, *18*, 087105.

(11) Stephani, K. A.; Goldstein, D. B. An Examination of Trapped Bubbles for Viscous Drag Reduction on Submerged Surfaces. *J. Fluids Eng.* **2010**, *132*, 041303−041303.

(12) Samaha, M. A.; Vahedi Tafreshi, H.; Gad-el-Hak, M. Sustainability of superhydrophobicity under pressure. *Phys. Fluids* **2012**, *24*, 112103.

(13) Dilip, D.; Jha, N. K.; Govardhan, R. N.; Bobji, M. S. Controlling air solubility to maintain "Cassie" state for sustained drag reduction. *Colloids Surf., A* **2014**, *459*, 217−224.

(14) Larsen, S. T.; Andersen, N. K.; Søgaard, E.; Taboryski, R. Structure Irregularity Impedes Drop Roll-Off at Superhydrophobic Surfaces. *Langmuir* **2014**, *30*, 5041−5045.

(15) Nosonovsky, M.; Bhushan, B. Biomimetic Superhydrophobic Surfaces: Multiscale Approach. *Nano Lett.* **2007**, *7*, 2633−2637.

(16) Rykaczewski, K.; Paxson, A. T.; Anand, S.; Chen, X.; Wang, Z.; Varanasi, K. K. Multimode Multidrop Serial Coalescence Effects during Condensation on Hierarchical Superhydrophobic Surfaces. *Langmuir* **2012**, *29*, 881−891.

(17) Huovinen, E.; Hirvi, J.; Suvanto, M.; Pakkanen, T. A. Micro−Micro Hierarchy Replacing Micro−Nano Hierarchy: A Precisely Controlled Way To Produce Wear-Resistant Superhydrophobic Polymer Surfaces. *Langmuir* **2012**, *28*, 14747−14755.

(18) Groten, J.; Ruhe, J. Surfaces with Combined Microscale and Nanoscale Structures: A Route to Mechanically Stable Superhydrophobic Surfaces? *Langmuir* **2013**, *29*, 3765−3772.

(19) Bae, W.-G.; Kim, H. N.; Kim, D.; Park, S.-H.; Jeong, H. E.; Suh, K.-Y. 25th Anniversary Article: Scalable Multiscale Patterned Structures Inspired by Nature: the Role of Hierarchy. *Adv. Mater.* **2014**, *26*, 675−700.

(20) Bormashenko, E.; Stein, T.; Pogreb, R.; Aurbach, D. Petal Effect" on Surfaces Based on Lycopodium: High-Stick Surfaces Demonstrating High Apparent Contact Angles. *J. Phys. Chem. C* **2009**, *113*, 5568−5572.

(21) Forsberg, P.; Nikolajeff, F.; Karlsson, M. Cassie-Wenzel and Wenzel-Cassie transitions on immersed superhydrophobic surfaces under hydrostatic pressure. *Soft Matter* **2011**, *7*, 104−109.

(22) Lei, L.; Li, H.; Shi, J.; Chen, Y. Diffraction Patterns of a Water-Submerged Superhydrophobic Grating under Pressure. *Langmuir* **2009**, *26*, 3666−3669.

(23) Bobji, M. S.; Kumar, S. V.; Asthana, A.; Govardhan, R. N. Underwater Sustainability of the "Cassie" State of Wetting. *Langmuir* **2009**, *25*, 12120−12126.

(24) Lee, C.; Kim, C.-J. Underwater Restoration and Retention of Gases on Superhydrophobic Surfaces for Drag Reduction. *Phys. Rev. Lett.* **2011**, *106*, 014502.

(25) Poetes, R.; Holtzmann, K.; Franze, K.; Steiner, U. Metastable Underwater Superhydrophobicity. *Phys. Rev. Lett.* **2010**, *105*, 166104.

(26) Lee, M.; Yim, C.; Jeon, S. Characterization of Underwater Stability of Superhydrophobic Surfaces Using Quartz Crystal Microresonators. *Langmuir* **2014**, *30*, 7931−7935.

(27) Emami, B.; Hemeda, A. A.; Amrei, M. M.; Luzar, A.; Gad-el-Hak, M.; Vahedi Tafreshi, H. Predicting longevity of submerged superhydrophobic surfaces with parallel grooves. *Phys. Fluids* **2013**, *25*, 062108.

(28) Cassie, A. B. D.; Baxter, S. Wettability of porous surfaces. *Trans. Faraday Soc.* **1944**, *40*, 546−551.

(29) Whyman, G.; Bormashenko, E.; Stein, T. The rigorous derivation of Young, Cassie−Baxter and Wenzel equations and the analysis of the contact angle hysteresis phenomenon. *Chem. Phys. Lett.* **2008**, *450*, 355−359.

(30) Lv, P.; Xue, Y.; Shi, Y.; Lin, H.; Duan, H. Metastable States and Wetting Transition of Submerged Superhydrophobic Structures. *Phys. Rev. Lett.* **2014**, *112*, 196101.

(31) Wenzel, R. N. Resistance of Solid Surfaces to Wetting by Water. *Ind. Eng. Chem.* **1936**, *28*, 988−994.

(32) Adera, S.; Raj, R.; Enright, R.; Wang, E. N. Non-wetting droplets on hot superhydrophilic surfaces. *Nat. Commun.* **2013**, *4*, 2518.

(33) Boreyko, J. B.; Chen, C.-H. Restoring Superhydrophobicity of Lotus Leaves with Vibration-Induced Dewetting. *Phys. Rev. Lett.* **2009**, *103*, 174502.

(34) Krupenkin, T. N.; Taylor, J. A.; Wang, E. N.; Kolodner, P.; Hodes, M.; Salamon, T. R. Reversible Wetting−Dewetting Transitions on Electrically Tunable Superhydrophobic Nanostructured Surfaces. *Langmuir* **2007**, *23*, 9128−9133.

(35) Lapierre, F.; Coffinier, Y.; Boukherroub, R.; Thomy, V. Electro-(de)wetting on Superhydrophobic Surfaces. *Langmuir* **2013**, *29*, 13346−13351.

(36) Lafuma, A.; Quere, D. Superhydrophobic states. *Nat. Mater.* **2003**, *2*, 457−460.

(37) Boreyko, J. B.; Collier, C. P. Dewetting Transitions on Superhydrophobic Surfaces: When Are Wenzel Drops Reversible? *J. Phys. Chem. C* **2013**, *117*, 18084−18090.

(38) Tsai, P.; Lammertink, R. G. H.; Wessling, M.; Lohse, D. Evaporation-Triggered Wetting Transition for Water Droplets upon Hydrophobic Microstructures. *Phys. Rev. Lett.* **2010**, *104*, 116102.

(39) Checco, A.; Ocko, B. M.; Rahman, A.; Black, C. T.; Tasinkevych, M.; Giacomello, A.; Dietrich, S. Collapse and Reversibility of the Superhydrophobic State on Nanotextured Surfaces. *Phys. Rev. Lett.* **2014**, *112*, 216101.

(40) Xu, X.; Vereecke, G.; Chen, C.; Pourtois, G.; Armini, S.; Verellen, N.; Tsai, W.-K.; Kim, D.-W.; Lee, E.; Lin, C.-Y.; Van Dorpe, P.; Struyf, H.; Holsteyns, F.; Moshchalkov, V.; Indekeu, J.; De Gendt, S. Capturing Wetting States in Nanopatterned Silicon. *ACS Nano* **2013**, *8*, 885−893.

(41) Samaha, M. A.; Ochanda, F. O.; Tafreshi, H. V.; Tepper, G. C.; Gad-el-Hak, M. In situ, noninvasive characterization of superhydrophobic coatings. *Rev. Sci. Instrum.* **2011**, *82*, 045109.
(42) Dufour, R.; Saad, N.; Carlier, J.; Campistron, P.; Nassar, G.; Toubal, M.; Boukherroub, R.; Senez, V.; Nongaillard, B.; Thomy, V. Acoustic Tracking of Cassie to Wenzel Wetting Transitions. *Langmuir* **2013**, *29*, 13129−13134.
(43) Patankar, N. A. Consolidation of Hydrophobic Transition Criteria by Using an Approximate Energy Minimization Approach. *Langmuir* **2010**, *26*, 8941−8945.
(44) Salvadori, M. C.; Cattani, M.; Oliveira, M. R. S.; Teixeira, F. S.; Brown, I. G. Design and fabrication of microcavity-array superhydrophobic surfaces. *J. Appl. Phys.* **2010**, *108*, 024908.
(45) Xue, Y.; Chu, S.; Lv, P.; Duan, H. Importance of Hierarchical Structures in Wetting Stability on Submersed Superhydrophobic Surfaces. *Langmuir* **2012**, *28*, 9440−9450.
(46) See the Supporting Information for this article.
(47) Larsen, S. T.; Taboryski, R. A Cassie-Like Law Using Triple Phase Boundary Line Fractions for Faceted Droplets on Chemically Heterogeneous Surfaces. *Langmuir* **2009**, *25*, 1282−1284.
(48) Feng, L.; Zhang, Y.; Xi, J.; Zhu, Y.; Wang, N.; Xia, F.; Jiang, L. Petal Effect: A Superhydrophobic State with High Adhesive Force. *Langmuir* **2008**, *24*, 4114−4119.
(49) Christiansen, A. B.; Clausen, J.; Asger Mortensen, N.; Kristensen, A. Minimizing scattering from antireflective surfaces replicated from low-aspect-ratio black silicon. *Appl. Phys. Lett.* **2012**, *101*, 131902.
(50) García-Vidal, F. J.; Pitarke, J. M.; Pendry, J. B. Effective Medium Theory of the Optical Properties of Aligned Carbon Nanotubes. *Phys. Rev. Lett.* **1997**, *78*, 4289−4292.
(51) Koishi, T.; Yasuoka, K.; Fujikawa, S.; Ebisuzaki, T.; Zeng, X. C. Coexistence and transition between Cassie and Wenzel state on pillared hydrophobic surface. *Proc. Natl. Acad. Sci. U.S.A.* **2009**, *106*, 8435−8440.
(52) Epstein, P. S.; Plesset, M. S. On the Stability of Gas Bubbles in Liquid - Gas Solutions. *J. Chem. Phys.* **1950**, *18*, 1505−1509.
(53) Ljunggren, S.; Eriksson, J. C. The lifetime of a colloid-sized gas bubble in water and the cause of the hydrophobic attraction. *Colloids Surf., A* **1997**, *129−130*, 151−155.

Appendix 4

Simon Tylsgaard Larsen, Nis Korsgaard Andersen, **Emil Søgaard**, and Rafael Taboryski. *Structure Irregularity Impedes Drop Roll-Off at superhydrophobic Surfaces.* Langmuir, Vol. 30 no. 17, pp 5041-5045. 2014.

Contribution: Participation in concept development of initial line based structures, and development of the fabrication process.

Langmuir

Article

pubs.acs.org/Langmuir

Structure Irregularity Impedes Drop Roll-Off at Superhydrophobic Surfaces

Simon Tylsgaard Larsen, Nis Korsgaard Andersen, Emil Søgaard, and Rafael Taboryski*

Department of Micro- and Nanotechnology, Technical University of Denmark, DTU Nanotech, Building 345E, DK-2800 Kongens Lyngby, Denmark

ABSTRACT: We study water drop roll-off at superhydrophobic surfaces with different surface patterns. Superhydrophobic microcavity surfaces were fabricated in silicon and coated with 1*H*,1*H*,2*H*,2*H*-perfluorodecyltrichlorosilane (FDTS). For the more irregular surface patterns, the observed increase in roll-off angles is found to be caused by a decrease of the receding contact angle, which in turn is caused by an increase of the triple phase contact line of the drops for those more irregular surfaces. To understand the observation, we propose to treat the microdrops as rigid bodies and apply a torque balance between the torque exerted by the projected gravity force and the torque exerted by the adhesion force acting along the triple line on the receding side of the drop. This simple model provides a proper order of magnitude estimate of the measured effects.

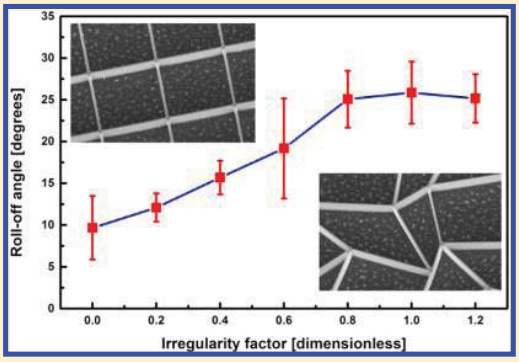

INTRODUCTION

Inspired by the water-repellant properties of many plant leaves,[1] artificial superhydrophobic surfaces have received much attention in the past decade.[2,3] Superhydrophobicity is often achieved by applying micro- and nanostructures to a flat and chemically hydrophobic surface. The surface structures will keep a drop resting on the surface in a suspended state, only touching the top of the structures. In this case, the contact angle is traditionally described in the framework of the Cassie equation[4,5] and depends only on the hydrophobicity of the surface material and the fractional area of contact between the water and the solid surface. Some recent work has however stressed the importance of the conditions along the triple-phase line of the droplets resting on the surface.[6] A common design for superhydrophobic surfaces is nanometer-sized, random surface roughness applied to regularly distributed, micrometer-sized pillars. A range of silicon microfabrication techniques have been used to fabricate surface structures,[7−12] including advanced pillar structures with undercut[13] and sidewall roughness.[14]

In many practical applications like underwater friction reduction[15,] and low-biofouling materials,[17] water repellency is not the only important property. Also, the surfaces have to be stable in their superhydrophobic state when immersed in water. The superhydrophobic nature of the surface relies on the existence of a thin layer of air pockets between the solid surface and the liquid. If the air layer is not stable, the liquid will wet the entire surface irreversibly, resulting in a transition from the Cassie state to the so-called Wenzel state and an associated abrupt decrease in contact angle. Structures made of pillars or other protrusions are especially vulnerable to this transition, since a local collapse of the Cassie state will spread out to the remaining surface.[18] In contrast, superhydrophobic surfaces made of microcavities are relatively stable underwater due to the existence of many separate, confined air pockets. However, for droplets moving across the surface, microcavity surfaces have been shown to possess different wetting properties from pillars even for similar surface coverage.[19] Microcavity surfaces have been fabricated in silicon[20,21] and polymer[18,22,23] with static contact angles in the same range as for pillar surfaces.

Superhydrophobic surfaces are often characterized by their contact angle. In terms of water repellency though, another interesting property of the surfaces is the roll-off angle—the angle which the substrate should be tilted to make the drop roll off. This angle depends not only on the contact angle but also on the difference between the advancing and receding contact angles of the drop, the so-called contact angle hysteresis.[24] In fact, surfaces can exhibit large equilibrium contact angles and still pin droplets at 90° tilting of the substrate.[11] Since drop roll-off is determined by the pinning of the triple-contact line of the drop,[25] it must depend on the local configuration of this line and thus the geometry of the surface microstructures. The pinning of the triple-contact line is caused by adhesion forces acting on the microscale by formation of capillary bridges along the triple-contact line on the receding side of the bridge.[26] For superhydrophobic surfaces made of round and square pillars, it was shown that the contact angle hysteresis was larger for square pillars.[27] This was explained by pinning of the drop to the sharper edges of these structures. In this paper, we present a systematic study of drop roll-off at superhydrophobic cavity surfaces with varying degree of regularity. Moreover, we provide a simple model to explain the often observed

Received: February 25, 2014
Revised: April 15, 2014
Published: April 15, 2014

   dx.doi.org/10.1021/la5007633 | *Langmuir* 2014, 30, 5041−5045

relationship between contact angle hysteresis and surface structure irregularity. In this model the effect is caused by adhesive forces with action predominantly along the triple-contact line on the receding side of the moving drop. Although demonstrated for cavity types of surface structures in this paper, we believe this effect is general and applies to any super-hydrophobic surface.

EXPERIMENTAL SECTION

The silicon wall structures shown in Figure 1 were fabricated from a photomask using photolithography and dry etching. A Python program was used to define the photomask text file. First a regular square-shaped array of (x, y) points was defined with side a length x_0. Next, irregularity was introduced by moving each point to a random position in a square centered on this point. The level of irregularity was adjusted by increasing the side length Δx_0 of the square in which the points could be moved to a random position and quantified by an irregularity factor defined as the side length of this square divided by the distance between points in the original array $\Delta x_0/x_0$. An irregularity factor of 0 thus represents an ordered square array while 1 represents an almost completely irregular array (see Figure 1). Grids were fabricated from arrays starting with respectively x_0 = 10 μm and x_0 = 20 μm side length and with irregularity factors of 0.0, 0.2, 0.4, 0.6, 0.8, 1.0, and 1.2. Finally the points were connected with thin rectangles defining the wall structures. The width of the walls is adjusted to ensure that the total projected area of the wall structures is constant and ranges from 400 nm for the ordered structures to 354 nm for the most irregular structures. The average length of the lines $\langle x' \rangle$ however increases with the irregularity factor $\Delta x_0/x_0$ and can readily be calculated from the photolithography mask layout file. This is shown in Figure 1e, where we calculated and plotted the quantity $l' = \langle x' \rangle / x_0$. We note that l' is an injective function of the irregularity factor.

A thin layer of photoresist was applied to 4 in. silicon wafers, and the photomask pattern was transferred to the photoresist using a Canon FPA-3000 EX4-Deep UV Stepper. Next, the wafers were etched with a D-RIE process (STS Pegasus DRIE) to a target depth of 3.0 μm. The photoresist was removed by an oxygen plasma process (ashing), and the hydrophobicity of the structured silicon surfaces was increased by applying a monolayer of 1*H*,1*H*,2*H*,2*H*-perfluorodecyltrichlorosilane (FDTS) by molecular vapor deposition with an Applied Microstructures MVD 100. Three identical wafers were fabricated, and all measurements were carried out within 1 week after FDTS coating. Scanning electron microscope (SEM) images were performed with a LEO 1550 scanning electron microscope. An Attension Theta optical tensiometer was used to measure roll-off angles and contact angles. Drop volumes were always 5 μL.

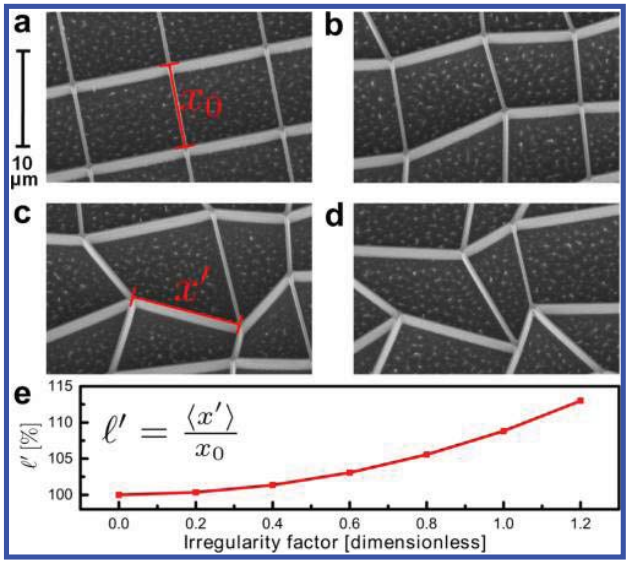

Figure 1. SEM images of wall structures in silicon. From (a) to (d) the imposed irregularity increases, going from square-shaped wall structures to a chaotic grid of walls. Irregularity factors are (a) 0, (b) 0.4, (c) 0.8, and (d) 1.2. (e) $l' = \langle x' \rangle / x_0$ plotted vs the irregularity factor. $\langle x' \rangle$ is the average side length of the perturbed structures. The irregularity factor is defined as the side length Δx_0 of the square in which the points could be moved to a random position divided by the distance between points in the original array $\Delta x_0/x_0$.

RESULTS AND DISCUSSION

Figure 1 shows SEM images of increasingly irregular wall structures starting from a regular grid with a square side length of 10 μm. Static contact angles were measured for all 14 different surface geometries on three different wafers, giving an average static contact angle of 158.6 ± 1.7°. For flat FDTS-coated areas on the same wafers over eight droplets, the contact angle was 113.7 ± 3.1°. The errors reported in our measurements are the standard deviations on each set of measurements. The increase in contact angle implies that the water drops are in the Cassie–Baxter state, only touching the top of the thin wall structures. Since the variation in static contact angle of the structured surfaces is very small, we can conclude that the static contact angle does not depend on the shape of the wall structures but rather on the surface coverage area fraction (which is constant for our surfaces) as predicted by the Cassie–Baxter equation.

Next, we studied the effect of pattern irregularity on the roll-off angle, i.e., the angle which the surface should be tilted for the drop to roll off. While pattern irregularity has little effect on the static contact angle, the effect on roll-off angles is significant. As seen from Figure 2, the angles at which a drop rolls completely off the surface (black lines) increase dramatically for more irregular structures. Also, for the smaller structures (10 μm, solid line) roll-off angles are higher than for larger structures (20 μm, dashed line). An interesting observation is made when we compare the tilting angles for complete roll-off with the angles where the drop makes its first

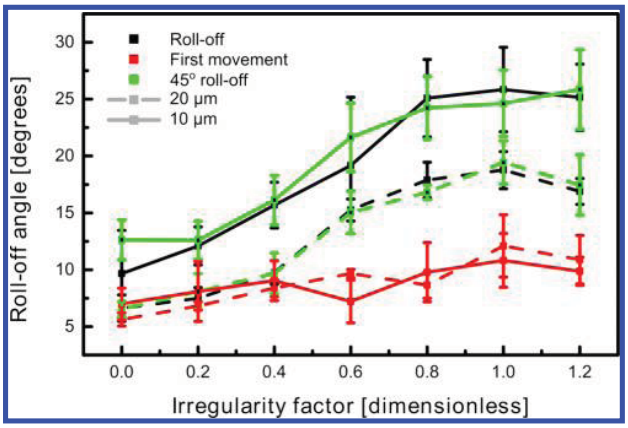

Figure 2. Water drop roll-off angles plotted against the irregularity factor of the microstructured surfaces. Red lines represent the tilted angle at which the drop makes the first sliding movement. Black lines represent the angle at which the drop rolls off the surface completely. Green lines represent complete roll-off angles for surfaces that are rotated 45° relative to the roll-off direction. Solid and dashed lines represents structures with x_0 = 10 μm and x_0 = 20 μm, respectively.

dx.doi.org/10.1021/la5007633 | *Langmuir* 2014, 30, 5041–5045

movement (red lines, Figure 2). Clearly, the latter remain relatively constant for the different surfaces. In other words, for the regular wall structures water drops roll off the surface completely, shortly after they make the first movement, while for the irregular surfaces they tend to move in steps until they roll off at a larger contact angle. Probably this behavior at irregular surfaces is connected to the many possible local configurations of the triple-contact line. For the drop to roll off completely, the configuration with the strongest adhesion along the triple-contact line has to be overcome.

Since the more regular structures are directional of nature, we repeated the roll-off measurements with the surfaces rotated 45° relative to the previous roll-off direction (green lines, Figure 2). Regardless of rotation of the sample, we observed the same roll-off angles, suggesting that pinning of the drop takes effect on a band at the perimeter of the drop, where the directional effects averages out, and the important parameter is the line density per area. Clearly, complete roll-off angles are larger for the more irregular structures. The observed roll-off angles appear to be closely connected to the contact angle hysteresis and can be understood as resulting from a force balance between the projected gravity force and the projected line force acting along the triple-contact line. This relationship can be expressed in the well-known equation[28]

$$\rho g V \sin \alpha = 2\gamma a(\cos \theta_R - \cos \theta_A) \quad (1)$$

where ρ is the mass density of the liquid, g the acceleration of gravity, V the volume of the sessile drop, α the inclination angle of the plane on which the drop will roll, γ the surface tension of the liquid, a the radius of the apparent interface area between the drop and the substrate, and θ_R, θ_A the receding and advancing contact angles, respectively. In Figure 3 we plot the

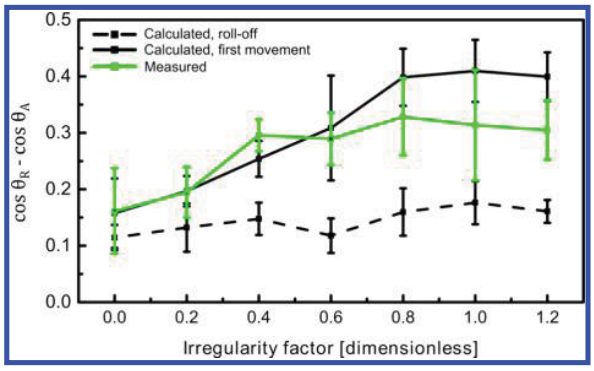

Figure 3. Contact angle hysteresis, plotted as the difference of the cosines of measured receding and advancing contact angles as a function the irregularity factor. The black full line shows the contact angle hysteresis calculated by eq 1 corresponding to the roll-off angles corresponding to complete roll-off, while the dashed black line is calculated using the tilt angles corresponding to the first movement of the drops. Only data for $x_0 = 10$ μm are shown. $2a = 726$ μm is used in the calculation, corresponding to a static contact angle of 160°. The error bars for the calculated hysteresis stem from the experimental variation in the tilt angle data.

difference of the cosines of measured receding and advancing contact angles as a function the irregularity factor for our structures together with the prediction given by eq 1. This is done using the tilt angles both for the first movement of the drop and for the complete roll-off. We see that the data fit well in between the two limits, first movement and complete roll-off, calculated using eq 1.

However, eq 1 only predicts the relationship between contact angle hysteresis and tilt angle but provides no explanation why contact angle hysteresis increases when the structures become more irregular. A deeper understanding of the behavior of the roll-off angles can be obtained by studying the advancing and receding contact angles of the surfaces, measured as the front and rear contact angles just before drop roll-off. Recent environmental scanning electron microscopic studies of contact line depinning from textured surfaces[26] show that while the drop on the advancing side simply rolls over the surface, the receding triple-contact line is pinned to the surface by the creation of capillary bridges that exerts an adhesion force between the surface textures and the drop surface.

As shown in Figure 4, this force F is effectively strongest at the most rear part of the triple-contact line, where the capillary

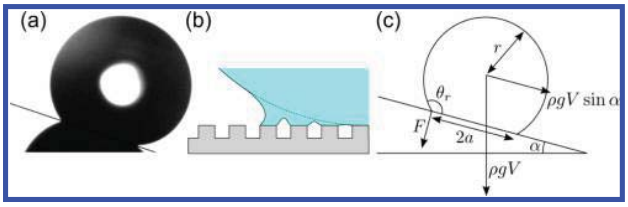

Figure 4. Graphical illustration of the model leading to eq 3. (a) Drop profile recorded with the camera on the contact angle goniometer at a tilt angle. (b) Sketch showing imagined formation of capillary bridges between the drop and the surface structure at the triple phase line. (c) Sketch of the drop geometry in the roll situation; the torque associated with the adhesion force F at the triple line is balanced by the torque associated with the gravity force ρgV projected through the tilt angle α.

bridge is most stretched. Because of its small size, a sessile drop is only slightly perturbed from a round shape even when the plane is tilted as seen in Figure 4a, and if we further make the approximation of treating the drop as a rigid body, we may look at the torque exerted by the adhesion force on the drop that will prevent the drop from rolling. The numerical value of this torque will be of order $\tau_\perp \sim aF$. The numerical value of the torque that on the other hand will roll the drop will be of order $\tau_\parallel \sim r \sin(\theta_R - \pi/2)\rho g V \sin \alpha$, where r is the radius of the drop. We may then express the rolling condition as $\tau_\parallel > \tau_\perp$. In order to relate the receding contact angle to the irregularity factor, we recall that the surface tension can be expressed as a force per unit of length and express the effective adhesion force as the product of surface tension and some length

$$F = \gamma l_0 l' \quad (2)$$

where l_0 is the characteristic length of the piece of triple-contact line along which the force effectively acts, while l' is the dimensionless relative length plotted in Figure 1e as a function of the irregularity factor. The justification for multiplying with l' is that the adhesion force acts through the formed capillary bridge and the longer the structure lines are, the longer will be the effective piece of triple-contact line along which the bridge can attach. We should expect that l_0, within a numerical constant, is of order the radius a of the apparent interface area but considerably larger than the structure side length x_0. By employing the roll condition and inserting $a = r \cos(\theta_R - \pi/2)$, we can equate the torques $\tau_\parallel$ and $\tau_\perp$ and solve for θ_R to predict the critical receding contact angle at which the drop will roll:

dx.doi.org/10.1021/la5007633 | Langmuir 2014, 30, 5041−5045

$$\theta_R = \tan^{-1}\left(\frac{\gamma l_0 l'}{\rho g V \sin\alpha}\right) + \frac{\pi}{2} \quad (3)$$

A somewhat similar expression but based on a force balance and leading to a different functional dependence was recently proposed by Papadopoulos et al.[29] for a pillar structure. In Figure 5, the receding and advancing contact angles are plotted against the irregularity factor of the surfaces. While the advancing contact angles stay approximately constant around 160°, the receding contact angles decrease with increasing irregularity. This implies that the pinning of the triple-contact line at the rear end of the drop is the most important factor for drop roll-off at these surfaces. This observation can be explained by a model where the drop depins from the surface by gradual stretching and eventual snatching of capillary bridges along the triple line on the receding side of the rolling drop. In Figure 5, we show the fit of the expression for the receding angle given by eq 3 to the data using l_0 as an adjustable fitting parameter. l' is given by the curve in Figure 1e, while the roll-off angle α is taken from the data in Figure 2, V = 5 μL, and γ = 72 mN/m. The fitting results in l_0 = 163 μm for the x_0 = 10 μm structures, while l_0 = 144 μm is obtained for the x_0 = 20 μm structures. For a sessile drop of 5 μL used in the experiment, the drop radius is $r \approx 1$ mm, and for a static contact angle of 160°, we get a radius of the interface area of $a \approx 363$ μm, which is very roughly within a factor of 2 from the fitted values for l_0. This seems consistent with the aforementioned averaging of the pinning force along the perimeter of the drop over a band that is broad enough to cancel the effect of the 45° rotation.

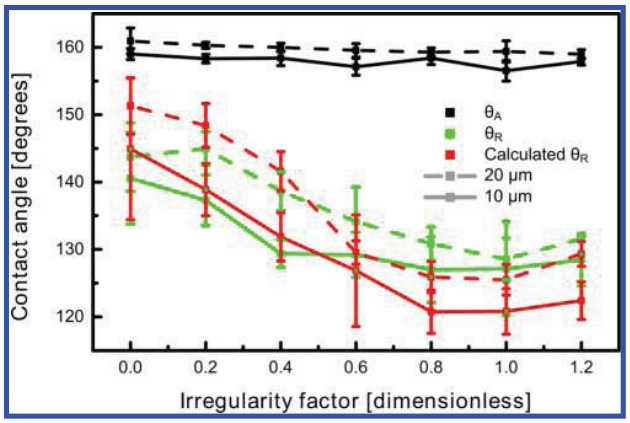

Figure 5. Receding and advancing contact angles plotted against the irregularity factor for the microstructured surfaces. The receding and advancing contact angles were measured as the front and rear contact angle of a water drop immediately before complete roll-off. The red lines are fitted to receding contact angle data using the characteristic length $l_0$as an adjustable fitting parameter in eq 3. Solid and dashed lines represents structures with x_0 = 10 μm and x_0 = 20 μm, where the fitting parameters obtained are l_0 = 163 μm, and l_0 = 144 μm, respectively.

CONCLUSION

In this paper, we studied the effect of microstructure geometry of superhydrophobic, cavity surfaces on water drop roll-off angles as well as receding and advancing contact angles. We observed that static and advancing contact angles remained constant over surfaces ranging from regular to completely irregular. Roll-off angles on the other hand increased for increasing irregularity regardless of roll-off direction. Receding contact angles decreased for increasing irregularity and could be described by a simple torque balance relationship involving the gravity force projected in the direction of motion and an adhesion force acting perpendicular to the direction of motion and acting along the rear section of the triple-contact line. This implies that an increased pinning of the triple-contact line at the rear end of the drop is responsible for larger roll-off angles at more irregular surfaces. For the regular wall structures water drops roll off the surface completely, shortly after they make the first movement, while for the irregular surfaces they tend to move in steps until they roll off at a larger angle. This behavior at irregular surfaces is probably connected to the many possible local configurations of the triple-contact line. For the drop to roll off completely, the configuration with the strongest adhesion corresponding to the longest triple-contact adhesion line has to be overcome. This work calls for a more exact theory. Such a theory would involve integration of the adhesion force from the whole interface area and take into account the capillary bridge nature of the adhesion. The effective adhesion force contributing to the torque will depend on the specific micro/nano topology of the surface texture, but we expect the physics to be the same for any superhydrophobic surface chemistry and surface texture.

AUTHOR INFORMATION

Corresponding Author

*E-mail rata@nanotech.dtu.dk (R.T.).

Author Contributions

S.T.L. and N.K.A. contributed equally.

Notes

The authors declare no competing financial interest.

ACKNOWLEDGMENTS

This work is supported by the Danish National Advanced Technology Foundation (HTF) through the "Advanced Technology Project LANI" (grant 011-2011-3) and through the "Advanced Technology Platform NanoPlast" (grant 007-2010-2).

REFERENCES

(1) Barthlott, W.; Neinhuis, C. Purity of the Sacred Lotus, or Escape from Contamination in Biological Surfaces. *Planta* **1997**, *202*, 1−8.

(2) Roach, P.; Shirtcliffe, N. J.; Newton, M. I. Progess in Superhydrophobic Surface Development. *Soft Matter* **2008**, *4*, 224−240.

(3) Feng, X.; Jiang, L. Design and Creation of Superwetting/Antiwetting Surfaces. *Adv. Mater.* **2006**, *18*, 3063−3078.

(4) Cassie, A. B. D.; Baxter, S. Wettability of Porous Surfaces. *Trans. Faraday Soc.* **1944**, *40*.

(5) Whyman, G.; Bormashenko, E.; Stein, T. The Rigorous Derivation of Young, Cassie-Baxter and Wenzel Equations and the Analysis of the Contact Angle Hysteresis Phenomenon. *Chem. Phys. Lett.* **2008**, *450*, 355−359.

(6) Larsen, S. T.; Taboryski, R. A Cassie-Like Law Using Triple Phase Boundary Line Fractions for Faceted Droplets on Chemically Heterogeneous Surfaces RID C-9321-2011. *Langmuir* **2009**, *25*, 1282−1284.

(7) Xiu, Y.; Zhu, L.; Hess, D. W.; Wong, C. P. Hierarchical Silicon Etched Structures for Controlled Hydrophobicity/Superhydrophobicity. *Nano Lett.* **2007**, *7*, 3388−3393.

(8) Bhushan, B.; Koch, K.; Jung, Y. C. Biomimetic Hierarchical Structure for Self-Cleaning. *Appl. Phys. Lett.* **2008**, *93*, 093101−093101.
(9) Chen, M.; Hsu, T.; Chuang, Y.; Tseng, F. Dual Hierarchical Biomimic Superhydrophobic Surface with Three Energy States. *Appl. Phys. Lett.* **2009**, *95*, 023702−023702.
(10) Sun, G.; Gao, T.; Zhao, X.; Zhang, H. Fabrication of Micro/Nano Dual-Scale Structures by Improved Deep Reactive Ion Etching. *J. Micromech. Microeng.* **2010**, *20*, 075028−075028.
(11) Winkleman, A.; Gotesman, G.; Yoffe, A.; Naaman, R. Immobilizing a Drop of Water: Fabricating Highly Hydrophobic Surfaces That Pin Water Droplets. *Nano Lett.* **2008**, *8*, 1241−1245.
(12) Kim, H.; Lee, C.; Kim, M. H.; Kim, J. Drop Impact Characteristics and Structure Effects of Hydrophobic Surfaces with Micro- and/or Nanoscaled Structures. *Langmuir* **2012**, *28*, 11250−11257.
(13) Wang, J.; Liu, F.; Chen, H.; Chen, D. Superhydrophobic Behavior Achieved from Hydrophilic Surfaces. *Appl. Phys. Lett.* **2009**, *95*, 084104−084104.
(14) Lee, C.; Kim, C. Maximizing the Giant Liquid Slip on Superhydrophobic Microstructures by Nanostructuring Their Sidewalls. *Langmuir* **2009**, *25*, 12812−12818.
(15) Voronov, R. S.; Papavassiliou, D. V.; Lee, L. L. Review of Fluid Slip Over Superhydrophobic Surfaces and Its Dependence on the Contact Angle. *Ind. Eng. Chem. Res.* **2008**, 47.
(16) Choi, C.; Ulmanella, U.; Kim, J.; Ho, C.; Kim, C. Effective Slip and Friction Reduction in Nanograted Superhydrophobic Microchannels. *Phys. Fluids* **2006**, *18*, 087105−087105.
(17) Marmur, A. Underwater Superhydrophobicity: Theoretical Feasibility. *Langmuir* **2006**, *22*, 1400−1402.
(18) Salvadori, M. C.; Cattani, M.; Oliveira, M. R. S.; Teixeira, F. S.; Brown, I. G. Design and Fabrication of Microcavity-Array Superhydrophobic Surfaces. *J. Appl. Phys.* **2010**, *108*, 024908−024908.
(19) Priest, C.; Albrecht, T. W. J.; Sedev, R.; Ralston, J. Asymmetric Wetting Hysteresis on Hydrophobic Microstructured Surfaces. *Langmuir* **2009**, *25*, 5655−5660.
(20) Bobji, M. S.; Kumar, S. V.; Asthana, A.; Govardhan, R. N. Underwater Sustainability of the "Cassie" State of Wetting. *Langmuir* **2009**, *25*, 12120−12126.
(21) Pietsch, T.; Gindy, N.; Fahmi, A. Nano- and Micro-Sized Honeycomb Patterns through Hierarchical Self-Assembly of Metal-Loaded Diblock Copolymer Vesicles. *Soft Matter* **2009**, *5*, 2188−2197.
(22) Huang, Y.; Wu, J.; Yang, S. Direct Fabricating Patterns Using Stamping Transfer Process with PDMS Mold of Hydrophobic Nanostructures on Surface of Micro-Cavity. *Microelectron. Eng.* **2011**, *88*, 849−854.
(23) Rasilainen, T.; Kirveslahti, A.; Nevalainen, P.; Suvanto, M.; Pakkanen, T. A. Controlling the Movement of Water Droplets with Micro- and Hierarchical Micro/nanostructures. *Surf. Rev. Lett.* **2011**, *18*, 209−222.
(24) McHale, G.; Shirtcliffe, N.; Newton, M. Contact-Angle Hysteresis on Super-Hydrophobic Surfaces. *Langmuir* **2004**, *20*, 10146−10149.
(25) Choi, W.; Tuteja, A.; Mabry, J. M.; Cohen, R. E.; McKinley, G. H. A Modified Cassie-Baxter Relationship to Explain Contact Angle Hysteresis and Anisotropy on Non-Wetting Textured Surfaces. *J. Colloid Interface Sci.* **2009**, *339*, 208−216.
(26) Paxson, A. T.; Varanasi, K. K. Self-Similarity of Contact Line Depinning from Textured Surfaces. *Nat. Commun.* **2013**, *4*, 1492.
(27) Cansoy, C. E.; Erbil, H. Y.; Akar, O.; Akin, T. Effect of Pattern Size and Geometry on the Use of Cassie-Baxter Equation for Superhydrophobic Surfaces. *Colloids Surf., A* **2011**, *386*, 116−124.
(28) Furmidge, C. Studies at Phase Interfaces. 1. Sliding of Liquid Drops on Solid Surfaces and a Theory for Spray Retention. *J. Colloid Sci.* **1962**, *17*, 309.
(29) Papadopoulos, P.; Mammen, L.; Deng, X.; Vollmer, D.; Butt, H. How Superhydrophobicity Breaks Down. *Proc. Natl. Acad. Sci. U. S. A.* **2013**, *110*, 3254−3258.

Appendix 5

Emil Søgaard, Kristian Smistrup, Nis Korsgaard Andersen and Rafael Taboryski. *Injection molded superhydrophobic surfaces based on microlithography and black silicon processing.* Nanotech 2012 - TechConnect World.

Contribution: Development of the idea for the injection molded hierarchical nanograss structures. Participation in the microstructure design. Cleanroom fabrication and injection molding of all structures. Characterization of samples and data processing. Manuscript preparation.

Injection molded superhydrophobic surfaces based on microlithography and black silicon processing

Emil Søgaard*, Kristian Smistrup**, Nis Korsgaard Andersen* and Rafael Taboryski*

* Department of Micro- and Nanotechnology, Technical University of Denmark, DTU Nanotech, Building 345B, DK-2800 Kongens Lyngby Denmark,
emil.sogaard@nanotech.dtu.dk, Mobile +45 21444236.
** NIL Technology, Diplomvej 381, DK-2800 Kongens Lyngby, Denmark.

ABSTRACT

This work is concerned with the design, development, and testing of nanostructured polymer surfaces with self-cleaning properties that can be manufactured by injection molding. In particular, the superimposed micro- and nanometer length scales of the so-called Lotus effect were investigated in detail with an engineering perspective on choice of materials and manufacturability by injection molding. Microscope slides with superhydrophobic properties were succesfully fabricated. Preliminary results indicate a contact angle increase from 95° for the unstructured polymer to a maximum 150°. The lowest drop roll off angles observed were in the range 1° to 5°.

Keywords: injection molding, black silicon, super-hydrophobic, polymer, surface functionalization

1 INTRODUCTION

Micro- and nanostructuring can be used to functionalize surfaces to obtain super hydrophobicity and self-cleaning properties [1].Traditionally surfaces are functionalized for such properties with chemical or nanoparticle coatings. However, chemical and nanoparticle surface coatingss add potentially hazardous chemicals or nanoparticles to the products, and are often expensive.might be toxic and therefore, their use is limited. Furthermore, the production is time consuming and often is expensive.

The Lotus effect [2] is used as inspiration for the fabrication of injection molded polymer surfaces with self-cleaning properties. Self-cleaning surface properties are often obtained by having hierarchical nano- and microstructures[3]. Injection molded hierarchical nano- and microstructures from thin aluminum foils have been demonstrated by e.g. Puukilainen et al [4]. Here, we present a new method for the fabrication of tool inserts with hierarchical nano- and microstructures (Figure 1). The method is based on a UV LIGA [5] process combined with a black silicon etch. FDTS coated silicon microstructures with black silicon are known to be superhydrophobic [6].

The advantage of our method is the industrial manufacturability associated with the LIGA process and injection molding combinded the superior superhydrophic properties due to the hierarchical micro and nanostructures. Surfaces with self-cleaning properties that imitate, e.g. the lotus flower, are of relevance for the medical equipment and food industries. Food containers can be designed so they can be completely emptied leading to less or no waste.

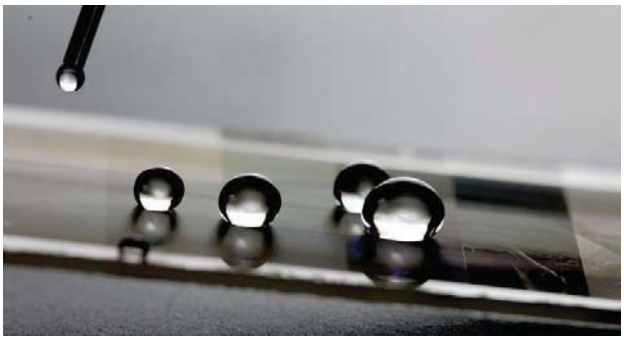

Figure 1: Drops on slightly tilted surface, excellent superhydrophobic properties.

2 METHODS

Test areas with microstructures in the form of circular pillars were fabricated with standard photolithography on clean Si wafers. The entire fabrication process is shown in Figure 2. A 1 µm photoresist layer was spin coated on to the silicon wafers. Circular pillars 3-8 µm in diameter with a pitch of 3-15 µm were defined with UV-lithography and etched to a depth of 3 µm with a DRIE process. These microstructures were combined with nanostructures fabricated by etching of black silicon.

The black silicon process was carried out in the DRIE system. No predefined mask was used; the structures were etched by perforating the native oxide layer combined with a passivation layer from the etching process. Holes in the native oxide layer were etched. With the correct choice of plasma parameters the results become cone shape structures [7]. The black silicon etch produced roughly 100 nm wide cone-like structures with an aspect ratio of about 1.

The injection molding insert (shim) was fabricated from the structured silicon wafer by deposition of a 100 nm thick layer of nickel vanadium followed by nickel electroplating. The silicon wafer was subsequently removed by a KOH etch, leaving a nickel insert with inverse polarity. A variotherm injection molding process was used to injection mold microscope slides in cyclic olefin copolymer (TOPAS 8007-04) [8]. SEM, AFM, and confocal microscopy were used to characterize the different steps in the fabrication process.

Characterization of the superhydrophobic surfaces was performed by a contact angle tennsiometer Data physics Contact Angle System OCA and a custom built tilting system with angle readout.

3 RESULTS

The fabrication process resulted in good replication in each of the fabrications steps, as shown in the SEM images in Figure

Figure 3. A small reduction in the size of microstructures occurred during the black silicon etch; the micro pillars were reduced aproxematly 0.5 µm in diameter. An AFM was used to measure the height of a single silicon pillar with black silicon and on a similar hole on the nickel shim. The resulting profile is shown in Figure 4. The height was measured to be approximately 3.2 µm and replication of black silicon in the nickel shim is clearly visible. Injection molding replicated both micro and nanostructures in the polymer (Figure 3D).

The super hydrophobic properties of the structured microscope slides were characterized by contact angle and drop roll off measurements with water. A microscope slide with water drops is shown in Figure 1. Preliminary results indicate a contact angle increase from 95° for the unstructured polymer to a maximum 150°, obtained for 3 µm pillars with a spacing of 8 µm (Figure 5). Roll of angles were measured as a function of pitch size for different pillar diameters and plotted in Figure 6.

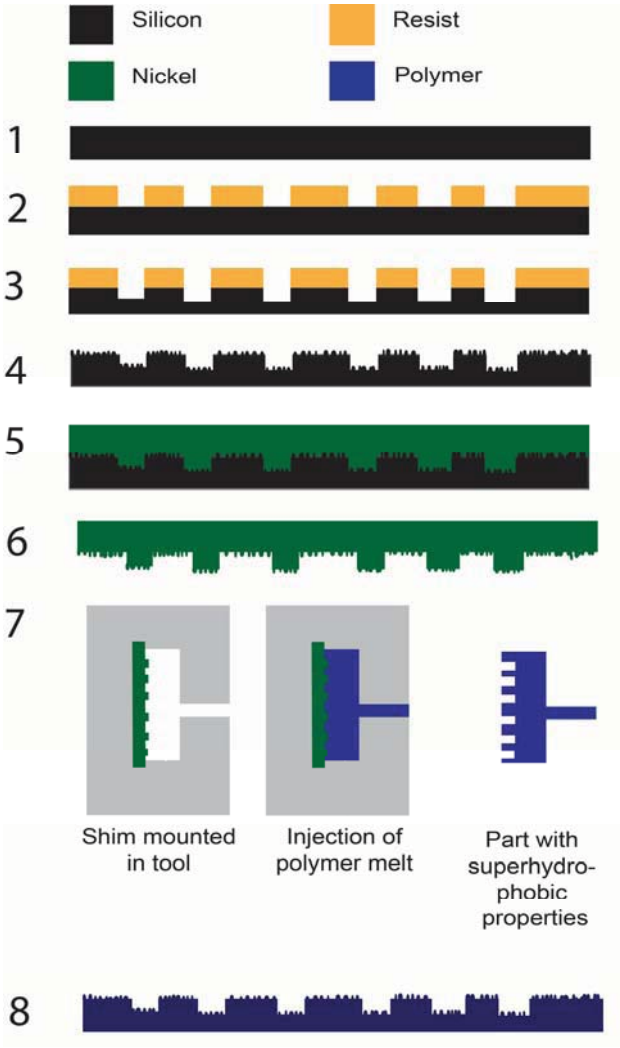

Figure 2: The entire fabrication method: 1 and 2) Lithography, 3) Dry etch , 4) resist strip and black silicon etch, 5) Electroplating of nickel shim , 6) removal of silicon wafer with KOH, 7) injection molding of polymer parts from nickel shim, 8) finished parts with super hydrophobic surfaces.

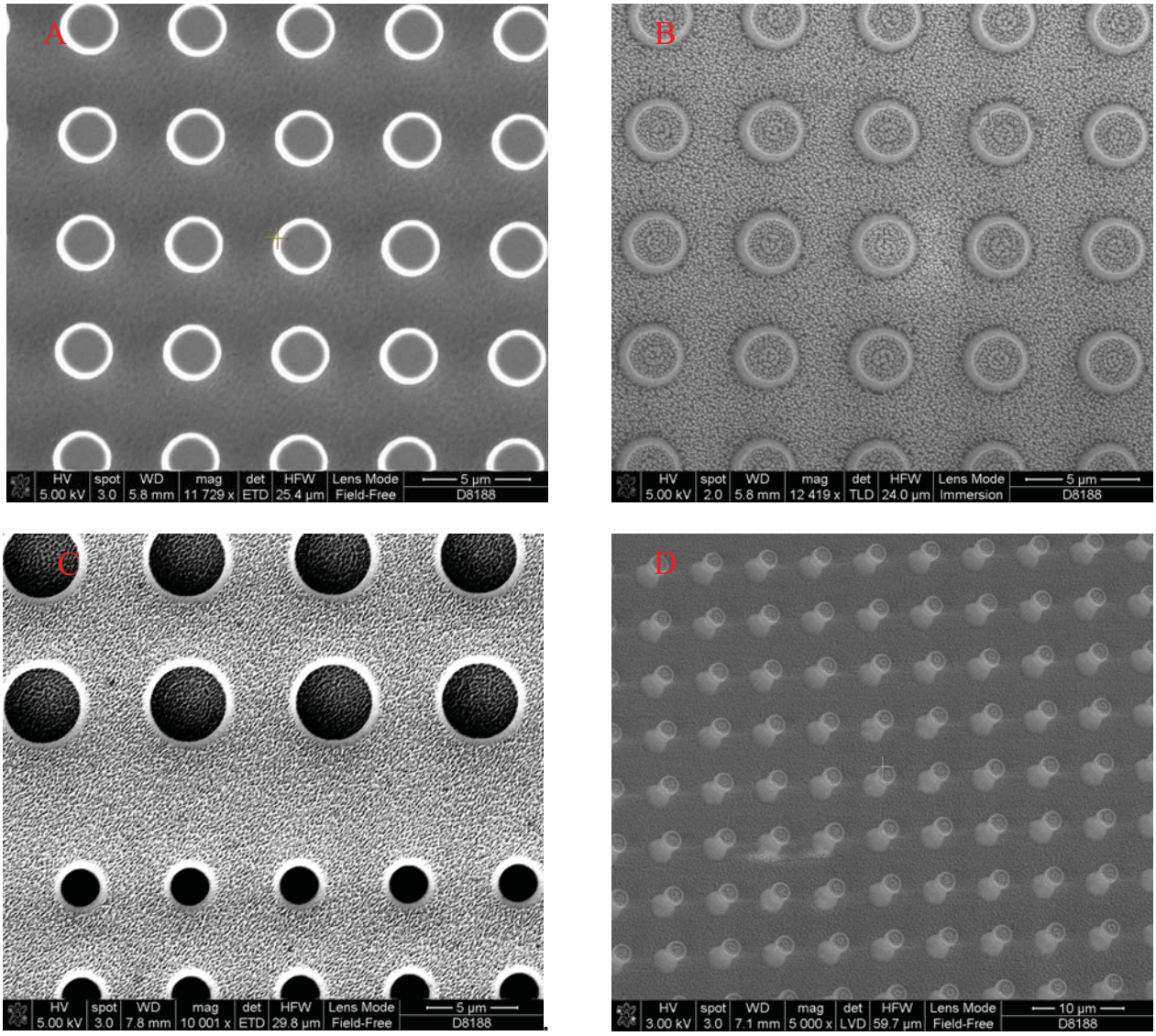

Figure 3: SEM images of different steps in the fabrication process. A) Micro pillars in etched in silicon. B) Etch of hierarchical black silicon. C) Electroplated nickel insert with inverse structures. D) Injection molded self-cleaning surface hierarchical structures.

Roll off angles decrease from approximately 45° for the areas with closely packed pillars, to below 5 degrees for areas with larger pitch size of the pillars. Similar roll off- and contact angles are reported for other super hydrophobic surfaces with hierarchical nano and microstructures [3, 4]. The lowest rolls off angles observed were in the range 1° to 5° for structures having the 8 µm spacing. It was nearly impossible to deposit a drop on the surface when the roll of angle was below 5° as it readily rolled or bounced to other test areas, or outside the structured surface. This clearly indicates that the drops do not wet the structures and are in the so-called Cassie Baxter state [9].

4 CONCLUSION

Polymer microscope slides with superimposed micro- and nanometer structures and with a minimum structure size of 100 nm were fabricated by injection molding. The microscope slides showed super hydrophobic properties; the contact angle was increased from 95° for the unstructured polymer to a maximum of 150° and the lowest drop roll of angle was approximately 1°.

5 ACKNOWLEDGEMENTS

This work is supported by the Danish Advanced Technology Foundation through the Advanced Technology Platform NanoPlast (grant no. 007-2010-2).

REFERENCES

1. Bhushan, B., Y.C. Jung, and M. Nosonovsky, *Lotus Effect: Surfaces with roughness-Induced superhydrophobicity, Self-Cleaning and low Adhesion*, in *Springer Handbook of Nanotechnology*, B. Bhushan, Editor. 2010, Springer: new york. p. 1438-1518.
2. Barthlott, W. and C. Neinhuis, *Purity of the sacred lotus, or escape from contamination in biological surfaces.* Planta, 1997. **202**(1): p. 1-8.
3. Bhushan, B., K. Koch, and Y.C. Jung, *Biomimetic hierarchical structure for self-cleaning.* Applied Physics Letters, 2008. **93**(9).
4. Puukilainen, E., et al., *Superhydrophobic polyolefin surfaces: Controlled micro- and nanostructures.* Langmuir, 2007. **23**(13): p. 7263-7268.
5. McCormick, R.M., et al., *Microchannel Electrophoretic Separations of DNA in Injection-Molded Plastic Substrates.* Analytical Chemistry, 1997. **69**(14): p. 2626-2630.
6. Sun, G., et al., *Fabrication of micro/nano dual-scale structures by improved deep reactive ion etching.* Journal of Micromechanics and Microengineering, 2010. **20**(7).
7. Kumaravelu, G., et al., *Surface texturing for silicon solar cells using reactive ion etching technique*. Conference Record of the Twenty-Ninth IEEE Photovoltaic Specialists Conference 2002. 2002. 258-261.
8. Andresen, K.O., et al., *Injection molded chips with integrated conducting polymer electrodes for electroporation of cells.* Journal of Micromechanics and Microengineering, 2010. **20**(5).
9. Cassie, A.B.D., *Contact angles.* Discussions of the Faraday Society, 1948. **3**: p. 11-16.

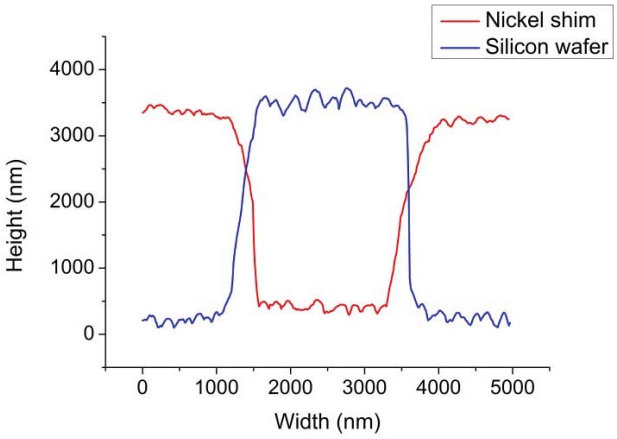

Figure 4: Profile of 2.5 µm micro pillar with hierarchical nanostructures (black silicon) and a similar hole from the electroplated nickel shim (inverse polarity).

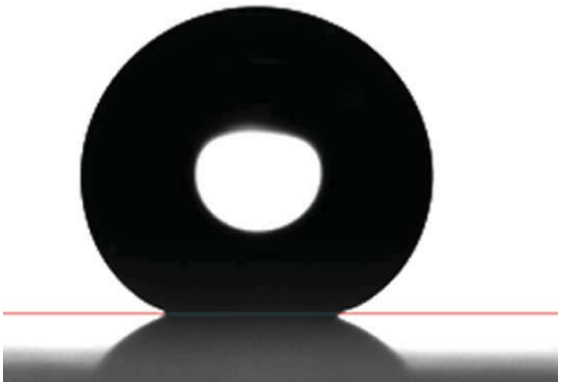

Figure 5: Drop with maximum contact angle at 150° on 3 µm pillars with a spacing of 8 µm.

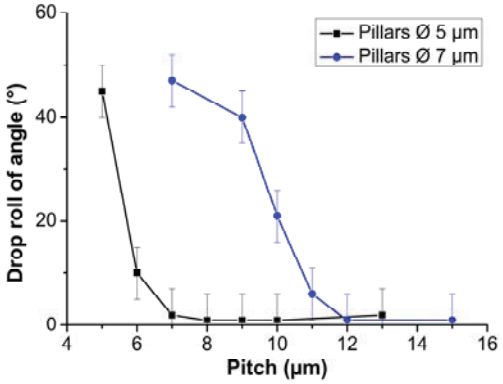

Figure 6: Drop roll of angle plotted as function of pitch.

Appendix 6

Emil Søgaard, Kristian Smistrup, and Rafael Taboryski. A method for manufacturing a tool part for an injection molding process, a hot embossing process, a nano-imprint process, or an extrusion process. International Application Number PCT/DK2013/050060. 2013.

Contribution: Development of the ideas behind the patent (injection molded hierarchical nanograss structures). Proof of concept. Participation in writing of the patent.

(12) INTERNATIONAL APPLICATION PUBLISHED UNDER THE PATENT COOPERATION TREATY (PCT)

(19) World Intellectual Property Organization
International Bureau

(43) International Publication Date
12 September 2013 (12.09.2013)

WIPO | PCT

(10) International Publication Number
WO 2013/131525 A1

(51) International Patent Classification:
G03F 7/00 (2006.01) *B29C 45/26* (2006.01)
B29C 33/42 (2006.01)

(21) International Application Number:
PCT/DK2013/050060

(22) International Filing Date:
8 March 2013 (08.03.2013)

(25) Filing Language: English

(26) Publication Language: English

(30) Priority Data:
12158834.7 9 March 2012 (09.03.2012) EP
61/608,828 9 March 2012 (09.03.2012) US

(71) Applicants: **DANMARKS TEKNISKE UNIVERSITET** [DK/DK]; Anker Engelundsvej 1, Bygning 101A, DK-2800 Lyngby (DK). **NIL TECHNOLOGY APS** [DK/DK]; Diplomvej 381, DK-2800 Kgs. Lyngby (DK).

(72) Inventors: **TABORYSKI, Rafael**; Jordbærvænget 11, DK-2880 Bagsværd (DK). **SØGAARD, Emil**; Molbechsvej 5, 4.th., DK-2500 Valby (DK). **SMISTRUP, Kristian**; Bellmansgade 35, 6.th., DK-2100 Copenhagen Ø (DK).

(74) Agent: **PLOUGMANN & VINGTOFT A/S**; Rued Langgaards Vej 8, DK-2300 Copenhagen S (DK).

(81) Designated States *(unless otherwise indicated, for every kind of national protection available)*: AE, AG, AL, AM, AO, AT, AU, AZ, BA, BB, BG, BH, BN, BR, BW, BY, BZ, CA, CH, CL, CN, CO, CR, CU, CZ, DE, DK, DM, DO, DZ, EC, EE, EG, ES, FI, GB, GD, GE, GH, GM, GT, HN, HR, HU, ID, IL, IN, IS, JP, KE, KG, KM, KN, KP, KR, KZ, LA, LC, LK, LR, LS, LT, LU, LY, MA, MD, ME, MG, MK, MN, MW, MX, MY, MZ, NA, NG, NI, NO, NZ, OM, PA, PE, PG, PH, PL, PT, QA, RO, RS, RU, RW, SC, SD, SE, SG, SK, SL, SM, ST, SV, SY, TH, TJ, TM, TN, TR, TT, TZ, UA, UG, US, UZ, VC, VN, ZA, ZM, ZW.

(84) Designated States *(unless otherwise indicated, for every kind of regional protection available)*: ARIPO (BW, GH, GM, KE, LR, LS, MW, MZ, NA, RW, SD, SL, SZ, TZ, UG, ZM, ZW), Eurasian (AM, AZ, BY, KG, KZ, RU, TJ, TM), European (AL, AT, BE, BG, CH, CY, CZ, DE, DK, EE, ES, FI, FR, GB, GR, HR, HU, IE, IS, IT, LT, LU, LV, MC, MK, MT, NL, NO, PL, PT, RO, RS, SE, SI, SK, SM, TR), OAPI (BF, BJ, CF, CG, CI, CM, GA, GN, GQ, GW, ML, MR, NE, SN, TD, TG).

Published:

— *with international search report (Art. 21(3))*

— *before the expiration of the time limit for amending the claims and to be republished in the event of receipt of amendments (Rule 48.2(h))*

(54) Title: A METHOD FOR MANUFACTURING A TOOL PART FOR AN INJECTION MOLDING PROCESS, A HOT EMBOSSING PROCESS, A NANO-IMPRINT PROCESS, OR AN EXTRUSION PROCESS

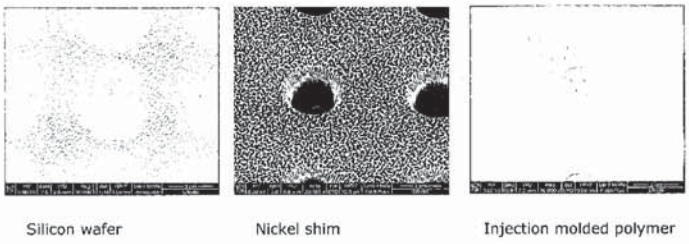

Fig. 3

(57) Abstract: The present invention relates to a method for manufacturing a tool part for an injection molding process, a hot embossing process, nano-imprint process or an extrusion process. First, there is provided a master structure (10) with a surface area comprising nanometre-sized protrusions (11) with a minimum density of approximately 105 protrusions/mm2, the protrusions being positioned in a non- periodic, irregular pattern, said protrusions being created by a process comprising alternating passivation and etching into the master structure. Secondly, there is made a transfer of the master structure into a metal insert (20), the metal insert having a corresponding nanometre-sized pattern (21) from said protrusions, and thirdly, adapting the metal insert into a tool part (30) for enabling nanometre- sized patterns being formed by the tool part. The invention provides an easier and faster way of manufacturing the master structure, e.g. a black silicon wafer. It is a further advantage of the present invention that it provides an advantageous way of making tools capable of producing self-cleaning surfaces without the need for chemical coating.

WO 2013/131525 A1

A METHOD FOR MANUFACTURING A TOOL PART FOR AN INJECTION MOLDING PROCESS, A HOT EMBOSSING PROCESS, A NANO-IMPRINT PROCESS, OR AN EXTRUSION PROCESS

FIELD OF THE INVENTION

The present invention relates to a method for manufacturing a tool part for an injection molding process, a hot embossing process, a nano-imprint process, or an extrusion process. The invention also relates to corresponding tool part, e.g. a tool part capable of producing a self-cleaning surface in an object.

BACKGROUND OF THE INVENTION

Injection molded polymer parts with micro- or nano-structured surfaces, has the ability to introduce wide range of new functionalities. Many consumer products today, use chemical coatings to lower adhesion or to repel water, these are potentially unhealthy or toxic. Surfaces with self-cleaning nano and microstructures that imitate the lotus flower. This is of high relevance for the medical and food producing industries. For example, medical and food containers can be designed so they can be completely emptied. Therefore, none of the expensive medicine or food is wasted. Furthermore, self-cleaning surfaces are relevant for hearing aids and medical equipment such as endoscopes.

Various solutions have been suggested in the past in order to meet this demand for self-cleaning surfaces. Solutions are available but they are either rather complicated to manufacture due to the intensive need for lithographic processing , or they are not sufficiently durable over time, e.g. by being dependent on chemical coatings that are worn off during use. Some chemical coatings used in consumer products today use e.g. fluorine containing chemical coatings, which are potentially unhealthy or toxic.

US patent application 2002/0164443 for example discloses an injection molding processes with the purpose of creating lotus-like structures with various mathematically based structures. Initially, a master structure is made which is then transferred into an injection-molding tool, for example by a LIGA process. The production of the master structure is however quite time consuming due to

the intensive need for complex, and therefore costly, lithography steps for designing the proposed mathematical structures resulting in a lotus-like functionality in the final product.

US patent application 2007/115554 relates to an antireflective viewing surface with a textured layer disposed upon the viewing surface; wherein the textured layer comprises randomly distributed protrusions having randomly distributed dimensions that are smaller than the wavelength of light. Disclosed herein is a method of manufacturing an antireflective viewing surface comprising: electroforming a metal upon a first template to form an electroformed metal template; wherein the first template comprises random, columnar structures; disposing a layer of a polymeric resin on a viewing surface; pressing the electroformed metal template against the viewing surface; and solidifying the polymeric resin. The layer having randomly distributed protrusions of e.g. titanium dioxide or carbon nanotube is grown on the surface by conventional methods. The protrusions have dimensions smaller than the wavelength of light in order to provide anti-reflection. The textured layer can be transferred from a so-called first template to an electroformed metal template that can be used for subsequent molding, or forming, cf. figure 4 and the corresponding description [0058]. The growth of such protrusions is typically somewhat time-consuming thereby representing a bottle neck for manufacturing use.

Hence, an improved method would be advantageous, and in particular a more efficient and/or reliable method would be advantageous.

OBJECT OF THE INVENTION

It is a further object of the present invention to provide an alternative to the prior art.

In particular, it may be seen as an object of the present invention to provide a method that solves the above mentioned problems of the prior art with complex and/or cost intensive manufacturing of tools part having functional surfaces.

SUMMARY OF THE INVENTION

Thus, the above described object and several other objects are intended to be obtained in a first aspect of the invention by providing a method for manufacturing a tool part for an injection molding process, a hot embossing process, nano-imprint process or an extrusion process, the method comprises

providing a master structure with a surface area comprising nanometre-sized protrusions with a minimum density of approximately 10^5 protrusions/mm^2, the protrusions being positioned in a non-periodic, irregular pattern, said protrusions being created by a process comprising:

alternating passivation and etching into the master structure,

and/or

simultaneous passivation and etching into the master structure,

and/or

etching into the master structure,

transferring the master structure into a metal insert, the metal insert having a corresponding nanometre-sized pattern from said protrusions, and

adapting the metal insert into a tool part for enabling nanometre-sized patterns being formed by the tool part.

The invention is particularly, but not exclusively, advantageous for obtaining a tool part in a more simple way than hitherto possible due the easier and/or faster way of manufacturing the master structure, e.g. in a semiconductor material such as a silicon wafer. It is a further advantage of the present invention that it provides an advantageous way of making tools capable of producing self-cleaning surfaces without the need for chemical coating.

Furthermore, an injection molding tool part according to the present invention can essentially manufacture final products in any thermoplastic material suitable for injection molding which may open up for wide spread application of the present invention, e.g. in every day consumer products already manufactured by injection molding.

In the context of the present invention, it is to be understood that the three options, (1, 2 and 3) for creation of protrusions:

1) alternating passivation and etching into the master structure,

and/or

2) simultaneous passivation and etching into the master structure,

and/or

3) etching into the master structure,

can be applied solely (i.e. only option 1, 2 or 3), in combination (i.e. 1 and 2, or 1 and 3, or 1 and 3), such as a period of performing option 1 followed by another period with option 2, etc., and a combination of all 3 options (1, 2, and 3), such as various combination of periods with options 1, 2, and 3 for creation of protrusions, as the skilled person will readily understand once the general principle of the invention is comprehended.

Notice that the present invention applies various etching processes, which is quite different from US patent application 2007/115554 were the random protrusions are grown, typically over several hours. The present invention is typically order of magnitude faster and less complex to implement, in particular when implemented on a semiconductor wafer or similar in a cleanroom environment. In general, the present invention relates to a master structure made of a non-metal, such as a semiconductor material.

The present invention is further advantageous over US2007/115554 in that the master origination is compatible with standard processes available in most cleanrooms for semiconductor fabrication, the term 'origination' meaning the way of modifying the master structure (in short the 'master') into a desired shape. Moreover, the present invention does not include nanoparticle coatings with potential health hazards, as the master structure is formed by structuring the substrate surface exclusively, or predominately, by etching processes in the most preferred embodiments. Finally, the present invention is primarily focussed on anti-wetting functionalities, though the present invention may also be applied in order to implement anti-reflection properties in the final product being manufactured by the tool according to the first aspect of the invention.

The present invention relates generally to tool parts for application in an injection molding process, a hot embossing process or an extrusion process, or other similar processes or equivalent manufacturing processes.

The master structure may have alternatively have a surface area comprising nanometre-sized protrusions with a minimum density of approximately 10^4 protrusions/mm^2, or alternatively approximately 10^6 protrusions/mm^2. It is to be understood that the density is calculated on an average basis as will be appreciated by a person working with micro-technologies.

The concept of a non-period, irregular pattern is to be understood by the skilled person as seen on as seen or viewed on a nanometer scale, e.g. using scanning electron microscopy (SEM) or an atomic force microscopy (AFM) as it will be demonstrated in the detailed description of the invention below. Using for example a pixel size of approximately 2-20 nm in SEM, the master structure will be shown to have a protrusion distribution with such a pattern.

The process for creating said nano-meter sized protrusions using alternating, and/or simultaneous, passivation and etching into the master structure may preferably take place in a vacuum chamber, more preferably the entire process of creating the protrusions takes place in a single vacuum chamber in order to facilitate fast processing i.e. without any significant delay between etching and passivation. Thus, by performing the process in a single process the invention may facilitate that the master structure is made in a quick way, e.g. less than 60 minutes, less than 30 minutes, or less than 10 minutes. Typically, the alternating process of passivation and etching into the master structure may be repeated a plurality of times, such as least 10 times, 50 times, 100 times, or 500 times.

Similarly, if the process for creating said nano-meter sized protrusions in a non-period, irregular pattern is obtained using etching into the master structure, e.g. by a chemical wet etching process in strong acid or base, the process may also be take place in a fast and advantageous way.

The step of transferring the master structure into a metal insert, the metal insert having a corresponding nanometre-sized pattern from said protrusions can be

made either by a positive transfer, or by a negative transfer of the master structure as the skilled person would readily understood once the general teaching and principle of the present inventions has been appreciated by the skilled person. There may be several intermediate steps in the transferring process. There may also be produced several duplicates ('families') of the same master structure.

The step of adapting the metal insert into a tool part can be performing in various ways, e.g. by mechanical securing the metal insert into the tool part. The adaption must be made so as to enable that the nanometre-sized patterns of the insert is replicated or formed into the moulded product by the tool part.

Preferably, the process for creating the protrusions may result in a random shape and/or a random position with respect to an individual protrusion i.e. essentially the process may be viewed as a non-deterministic process, though of course some overall control of the average shape and position of the protrusions are possible. Nevertheless, the advantage in speed of manufacturing outweighs this apparent disadvantage. More specifically, the dimensions of the protrusions may defined by corresponding intervals for each dimension, each dimension being randomly scattered within a corresponding interval, preferably at least one dimension having a scattering of at least 50% of the average value e.g. height of the protrusion may be a height range of : average height +/- 100%, 80%, 60%, 40%, 20% etc. or a thickness, or width, with a thickness range of : average thickness +/- 100 %, 80%, 60%, 40%, 20% etc.

Alternatively, the process may be defined by a set of global process parameters, said parameters being common for the creation of at least a main portion of the protrusions such as gas, bias, temperature, pressure, switching frequency etch/passivation. Thus, there are no process parameters related to the individual protrusions like for instance in conventional lithography. Thus, the process may be defined by a set of process parameters, said parameters not being directly related to the size and/or the position of the individual protrusion.

It may be said that the nanometer-sized protrusions may be created by the process does not require any lithographic process step for defining shape and/or

position of the protrusions, at least for the main part of the protrusions. The main part of the protrusions may e.g. 90% or 95%.

Typically, the passivation may comprise the formation of an inert polymer, or an oxide, on the master structure, using e.g. a fluoro-carbon like C3F for creating such a temporarily layer. Preferably, the etching may comprise reactive ion etching (RIE) in the master structure e.g. Bosch or cryogenic.

Alternatively or additionally, the etching may comprise a wet chemical etching such as a strong base, or acid, e.g. KOH. The master structure, e.g. a silicon wafer, is submerged in the etching liquid which makes the surface rough or etches in certain crystallographic plane. A mask may be used or not. A possible mask is a photoresist or SiO_2/Nitride.

Alternatively, wherein the etching may comprise laser-assisted etching, such as femtosecond pulse laser process as described by Crouch et al. in Appl. Phys. Lett. 84, 1850 (2004); doi: 10.1063/1.1667004, which is hereby incorporated by reference in its entirety.

Typically, the master structure is a semiconductor wafer, a glass wafer, a metal wafer, or a ceramic wafer, as it will be appreciated by the skilled person. Thus, in one embodiment, the master structure may be a silicon wafer, and preferably the nanometer-sized protrusions constitute nano-grass and/or black silicon. Black silicon is a known surface type produced by e.g. repeated directional etching and passivation resulting in large amount of needle-like, or spike-like, structures pointing away from the surface, the surface has a relatively low reflectivity (hence the name). Nano-grass may similarly be defined as a large amount of protruding, randomly oriented structures resembling to some extent natural grass as seen in a microscopic view.

Typically, the nanometer-sized protrusions may have an aspect ratio (A), i.e. height / width of structure on average, of minimum 10, 1, 0.1 or 0.01. Alternatively, the nanometer-sized protrusions may have an aspect ratio (A), i.e. height / width of structure on average, of maximum 10, 1, 0.1 or 0.01.

Typically, the nanometer-sized protrusions have a density within an interval of 10^3 - 10^{10} /mm^2, preferably within an interval of 10^4 - 10^7 /mm^2.

Advantageously, the nanometer-sized protrusions may have an average height of minimum 10 nm, 20 nm, 30 nm, 40 nm, 50 nm or 100 nm, 200 nm, or 300 nm. Alternatively, the nanometer-sized protrusions may have an average height of maximum 10 nm, 20 nm, 30 nm, 40 nm, 50 nm or 100 nm, 200 nm, or 300 nm.

The dimensions of the protrusions should, on one hand satisfy the functional purpose of e.g. providing a self-cleaning surface by having sufficiently high protrusions, and, on one the other hand, being within a feasible level of manufacturing and durability. Thus, too high protrusions may be difficult to mold, e.g. un-molding, and may wear off quickly during mechanical stresses during applications.

In one preferred embodiment, the master structure may comprise a hierarchical structure with a plurality of surface areas comprising nanometre-sized protrusions with a minimum density of 10^5 protrusions/mm^2, and a plurality of surface areas comprising micrometer-sized surface structures, either protruding away from the surface and/or being holes in the surface, the said structures preferably having a characteristic length scale of 1-1000 micrometer, more preferably 1-100 micrometre, even more preferably 2-50 micrometer. Such a hierarchical structure is particularly advantageous for obtaining self-cleaning functional properties of the resulting surface. The nanometre-sized protrusions may cover, i.e. being positioned upon, both the micrometer-sized surface structures protruding away from the surface and/or the holes in the surface, and possibly the surface not being protruded or lowered relative to the overall or average surface level.

Beneficially, the step of transferring the master structure into a metal insert may be performed by method chosen from the list consisting of:

- material deposition, such as electroplating
- imprint lithography,
- soft lithography,

- hot embossing combined with etching, and
- casting.

Other available transferring techniques may readily be considered by the skilled person once the general teaching and principle of the present invention is acknowledged. Thus, both inverse transfer (negative) and direct transfer (positive) of the master is envisioned within the context of the present invention.

Particularly, the transferring the master structure into a metal insert may be performed by electrochemical deposition of a shim on the master structure, the shim being used on, or in, the metal insert as a part of the tool part. Beneficially, the manufacturing may include duplication of the master into a so-called 'family' of shims for facilitating high speed productions.

In a second aspect, the invention relates to a tool part having a metal insert with nano-meter-sized protrusions, the protrusions being manufactured according to the first aspect.

IIn a third aspect, the present invention relates to a polymer product manufactured by a tool according to the second aspect.

Such as product is particularly beneficial in that the fabrication of a hierarchical surface structure may comprise both micro and nanostructures, where the microstructure is e.g. composed of holes rendering the surface repellent such that liquid is prevented from wetting the surface inside the holes due to surface tension when the entire surface is covered by liquid. This will of course depend on the properties of the master structure as will readily be understood.

Alternatively or additionally, the combination of micro- and nanostructures may ensure that the structured surface is self-cleaning, e.g. such that sessile drops will form high contact angles with the surface, as measured with water (WCA), and in addition the contact angle hysteresis between advancing and receding contact angle is small. A high contact angle may be considered to be above 130° and more preferably above 150°, while a low contact angle hysteresis may be considered to be below 30°, and more preferably below 5°. An advantageous use

of such a surface will be the inside of liquid containers, e.g. paint, dairy products, or cosmetics, and will ensure that the liquid container can be emptied and/or cleaned more easily.

The individual aspects of the present invention may each be combined with any of the other aspects. These and other aspects of the invention will be apparent from the following description with reference to the described embodiments.

BRIEF DESCRIPTION OF THE FIGURES

The invention will now be described in more detail with regard to the accompanying figures. The figures show one way of implementing the present invention and is not to be construed as being limiting to other possible embodiments falling within the scope of the attached claim set.

Figure 1 shows a schematic overview of the three main steps of the invention; providing a master structure, transferring to a metal insert, and adapting to a tool part,

Figure 2 shows schematically a more detailed illustration of a method according to the present invention,

Figure 3 shows three SEM images of a master structure in silicon, a Nickel shim where the hierarchical structure with nanometre-sized and micrometre-size pattern has transferred to, and a resulting molded polymer product,

Figures 4 and 5 shows more detailed SEM images of a silicon master structure according to the present invention,

Figure 6 shows a more detailed AFM image of silicon master structure,

Figure 7 shows SEM images of a Nickel metal insert according to the present invention,

Figure 8 shows a more detailed AFM image of a Nickel metal insert according to the present invention,

Figures 9 and 10 shows SEM images of a molded polymer product manufactured with tool according to the present invention,

Figure 11 illustrates the result of the wetting experiment for a flat structure without the invention (left) and a polymer product manufactured with tool according to the present invention (right), and

Figure 12 is a schematic system-chart representing a method according to the invention.

DETAILED DESCRIPTION OF AN EMBODIMENT

Figure 1 shows a schematic overview of the three main steps forming part of the invention; providing a master structure 10, transferring to a metal insert 20, and adapting to a tool part 30.

The master structure 10 has a surface area comprising nanometre-sized protrusions 11 (not to scale) with a minimum density of approximately 10^5 protrusions/mm^2, the protrusions being positioned in a non-periodic, irregular pattern i.e. essentially a random or non-deterministic pattern, said protrusions being created by a process comprising:

1) alternating passivation and etching into the master structure, e.g. reactive ion etching by the so-called Bosch method,
   and/or
2) simultaneous passivation and etching into the master structure, e.g. reactive ion etching by the so-called cryogenic method,
   and/or
3) etching into the master structure, e.g. by a chemical wet etching.

Subsequently, the pattern of the protrusions 11 is transferred from the master structure 10 into a metal insert 20, the metal insert having a corresponding nanometre-sized pattern 21 from said protrusions, such as a LIGA technique or other similar or equivalent techniques.

Finally, the step of adapting the metal insert 20 into a tool part 30 is performed for enabling nanometre-sized patterns being formed by the tool part 30. In Figure 1, the tool part is shown to have two half-parts 30a and 30b, respectively, where the metal insert 20 is positioned in the lower part 30b. However, the present invention is contemplated also to include a plurality of metal inserts like the one shown in Figure 1. Also schematically indicated are feeding channel 31 for supplying molten polymer under pressure into the molding chamber 32 of the tool 30.

Figure 2 shows schematically a more detailed illustration of a method according to the present invention. The fabrication for the insert 30 with combined nano structures is described step by step as indicated by number 1-9 right of the panel; the size range is 1µm (micrometer) to 100 µm for the micro structures and 50 nm to 2500 nm for the nanostructures (black silicon)

The method has the following steps:

1. The starting point of the insert fabrication is a new wafer of silicon.

2. A resist layer is deposited on the wafer; this could be done by spin coating, spray coating as well as other methods.

3. The microstructures is defined in the resist with lithography e.g. UV, E-beam, Imprint etc. The resist is then developed leaving the structures in the resist layer.

4. The microstructures are transferred to the wafer e.g. by reactive ion etching.

5. The resist layer is stripped leaving the microstructures in the wafer.

6. Black silicon is etched, to produce nano structures having protrusions 11 in the master structure. One of several methods for producing so-called black silicon surfaces is to apply the so-called Bosch process for reactive ion etching (RIE), where a black silicon structure can be achieved by repeatedly switching between etching and passivation.

7. Three options can for example be used to transfer the structures from the wafer to the insert. 1) material depositing such as electroplating 2) imprint lithography, soft lithography, or hot embossing followed by etching by either reactive ion etching, or sputtering, or 3) Casting. As indicated by the corresponding pattern or protrusions 21, as visible and separated in step 8, the protrusions 11 are accordingly transferred from the master 10 into the insert 20.

8. An insert made of softer materials such as aluminium or nickel, cannot withstand as many injection molding cycles as tool steel. The insert therefore may optionally require a hard coating to make it more durable or a coating to make demolding easier.

9. The final step is repeating injection molding or embossing cycles, for the mass production of super hydrophobic/super hydrophilic and self-cleaning polymer parts 35.

Figure 3 shows three SEM images of a master structure in silicon (left), a nickel shim where the hierarchical structure with nanometre-sized and micrometre-size pattern has been transferred to (middle), and a resulting molded polymer product (right). Notice how the etched shape of the protrusions and the overall hierarchical structure is transferred from the master structure 'negatively' to the nickel shim, and the resulting polymer product therefore being a 'positive' transfer of the silicon master structure.

An injection molding insert with microstructures (circular pillars) in the size range 3 to 7 µm with a pitch 3 to 16 µm (on mask) has been fabricated with photolithography and DRIE of a silicon wafer. In addition nanostructures were added by etching so-called black silicon. The process time was 8 min, gas flow SF6: 70 sccm and O2 :110 sccm. Plasma generators settings was 13.56 MHz coil, 2700W 13.56 MHz, platten 30w and platten (substrate) temperature -10 °C. Further details on producing black silicon can be found in a recent review article by Shieh et al. in Phys. D: Appl. Phys. 44 (2011) 174010 *Plasma-made silicon nanograss and related structures*, which is hereby incorporated by reference in its entirety. Without being bound by any specific theory, it is believed that etching fluorine radicals and passivating oxide radicals are competing, and at a certain

level of oxygen there will be created protrusions due to the inherent micromask made up by impurities in the wafer, dust, etc. and the direction of the etching.

The wafer was electroplated with a 320 µm nickel layer. The wafer was removed in 30% KOH at 80°C, leaving a nickel insert with inverse structures.

Injection molding of microscope slides were carried out in a variotherm injection mold tool. The polymer used was Topas® 8007 and polypropylene, an optical profilometer was used to measure the structure height to 3.2 µm, and results for this polymer will also be shown below in Figure 4-11. It should be mentioned that the present inventors has also validated the invention in polypropylene (PP) but results are not shown here.

Figures 4 and 5 shows more detailed SEM images of a silicon master structure according to the present invention.

In Figure 4A, a tilted (30°) SEM image of a silicon master with 3 µm micro holes and black silicon protrusions is shown. In Figure 4B, a SEM image of a silicon master with 7 µm holes and black silicon protrusions is shown. In Figure 4C, another tilted (30°) SEM images of black silicon in higher resolution is shown, and in Figure 4D, the same black silicon is seen in a top view.

Figure 5 shows two SEM images with tilted (30°) SEM images of Silicon master with micro pillars i.e. micrometre-sized structures, and black silicon structures i.e. nanometre sized-structures according to the present invention.

Figure 6 shows a more detailed AFM image of a silicon master structure. The AFM image of black silicon has average height measured to be approximately 70nm.

Figure 7 shows SEM images of a Nickel metal insert according to the present invention, with tilted (30°) SEM image of nickel shim with inverse structures, both micro structures and nano structures can be seen to the left. To the right, a corresponding top view.

Figure 8 shows a more detailed AFM image of a Nickel metal insert according to the present invention, the AFM image of nickel shim showing inverse structures, micro structures (2.5 µm hole) and also nano structures from the black silicon can be seen.

Figures 9 and 10 shows SEM images of a molded polymer product manufactured with tool according to the present invention.

In Figure 9, a tilted (30°) SEM image of an injection molded polymer with 2.5µm pillars and nanostructures (black SI) is shown, in large scale on the left and small scale on the right.

Figure 10 shows a tilted (30°)SEM image of an injection molded polymer with 5 µm pillars and nanostructures (black silicon). Notice how all the pillars are slightly distorted to one side. This is believed to be caused by the extraction of the molding process.

Figure 11 illustrates the result of the wetting experiment for a flat structure without the invention (left) and a polymer product manufactured with tool according to the present invention. The contact angle was measured to 95° for the non-structured (flat) surface. The contact angle increased to 150° for the micro- and nanometer structures. The injection molded microscopes slides shown were also fabricated in Topas® 8007-04.

Roll off angles measurements were also used to describe super hydrophobic and self-cleaning surfaces. The contact angles shown alone are not sufficient to describe a self-cleaning surface since the drops can be pinned on the structured surface. The injection molded test areas had roll off angels down to 1°. It is nearly impossible to deposit a drop on the surface of one of these test areas. This clearly indicates that the drops do not wet the structures and they are in the so-called Cassie Baxter state. Further systematic studies of contamination and self-cleaning experiments are planned.

Figure 12 is a schematic system-chart representing an out-line of/in detail the operations of the method for manufacturing a tool part for an injection molding

process, a hot embossing process, nano-imprint process or an extrusion process, the method comprises the steps of

S1 providing a master structure 10 with a surface area comprising nanometre-sized protrusions 11 with a minimum density of approximately 10^5 protrusions/mm^2, the protrusions being positioned in a non-periodic, irregular pattern, said protrusions being created by a process comprising:

alternating passivation and etching into the master structure,

and/or

simultaneous passivation and etching into the master structure,

and/or

etching into the master structure,

S2 transferring the master structure into a metal insert 20, the metal insert having a corresponding nanometre-sized pattern 21 from said protrusions, and

S3 adapting the metal insert into a tool part 30 for enabling nanometre-sized patterns being formed by the tool part.

In short, the invention relates to a method for manufacturing a tool part for an injection molding process, a hot embossing process, nano-imprint process or an extrusion process. First, there is provided a master structure 10 with a surface area comprising nanometre-sized protrusions 11 with a minimum density of approximately 10^5 protrusions/mm^2, the protrusions being positioned in a non-periodic, irregular pattern, said protrusions being created by a process comprising alternating passivation and etching into the master structure. Secondly, there is made a transfer of the master structure into a metal insert 20, the metal insert having a corresponding nanometre-sized pattern 21 from said protrusions, and thirdly, adapting the metal insert into a tool part 30 for enabling nanometre-sized patterns being formed by the tool part. The invention provides an easier and faster way of manufacturing the master structure, e.g. a black silicon wafer. It is a further advantage of the present invention that it provides an advantageous way of making tools capable of producing self-cleaning surfaces without the need for chemical coating.

The invention can be implemented by means of hardware, software, firmware or any combination of these. The invention or some of the features thereof can also be implemented as software running on one or more data processors and/or digital signal processors.

The individual elements of an embodiment of the invention may be physically, functionally and logically implemented in any suitable way such as in a single unit, in a plurality of units or as part of separate functional units. The invention may be implemented in a single unit, or be both physically and functionally distributed between different units and processors.

Although the present invention has been described in connection with the specified embodiments, it should not be construed as being in any way limited to the presented examples. The scope of the present invention is to be interpreted in the light of the accompanying claim set. In the context of the claims, the terms "comprising" or "comprises" do not exclude other possible elements or steps. Also, the mentioning of references such as "a" or "an" etc. should not be construed as excluding a plurality. The use of reference signs in the claims with respect to elements indicated in the figures shall also not be construed as limiting the scope of the invention. Furthermore, individual features mentioned in different claims, may possibly be advantageously combined, and the mentioning of these features in different claims does not exclude that a combination of features is not possible and advantageous.

CLAIMS

1. Method for manufacturing a tool part for an injection molding process, a hot embossing process, nano-imprint process or an extrusion process, the method comprises

providing a master structure (10) with a surface area comprising nanometre-sized protrusions (11) with a minimum density of approximately 10^5 protrusions/mm^2, the protrusions being positioned in a non-periodic, irregular pattern, said protrusions being created by a process comprising:

alternating passivation and etching into the master structure,

and/or

simultaneous passivation and etching into the master structure,

and/or

etching into the master structure,

transferring the master structure into a metal insert (20), the metal insert having a corresponding nanometre-sized pattern (21) from said protrusions, and

adapting the metal insert into a tool part (30) for enabling nanometre-sized patterns being formed by the tool part.

2. The method according to claim 1, wherein the process for creating the protrusions result in a random shape and/or a random position with respect to an individual protrusion.

3. The method according to claim 1, wherein the dimensions of the protrusions are defined by corresponding intervals for each dimension, each dimension being randomly scattered within a corresponding interval, preferably at least one dimension having a scattering of at least 50% of the average value.

4. The method according to claim 1, wherein the process is defined by a set of global process parameters, said parameters being common for the creation of at least a main portion of the protrusions.

5. The method according to claim 1, wherein the process is defined by a set of process parameters, said parameters not being directly related to the size and/or the position of the individual protrusion.

6. The method according to claim 1, wherein the nanometer-sized protrusions being created by the process does not require any lithographic process step for defining shape and/or position of the protrusions, at least for the main part of the protrusions.

7. The method according to claim 1, wherein the passivation comprises the formation of an inert polymer, or an oxide, on the master structure.

8. The method according to claim 1, wherein the etching comprises reactive ion etching (RIE) in the master structure.

9. The method according to claim 1, wherein the etching comprises a wet chemical etching.

10. The method according to claim 1, wherein the etching comprises laser-assisted etching.

11. The method according to claim 1, wherein the master structure is a semiconductor wafer, a glass wafer, a metal wafer, or a ceramic wafer.

12. The method according to claim 1, wherein the master structure is a silicon wafer, and preferably the nanometer-sized protrusions constitute nano-grass and/or black silicon.

13. The method according to claim 1, wherein the master structure comprises a hierarchical structure with a plurality of surface areas comprising nanometre-sized protrusions with a minimum density of 10^5 protrusions/mm^2, and a plurality of surface areas comprising micrometer-sized surface structures, the said structures preferably having a characteristic length scale of 1-1000 micrometer, more preferably 1-100 micrometre, even more preferably 2-50 micrometer.

14. The method according to claim 1, wherein transferring the master structure into a metal insert is performed by method chosen from the list consisting of:

- material deposition, such as electroplating
- imprint lithography,
- soft lithography,
- hot embossing combined with etching, and
- casting.

15. The method according to claim 1, wherein transferring the master structure into a metal insert is performed by electrochemical deposition of a shim on the master structure, the shim being used on, or in, the metal insert as a part of the tool part.

16. A tool part (30) having a metal insert (20) with nano-meter-sized protrusions (21), the protrusions being manufactured according to any of the preceding claims.

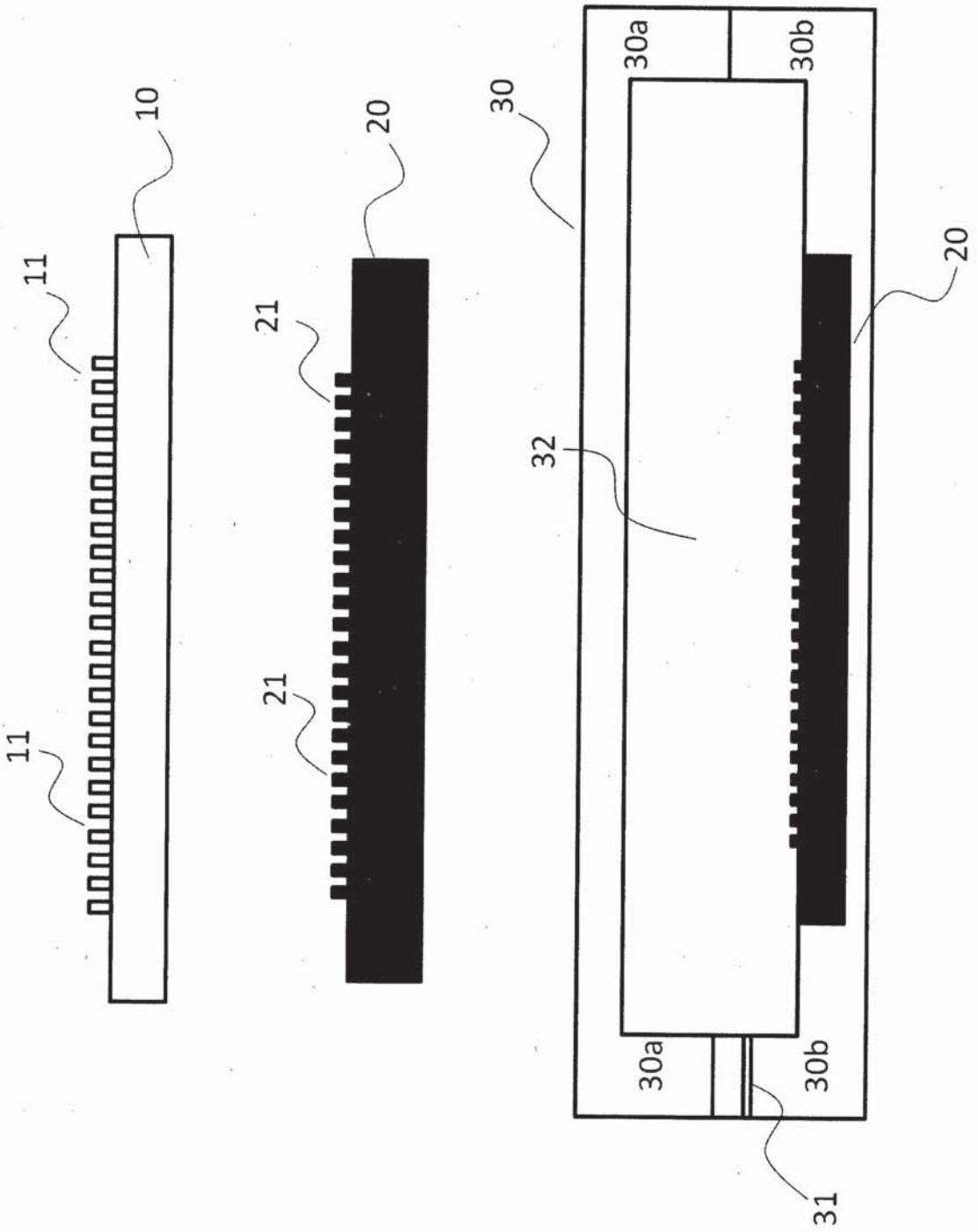

Fig. 1

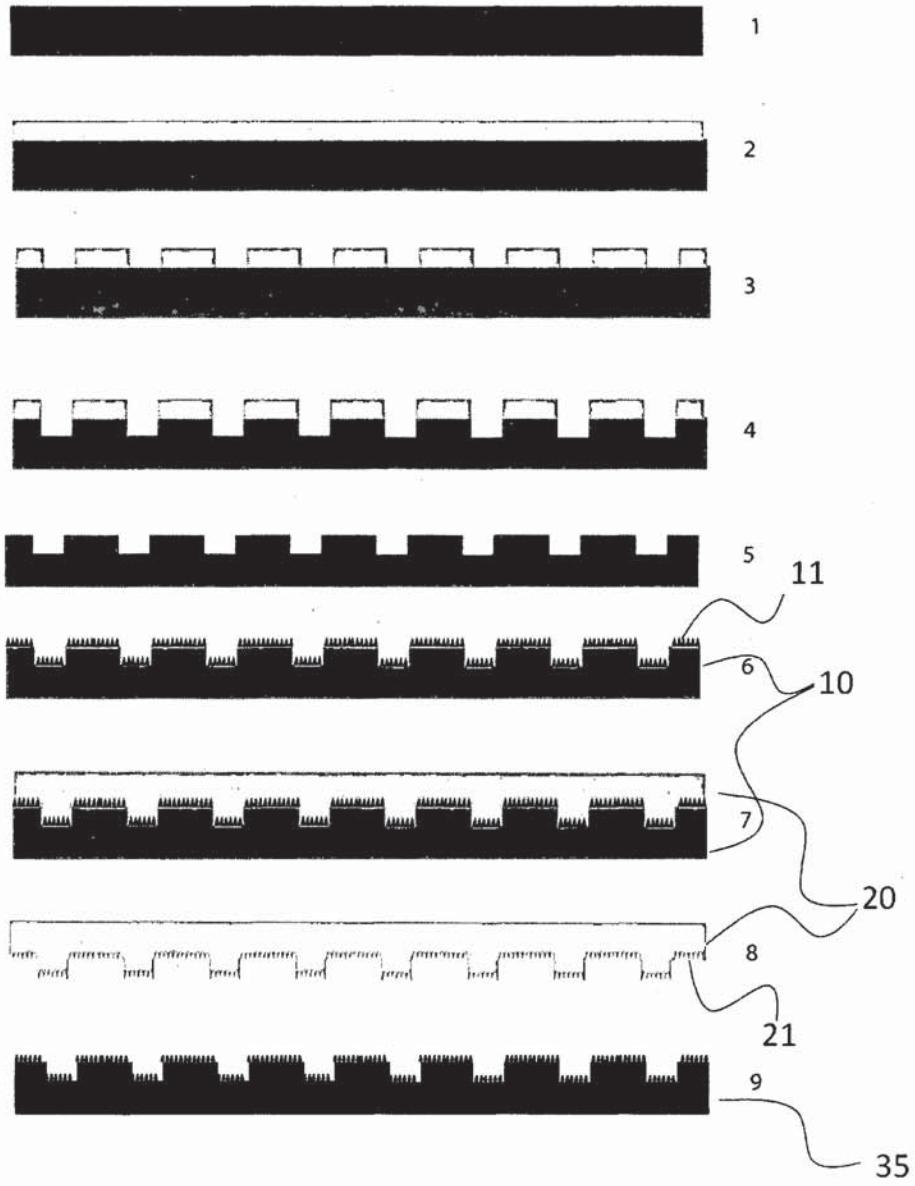

Fig. 2

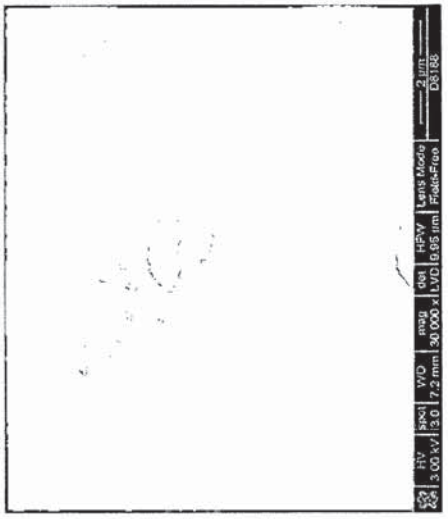

Injection molded polymer

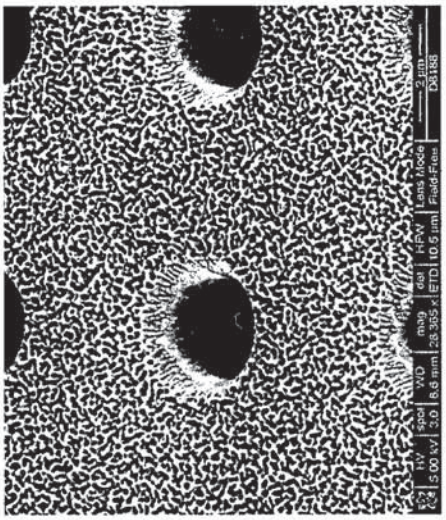

Nickel shim

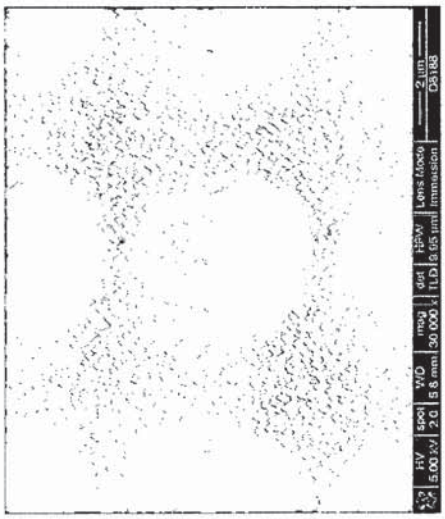

Silicon wafer

Fig. 3

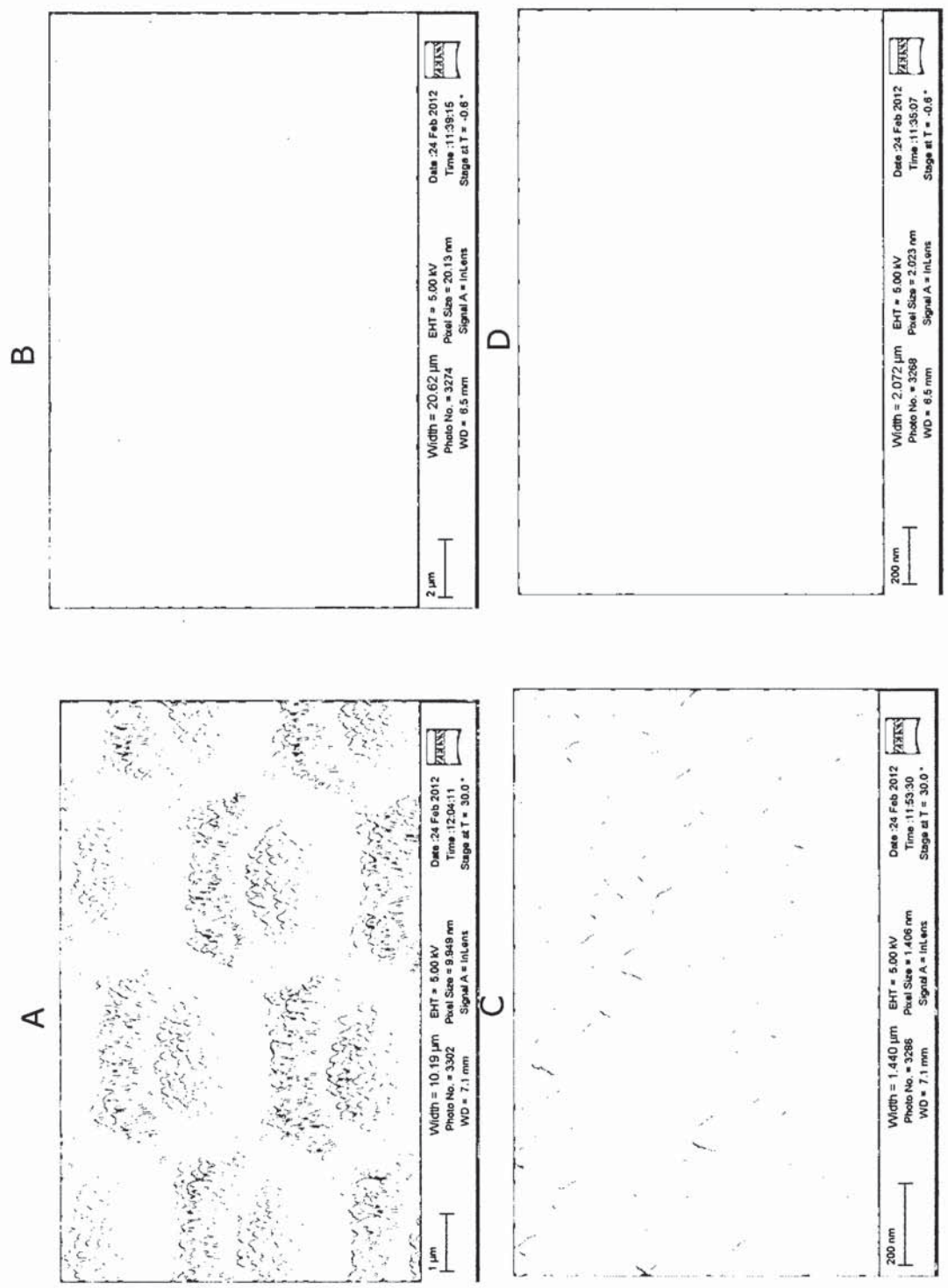
A
1 µm
Width = 10.19 µm
Photo No. = 3302
WD = 7.1 mm
EHT = 5.00 kV
Pixel Size = 9.949 nm
Signal A = InLens
Date :24 Feb 2012
Time :12:04:11
Stage at T = 30.0 °
B
2 µm
Width = 20.62 µm
Photo No. = 3274
WD = 6.5 mm
EHT = 5.00 kV
Pixel Size = 20.13 nm
Signal A = InLens
Date :24 Feb 2012
Time :11:38:15
Stage at T = -0.6 °
C
200 nm
Width = 1.440 µm
Photo No. = 3288
WD = 7.1 mm
EHT = 5.00 kV
Pixel Size = 1.406 nm
Signal A = InLens
Date :24 Feb 2012
Time :11:53:30
Stage at T = 30.0 °
D
200 nm
Width = 2.072 µm
Photo No. = 3268
WD = 6.5 mm
EHT = 5.00 kV
Pixel Size = 2.023 nm
Signal A = InLens
Date :24 Feb 2012
Time :11:35:07
Stage at T = -0.6 °

Fig. 4

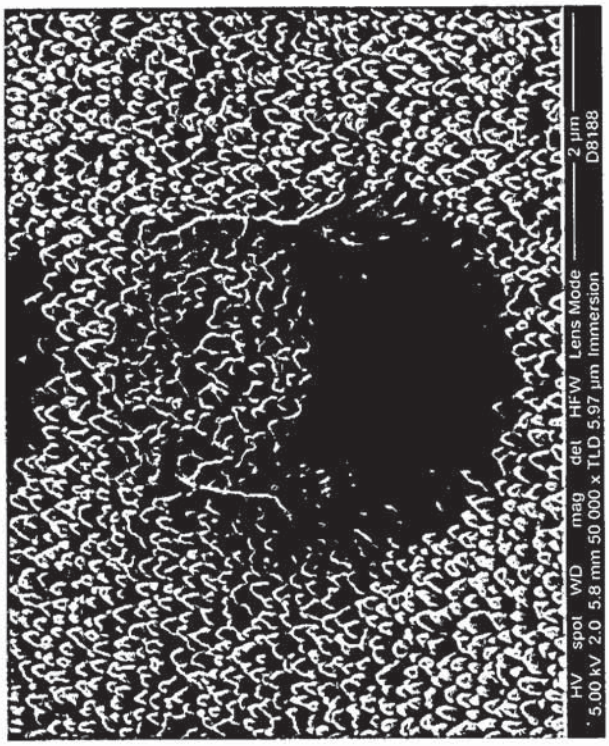
HV spot WD mag det HFW Lens Mode 2 µm
5.00 kV 2.0 5.8 mm 50 000 x TLD 5.97 µm Immersion D8188

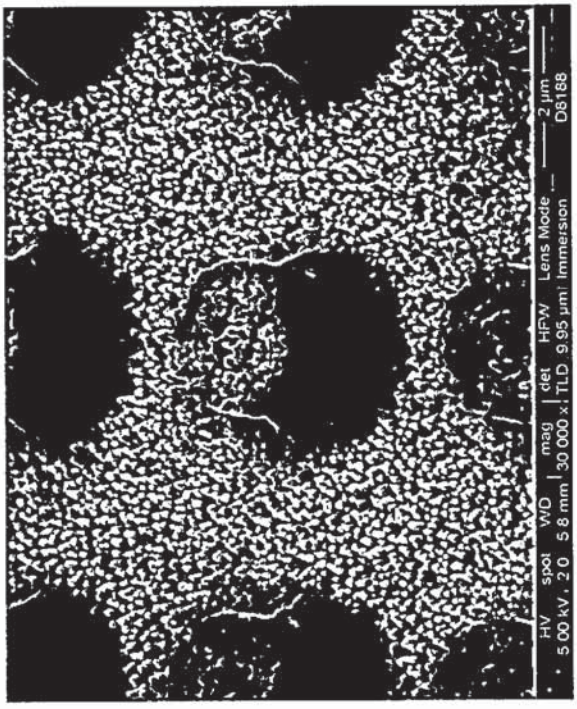
HV spot WD mag det HFW Lens Mode 2 µm
5.00 kV 2.0 5.8 mm 30 000 x TLD 9.95 µm Immersion D8188

Fig. 5

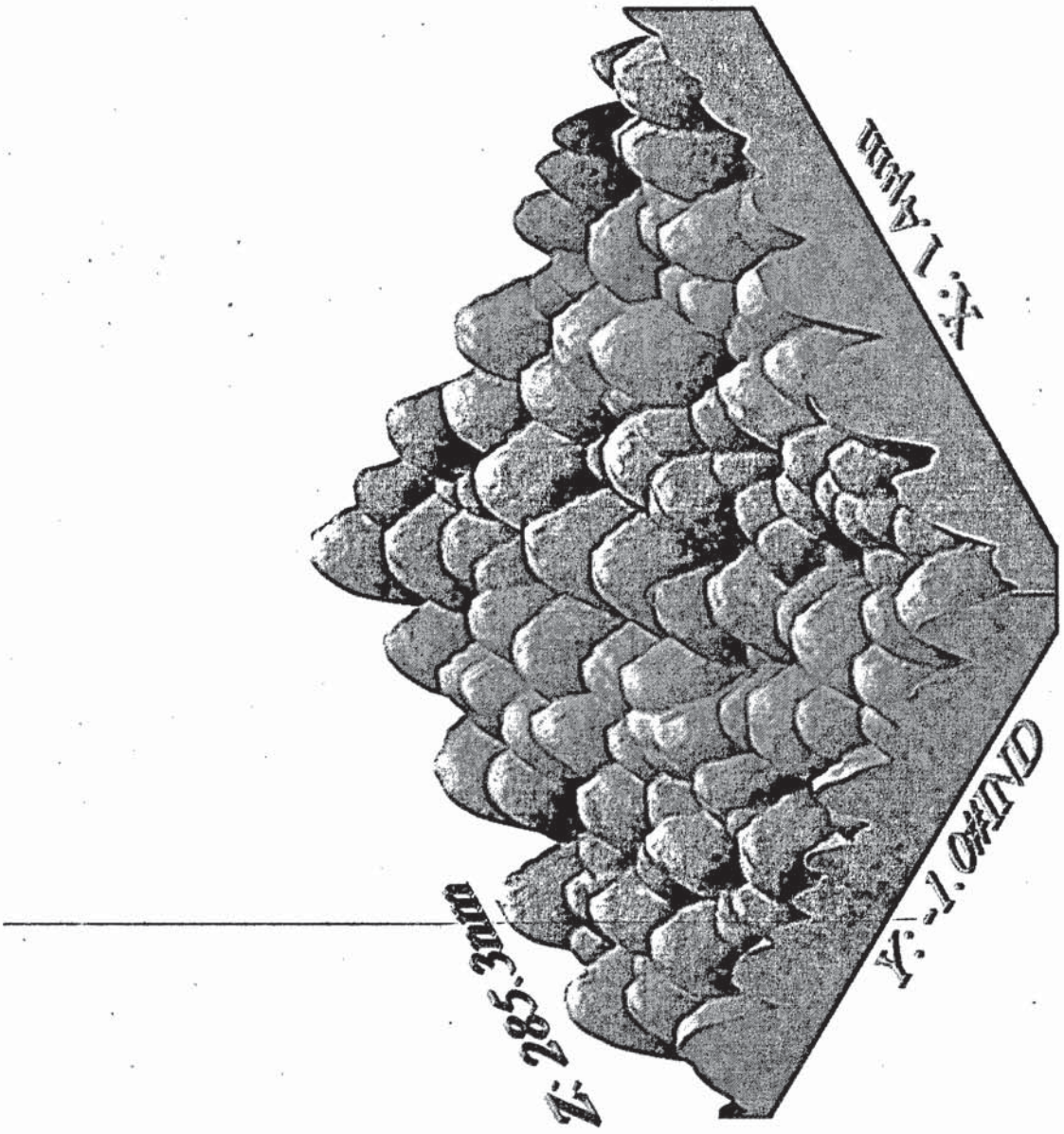

Fig. 6

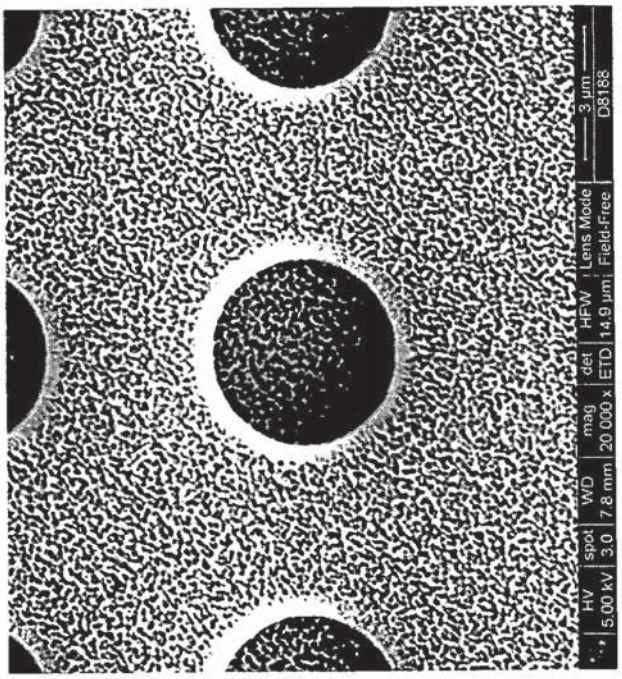
HV
5.00 kV
spot
3.0
WD
7.8 mm
mag
20 000 x
det
ETD
HFW
14.9 µm
Lens Mode
Field-Free
3 µm
D8188

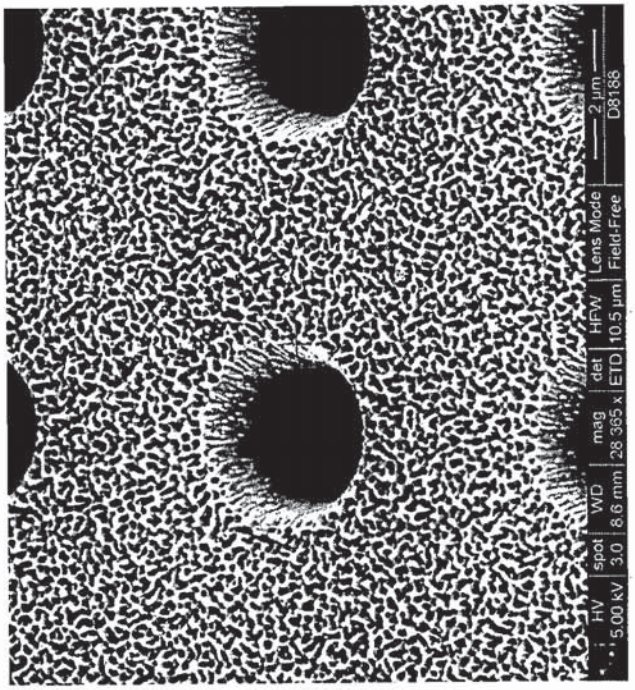
HV
5.00 kV
spot
3.0
WD
8.6 mm
mag
28 385 x
det
ETD
HFW
10.5 µm
Lens Mode
Field-Free
2 µm
D8188

Fig. 7

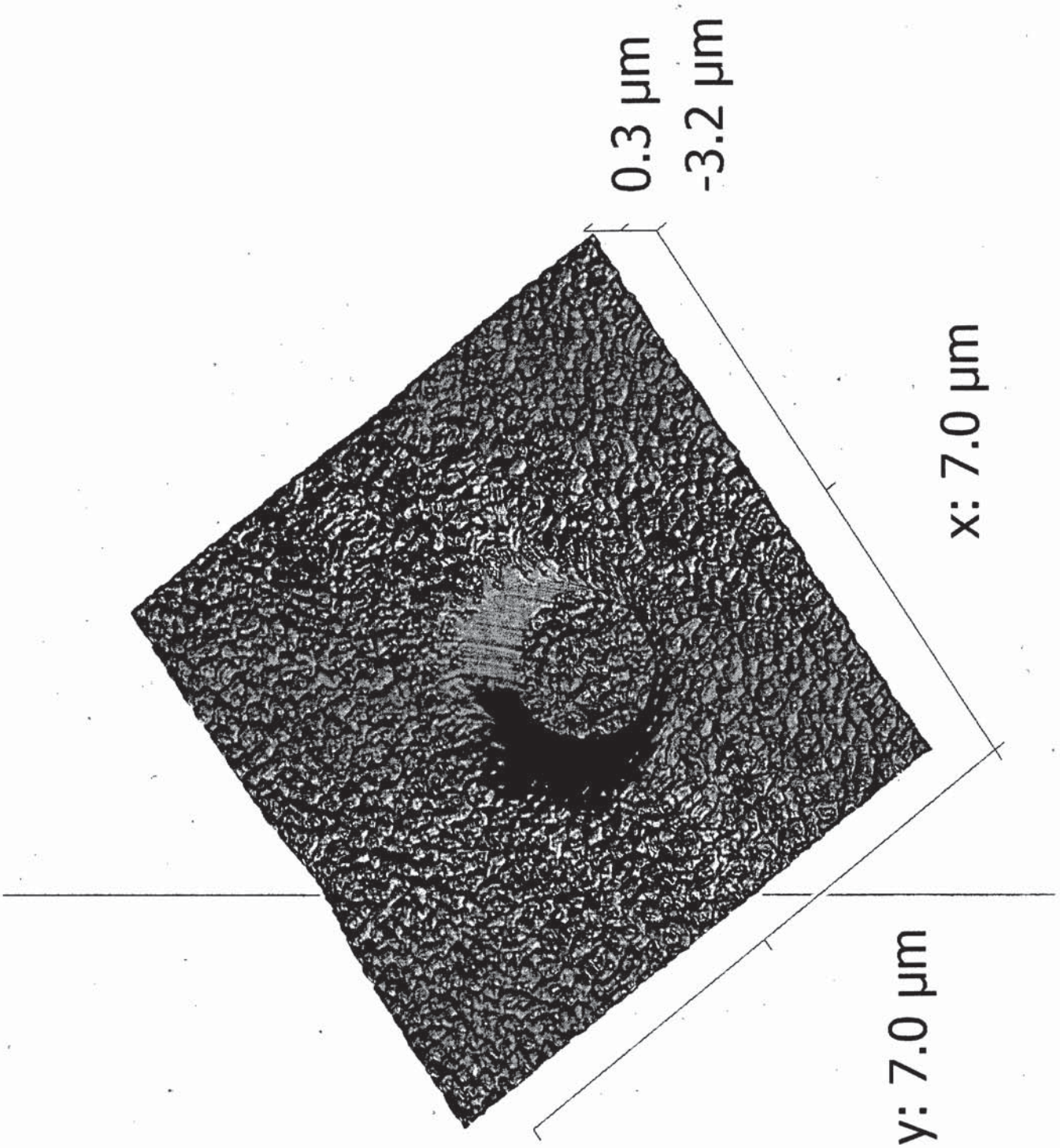

Fig. 8

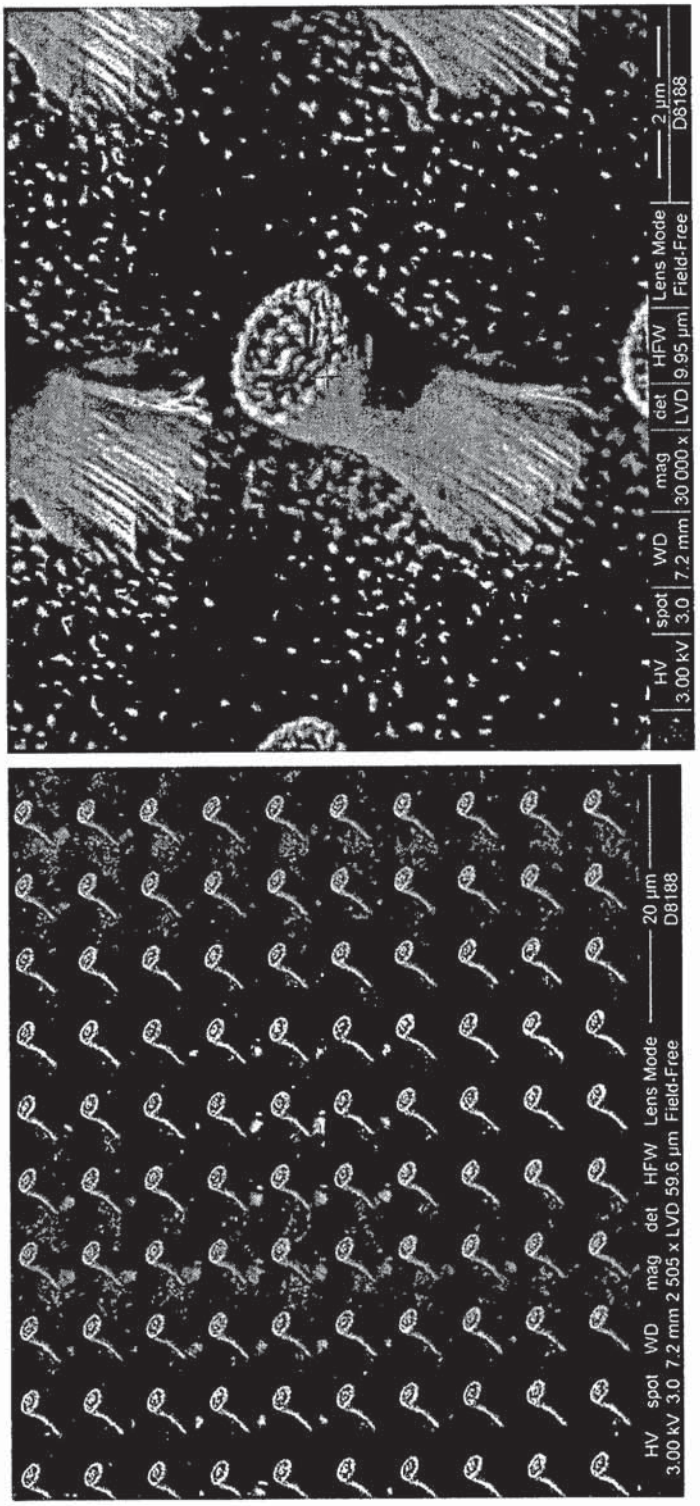
HV 3.00 kV
Spot 3.0
WD 7.2 mm
mag 30 000 x
det LVD
HFW 9.95 µm
Lens Mode Field-Free
2 µm
D8188
HV 3.00 kV
spot 3.0
WD 7.2 mm
mag 2 505 x
det LVD
HFW 59.6 µm
Lens Mode Field-Free
20 µm
D8188

Fig. 9

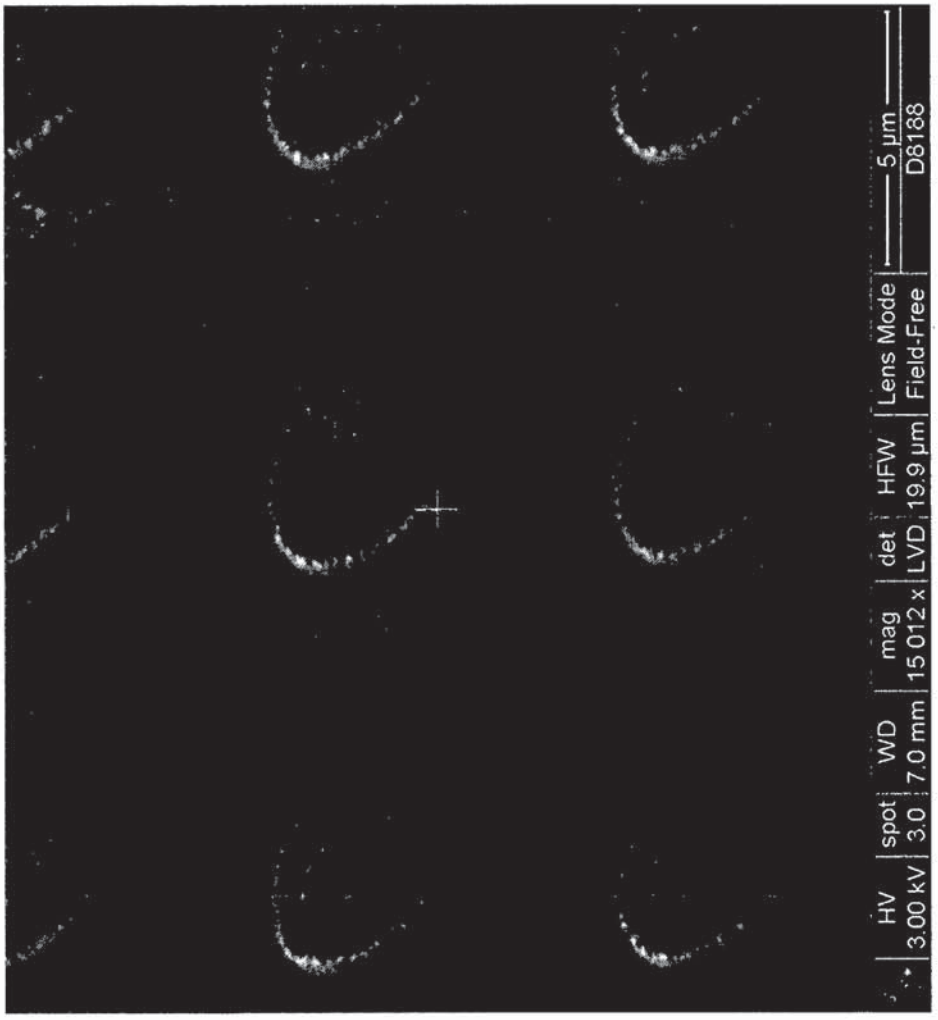
HV
3.00 kV
spot
3.0
WD
7.0 mm
mag
15 012 x
det
LVD
HFW
19.9 µm
Lens Mode
Field-Free
5 µm
D8138

Fig. 10

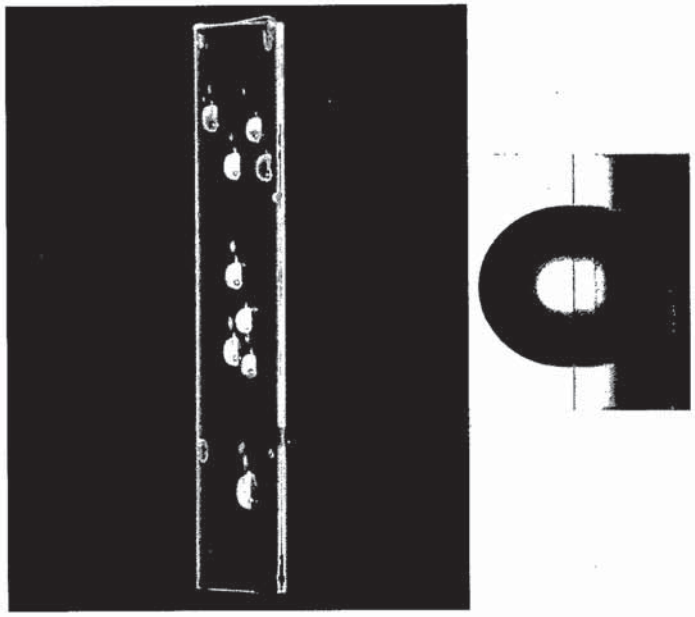

Fig. 11

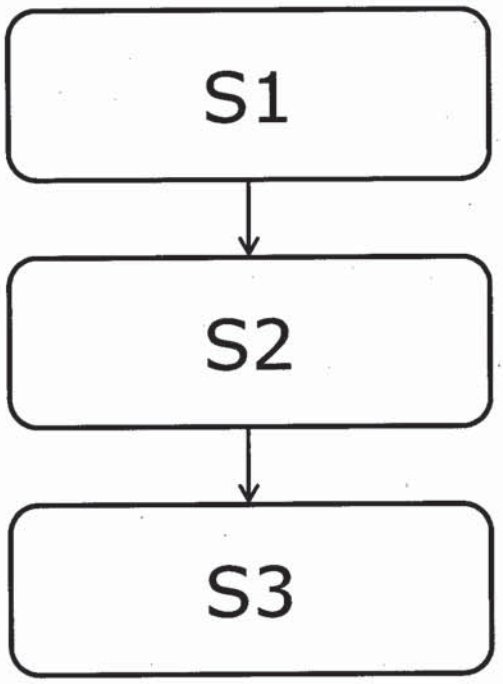

Fig. 12

INTERNATIONAL SEARCH REPORT

International application No
PCT/DK2013/050060

A. CLASSIFICATION OF SUBJECT MATTER
INV. G03F7/00 B29C33/42 B29C45/26
ADD.

According to International Patent Classification (IPC) or to both national classification and IPC

B. FIELDS SEARCHED

Minimum documentation searched (classification system followed by classification symbols)
G03F B29C

Documentation searched other than minimum documentation to the extent that such documents are included in the fields searched

Electronic data base consulted during the international search (name of data base and, where practicable, search terms used)
EPO-Internal, WPI Data, IBM-TDB, INSPEC, COMPENDEX

C. DOCUMENTS CONSIDERED TO BE RELEVANT

Category*	Citation of document, with indication, where appropriate, of the relevant passages	Relevant to claim No.
X	US 2007/115554 A1 (BREITUNG ERIC M [US] ET AL) 24 May 2007 (2007-05-24)	16
Y	paragraph [0020] - paragraph [0025]; figures 4,5 paragraph [0032]	1-15

X	US 2011/287203 A1 (VICTOR JARED J [CA] ET AL) 24 November 2011 (2011-11-24)	16
Y	paragraph [0082] - paragraph [0087]; figure 1	1-15

X	WO 02/22304 A1 (BAERLOCHER GMBH [DE]; HAUK JUERGEN [DE]; REITH WALTER [DE]; KUERZINGER) 21 March 2002 (2002-03-21)	16
Y	page 3, line 12 - line 25 page 6, line 1 - line 8; claim 5	1-15

	-/--	

[X] Further documents are listed in the continuation of Box C.

[X] See patent family annex.

* Special categories of cited documents :

"A" document defining the general state of the art which is not considered to be of particular relevance

"E" earlier application or patent but published on or after the international filing date

"L" document which may throw doubts on priority claim(s) or which is cited to establish the publication date of another citation or other special reason (as specified)

"O" document referring to an oral disclosure, use, exhibition or other means

"P" document published prior to the international filing date but later than the priority date claimed

"T" later document published after the international filing date or priority date and not in conflict with the application but cited to understand the principle or theory underlying the invention

"X" document of particular relevance; the claimed invention cannot be considered novel or cannot be considered to involve an inventive step when the document is taken alone

"Y" document of particular relevance; the claimed invention cannot be considered to involve an inventive step when the document is combined with one or more other such documents, such combination being obvious to a person skilled in the art

"&" document member of the same patent family

Date of the actual completion of the international search	Date of mailing of the international search report
24 July 2013	01/08/2013

Name and mailing address of the ISA/	Authorized officer
European Patent Office, P.B. 5818 Patentlaan 2 NL - 2280 HV Rijswijk Tel. (+31-70) 340-2040, Fax: (+31-70) 340-3016	Haenisch, Ulrich

INTERNATIONAL SEARCH REPORT

International application No
PCT/DK2013/050060

C(Continuation). DOCUMENTS CONSIDERED TO BE RELEVANT

Category*	Citation of document, with indication, where appropriate, of the relevant passages	Relevant to claim No.
Y	US 5 674 592 A (CLARK JOHN C [US] ET AL) 7 October 1997 (1997-10-07) abstract; figures 2,4 -----	1-15

INTERNATIONAL SEARCH REPORT

Information on patent family members

International application No
PCT/DK2013/050060

Patent document cited in search report	Publication date	Patent family member(s)	Publication date
US 2007115554 A1	24-05-2007	TW 200823485 A	01-06-2008
		US 2007115554 A1	24-05-2007
US 2011287203 A1	24-11-2011	CA 2800381 A1	01-12-2011
		EP 2576171 A1	10-04-2013
		US 2011287203 A1	24-11-2011
		WO 2011147757 A1	01-12-2011
WO 0222304 A1	21-03-2002	NONE	
US 5674592 A	07-10-1997	AU 5373996 A	21-11-1996
		CA 2216378 A1	07-11-1996
		CN 1183739 A	03-06-1998
		DE 69604915 D1	02-12-1999
		DE 69604915 T2	18-05-2000
		EP 0825901 A1	04-03-1998
		JP 3723218 B2	07-12-2005
		JP H11504281 A	20-04-1999
		US 5674592 A	07-10-1997
		WO 9634697 A1	07-11-1996

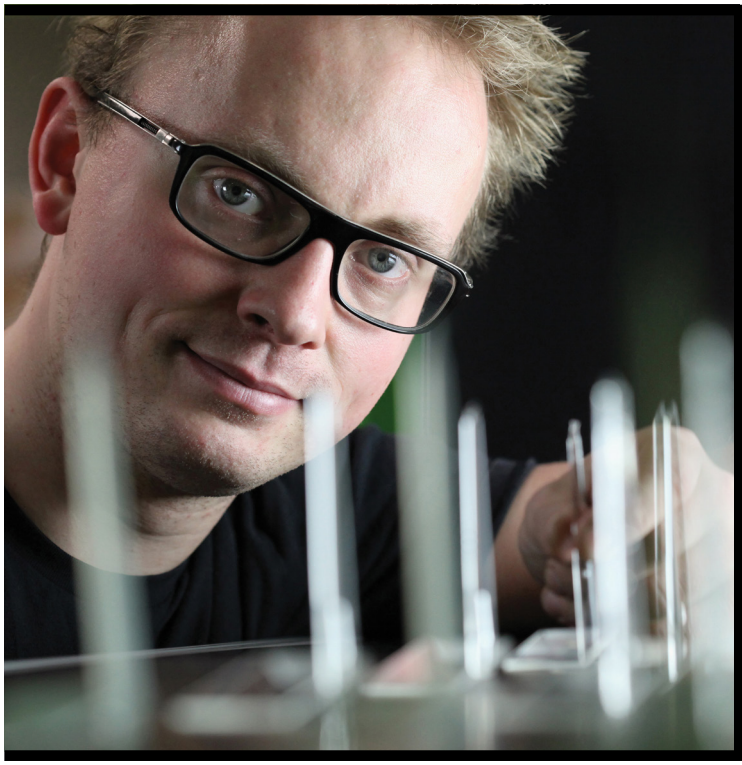

Published by:
DTU Nanotech
Department of Micro- and Nanotechnology
Technical University of Denmark
Ørsteds Plads, building 345B
DK-2800 Kgs. Lyngby